

Spring 4-13-2015

# Development and Application of a Numerical Framework for Improving Building Foundation Heat Transfer Calculations

Nathanael John Frothingham Kruis  
*University of Colorado at Boulder*, [kruis@colorado.edu](mailto:kruis@colorado.edu)

Follow this and additional works at: [https://scholar.colorado.edu/cven\\_gradetds](https://scholar.colorado.edu/cven_gradetds)

 Part of the [Architectural Engineering Commons](#), and the [Energy Systems Commons](#)

---

## Recommended Citation

Kruis, Nathanael John Frothingham, "Development and Application of a Numerical Framework for Improving Building Foundation Heat Transfer Calculations" (2015). *Civil Engineering Graduate Theses & Dissertations*. 125.  
[https://scholar.colorado.edu/cven\\_gradetds/125](https://scholar.colorado.edu/cven_gradetds/125)

This Dissertation is brought to you for free and open access by Civil, Environmental, and Architectural Engineering at CU Scholar. It has been accepted for inclusion in Civil Engineering Graduate Theses & Dissertations by an authorized administrator of CU Scholar. For more information, please contact [cuscholaradmin@colorado.edu](mailto:cuscholaradmin@colorado.edu).

**Development and Application of a Numerical Framework  
for Improving Building Foundation Heat Transfer  
Calculations**

by

**Nathanael J. F. Kruis**

B.S., Calvin College, 2007

A thesis submitted to the  
Faculty of the Graduate School of the  
University of Colorado in partial fulfillment  
of the requirements for the degree of  
Doctor of Philosophy  
Department of Civil, Environmental and Architectural Engineering

2015

This thesis entitled:  
Development and Application of a Numerical Framework for Improving Building Foundation Heat  
Transfer Calculations  
written by Nathanael J. F. Kruis  
has been approved for the Department of Civil, Environmental and Architectural Engineering

---

Prof. Moncef Krarti

---

Michael Brandemuehl

---

Harihar Rajaram

---

Marcus Bianchi

---

Michael Deru

Date \_\_\_\_\_

The final copy of this thesis has been examined by the signatories, and we find that both the content and the form meet acceptable presentation standards of scholarly work in the above mentioned discipline.

Kruis, Nathanael J. F. (Ph.D.)

Development and Application of a Numerical Framework for Improving Building Foundation Heat Transfer Calculations

Thesis directed by Prof. Moncef Krarti

Heat transfer from building foundations varies significantly in all three spatial dimensions and has important dynamic effects at all timescales, from one hour to several years. With the additional consideration of moisture transport, ground freezing, evapotranspiration, and other physical phenomena, the estimation of foundation heat transfer becomes increasingly sophisticated and computationally intensive to the point where accuracy must be compromised for reasonable computation time. The tools currently available to calculate foundation heat transfer are often either too limited in their capabilities to draw meaningful conclusions or too sophisticated to use in common practices.

This work presents Kiva, a new foundation heat transfer computational framework. Kiva provides a flexible environment for testing different numerical schemes, initialization methods, spatial and temporal discretizations, and geometric approximations. Comparisons within this framework provide insight into the balance of computation speed and accuracy relative to highly detailed reference solutions.

The accuracy and computational performance of six finite difference numerical schemes are verified against established *IEA BESTEST* test cases for slab-on-grade heat conduction. Of the schemes tested, the Alternating Direction Implicit (ADI) scheme demonstrates the best balance between accuracy, performance, and numerical stability.

Kiva features four approaches of initializing soil temperatures for an annual simulation. A new accelerated initialization approach is shown to significantly reduce the required years of pre-simulation.

Methods of approximating three-dimensional heat transfer within a representative two-dimensional context further improve computational performance. A new approximation called the boundary layer adjustment method is shown to improve accuracy over other established methods with a negligible increase in computation time. This method accounts for the reduced heat transfer from concave foundation shapes, which has not been adequately addressed to date. Within the Kiva framework, three-dimensional heat transfer that can require several days to simulate is approximated in two-dimensions in a matter of seconds while maintaining a mean absolute deviation within 3%.

## Acknowledgements

This work was funded in part by an American Society of Heating Refrigeration and Air conditioning Engineers (ASHRAE) Graduate Student Grant-in-Aid award.

Simulations were performed on the Janus supercomputer, which is supported by the National Science Foundation (award number CNS-0821794) and the University of Colorado.

This work would not be possible without the help and guidance of my advisor Dr. Moncef Krarti. You always encouraged me to explore deeper and develop a broader understanding.

I would like to thank Peter Ellis, President of Big Ladder Software, for allocating time and resources to enable this work. Also, thanks to Joe Huang President of White Box Technologies for giving me the idea for a faster ground temperature initialization method.

A special thanks to Ben Rohrs, for his friendship, support, and accountability, and Becky McKay, who generously volunteered time to edit parts of this thesis.

To Dr. Mary Poel and Dr. Rick Kruis, without whom I would not have made it where I have (let alone existed). Thank you, mom and dad, for your love, support, and the opportunities you have enabled for me through your own hard work.

Most importantly I want to thank my wife, Cameron Frothingham Kruis, for the support and encouragement she provided throughout working on this thesis. You demonstrated confidence in me when I could not find it in myself.

## Contents

### Chapter

<b>1</b>	Introduction	1
1.1	Motivation . . . . .	1
1.2	Objectives . . . . .	3
1.3	Organization of the Thesis . . . . .	3
<b>2</b>	Literature Review	5
2.1	Terminology . . . . .	5
2.2	Description of Modeling and Simulation Capabilities . . . . .	6
2.2.1	Foundation Design . . . . .	6
2.2.2	Ground Domain . . . . .	12
2.2.3	Boundary Conditions . . . . .	14
2.2.4	The Whole-Building Context . . . . .	24
2.3	Computational Algorithms . . . . .	25
2.3.1	Heat Diffusion . . . . .	26
2.3.2	Moisture Diffusion . . . . .	29
2.3.3	Common Simplifications . . . . .	32
2.3.4	Solution Methods . . . . .	33
2.3.5	Discretization . . . . .	37
2.4	Validation, Verification, and Testing . . . . .	41

2.4.1	Empirical Validation . . . . .	42
2.4.2	Analytical Verification . . . . .	43
2.4.3	Comparative Testing . . . . .	44
2.5	Comparison of Prominent Tools and Methods . . . . .	44
2.5.1	ASHRAE Design Calculations . . . . .	46
2.5.2	Interzone Temperature Profile Estimation (ITPE) Technique . . . . .	46
2.5.3	EnergyPlus Preprocessors . . . . .	46
2.5.4	eQUEST . . . . .	47
2.5.5	Ground Heat and Moisture Transfer (GHMT) . . . . .	48
2.5.6	TRNSYS . . . . .	48
<b>3</b>	<b>Tool Development</b>	<b>50</b>
3.1	Kiva . . . . .	50
3.2	Development Philosophy . . . . .	53
3.3	Modeling and Simulation Capabilities . . . . .	53
3.3.1	Foundation Design . . . . .	54
3.3.2	Ground Domain . . . . .	57
3.3.3	Boundary Conditions . . . . .	58
3.3.4	The Whole-Building Context . . . . .	60
3.4	Computational Algorithms . . . . .	60
3.4.1	Heat Diffusion . . . . .	60
3.4.2	Discretization . . . . .	61
3.4.3	Finite Difference Methods . . . . .	64
3.5	Outputs . . . . .	73
<b>4</b>	<b>Solution Verification</b>	<b>76</b>
4.1	<i>IEA BESTEST</i> for Ground Coupled Heat Transfer . . . . .	77
4.1.1	Steady-State Test Cases . . . . .	79



4.1.2	Steady-State Test Case Results . . . . .	86
4.1.3	Harmonic (Unsteady) Test Cases . . . . .	90
4.1.4	Harmonic (Unsteady) Test Case Results . . . . .	96
4.2	Summary and Conclusions . . . . .	100
<b>5</b>	<b>Two-Dimensional Approximation Methods</b>	<b>103</b>
5.1	Current Approximation Methods . . . . .	104
5.1.1	Perimeter . . . . .	104
5.1.2	Area-to-Perimeter Ratio . . . . .	105
5.1.3	Rounded Rectangle . . . . .	109
5.2	Heat Transfer from Concave Foundation Shapes . . . . .	110
5.2.1	Opposing Parallel Edges . . . . .	111
5.2.2	Concave Corners . . . . .	116
5.2.3	Compounding Cavity Effects . . . . .	122
5.3	Boundary Layer Adjustment Method . . . . .	124
5.3.1	Opposing Parallel Edges . . . . .	125
5.3.2	Concave Corners . . . . .	126
5.4	Description of Approximation Method Tests . . . . .	127
5.4.1	Climates . . . . .	127
5.4.2	Foundation Designs . . . . .	128
5.4.3	Foundation Shapes . . . . .	129
5.5	Initial Shape Analysis . . . . .	131
5.6	Approximation Method Accuracy . . . . .	134
5.7	Approximation Method Simulation Time . . . . .	140
5.8	Summary and Conclusions . . . . .	142
<b>6</b>	<b>Conclusions and Future Work</b>	<b>144</b>
6.1	Conclusions . . . . .	144

6.2	Future Work . . . . .	145
6.2.1	Whole-Building Energy Simulation Tools . . . . .	145
6.2.2	Foundation Design Guidelines . . . . .	146
6.2.3	Additional Capabilities . . . . .	146
6.2.4	Sensitivity to Model Parameters . . . . .	147
6.2.5	Performance Optimization . . . . .	147
<b>Bibliography</b>		149
<b>Appendix</b>		
<b>A</b>	Finite Difference Discretizations	158
A.1	Continuous Equation . . . . .	158
A.2	Boundary Conditions . . . . .	159
A.3	Discretized Equations . . . . .	160
A.3.1	Explicit Scheme . . . . .	163
A.3.2	Fully Implicit Scheme . . . . .	164
A.3.3	Crank-Nicolson Scheme . . . . .	165
A.3.4	Alternating Direction Explicit (ADE) Scheme . . . . .	166
A.3.5	Alternating Direction Implicit (ADI) Scheme . . . . .	168
A.3.6	Steady-State Solution . . . . .	170
A.4	Solving the Linear System of Equations . . . . .	171
<b>B</b>	Mixed Climate Two-Dimensional Approximation Method Test Results	172
<b>C</b>	Cold Climate Two-Dimensional Approximation Method Test Results	177
<b>D</b>	Hot Climate Two-Dimensional Approximation Method Test Results	184

**E** Comparisons of Minimum and Maximum Foundation Heat Transfer

191

## Tables

### Table

2.1	Example roughness factors . . . . .	18
2.2	Terrain parameters for wind speed corrections . . . . .	19
2.3	Comparison of prominent foundation heat transfer tools and methods . . . . .	45
3.1	Example foundation types available in Kiva . . . . .	75
4.1	<i>BESTEST</i> steady-state test case specifications . . . . .	79
4.2	Mesh detail parameters selected by each tool for <i>IEA BESTEST</i> analyses . . . . .	83
4.3	Selected numerical parameters for Kiva analyses . . . . .	86
4.4	<i>BESTEST</i> steady-state test case results: Slab heat loss [W] . . . . .	88
4.5	<i>BESTEST</i> steady-state test case simulation wall times [s] . . . . .	88
4.6	<i>BESTEST</i> harmonic test cases specifications . . . . .	90
4.7	<i>BESTEST</i> GC40a initialization method percent difference from “ideal” for seven years of simulation . . . . .	94
4.8	<i>BESTEST</i> harmonic (unsteady) test case results: Annual slab heat loss [MWh] . . .	96
4.9	<i>BESTEST</i> GC40 harmonic parameters for each solution (shading indicates deviation from the median value for each case) . . . . .	99
4.10	ADE time-step size for harmonic <i>BESTEST</i> cases . . . . .	99
4.11	<i>BESTEST</i> harmonic (unsteady) test case results: Simulation wall time [s] . . . . .	101
5.1	Approximation method testing conditions . . . . .	128

5.2	Compactness of various shapes . . . . .	133
5.3	List of two-dimensional approximation methods tested . . . . .	134
5.4	Average simulation wall time for two-dimensional approximation methods . . . . .	140
6.1	Recommended methods and numerical parameters for foundation heat transfer . . .	145

## Figures

### Figure

2.1	Types of building foundations . . . . .	7
2.2	Examples of insulation designs . . . . .	8
2.3	Examples of thermal bridges for a slab-on-grade foundation . . . . .	10
2.4	Illustration of ITPE zones (1, 2, and 3) for a basement foundation (adapted from Krarti et al. [70]) . . . . .	49
2.5	Concentric heat flow paths (adapted from Latta and Boileau [79]) . . . . .	49
3.1	Two-dimensional context for defining foundation design in Kiva . . . . .	54
3.2	Insulation and structural design elements in Kiva . . . . .	56
3.3	Plan view illustration of far-field boundary definition in three-dimensions and foundation shape vertex definition . . . . .	57
3.4	Discretization regions . . . . .	62
3.5	Example Kiva discretizations . . . . .	62
3.6	Boundary cells and resulting zero-thickness cells. Black nodes = normal solid cells, white nodes = boundary cells, gray nodes = zero-thickness cells, hollow nodes = air cells. . . . .	63
3.7	Example finite difference scheme (black nodes are known values, white nodes are unknown values) . . . . .	64
3.8	Illustration of simple explicit finite difference scheme . . . . .	65

3.9	Illustration of fully implicit finite difference scheme . . . . .	66
3.10	Illustration of Crank-Nicolson finite difference scheme . . . . .	67
3.11	Illustration of ADE finite difference scheme: upward sweep . . . . .	68
3.12	Illustration of ADE finite difference scheme: downward sweep . . . . .	69
3.13	Typical implicit matrix sparsity pattern for three dimensions (up to seven unknowns per equation) . . . . .	70
3.14	ADI matrix sparsity pattern for three dimensions (up to three unknowns per equation)	71
3.15	Example Kiva graphical output . . . . .	74
4.1	<i>BESTEST</i> GC10a mesh growth near the wall boundary . . . . .	81
4.2	<i>BESTEST</i> GC10a slab heat loss sensitivity to mesh detail parameters . . . . .	82
4.3	<i>BESTEST</i> GC10a simulation wall time sensitivity to mesh detail parameters . . . . .	82
4.4	<i>BESTEST</i> GC10a slab heat loss sensitivity to boundary distances . . . . .	84
4.5	<i>BESTEST</i> GC10a simulation wall time sensitivity to boundary distances . . . . .	84
4.6	<i>BESTEST</i> GC10a slab heat loss and simulation wall time sensitivity to linear solver tolerance . . . . .	85
4.7	<i>BESTEST</i> steady-state test case slab heat loss . . . . .	87
4.8	<i>BESTEST</i> steady-state test case simulation wall times (note logarithmic $y$ -axis) . . . . .	88
4.9	<i>BESTEST</i> GC40a comparison of initialization methods: First year slab heat loss . . . . .	92
4.10	<i>BESTEST</i> GC40a comparison of initialization methods: Annual slab heat loss for seven years after initialization . . . . .	93
4.11	<i>BESTEST</i> GC40a comparison of first year slab heat loss for traditional and accel- erated initialization methods . . . . .	95
4.12	<i>BESTEST</i> harmonic (unsteady) test case annual slab heat loss (results for GC50b are divided by 10 to maintain a consistent scale) . . . . .	97
4.13	<i>BESTEST</i> GC40a harmonic (unsteady) test case hourly results . . . . .	98
4.14	<i>BESTEST</i> harmonic (unsteady) test case simulation wall times . . . . .	100

5.1	Typical context for two-dimensional approximations . . . . .	104
5.2	Characteristic length of a circle in a cylindrical coordinate system . . . . .	107
5.3	Characteristic length of a infinite rectangle in a Cartesian coordinate system . . . . .	108
5.4	Dimensions of a rounded rectangle with equivalent area and perimeter . . . . .	110
5.5	Determination of cavities for various shapes . . . . .	111
5.6	Plan view cross-section at grade height of heat flux near a concave slab corner (ex- terior grade in the upper left) . . . . .	112
5.7	Plan view of parallel concave edges . . . . .	113
5.8	Reduction in heat loss between two parallel concave edges over a range of area-to- perimeter ratios ( $k_{soil} = 1.0$ W/m·K, R-10 insulation) . . . . .	113
5.9	Reduction in heat loss between two parallel concave edges over a range of soil con- ductivity ( $A/P = 4.6$ m, R-10 insulation) . . . . .	114
5.10	Reduction in heat loss between two parallel concave edges over a range of insulation R-values [ $\text{hr}\cdot\text{ft}^2\cdot\text{R}/\text{Btu}$ ] ( $k_{soil} = 1.0$ W/m·K, $A/P = 4.6$ m) . . . . .	115
5.11	Illustration of a heat flux boundary layer profile for a slab with exterior horizontal insulation . . . . .	116
5.12	Example boundary layer profile for a slab with exterior horizontal insulation ( $k_{soil} =$ $1.0$ W/m·K, $A/P = 4.6$ m, R-10 insulation) . . . . .	117
5.13	Shapes with equal area and perimeter but different number of concave corners . . . . .	118
5.14	Reduction in heat loss due to corners over a range of area-to-perimeter ratios ( $k_{soil} =$ $1.0$ W/m·K, R-10 insulation) . . . . .	119
5.15	Reduction in heat loss due to corners over a range of soil conductivity ( $A/P = 4.6$ m, R-10 insulation) . . . . .	119
5.16	Reduction in heat loss due to corners over a range of insulation R-values ( $k_{soil} = 1.0$ W/m·K, $A/P = 4.6$ m) . . . . .	120
5.17	Illustration of corner bisector and unaffected edge boundary profile cross-sections . . . . .	121
5.18	Comparison of straight boundary profile and corner bisector . . . . .	122



5.19	Heat loss reduction from H-shaped slabs . . . . .	123
5.20	Variables used to adjust perimeter of opposing parallel edges . . . . .	125
5.21	Variables used to adjust perimeter of concave corners . . . . .	126
5.22	Annual outdoor dry-bulb temperatures from weather data files for selected climates. Hot = Phoenix, Arizona; Mixed = Albuquerque, New Mexico; Cold = Anchorage, Alaska . . . . .	129
5.23	Slab insulation configurations for approximation method tests . . . . .	130
5.24	Crawlspace insulation configurations for approximation method tests . . . . .	131
5.25	Basement insulation configurations for approximation method tests . . . . .	132
5.26	Shapes simulated in three dimensions for approximation method testing. Each plot is 200 m $\times$ 200 m. $A$ = Area, $C$ = Compactness. . . . .	134
5.27	Comparison of heat flux from a range of uninsulated foundation shapes . . . . .	135
5.28	Heat flux reduction relative to uninsulated foundations in mixed climate for a range of foundation shapes . . . . .	136
5.29	Comparison of annual total heat transfer between three-dimensions and two-dimensional approximations for mixed climate simulations . . . . .	137
5.30	Comparison of annual total heat transfer between three-dimensions and two-dimensional approximations for cold climate simulations . . . . .	138
5.31	Comparison of annual total heat transfer between three-dimensions and two-dimensional approximations for hot climate simulations . . . . .	139
5.32	Example comparison of hourly three-dimensional heat transfer and approximated two-dimensional heat transfer . . . . .	140
5.33	Two-dimensional approximation simulation wall times . . . . .	141
5.34	Deviation from three-dimensional annual heat transfer vs. simulation wall time for different combinations of discretization parameters . . . . .	142

B.1	Percent difference in annual heat transfer between three-dimensional square foundation shapes and two-dimensional approximations . . . . .	173
B.2	Percent difference in annual heat transfer between three-dimensional cross-shaped foundations and two-dimensional approximations . . . . .	174
B.3	Percent difference in annual heat transfer between three-dimensional narrow-H foundation shapes and two-dimensional approximations . . . . .	175
B.4	Percent difference in annual heat transfer between three-dimensional wide-H foundation shapes and two-dimensional approximations . . . . .	176
C.1	Comparison of heat flux from a range of uninsulated foundation shapes in the cold climate . . . . .	178
C.2	Heat flux reduction relative to uninsulated foundations in mixed climate for a range of foundation shapes in the cold climate . . . . .	179
C.3	Percent difference in annual heat transfer between three-dimensional square foundation shapes and two-dimensional approximations in the cold climate . . . . .	180
C.4	Percent difference in annual heat transfer between three-dimensional cross-shaped foundations and two-dimensional approximations in the cold climate . . . . .	181
C.5	Percent difference in annual heat transfer between three-dimensional narrow-H foundation shapes and two-dimensional approximations in the cold climate . . . . .	182
C.6	Percent difference in annual heat transfer between three-dimensional wide-H foundation shapes and two-dimensional approximations in the cold climate . . . . .	183
D.1	Comparison of heat flux from a range of uninsulated foundation shapes in the hot climate . . . . .	185
D.2	Heat flux reduction relative to uninsulated foundations in mixed climate for a range of foundation shapes in the hot climate . . . . .	186
D.3	Percent difference in annual heat transfer between three-dimensional square foundation shapes and two-dimensional approximations in the hot climate . . . . .	187

D.4	Percent difference in annual heat transfer between three-dimensional cross-shaped foundations and two-dimensional approximations in the hot climate . . . . .	188
D.5	Percent difference in annual heat transfer between three-dimensional narrow-H foundation shapes and two-dimensional approximations in the hot climate . . . . .	189
D.6	Percent difference in annual heat transfer between three-dimensional wide-H foundation shapes and two-dimensional approximations in the hot climate . . . . .	190
E.1	Comparison of annual minimum heat transfer between three-dimensions and two-dimensional approximations for mixed climate simulations . . . . .	192
E.2	Comparison of annual maximum heat transfer between three-dimensions and two-dimensional approximations for mixed climate simulations . . . . .	193
E.3	Comparison of annual minimum heat transfer between three-dimensions and two-dimensional approximations for cold climate simulations . . . . .	194
E.4	Comparison of annual maximum heat transfer between three-dimensions and two-dimensional approximations for cold climate simulations . . . . .	195
E.5	Comparison of annual minimum heat transfer between three-dimensions and two-dimensional approximations for hot climate simulations . . . . .	196
E.6	Comparison of annual maximum heat transfer between three-dimensions and two-dimensional approximations for hot climate simulations . . . . .	197

## Chapter 1

### Introduction

#### 1.1 Motivation

Building energy modeling has become an integral part of the design process for both new building projects and existing building retrofit projects. The tools used to simulate building performance allow designers to make informed, economic decisions on how to best invest in energy efficient improvements to buildings, even in the earliest planning stages.

Simulation tools can aid in the design of building foundations, just as they serve to inform the design of other components in buildings (walls, windows, lighting, HVAC equipment, etc.). To accomplish this, simulation tools must be capable of estimating the heat loss through building foundations under a range of conditions and insulation designs.

Heat loss from building foundations varies significantly in all three spatial dimensions and has important dynamic effects at all timescales, from one hour to several years. With the additional consideration of moisture transport, ground freezing, evapotranspiration, and other physical phenomena, the estimation of foundation heat transfer becomes increasingly sophisticated and computationally intensive to the point where accuracy must be compromised for reasonable computation time.

Traditional approaches to foundation heat transfer tend to be oversimplified or neglect the problem entirely because the overall magnitude of foundation heat fluxes is considered to be small relative to the other thermal loads in a building. However, as buildings become progressively more efficient, foundation heat loss begins to represent a larger portion of the total building load, thus

increasing the importance of accuracy in the calculations. It is estimated that heat transfer through foundations can account for 30%–50% of the total heating load in certain buildings [39].

Unfortunately, the tools currently available to calculate foundation heat transfer are often either too simplistic and limited in their capabilities to draw meaningful conclusions from the results or too sophisticated to use in common practices.

A common practice to address the computational complexity of foundation heat transfer is to ignore the problem altogether. Many practitioners use an adiabatic boundary condition for ground-coupled building surfaces in their models. As a result, the foundation of the building remains underdesigned relative to the rest of the energy-related features captured in the building simulation.

Another practice is to avoid simulating the heat transfer from the building foundation by simply overdesigning the foundation insulation. The Passivhaus strategy can specify up to 25.4 cm (10 in) of rigid foam insulation beneath the entire slab foundation [83]. Although some level of design does go into the Passivhaus specification, the level of detail and accuracy involved in the analysis is suspect, especially considering the economic implications.

In one extreme, there is the possibility of unrealized energy savings, and in the other, the builder is likely over-paying for the diminishing returns of additional insulation.

Heat transfer from building foundations remains a large uncertainty in the estimation of building energy use. An informal survey of energy modeling professionals indicates that the current practice with regard to modeling foundation heat transfer is either oversimplified or ignored entirely leading to low confidence in both simulation results and foundation design decisions. Many modelers are under the impression that foundation heat transfer is negligible and, therefore, justly ignored. However, when seeking a reference for such a claim, the author has found no such evidence.

The research presented in this thesis holds the following premise: Heat transfer through building foundations is not always negligible and, therefore, warrants the careful consideration of insulation design alternatives.

## 1.2 Objectives

The primary hypothesis of this research is as follows: A foundation heat transfer simulation tool can be developed to balance capability, complexity, computational performance, and algorithmic confidence to provide building designers with a tool that will allow them to make informed decisions on how to insulate building foundations.

The list below states the research questions that are answered within the content of this thesis:

- (1) What algorithmic assumptions and simplifications can reduce computation time while retaining accuracy and the more important modelling capabilities?
- (2) What are the accuracy and speed implications of these assumptions and simplifications?

To answer the research questions, the following objectives must be met:

- (1) Develop a detailed numerical truth standard as a benchmark for all subsequent assumptions and simplifications.
- (2) Recommend a set of assumptions and simplifications to perform accurate, computationally-efficient calculations of building foundation heat transfer within the context of whole-building energy analysis.

## 1.3 Organization of the Thesis

This thesis is organized into five chapters:

**Chapter 2: Literature Review:** A review of the foundation heat transfer methods and tools found in literature, including common capabilities, computational algorithms, and attempts to evaluate tool accuracy.

**Chapter 3: Tool Development:** A description of the tool developed for the work in this thesis.

**Chapter 4: Solution Verification:** Verification of the six solution methods implemented in said tool. This chapter also investigates solution sensitivity to selected numeric parameters and the efficiency of several initialization techniques within the context of a well-defined test specification.

**Chapter 5: Two-Dimensional Approximation Methods:** Approaches reducing computation time by approximating three-dimensional heat transfer using two-dimensional calculations.

**Chapter 6: Conclusions and Future Work:** Concluding statements and suggestions for future work.

## Chapter 2

### Literature Review

This chapter contains four sections, each describing a different aspect of foundation heat transfer simulations:

- (1) Terminology
- (2) Description of Modeling and Simulation Capabilities
- (3) Computational Algorithms
- (4) Validation, Verification, and Testing

A final section provides a comparison of prominent methods and tools found in both the literature and practice.

#### 2.1 Terminology

For the sake of consistency, standard terminology used throughout this thesis is defined below. These definitions are adapted from Fritzson [45] and Judkoff and Neymark [60]:

**System:** A system is an object or collection of objects whose properties are studied. The system under consideration in this thesis is the physical construction of the building foundation and the semi-infinite domain of ground surrounding the foundation.



**Model:** A model is an approximate representation of a system. The model is the set of input and output data values relevant to the study of the system. In this case, the model is the quantitative and qualitative description of the foundation and ground domain.

**Simulation:** Simulation is the process of applying controlled inputs to the model and observing the resulting outputs.

**Solution Method:** The solution method describes the algorithmic translation between model input and model output. For a foundation and ground system, the solution method generally refers to how the conduction-diffusion partial differential equations are solved including the algorithms that define the boundary conditions of the system.

**Tool:** A software implementation of a solution method (or multiple methods) capable of performing simulations on a defined model.

## 2.2 Description of Modeling and Simulation Capabilities

The following sections provide a review of modeling capabilities, both available in and missing from current foundation heat transfer tools. This informs which capabilities are important for the development of new tools and the challenges associated with implementing them.

### 2.2.1 Foundation Design

Foundation design capabilities are the tool's ability to define the physical construction details and engineering design of the foundation system.

#### 2.2.1.1 Foundation Types

Figure 2.1 shows a range of foundation types found throughout the architectural domain. Most tools can model the three standard foundation types (Figures 2.1(a)–2.1(c)). Even among these common foundation types, tools are often limited to specific foundation depths. Few tools have the capability to model less-common foundation types (Figures 2.1(d)–2.1(g)).

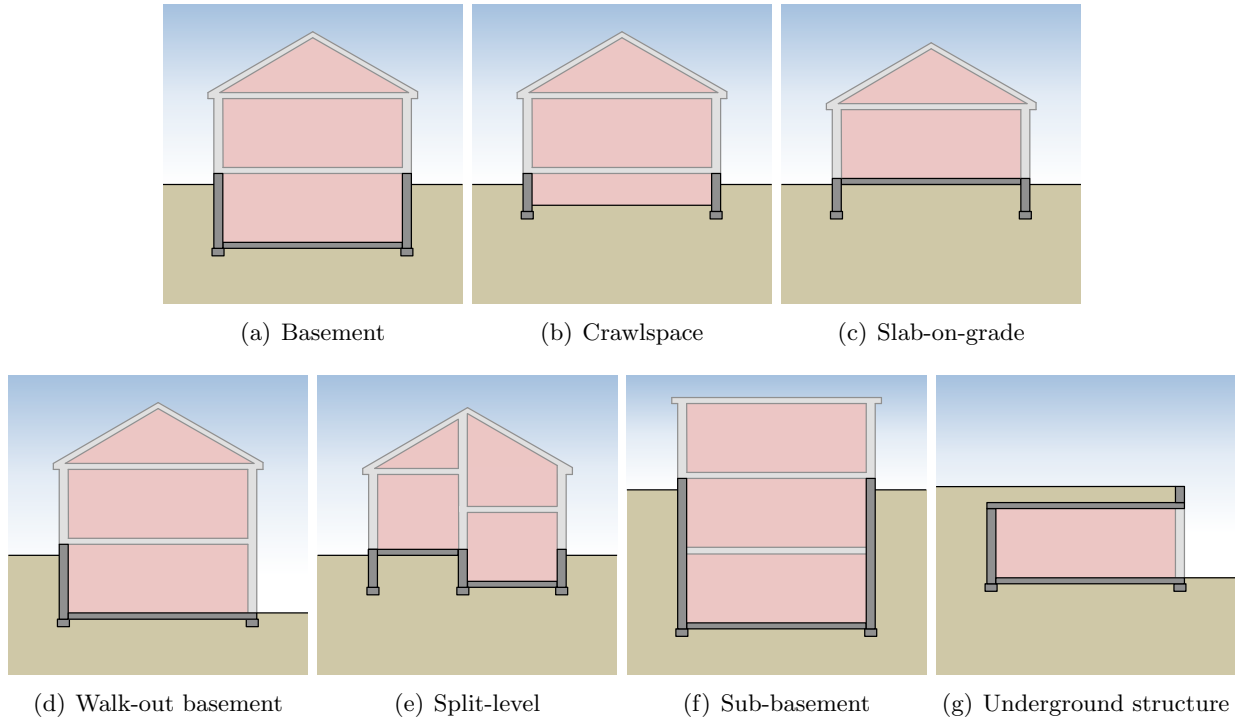


Figure 2.1: Types of building foundations

A few case studies in literature investigate heat loss from underground structures [23, 84] and slabs with a stepped-exterior grade [22], but these capabilities are rarely integrated into publicly available tools.

Accommodating many of these additional foundation types requires a more detailed description of a three-dimensional domain.

### 2.2.1.2 Insulation Design

For a given foundation type, a continuous range of potential foundation designs exists. Figure 2.2 shows examples of typical insulation designs for foundations. While Figure 2.2 represents only a small subset of the possible insulation designs, the full parameter space includes combinations of values of the following variables:

- The insulation material
- The level of insulation (insulation thickness)

- The location of the insulation (whole slab, interior horizontal, interior vertical, slab gap, interior vertical, in-wall, exterior vertical, exterior horizontal, and all combinations thereof)
- Insulation dimensions (depth of vertical insulation, width and depth of horizontal insulation)

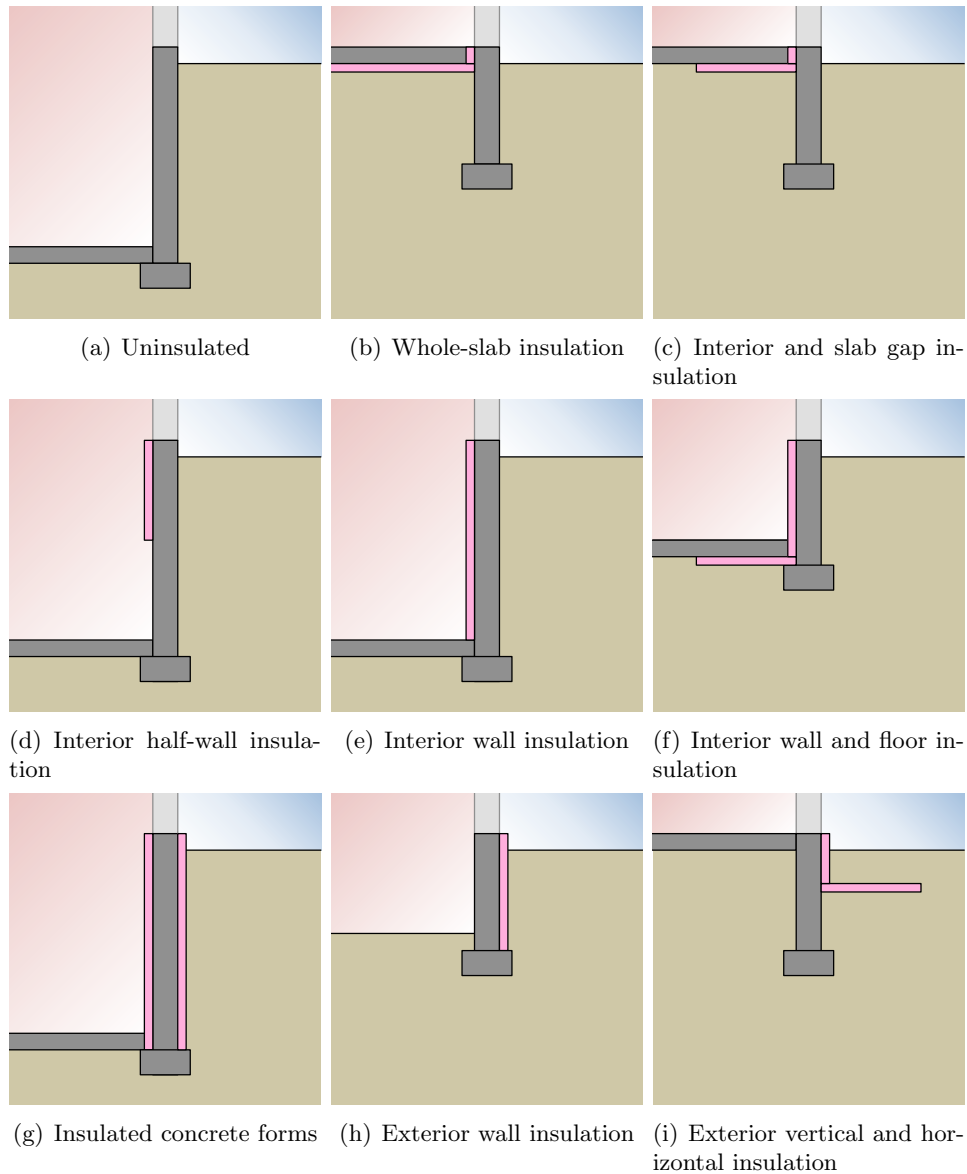


Figure 2.2: Examples of insulation designs

Many simulation tools only model a discrete set of insulation designs either because they do not generalize a meshing strategy for a continuous range of dimensions or because they are based on regression models for a specific subset of designs.

#### **2.2.1.3 Foundation Shape**

Relatively few researchers have investigated the impact of foundation shape on heat loss. Many of the tools used today apply one-dimensional or two-dimensional approximations based on the area and perimeter of the foundations. Few tools have the capability to simulate heat transfer from non-rectangular three-dimensional foundation shapes. The capability to simulate a wider range of foundation shapes in three dimensions is necessary to justify approximations with fewer dimensions. Descriptions of analyses of dimensional reduction strategies found in literature are discussed in more detail in Chapter 5.

#### **2.2.1.4 Multiple Interior Thermal Zones**

Common simplifications for foundation heat transfer calculations only account for heat transfer from the surfaces of a single thermal zone, neglecting heat transfer between thermal zones through the ground.

Capturing these effects requires an explicit three-dimensional model with distinct boundary conditions representing each thermal zone adjacent to a building's foundation.

Few examples of foundation heat transfer between multiple interior thermal zones exist in the literature. The temperature difference between interior thermal zones is often not great enough to cause significant heat transfer. Xie et al. [119] and McDowell et al. [86] describe tools with multiple interior zone boundaries; however, they do not quantify the magnitude of heat transfer between the zones.

### 2.2.1.5 Thermal Bridging

As with any construction element in a building, thermal bridging in foundations is a significant concern. The placement of insulation to eliminate potential heat flow paths through the most conductive building materials is an important design consideration. In foundations, thermal bridging is common along the perimeter—at the interface of the above-grade foundation wall with the exterior environment. Many studies investigate the optimal configuration of insulation on both exterior and interior portions of the foundation wall to minimize heat loss through thermal bridges such as the edge of the slab and sill plate (Figure 2.3).

The construction elements near the perimeter, which lead to thermal bridges, require a high-resolution description of the foundation details. Such high resolutions are time consuming to model and simulate. Many of the computational methods employed in foundation heat transfer models do not describe the geometry at a resolution that adequately represents thermal bridging.

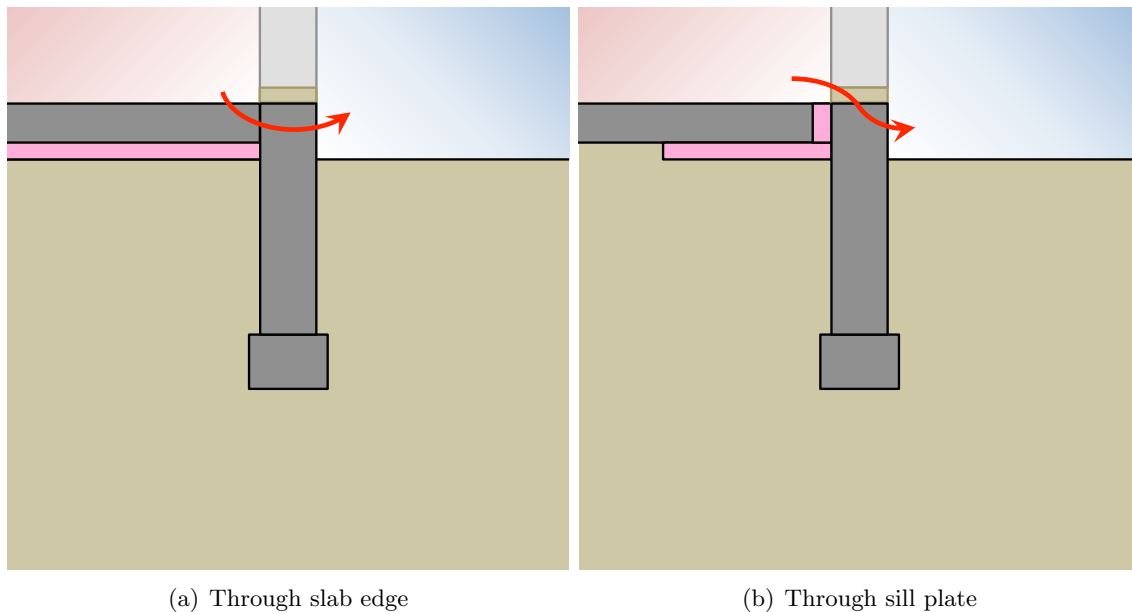


Figure 2.3: Examples of thermal bridges for a slab-on-grade foundation

Wang [115] found that neglecting the heat transfer through the sill plate interface between the above-grade and below-grade walls can result in a 46% underprediction in the basement wall

heat transfer. He also found that exterior foundation wall insulation can have a 25%–32% difference in heat transfer from interior insulation.

A number of other potential thermal bridges exist along foundation perimeters. Rock [99] explored the effect of expansion joints on thermal bridging through the slab edge.

#### **2.2.1.6 Impacts on Above-Grade Walls**

Most simulation algorithms assume one-dimensional heat transfer for above-grade walls. However, select studies show that the two-dimensional effects near the interface of above-grade walls and the foundation can have a significant impact on the overall building heat balance [67].

#### **2.2.1.7 System/Ground Interaction**

There are a number of systems that are designed to exchange heat with the ground near the building. These systems are rarely considered when calculating the heat transfer through the building foundation. Examples of such systems are listed below:

- Snow-melt systems [92, 82]
- In-slab radiant heating
- Foundation heat exchangers [32]
- Ground-source heat pumps

Inclusion of such systems in the foundation heat transfer model requires an iterative solution to ensure that the corresponding heat fluxes across the boundary between the system and the ground domain are balanced.

## 2.2.2 Ground Domain

### 2.2.2.1 Soil Spatial Variation

One of the largest challenges in creating a ground domain model is establishing the thermal properties of the soil. The thermal properties at any location within the ground domain are largely determined by the soil composition. Soil is typically comprised of up to six components:

- Quartz
- Clay minerals
- Organic matter
- Water
- Ice
- Air

The relative fraction of each of these components can vary significantly throughout the ground domain. Because these variations are both difficult to measure and burdensome to describe within a model, a majority of the work found in literature assumes that soil properties are spatially homogeneous.

A few authors have explored the impact of spatial variation on foundation heat transfer calculations. Krarti [65] explored the effect of lateral variation in soil types and Rees et al. [96] explored the effect of vertical variation of moisture content based on a static one-dimensional moisture profile. Deru [39] demonstrated that spatial variations of moisture content can be approximated using different properties deeper in the domain than near the surface.

The moisture distribution in soils is not static but instead is driven by determinable forces. Simulating the actual distribution of moisture throughout the ground domain requires calculation of moisture throughout the domain.

### **2.2.2.2 Soil Moisture Content**

Few authors have explored the impact of both heat and moisture balances on foundation heat transfer. However, two notable contributions, Deru [39] and Janssen [56], have developed solutions incorporating a moisture balance that drives spatial and temporal changes to the soil thermal properties.

Authors who have compared heat-and-moisture-transfer calculations to heat-transfer-only calculations have found that the heat-transfer-only calculation underpredicts foundation heat transfer by 9%–40% [102, 39, 57].

When simulating the effect of rainfall, authors have shown disparate results. Though most published results range between 0.1% and 10% difference from heat-transfer-only calculations [39, 52, 56], dos Santos and Mendes [42] show up to a 100% difference.

### **2.2.2.3 Soil Freezing and Thawing**

An important aspect of structural design for building foundations is the construction of the foundation footer below the frost line. Though it is a common consideration in structural design, the impact of ground freezing is rarely considered in building energy analysis. Freezing provides the building with additional thermal storage in the form of latent energy and influences the apparent thermal conductivity of the soil. Ice within soil voids also impedes moisture transfer.

A number of authors have discussed heat and mass transfer in frozen soils, though the theory has primarily been applied to frost heaving and structural design [61, 81]. Few foundation heat transfer tools calculate freezing, and the overall impact of freezing has not yet been thoroughly quantified.



## 2.2.3 Boundary Conditions

### 2.2.3.1 Interior Convection

Interior convection is usually assumed to be buoyancy driven and is thus a function of the temperature difference between the surface and the nearby air. Though several correlations exist for defining natural convection coefficients, the correlations developed by Walton [113] are widely accepted and account for different surface orientations:

$$h_n = \begin{cases} \frac{c_1 |T_s - T_{air}|^{1/3}}{c_2 - |\cos \beta|} & \text{(for unstable heat flow)} \\ \frac{c_3 |T_s - T_{air}|^{1/3}}{c_4 + |\cos \beta|} & \text{(for stable heat flow),} \end{cases} \quad (2.1)$$

where

- $h_n$  is the natural convection coefficient [W/m<sup>2</sup>-K],
- $T_s$  is the surface temperature [K],
- $T_{air}$  is the ambient air temperature [K]
- $\beta$  is the tilt of the surface (from 0 at horizontal facing up, to  $\pi$  at horizontal facing down) [radians],
- $c_1$  is a correlation constant of 9.482 [W/m<sup>2</sup>-K<sup>4/3</sup>],
- $c_2$  is a correlation constant of 7.283,
- $c_3$  is a correlation constant of 1.810 [W/m<sup>2</sup>-K<sup>4/3</sup>], and
- $c_4$  is a correlation constant of 1.328.

Unstable heat flow refers to situations where the heat flow is upward and enhances buoyancy—the surface is tilted up and is hotter than the ambient air, or the surface is tilted down and is colder than the ambient air. Stable heat flow refers to situations where the heat flow is downward.

Because the convective coefficient is a non-linear function of the surface temperature, an exact solution requires an iterative approach. Some tools calculate the convection coefficient using

the surface temperature from a previous timestep or set the convection coefficient to a constant value.

The ambient air temperature is also determined by a heat balance performed on the adjacent thermal zone. For the case of conditioned spaces, it is acceptable to assume a constant space temperature; however, in cases where the space is unconditioned or the HVAC system is not able to meet the set-point, the resulting ambient and surface temperatures must be calculated using an iterative approach.

There are relatively few existing models that incorporate a direct coupling between the ground domain and the thermal zones of the building.

### 2.2.3.2 Interior Long-Wave Radiation

Long-wave radiation is exchanged among the interior surfaces of a room based on the temperatures, emissivities of the surfaces, and the view factors between the surfaces. Calculating radiation exchange becomes increasingly expensive with more surfaces, as it requires calculating all the surface temperatures simultaneously in conjunction with the convective and conductive heat transfer calculations. The EnergyPlus simulation engine [111] performs these calculations using an algebraic method called the script-F method described by Hottel and Sarofim [53]. Cogil [30] developed a tool for calculating heat transfer from basements, which used a similar algebraic method using surface radiosities. Alternative algebraic methods are described by Clark and Korybalski [28].

Most tools do not solve the set of algebraic equations required for a complete radiation heat balance. A common simplification is to treat all radiation from a surface as though it were only radiating to a black body at the air temperature. This is written as

$$\dot{q}_{rad,lw} = \varepsilon_s \sigma [T_s^4 - T_{air}^4] \quad (2.2)$$

or as a heat transfer coefficient,

$$h_{rad} = \varepsilon_s \sigma [T_s^2 + T_{air}^2] [T_s + T_{air}], \quad (2.3)$$

where

- $\dot{q}_{rad}$  is the radiative heat flux from the surface [ $\text{W}/\text{m}^2$ ],
- $\varepsilon_s$  is the surface emissivity,
- $\sigma$  is the Stefan-Boltzmann constant of  $5.67 \times 10^{-8}$  [ $\text{W}/\text{m}^2\text{-K}^4$ ],
- $T_s$  is the surface temperature [K],
- $T_{air}$  is the air temperature [K], and
- $h_{rad}$  is the radiative heat transfer coefficient [ $\text{W}/\text{m}^2\text{-K}$ ].

Like the natural convection coefficient, the radiative coefficient is a non-linear function of the surface temperature. To calculate radiation within the context of a linear system of equations, the coefficient is calculated using the previous time-step's surface temperature at the loss of some accuracy.

Many tools, for example DOE-2 [80], are not capable of simulating dynamic coefficients and use a single constant coefficient to represent both convection and radiation from a surface.

### 2.2.3.3 Interior Short-Wave Radiation

Interior foundation surfaces are sometimes exposed to short-wave solar radiation transmitted through windows. Passive solar buildings are designed and oriented specifically to expose slab foundation surfaces to incoming solar radiation to store heat. Most whole-building simulation tools lack the coupling between the foundation heat transfer and interior short-wave radiation to capture the benefits of passive solar building designs.

The effect of short-wave radiation incident on interior surfaces is calculated using a constant heat flux. However, calculating the effect of transmitted solar radiation on foundation surfaces requires integration with a more comprehensive building simulation tool to capture the effects of shading and transmission losses through windows.

### 2.2.3.4 Exterior Convection

Exterior convection is typically dominated by forced, wind-driven convection, though there is also a natural buoyancy-driven component. Numerous convection correlations appear in the literature with varying complexity. EnergyPlus combines several correlations to account for a wide range of conditions into the somewhat misleadingly termed the “DOE-2 Model.” The algorithm combines the MoWiTT correlations developed by Yazdanian and Klems [120] to account for wind speed and wind direction, the natural convection algorithm described by Walton [113], some adjustments made by Booten et al. [18] to correct for the height of the surface, and an addition from the DOE-2 to account for the roughness of the surface:

$$h_{conv} = h_n + R_f [h_{conv,smooth} - h_n], \quad (2.4)$$

where

- $h_{conv}$  is the total convection coefficient [W/m<sup>2</sup>-K],
- $h_n$  is the natural convection coefficient defined by Equation 2.1 [W/m<sup>2</sup>-K],
- $R_f$  is a dimensionless roughness factor, and
- $h_{conv,smooth}$  is the convection coefficient for a perfectly smooth surface [W/m<sup>2</sup>-K] defined by Equation 2.5:

$$h_{conv,smooth} = \sqrt{h_n^2 + h_f^2}, \quad (2.5)$$

where  $h_f$  is defined by

$$h_f = av^b, \quad (2.6)$$

where

- $h_f$  is the forced convection coefficient [W/m<sup>2</sup>-K],
- $v$  is the wind speed at the surface [m/s],

- $a$  is a correlation constant of
  - 3.26 [W/m<sup>2</sup>-K-(m/s) <sup>$b$</sup> ] for windward surfaces,
  - 3.55 [W/m<sup>2</sup>-K-(m/s) <sup>$b$</sup> ] for leeward surfaces, and
- $b$  is a correlation constant of
  - 0.89 for windward surfaces,
  - 0.617 for leeward surfaces.

The roughness factor described in Equation 2.4 is a qualitatively defined factor based on example surfaces as shown in Table 2.1.

Table 2.1: Example roughness factors

<b>Example Surface</b>	$R_f$	<b>Estimated <math>R_t</math> [mm]</b>
Glass	1.00	0.00
Smooth plaster	1.11	0.44
Clear pine	1.13	0.52
Concrete	1.52	2.08
Brick	1.67	2.68
Stucco	2.17	4.68

No references were found to provide surface roughness factors for roughnesses beyond the range shown here. As none of the example surfaces describe typical ground coverings, the roughness factor will have to be extrapolated to account for soils, asphalts, grasses, and other vegetation. As a crude approximation, the roughness factors of other surfaces beyond the examples given here are estimated by

$$R_f = 1 + R_t/R_n, \quad (2.7)$$

where

- $R_t$  is the maximum peak-to-valley surface relief [mm], and
- $R_n$  is a normalizing constant of 4 [mm].

The resulting estimated value of  $R_t$  for each of the examples is also shown in Table 2.1.

Wind speed values are typically measured at a weather station in an open area several meters above any nearby obstructions and are not appropriate for calculating forced convection near the ground adjacent to a building. The wind speed,  $v$ , in Equation 2.6 is often adjusted from the weather station measurements provided in standard weather data sets using a procedure from the *ASHRAE Handbook of Fundamentals* [7]:

$$v_{ground} = v_{ws} \left[ \frac{\delta_{ws}}{z_{ws}} \right]^{\alpha_{ws}} \left[ \frac{z_{veg}}{\delta_{local}} \right]^{\alpha_{local}}, \quad (2.8)$$

where

- $v_{ground}$  is the wind speed near the ground [m/s],
- $v_{ws}$  is the wind speed recorded at the weather station [m/s],
- $\delta_{ws}$  and  $\delta_{local}$  are the boundary layer thicknesses [m] (Table 2.2) at the weather station and the local building, respectively,
- $z_{ws}$  and  $z_{veg}$  are the heights [m] of the weather station and the local vegetation, respectively, and
- $\alpha_{ws}$  and  $\alpha_{local}$  are the terrain exponents (Table 2.2) at the weather station and the local building, respectively.

Table 2.2: Terrain parameters for wind speed corrections

<b>Terrain Description</b>	$\delta$ [m]	$\alpha$
Ocean	210	0.10
Flat, open country	270	0.14
Towns, cities and forests	370	0.22
Urban centers	460	0.33

### 2.2.3.5 Exterior Long-Wave Radiation

Long-wave radiation is exchanged among exterior building surfaces, the ground surface, the outdoor air, and the sky. The exterior long-wave radiation exchange calculation requires that each component has a defined temperature.

The air temperature is often provided by weather data for the building location, and the ground surface temperatures are calculated through a heat balance. The ground and building surface temperatures are rarely, if ever, solved simultaneously using algebraic methods similar to those described for interior long-wave radiation. Instead, long-wave radiation from exterior building surfaces is calculated assuming that the ground is at the same temperature as the air, and long-wave radiation from the ground is calculated assuming that the ground does not have a view-factor to the building's surfaces.

Sky temperature is often correlated to information available in standard weather data sets. The correlation used in both EnergyPlus and DOE-2 is shown in Equation 2.9:

$$T_{sky} = \varepsilon_{sky}^{1/4} T_{air}, \quad (2.9)$$

where

- $T_{sky}$  is the sky temperature [K],
- $\varepsilon_{sky}$  is the sky emissivity [0–1] defined by Equation 2.10, and
- $T_{air}$  is the exterior air temperature [K].

$$\varepsilon_{sky} = 0.787 + 0.764 \ln \left( \frac{T_{dewpoint}}{T_{air}} \right) [1 + 0.0224f_c - 0.0035f_c^2 + 0.00028f_c^3], \quad (2.10)$$

where

- $T_{dewpoint}$  is the dew point temperature of the air [K], and
- $f_c$  is the cloud covered fraction of the sky [tenths (i.e., 0–10)]

The exterior long-wave radiative flux is then given by the following:

$$\dot{q}_{rad,lw} = \varepsilon_s \sigma [T_s^4 - F_{sky} f_s T_{sky}^4 + F_{sky} [1 - f_s] T_{air}^4 + F_{ground} T_{ground}^4], \quad (2.11)$$

where

- $\varepsilon_s$  is the emissivity of the surface [0–1],
- $\sigma$  is the Stefan-Boltzmann constant of  $5.67 \times 10^{-8}$  [W/m<sup>2</sup>-K<sup>4</sup>],
- $T_s$  is the surface temperature [K],
- $F_{sky}$  is the view factor from the surface to the sky [0–1],
- $f_s$  is the fraction defined by Equation 2.12, which distinguishes radiation to the sky from radiation to the air [0–1],
- $F_{ground}$  is the view factor from the surface to the ground [0–1], and
- $T_{ground}$  is the ground surface temperature [K].

$$f_s = \cos(\beta/2) \quad (2.12)$$

The view factors can be calculated as follows:

$$F_{sky} = 0.5 [1 + \cos \beta], \quad (2.13)$$

and

$$F_{ground} = 0.5 [1 - \cos \beta] \quad (2.14)$$

where  $\beta$  is the tilt of the surface in radians (from 0 at horizontal facing up, to  $\pi$  at horizontal facing down).

The radiative flux can be simplified when substituting the definition of sky temperature and assuming that the ground temperature is the same as the air temperature:

$$\begin{aligned} \dot{q}_{rad,lw} &= \varepsilon_s \sigma [T_s^4 - F_{sky} f_s \varepsilon_{sky} T_{air}^4 + F_{sky} [1 - f_s] T_{air}^4 + [1 - F_{sky}] T_{air}^4] \\ &= \varepsilon_s \sigma [T_s^4 - T_{air}^4 F^*], \end{aligned} \quad (2.15)$$



where  $F^*$  is a placeholder for the more verbose  $[F_{sky} f_s [\varepsilon_{sky} - 1] + 1]$ .

Defining the radiative heat transfer coefficient as

$$h_{rad} = \varepsilon_s \sigma \left[ T_s^2 + T_{air}^2 F^{*1/2} \right] \left[ T_s + T_{air} F^{*1/4} \right] \quad (2.16)$$

while using the surface temperature from the previous time-step, the calculation of exterior radiation can be solved in a linear system of equations:

$$\dot{q}_{rad,lw} = h_{rad} \left[ T_s - T_{air} F^{*1/4} \right]. \quad (2.17)$$

### 2.2.3.6 Exterior Short-Wave Radiation

Short-wave solar radiation is calculated as a heat flux on the ground surface. Many tools will simulate solar incidence on the ground, but often the solar absorptivity of the ground surface is assumed to be homogeneous and does not account for shading from building surfaces or ground cover.

A couple authors have explicitly simulated the effect of shading on the ground in their tools. Bahnfleth and Pedersen [11] showed that shade from the building can increase the mean heat loss from a slab by 27.4% in Phoenix, Arizona and 14% in Medford, Oregon. dos Santos and Mendes [41] estimated that shading can cause up to a 30°C range of variation in the ground surface temperatures surrounding the building.

### 2.2.3.7 Evapotranspiration

Evapotranspiration describes the evaporation of water from ground and plant surfaces. Many models do not incorporate evapotranspiration despite its cooling effect on the exterior ground surface boundary.

The rate of evaporative heat loss from the soil depends on the vapor pressure at the soil's surface relative to the vapor pressure of the air. In the absence of moisture transfer calculations, the evaporative effect can only be approximated based on an assumption of the wet-bulb temperature at the soil's surface. The actual evapotranspiration rate is between zero and a maximum where the

soil surface wet-bulb temperature is the same as the wet-bulb temperature of the air. When the soil is saturated with moisture, it is safe to assume maximum evapotranspiration. However, for dry soil the low surface wet-bulb temperatures can lead to unrealistic results.

Using the maximum potential evapotranspiration, Bahnfleth and Pedersen [11] demonstrated that neglecting the effect can reduce the annual average heat loss by up to 170% (i.e., a heat gain) in Phoenix, Arizona; 28.4% in Philadelphia, Pennsylvania; 18.7% in Minneapolis, Minnesota; and 32.3% in Medford, Oregon. Deru [39] also showed an 11.2% difference in Fort Collins, Colorado.

#### **2.2.3.8 Snow Cover**

Snow cover has several effects on the exterior ground surface boundary condition:

- Fresh snow has a solar reflectivity of 0.98.
- Snow acts as an insulating layer on the ground. Gilpin and Wong [47] refer to this as the heat-valve effect.

Snow-related boundary conditions are discussed in more detail in references pertaining to snow-melting system analysis [92, 82].

One significant challenge in simulating snow cover is that snow amounts are not typically provided in standard weather data. While there are data fields available for snow depth, they are not actually populated in weather data files.

#### **2.2.3.9 Far-Field Boundary**

The far-field boundary represents the distance from the building where there is no longer heat transfer in the horizontal directions. This may be at a distance sufficiently far from the building or, alternatively, along a plane of symmetry (e.g., half-way between two similar buildings).

Most tools simulate this boundary as either a zero-heat-flux condition or an independently-calculated, one-dimensional temperature profile. If the boundary is sufficiently far away from the

building, then both approaches should produce the same result. However, the zero-flux boundary requires fewer calculations.

### **2.2.3.10 Deep-Ground Boundary**

The deep-ground boundary is usually defined as either the distance to the water table or the distance to a point in the ground deep enough that it is not affected by the annual temperature fluctuations at the surface.

If the water table is shallower than the unaffected ground depth, then a constant temperature condition is applied (usually the water table temperature is approximated as the annual average outdoor dry-bulb temperature for the location). In a case where the water table is below the unaffected ground depth, a zero-heat-flux condition is applied, although this is also sometimes approximated by using a constant temperature condition equal to the annual average outdoor dry-bulb temperature.

Bahnfleth and Pedersen [11] found that the type of boundary condition (zero-heat-flux versus constant temperature) only accounts for a 1.3–3.5% change in average annual heat loss. Contrarily, the depth of the boundary was found to have a fairly significant impact on results. Between depths of 10 m and 15 m, the mean heat loss can change by up to 12%.

Several authors have explored the impact of water table depth on foundation heat transfer [37, 11, 96, 39]; however, no tool accounts for the annual variation in water table depth observed by Thomas and Rees [107].

### **2.2.4 The Whole-Building Context**

Some foundation heat transfer tools are used in the context of a whole-building energy simulation engine. Current whole-building simulation tools require tens of seconds to several hours to simulate a single building's energy use, depending on the complexity of the building model and the solution methodologies employed. As foundation heat transfer represents only a fraction of the energy load on the building, the calculations should represent a relatively similar fraction of the

overall computation time and not several orders of magnitude longer, which is the case for many of the more detailed numerical solutions.

To minimize the computation time devoted to foundation heat transfer, many whole-building simulation tools employ simplistic methods with limited capability based on preprocessed or regression results generated by a more detailed foundation heat transfer tool.

Most whole-building simulation tools are not designed for multidimensional heat transfer calculations. Often there is an artificial boundary created between the foundation heat transfer calculations and the one-dimensional foundation surface constructions represented in a whole-building model.

The TRNSYS (TRaNsient SYtems Simulation) software program [104] has a very detailed ground heat transfer library, which can be coupled to a whole-building energy simulation. The heat balance between the thermal zone and the foundation requires a computationally expensive iterative solution.

Decoupling is not without its advantages. Al-Anzi and Krarti [6] developed a method that used decoupling as an opportunity to employ separate solution methods that have advantages at different time scales. In their work titled “Local-Global Analysis,” the global domain of ground heat transfer is calculated using a faster analytical model, and the local domain (near the interface of the building) is calculated using a numerical method with high resolution to capture thermal bridging effects.

Using whole-building energy simulation tools for foundation insulation design requires coupled foundation heat transfer calculations that are both faster than the detailed three-dimensional tools like TRNSYS and more capable than the simplistic regression-based tools.

### **2.3 Computational Algorithms**

The real limitation in estimating heat loss from building foundations is not in our understanding of the physics but in the sheer number of calculations required to solve the heat diffusion equation for the spatial and temporal domains at a reasonably high resolution of detail.

The following sections describe the calculations required to simulate the physics of foundation heat transfer as it is understood in literature.

### 2.3.1 Heat Diffusion

An energy balance of heat flow through soil is commonly treated as a completely conductive problem. In reality, there are several mechanisms that contribute to heat transfer [39]:

- Conduction through soil grains, water, ice, and entrained gasses (e.g., air)
- Latent heat transfer as water evaporates within the soil matrix
- Latent heat transfer as water freezes and thaws within the soil matrix
- Advection from bulk liquid flow (e.g., rainfall)
- Advection from bulk gas flow
- Diffusion of liquid and vapor through the soil matrix
- Radiation exchange in the soil voids

Of the mechanisms listed above, conduction is considered the dominant form of heat transfer for most cases. Depending on the composition of the soil, other mechanisms may play greater roles in the overall heat transfer.

A heat balance on an infinitesimally small volume yields a relationship between two independent variables,  $T$ , temperature (the potential for heat flow), and  $\Psi$ , matric potential (the potential for moisture flow):

$$C_{H,T} \frac{\partial T}{\partial t} + C_{H,\Psi} \frac{\partial \Psi}{\partial t} = \nabla \cdot [k \nabla T] + \nabla \cdot [D_{H,\Psi} \nabla \Psi] + C_{p,l} \dot{m}_l \cdot \nabla T + \dot{q}, \quad (2.18)$$

where

- $C_{H,T}$  is the thermal heat capacitance [J/m<sup>3</sup>-K],

- $T$  is the temperature at a given spatial position and point in time [K],
- $t$  is time [s],
- $C_{H,\Psi}$  is the matric heat capacitance [J/m<sup>4</sup>]
- $\Psi$  is the matric potential at a given spatial position and point in time [m],
- $\nabla$  is the differential spatial gradient operator,
- $k$  is the thermal conductivity [W/m-K],
- $D_{H,\Psi}$  is the matric heat diffusivity [W/m<sup>2</sup>],
- $C_{p,l}$  is the specific heat capacity of liquid water [J/kg-K],
- $\dot{m}_l$  is the mass flow rate vector [kg/m<sup>3</sup>-s], and
- $\dot{q}$  is the heat source or sink [W/m<sup>3</sup>].

The first two terms in Equation 2.18,  $C_{H,T} \frac{\partial T}{\partial t}$  and  $C_{H,\Psi} \frac{\partial \Psi}{\partial t}$ , represent the rate of thermal energy stored as a result of changes in temperature and matric potential, respectively.

Here,  $C_{H,T}$  is the thermal heat capacitance, which accounts for the volume-average heat capacity of the soil and its constituents as well as the internal energy of water vapor associated with changes in temperature:

$$C_{H,T} = (1 - \eta_s) \rho_s C_{p,s} + \theta_l \rho_l C_{p,l} + \theta_v \rho_v C_{p,v} + \rho_l h_{fg} C_{v,T}, \quad (2.19)$$

where the subscripts  $s$ ,  $l$ , and  $v$  refer to the soil, liquid water, and vapor water components, respectively, and

- $\eta_s$  is the porosity of the soil [0–1],
- $\rho$  is the density [kg/m<sup>3</sup>],
- $C_p$  is the specific heat capacity [J/kg-K],

- $\theta$  is the volumetric fraction of a given component [ $\text{m}^3/\text{m}^3$ ],
- $h_{fg}$  is the latent heat of vaporization of water [ $\text{J}/\text{kg}$ ], and
- $C_{v,T}$  is the thermal vapor capacitance [ $\text{K}^{-1}$ ].

$C_{H,\Psi}$  is the matric heat capacitance, which accounts for the internal energy of water vapor associated with changes in matric potential defined as follows:

$$C_{H,\Psi} = \rho_l h_{fg} C_{v,\Psi}, \quad (2.20)$$

where  $C_{v,\Psi}$  is the matric vapor capacitance which, as Janssen [56] explains, has very little influence on the overall solution and can be assumed to be negligible.

The third term in Equation 2.18,  $\nabla \cdot (k \nabla T)$ , represents the Fourier heat conduction.

The effective thermal conductivity,  $k$ , represents the combined conductivity of all the soil constituents (soil grains, water, air, ice, etc.) as well as the effect of vapor distillation [35].

The effective conductivity can be calculated based on the conductivities and volumetric fractions of the constituents as well as the geometry of the soil grains (details of this calculation can be found in De Vries [35] and Deru [39]):

$$k = \frac{\theta_l k_l + \xi_p \theta_p k_p + \sum_{i=1}^n \xi_i \theta_i k_i}{\theta_l + \xi_p \theta_p + \sum_{i=1}^n \xi_i \theta_i}, \quad (2.21)$$

where

- Subscript  $p$  indicates the gas-filled (i.e., air and water vapor) portion of the soil matrix whose conductivity is calculated to include the effect of vapor distillation in Equation 2.22, and
- $\xi$  is the ratio of the average temperature gradient in the constituent and the average temperature gradient of the medium defined in Equation 2.23.

$$k_p = k_a + \phi h_{fg} D_a \frac{\partial \rho_{vs}}{\partial T}, \quad (2.22)$$

where

- $\phi$  is the relative humidity [0–1],
- $D_a$  is the vapor diffusion coefficient in air [m<sup>2</sup>/s], and
- $\rho_{vs}$  is the density of saturated water vapor [kg/m<sup>3</sup>].

$$\xi_i = \frac{3}{k_i/k_l + 2}. \quad (2.23)$$

The fourth term in Equation 2.18,  $\nabla \cdot (D_{H,\Psi} \nabla \Psi)$ , represents heat transfer caused by moisture diffusion. Here,  $D_{H,\Psi}$  is the matric heat diffusivity, which is proportional to the matric vapor diffusivity:

$$D_{H,\Psi} = \rho_l h_{fg} D_{v,\Psi}, \quad (2.24)$$

where  $D_{v,\Psi}$  is the matric vapor diffusivity defined in Equation 2.29 in Section 2.3.2 on moisture diffusion.

The fifth term in Equation 2.18,  $C_{p,l} \dot{m}_l \cdot \nabla T$ , represents the sensible heat transfer by bulk fluid flow. The assumption here is that the bulk fluid and the surrounding media are in thermal equilibrium.

### 2.3.2 Moisture Diffusion

A moisture balance on an infinitesimally small volume yields:

$$C_{M,\Psi} \frac{\partial \Psi}{\partial t} + C_{M,T} \frac{\partial T}{\partial t} = \nabla \cdot [D_{M,\Psi} \nabla \Psi] + \nabla \cdot [D_{M,T} \nabla T] + \frac{\partial K}{\partial z}, \quad (2.25)$$

where

- $C_{M,\Psi}$  is the matric moisture capacitance [m<sup>-1</sup>],
- $\Psi$  is the matric potential at a given spatial position and point in time [m],
- $t$  is time [s],
- $C_{M,T}$  is the thermal moisture capacitance [K<sup>-1</sup>],



- $T$  is the temperature at a given spatial position and point in time [K],
- $\nabla$  is the differential spatial gradient operator,
- $D_{M,\Psi}$  is the matric moisture diffusivity [m/s],
- $D_{M,T}$  is the thermal moisture diffusivity [(K-s)<sup>-1</sup>],
- $K$  is the hydraulic conductivity [m/s], and
- $z$  is the gravitational potential [m].

The first two terms in Equation 2.25,  $C_{M,\Psi} \frac{\partial \Psi}{\partial t}$  and  $C_{M,T} \frac{\partial T}{\partial t}$ , represent the rate of moisture stored as a result of changes in temperature and matric potential, respectively.

$C_{M,\Psi}$  is the matric moisture capacitance, which is comprised vapor and liquid matric capacitances:

$$C_{M,\Psi} = C_{v,\Psi} + C_{l,\Psi}, \quad (2.26)$$

where

$$C_{l,\Psi} = \left( \frac{\partial \theta_l}{\partial \Psi} \right)_T, \quad (2.27)$$

and, as previously noted,  $C_{v,\Psi}$  can be assumed to be negligible.

$C_{M,T}$  is the matric moisture capacitance, which also has a negligible effect on the solution [56].

Calculating the derivatives in Equation 2.27 requires moisture retention curves for specific soil types, which can be difficult to obtain or generalize for a range of soil compositions and grain geometries.

The third and fourth terms in Equation 2.25,  $\nabla \cdot (D_{M,\Psi} \nabla \Psi)$  and  $\nabla \cdot (D_{v,T} \nabla T)$ , represent the diffusion of moisture driven by the matric and temperature gradients, respectively.

$$D_{M,\Psi} = K_s + D_{v,\Psi}, \quad (2.28)$$

where  $K_s$  is the hydraulic conductivity of the soil [m/s] and

$$D_{v,\Psi} = \begin{cases} \eta_s D_a \frac{\rho_{vs} \phi g}{\rho_l R_v T} & \text{for } \theta_l \leq \theta_{l,c} \\ \left[ \theta_a + \frac{\theta_a \theta_l}{\eta_s - \theta_{l,c}} \right] D_a \frac{\rho_{vs} \phi g}{\rho_l R_v T} & \text{for } \theta_l < \theta_{l,c}, \end{cases} \quad (2.29)$$

where

- $\eta_s$  is the porosity of the soil [0–1],
- $D_a$  is the vapor diffusion coefficient in air [m<sup>2</sup>/s],
- $\rho_{vs}$  is the density of saturated water vapor [kg/m<sup>3</sup>],
- $\phi$  is the relative humidity [0–1],
- $g$  is the gravitational constant of 9.81 [m/s<sup>2</sup>],
- $\rho_l$  is the density of liquid water [kg/m<sup>3</sup>],
- $R_v$  is the gas constant of water vapor [J/kg-K],
- $T$  is the temperature at a given spatial position and point in time [K],
- $\theta$  is the volumetric fraction of a given component (air  $a$ , or liquid water  $l$ ) [m<sup>3</sup>/m<sup>3</sup>], and
- $\theta_{l,c}$  represents the liquid moisture content, below which the liquid water is no longer considered continuous throughout the porous structure and the relative humidity drops below 100%. This usually occurs between values of 0.1 and 0.2 m<sup>3</sup>/m<sup>3</sup>.

The fifth term in Equation 2.25,  $D_{M,T}$ , is the thermal moisture capacitance, which Janssen [56] explains is negligible.

The final term in Equation 2.25,  $\frac{\partial K}{\partial z}$ , represents the additional moisture flow potential due to gravity.

### 2.3.3 Common Simplifications

The equations established by Deru [39] with the assumptions explained by Janssen [56], lead to the following system of two non-linear partial differential equations:

$$C_{H,T} \frac{\partial T}{\partial t} + C_{H,\Psi} \frac{\partial \Psi}{\partial t} = \nabla \cdot [k \nabla T] + \nabla \cdot [D_{H,\Psi} \nabla \Psi] + C_{p,l} \dot{m}_l \cdot \nabla T + \dot{q} \quad (2.30)$$

and

$$C_{M,\Psi} \frac{\partial \Psi}{\partial t} = \nabla \cdot [D_{M,\Psi} \nabla \Psi] + \frac{\partial K}{\partial z}. \quad (2.31)$$

Equations 2.30 and 2.31 must be solved simultaneously using an iterative, non-linear solution method such as the Newton-Raphson method in order to satisfy the conservation of both mass and energy. Several of the terms in these equations are highly non-linear and can increase the number of calculations significantly.

Solving the combined heat and moisture diffusion equations requires significantly more information about the soil properties than is typically available to building energy simulators. A number of methods have been developed to calculate the thermal and matric properties based on a soil's composition [36, 88, 112], but it is not common practice to collect and characterize soil samples before conducting an energy simulation.

Most foundation heat transfer tools will simplify the calculations by assuming that the thermal properties are linear (i.e., they do not depend on the temperature of the soil) and without calculating coupled moisture diffusion. These simplifications reduce the calculations to a single equation:

$$C_{H,T} \frac{\partial T}{\partial t} = \nabla \cdot (k \nabla T) + \dot{q}. \quad (2.32)$$

The apparent thermal conductivity,  $k$ , in Equation 2.32 approximates all mechanisms of heat diffusion in the porous soil medium and not solely the conduction. The value of  $k$  may vary spatially and temporally while still solving the discretized equation using linear algebra methods; however, the value of  $k$  cannot depend on the calculated temperatures in the domain without invoking computationally-expensive, non-linear solution techniques.

With Equation 2.32, the estimated foundation heat transfer is most sensitive to the value of soil thermal conductivity [1]. Sterling et al. [105] conducted a survey of the apparent conductivity of soils found in the United States, which revealed that the value can range between 0.2 W/m-K and 4.0 W/m-K depending on moisture content and soil composition. Rock [99] showed that between soil conductivities of 0.9 W/m-K and 2.0 W/m-K there can be a 100% difference in the predicted heat loss rate from a slab.

### 2.3.4 Solution Methods

When it comes to methods for solving the diffusion equations in the context of foundation heat transfer, there is no “silver bullet.” Many such methods have been presented throughout the literature, and each method brings unique advantages and disadvantages. For a more in-depth review of numerical techniques used in solving foundation heat transfer problems, consult MacArthur et al. [85]. The following sections will provide a brief description and explain the advantages and disadvantages of several solution methods found in the literature.

#### 2.3.4.1 Analytical Solutions

Lachenbruch [78] demonstrated one of the first analytical solutions for slab-on-grade heat transfer using Green’s function. Delsante et al. [38] later developed a similar model using Fourier transforms. These two models, compared by Kusuda and Bean [76], were shown to produce nearly identical results. The major limitation of both Lachenbruch’s and Delsante’s solutions is that they are only appropriate for rectangular, uninsulated slabs.

Many analytical solutions, including those using Fourier transforms, take the form of an infinite series. The calculated solution is then an approximation where the series is calculated up to a large number,  $N$ , after which the series is truncated. Larger values of  $N$  will improve the numerical accuracy of the solution but will require more computation time.

Analytical methods are typically faster than the numerical alternatives where finer discretizations require proportionally more computation time. The major drawback of analytical methods

is solutions only exist for a small subset of problems with highly constrained—and not always realistic—boundaries and geometries.

Hagentoft and Claesson [48, 26, 51, 49, 50, 52] have developed a number of solutions using the superposition of analytical solutions and conformal mapping.

Krarti [62] is another prominent contributing author of analytical solutions. His work is described in more detail in Section 2.5.2.

#### 2.3.4.2 Finite Difference Method

The finite difference method is one of the more prominent solution methods encountered in foundation heat transfer tools. Variants of the method can be found in work by Bazjanac et al. [13], Bahnfleth [9], Cogil [30], and Rock [99].

The finite difference method often uses spatial discretization aligned with the axes of the coordinate system. This imposes a limitation on the range of geometries that can be simulated. However, this same constraint enables computationally efficient storage and execution of the linear algebra routines.

Furthermore, building foundations are often constructed using orthogonal surfaces and rarely require geometries that are not aligned with a Cartesian coordinate system. The restriction that the finite difference method imposes on the shape of the domain only poses a problem for a small minority of design cases.

Finite difference methods are typically categorized as either explicit or implicit schemes depending on how the solution is calculated relative to the solution of the previous time-step. Explicit schemes do not require the use of linear algebra algorithms and, therefore, require fewer calculations. Conversely, implicit schemes yield more reliably stable and realistic results. For the standard explicit scheme formulated in Cartesian coordinates with a uniform spatial discretization and homogeneous thermal properties, the stability criterion is defined as follows:

$$\frac{\alpha\Delta t}{\Delta x^2} + \frac{\alpha\Delta t}{\Delta y^2} + \frac{\alpha\Delta t}{\Delta z^2} \leq \frac{1}{2}, \quad (2.33)$$

where

- $\alpha$  is the thermal diffusivity [ $\text{m}^2/\text{s}$ ],
- $\Delta t$  is the time-step [s], and
- $\Delta x$ ,  $\Delta y$ , and  $\Delta z$  are the spatial cell size [m] in the  $x$ ,  $y$ , and  $z$  directions, respectively.

Several other variants of the finite difference method are discussed in greater detail in Section 3.4.3.

#### **2.3.4.3 Finite Element Method**

Finite element methods are implicit in nature and require the use of linear algebra algorithms to solve the set of simultaneous equations resulting from the domain discretization. Computation times are similar to those of the implicit finite difference methods.

Unlike finite difference methods, the spatial discretization does not have to align with the coordinate system axes. The unconstrained discretization enables the simulation of a wider range of domain geometries. However, off-axes geometry makes the discretized mesh difficult to generate.

The finite element method is used in the foundation heat transfer tools developed by Mitalas [87], Baylon and Kennedy [12], Beausoleil-Morrison et al. [17], Deru [39], and Janssen [56].

#### **2.3.4.4 Response Factors**

Response factors are a set of values that relate the heat transfer between two surface boundaries to a series of temperature histories. DOE-2 uses response factors to calculate heat conduction between interior and exterior surfaces of above-grade walls, roofs, ceilings, and floors. EnergyPlus uses a modified response factor approach called conduction transfer functions or CTFs [111]. A number of other response-factor-type calculations are employed in foundation heat transfer tools developed by Davies et al. [34], Krarti et al. [73], Zhang and Ding [121], and Wentzel [116]. Bahnfleth and Amber [10] developed Ground Conduction Functions (GTFs) and demonstrated that the GTFs produce results with 1% of the results from a detailed finite difference model.

Response factors must be generated before the simulation, either through analytical calculations or a numerical preprocessor. Response factors are determined by recording the system's response to temperature pulses at the boundaries. Once established, the calculation of heat transfer based on thermal history can be very computationally effective. The trade off between computation time and numerical accuracy is determined by the additional computation time required by the preprocessor relative to the computation time saved in the simulation.

One concern of accuracy when using response factors is the amount of time required to establish a reasonably consistent thermal history before the results can be valid for use in a simulation. The ground domain has a very slow response to temperature variations, with some effects verging on the magnitude of several years. Even if the response factors were to capture an adequately long thermal history, the conduction calculated in the simulation would still have to be initialized with an adequate history before the simulation commenced.

Response factors are also generated for a specific set of thermal properties that are assumed to be static for the duration of the simulation. This approach works for most instances of the diffusion equation but does not work for any non-linear or time-varying thermal properties.

Another approach related to response factors is establishing one-dimensional calculations that have an equivalent thermal response. Xie et al. [119] describe a method for creating two (or more) layered equivalent slabs that represent the foundation heat transfer for the more important diurnal and annual harmonics.

#### **2.3.4.5 Regression Methods**

Regression methods have been established by fitting correlations to calculated or experimental data. Mitalas [87] developed a regression method that provides steady-state and periodic heat loss factors to describe below-grade heat loss. Although originally intended for use in deep basements, the method was later adapted to describe shallow basements and slabs-on-grade. The below-grade surfaces are separated into subsurfaces, usually an upper and lower wall and a perimeter and core floor. The heat flux through each section is calculated by steady-state and dynamic heat loss factors

derived from a two-dimensional finite element program and tabulated for nearly 100 combinations of insulation configurations, foundation types, and soil properties.

Mitalas's finite element tool was later used to develop the more general BASESIMP regression by Beausoleil-Morrison and Mitalas [15]. Krarti [64] created a separate regression based on neural networks, and later compared the methodology to the BASESIMP regressions with consistent results [14]. Additional regression methods are described by Krarti and Choi [68], Bazjanac et al. [13], and Winkelmann [118].

Most regression methods require little computation time, but the modeling capability of most regression methods is limited by the robustness of the data set that originally informed the regression. For example, Mitalas's regression factors were developed for use in Canada, with consistent snow cover on the ground, limiting the applicability of the regressions to snowy locations.

### **2.3.5 Discretization**

Of the solution methods described above, the analytical methods are too constrained to be broadly applicable to foundation insulation design. The other four methods are either numerical in nature or are dependent on a numerical method as a preprocessor. A numerical method will inevitably play a role in developing more capable and computationally efficient foundation heat transfer simulation tools.

All numerical approximations of the diffusion equation require that both spatial and temporal domains are divided into discrete cells or time-steps, respectively. The total computational requirement for a simulation is directly proportional to the number of cells in the spatial domain multiplied by the number of time-steps in the temporal domain. This section describes how the numerical discretization is defined and some methods developed to reduce the number of associated calculations.



### 2.3.5.1 Spatial Domain

The spatial domain can be idealized as a semi-infinite solid extending laterally outward and extending downward from the exterior grade. In a numerical model, the domain is bounded by the lateral far-field boundaries and the deep-ground boundary. These boundaries must extend sufficiently far from the building to capture the influence on the soil.

As part of the *IEA BESTEST: In-Depth Diagnostic Cases for Ground Coupled Heat Transfer Related to Slab-On-Grade Construction*, Thornton [109] demonstrated that these boundaries had less than a 0.01% impact when the deep-ground boundary was more than 30 meters below the building and far-field boundaries were more than 20 meters from the building. A smaller domain requires fewer discretized cells but may not reflect a semi-infinite nature.

The cells created by the discretization are numerical approximations of the infinitesimally small elements for which the partial differential equations were derived. As cell size decreases the approximation approaches the continuous solution. Many authors demonstrate that below a certain cell size, the results achieve “discretization independence” and are no longer sensitive to the numerical approximation. This is the lower bound of cell size.

The upper bound on cell size is often determined by the level of detail required in the model. For the case of foundations, the upper bound is determined by the size of the thinnest component of the foundation construction represented in the thermal model. For example, a board of rigid insulation may be as thin as an inch, though cells elsewhere in the domain can be larger.

Often it is necessary to have fine cell spacing near the foundation perimeter, but the spacing can gradually increase in the direction away from the perimeter. Usually, the cell spacing increases according to a geometric series:

$$\Delta x_i = f_g \Delta x_{i-1} = f_g^2 \Delta x_{i-2} = \dots = f_g^N \Delta x_{i-N}, \quad (2.34)$$

where  $f_g$  is a constant growth coefficient, typically somewhere between 1.05 and 1.50. Geometric cell growth drastically reduces the number of cells in the domain.

The total number of cells in the domain is the product of the number of cells in each of the coordinate axis directions. Utilizing planes of symmetry eliminates half of the cells in the direction perpendicular to the plane; however, this only works if the entire problem is symmetric, including the geometry, thermal properties, and boundary conditions. This means convection algorithms that are dependent on wind direction and solar incidence on non-horizontal surfaces must be generalized to account for both halves of symmetry.

Another effective way to reduce the number of cells is to eliminate an entire computational dimension. Foundation heat transfer is dominantly two-dimensional with some three-dimensional effects near the corners of the foundation. Many tools either neglect the third dimension (along one of the horizontal axes) or approximate the three-dimensional effects in a two-dimensional coordinate system.

Several attempts to incorporate the three-dimensional effects into a two-dimensional model are discussed in Chapter 5.

### **2.3.5.2 Temporal Domain**

Most whole-building energy simulation tools simulate a single year of operation, largely because they are driven by a single year of weather data. Additionally, most of the energy-related features of a building do not have effects at longer time scales. This is not the case for features that interact with the ground. After a building is first heated, the ground can take several years to come into a steady periodic equilibrium with the building. *IEA BESTEST* [90] showed that the initialization period for slab-on-grade simulations can take anywhere from three to ten years to reach a steady-periodic state, within 0.1% annual heat loss of the previously simulated year. Bazjanac et al. [13] used an initialization period of four years for the simulations that informed their regression method. Other mechanisms which transfer heat to the ground, including ground-source heat pumps [44] and seasonal heat storage [103], also demonstrate similarly long time responses. For single year analyses, it is best to use simulation results for steady periodic ground conditions since this represents the state of the building for most of its existence.

The number of years required to arrive at steady periodic ground conditions in a simulation is dependent on how well the initial temperatures reflect the state of the ground at the beginning of the simulation period. Poor estimates of initial ground temperatures can lead to additional years of “warm-up” simulation prior to the actual simulation period.

The literature describes several approaches to estimating initial ground temperatures:

**Constant temperature:** Setting all the cells to a single spatially constant temperature is the simplest approach to initializing ground temperatures. Many authors have used the annual mean dry-bulb temperature as specified by Neymark and Judkoff [90] for the *IEA BESTEST* work.

**Kusuda:** Kusuda and Achenbach [75] developed a one-dimensional analytical solution for undisturbed soil. This solution is based on heat diffusion into a semi-infinite domain driven by a harmonic temperature variation at the surface:

$$T(t, z) = T_{y,ave} - \left[ \frac{\Delta T_m}{2} \right] \exp\left(-z \sqrt{\frac{\pi}{t_y \alpha}}\right) \cos\left(\frac{2\pi}{t_y} \left[ t - \Delta t_{shift} - \frac{z}{2} \sqrt{\frac{t_y}{\pi \alpha}} \right]\right), \quad (2.35)$$

where

- $T$  is the temperature at depth  $z$  and time  $t$  [K],
- $T_{y,ave}$  is the annual average outdoor dry-bulb temperature at the location [K],
- $\Delta T_m$  is the range of monthly average dry-bulb temperatures throughout a year [K],
- $t_y$  is the time of an annual cycle,  $3.1536 \times 10^7$  [s],
- $\alpha$  is the thermal diffusivity of the soil [ $\text{m}^2/\text{s}$ ], and
- $\Delta t_{shift}$  is the time difference between the calendar cycle and the temperature cycle [s]. This is the time from the beginning of the calendar year to the time of the annual minimum outdoor dry-bulb temperature.

This approach approximates the entire ground domain as undisturbed by the presence of a heated building. Though it does not account for lateral variation in soil temperatures,

the Kusuda approach is considered a better estimate than a spatially constant temperature field.

**Steady-state solution:** A steady-state solution provides a rough approximation of spatial variation in all dimensions, but it does not account for the long-term thermal response provided by the Kusuda estimation.

Each of these approaches, along with a new initialization method, are compared in Chapter 4 to illustrate the effect each has on reducing the duration of the initialization period.

The discretized time-steps in the temporal domain must be short enough to both capture the variation in boundary conditions (typically, hourly weather data) and ensure numerical stability in the solution as exemplified in Equation 2.33.

## 2.4 Validation, Verification, and Testing

Judkoff and Neymark [60] characterize three primary methods of evaluating the accuracy of building energy simulation tools. These methods are described as follows:

**Empirical Validation:** Calculated results from a tool or method are compared to monitored data from a real building, test cell, or laboratory experiment.

**Analytical Verification:** Outputs from a tool or method are compared to results from a known analytical solution or generally accepted numerical method for isolated heat transfer under very simple, highly-constrained boundary conditions.

**Comparative Testing:** A program is compared to itself or to other programs.

Each of these methods is discussed in further detail, along with relevant efforts in evaluating the accuracy of foundation heat transfer calculations.

### 2.4.1 Empirical Validation

Empirical data provides quantifiable results that are accurate within the uncertainty of the measurements, but such measurements can be expensive and time consuming. This is particularly true in the case of foundation heat transfer where measurements may require multiple seasons or years to produce an adequate data set. A well-designed experiment requires that all unknown quantities be carefully measured, which in the case of foundation heat transfer would require the measurement of the thermal properties of the soil at every point in the spatial and temporal domain of the experiment.

Another disadvantage of empirical validation is that the results are only applicable to the specific experimental setup at the time of measurement. The range of foundation designs, ground domain properties, and boundary conditions that affect heat transfer are difficult to capture through experiment, meaning that the results of the experiments would only serve to validate a small subset of the parameter space.

There have been relatively few efforts in the past to validate the accuracy of foundation heat transfer tools. Experimental validation has traditionally been cost and time prohibitive and has produced only a limited set of measurements. Two of the more significant efforts of experimental validation are authored by Rees et al. [94, 93, 107, 97, 98, 108] and Adjali et al. [1, 3, 4]. They found that in many cases the models produce reasonably accurate results and that most of the errors were related to uncertainty in the model input (namely the thermal properties of the soil) and the inability to model the impacts of rain and snow. Additional empirical validation efforts can be found in Trethowen and Delsante [110] and Rantala and Leivo [91]. A more comprehensive review of empirical case studies is available in Adjali et al. [5].

In many cases, attempts to validate foundation heat transfer tools becomes an exercise in calibrating a model rather than a true validation of the tool due to the high degree of uncertainty in the model inputs.

### 2.4.2 Analytical Verification

Analytical solutions can be used to verify the implementation of the algorithms in computer code. Since analytical solutions are well defined and highly constrained, analytical verification does not introduce the same problem of input uncertainty inherent to experimental validation. However, these constraints also limit the application of the verified results to a similarly small subset of the parameter space.

Numerical solutions demonstrating discretization independence are used as a surrogate in analytical verification for cases where an analytical solution cannot be derived. These solutions must first be verified against the analytical solutions, where they exist, to anchor the veracity of their implementation.

For analytical verification, once the solution has been established, it is relatively quick and inexpensive to verify other tools against it. However, verification is limited to the ground domain subsystem of the building where a problem is reasonably well-defined and cannot encompass the added complexity at the whole-building level without straying from the well defined analytical anchor.

The most comprehensive example of analytical verification is the International Energy Agency Building Energy Simulation Test and Diagnostic Method (*IEA BESTEST*) for ground coupled heat transfer related to slab-on-grade construction [90]. The *IEA BESTEST* procedures include verification against the analytical solution developed by Delsante et al. [38] and several verified numerical solutions.

The *IEA BESTEST* for ground coupled heat transfer related to slab-on-grade construction establishes test cases for rectangular, uninsulated slabs with constant thermal properties of soil and constant convective boundary conditions. *IEA BESTEST* has yet to produce additional test cases to explore other foundation shapes, types, insulation designs, and boundary conditions.

### 2.4.3 Comparative Testing

Comparisons of simulation results among different tools or methods reveal inaccuracies where there is poor agreement. However, agreement under comparative testing does not guarantee accurate results since there is no absolute truth standard like there is in empirical validation and analytical verification.

Like analytical verification, comparative tests can be executed inexpensively to quickly identify discrepancies. The tests can also be designed to focus on any portion of the system as well as establish high-level comparisons at the whole-building level.

Previous whole-building comparative tests described in the *Home Energy Rating System (HERS) BESTEST* include four cases highlighting heat loss through foundations [59]. These cases include insulated and uninsulated slabs, and insulated and uninsulated basements, illustrated by Deru et al. [40]. Several comparative test cases in the *IEA BESTEST* specification [90] revealed disagreements in predicted heat loss between 1%–24% across a number of simulation tools.

The *BESTEST* procedures have laid the foundation for improving the accuracy of foundation heat transfer tools but are limited in the range of capability they can test. Additional validation is still needed for a wide range of foundation designs, ground domain properties, and boundary conditions.

## 2.5 Comparison of Prominent Tools and Methods

This section takes a closer look at some of the more prominent foundation heat transfer tools and methods either frequently used by energy modeling practitioners or cited often in the literature. The methods and tools discussed in this section are qualitatively compared side-by-side along with the tool developed as part of this thesis work in Table 2.3. Kiva is described in detail in Chapter 3. Claridge [27], Adjali et al. [2], Krarti [66] and Deru [39] also provide thorough reviews of the various foundation heat transfer methods and tools found throughout literature.

Table 2.3: Comparison of prominent foundation heat transfer tools and methods

Method/Tool	ASHRAE		ITPE	EnergyPlus Preprocessors		eQUEST	GHMT	TRNSYS	Kiva
Author	Latta	Wang	Krarti	Bahnfleth	Cogil	Huang & Winkelmann	Deru	Thornton	Kruis
<b>Foundation Type:</b>									
Slab-on-Grade	-	✓	✓	✓	-	✓	✓	✓	✓
Basement	✓	-	✓	-	✓	✓	✓	✓	✓
Crawlspace	✓	-	✓	-	✓	✓	✓	✓	✓
<b>Insulation Design:</b>									
Interior Horizontal	✓	-	✓	✓	✓	Slab, Crawl Only	✓	✓	✓
Interior Vertical	✓	✓	✓	✓	-	✓	✓	✓	✓
Exterior Horizontal	-	-	✓	-	✓	Slab Only	✓	✓	✓
Exterior Vertical	-	-	-	-	-	✓	✓	✓	✓
Whole Slab	✓	-	✓	-	-	-	✓	✓	✓
<b>Boundary Conditions:</b>									
Interior Air Temperature	Constant	Constant	Constant	Sinusoidal	Simulated	Constant	Constant	Simulated	Constant
Interior Surface Convection	-	-	-	Constant	Constant	Constant	Constant	Constant	Correlation
Interior Surface Radiation	-	-	-	-	✓	-	-	-	-
Exterior Air Temperature	Constant	Constant	Sinusoidal	Weather File	Weather File	Sinusoidal	Weather File	Weather File	Weather File
Exterior Surface Convection	-	-	-	Constant	Correlation	-	Correlation	Correlation	Correlation
Exterior Surface Long-Wave Radiation	-	-	-	✓	✓	-	✓	✓	✓
Exterior Surface Short-Wave Radiation	-	-	-	✓	✓	-	✓	✓	✓
<b>Other Capabilities:</b>									
Multiple Interior Thermal Zones	-	-	-	-	-	-	-	✓	-
Thermal Bridging	-	✓	-	-	-	✓	✓	✓	✓
Moisture Balance	-	-	-	-	-	-	✓	-	-
Simulation Integration	-	-	-	Preprocess Calculation	Preprocess Calculation	Preprocess Library	-	Full Integration	Preprocess Calculation
Number of Dimensions	1	1	2-3	3	3	2	2	3	2-3
Scaling Parameter	$P$	$P$	$A, P$	$A, P$	$A, P$	$P$	$P$	-	$A, P$
Characteristic length(s)	-	-	$A/P$	$A/P$	$A/P$	$A/P$	width/2	-	Multiple
Solution Method	Analytical	Regression	Analytical	Finite Difference (Explicit)	Finite Difference (ADI)	Regression	Finite Element	Finite Difference (Implicit)	Finite Difference (Multiple)
Mesh Generation	-	-	-	Automatic	Automatic	-	Manual	Manual	Automatic



### 2.5.1 ASHRAE Design Calculations

Some of the oldest foundation heat transfer calculation methods can be found in the *ASHRAE Handbook of Fundamentals* [7]. The handbook describes separate methods corresponding to the type of foundation. Heat flow from insulated basement walls is calculated based on a method developed by Latta and Boileau [79] in 1969 where steady-state conduction is approximated through a series of one-dimensional concentric radial paths (Figure 2.5).

The basement wall and floor are separated into discrete sections, each with its own radial path with only angular variation in thermal properties. This allows for relatively simple calculation using polar coordinates where each section of the wall or floor can have different levels of insulation. This method can also be applied to crawlspace walls and floors.

Heat transfer through slabs is defined by a perimeter conductance factor found in look-up tables. The factors are provided for only four slab configurations based on regressions from finite element simulations [115].

### 2.5.2 Interzone Temperature Profile Estimation (ITPE) Technique

The ITPE technique developed by Krarti et al. [71, 70, 72] is the most complete analytical solution for foundation heat transfer. The basic premise of this method is to break up the domain into zones so that each zone is a rectangular region with unique boundary conditions. The heat diffusion equation is solved for each zone using an estimated temperature profile as the boundary condition between zones, which satisfies a continuity of heat flux across the boundary. This method has been adapted to work in either two- or three-dimensions. Applications of the ITPE technique can be found in several references [63, 65, 22, 23, 25].

### 2.5.3 EnergyPlus Preprocessors

Bahnfleth [9] and Bahnfleth and Pedersen [11] established a three-dimensional finite difference solution for slab-on-grade floors using a standard explicit solution scheme. This solution was

originally used to examine sensitivity to shading caused by the building, evapotranspiration, and different deep-ground boundary condition assumptions.

Later, Cogil [30] developed a similar solution for basements using an alternating direction implicit (ADI) finite difference scheme. The solution included a detailed radiation exchange model and heat balance for the basement space (including heat losses through the sill box) that was used to calculate the interior surface boundary condition.

Bahnfleth's and Cogil's tools were adapted by Clements [29] to provide preprocessed results for use in the EnergyPlus simulation engine [111]. In the process of adapting the code for use in EnergyPlus, the shading algorithm in the slab program and the radiative exchange model in the basement program were removed to reduce computation time. The preprocessors output monthly-average surface temperatures for ground-coupled surfaces. These temperatures serve as boundary conditions for the Conduction Transfer Functions (CTFs) used to calculate one-dimensional unsteady heat flow through buildings surfaces.

#### **2.5.4 eQUEST**

eQUEST (the QUick Energy Simulation Tool) is a popular graphical user interface to the DOE-2 simulation engine [55]. Huang et al. [54] integrated a fully implicit, two-dimensional finite difference solution into DOE-2 to establish foundation insulation guidelines for the *Building Foundation Design Handbook* [77]. A large set of simulation data, 88 foundation configurations in 13 cities, was generated and used to establish the regression method employed by Winkelmann [118], where perimeter conduction factors characterize the effective steady-state resistance of an underground surface. The dynamic effects of heat transfer through surfaces in DOE-2 are calculated using a form of response factors. As implemented in DOE-2, the response factors are limited to a thermal history of 100 hours and are unable to capture the longer time-frame responses typically seen in foundation heat transfer [13]. To best represent the thermal response under this constraint, the actual wall is modeled as a layered construction with one foot of soil.

Krarti and Choi [69] found that this approach tends to underestimate the mass effect of the ground and cannot properly represent indoor temperature changes within the course of a day.

### **2.5.5 Ground Heat and Moisture Transfer (GHMT)**

Deru [39] developed one of the most complete solutions with coupled heat and moisture transfer. His solution employs a two-dimensional finite element method with moisture and temperature dependent thermal properties. The tool can also simulate the effects of evapotranspiration and ground freezing.

### **2.5.6 TRNSYS**

TESS (Thermal Energy Systems Specialists) created a ground coupling library for use in the TRNSYS simulation engine [104]. The library employs a three-dimensional finite difference model that can interface with any number of zones in a building. The TRNSYS ground-coupling library is currently one of the only tools where the foundation heat transfer calculations are directly coupled to the zone heat balance model through iterative simulation. TRNSYS is the only whole-building simulation tool with a ground heat transfer solution that was used as a secondary truth standard in *IEA BESTEST* for ground-coupled heat transfer [90]. TESS also compared TRNSYS to several of the other simplified methods described above [86].

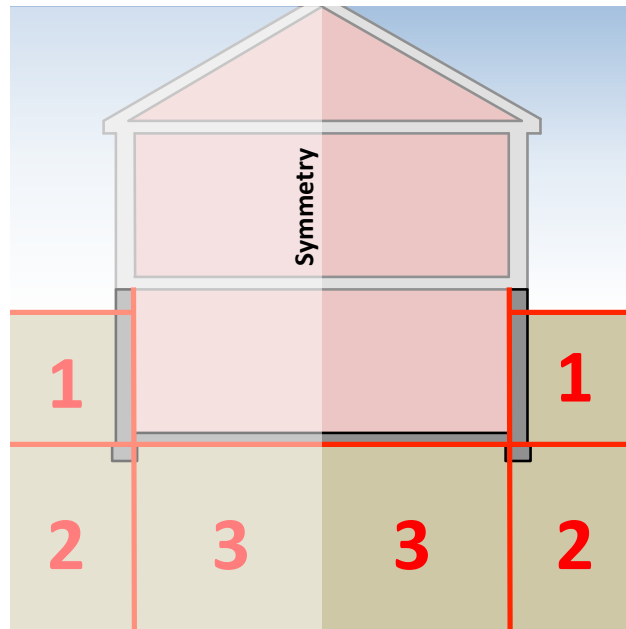


Figure 2.4: Illustration of ITPE zones (1, 2, and 3) for a basement foundation (adapted from Krarti et al. [70])

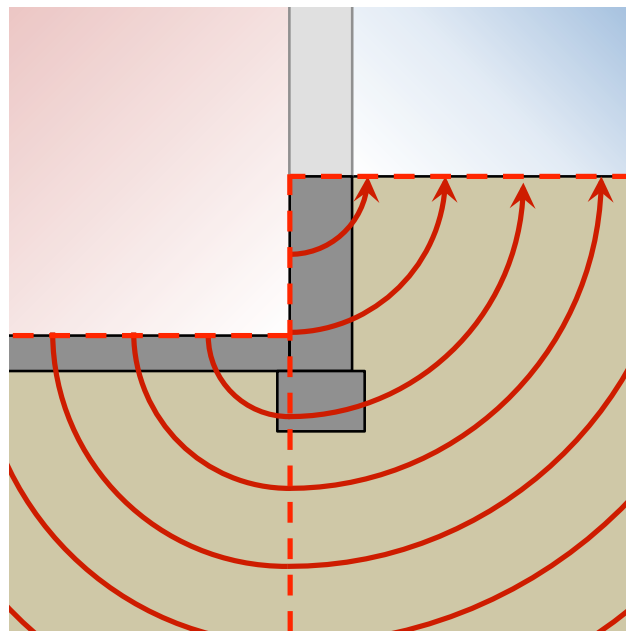


Figure 2.5: Concentric heat flow paths (adapted from Latta and Boileau [79])

## Chapter 3

### Tool Development

#### 3.1 Kiva

Kiva is a free and open-source C++ program developed by the author for the purposes of this thesis and the source code is currently hosted at GitHub.com [74]. The name comes from the subterranean ceremonial structures used by the ancient Puebloan peoples of the present-day states of Colorado, Utah, Arizona, and New Mexico. Kivas are among the earliest constructed structures in North America and are still actively preserved today.

The need for Kiva was established by observing the difficulty of the current tools to achieve an acceptable balance of capability, complexity, computational performance, and algorithmic confidence. Such a balance is a subjective assessment and will vary depending on the application of the tool. However, in the context of whole-building energy simulation, there are some precedents that must be set before such a tool is widely adopted:

**Capability:** The tool should provide methods of describing a large range of potential foundation insulation designs. Such a range cannot be objectively defined, but some of the more common design considerations should be accommodated by the tools capability. Examples include the following:

- Basement, crawlspace, and slab foundation types.
- A range of foundation shapes beyond a rectangle.
- Continuously variable foundation depth (for different basement and crawlspace heights).

- Continuously variable exterior/interior and horizontal/vertical insulation placement.
- User-specified thermal properties (for insulation, structural elements, and surrounding soil).

**Complexity:** The level of complexity required to describe a foundation system should be within the expected domain knowledge of the user. In this case, users are typically mechanical engineers or architects with domain knowledge pertaining to buildings and heat transfer. Users should be able to confidently define a foundation system without being confronted by the numerical settings that are only tangentially related to estimating building energy use (e.g., spatial discretization, or meshing, and convergence tolerance for a linear solver). While it is important for these settings to be available to a user, the settings should not be required inputs that distract from modeling information relevant to the foundation design.

**Computational Performance:** Current whole-building simulation tools require from tens of seconds to several hours to simulate a single building’s energy use, depending on the complexity of the building model and the solution methodologies employed. As foundation heat transfer represents only a fraction of the energy load on the building, the calculations should represent a relatively similar fraction of the overall computation time and not several orders of magnitude longer, which is the case for many of the more detailed numerical solutions. Computation performance in this paper is measured in wall time, or “real world” time, as it is perceived by the user. This is used to differentiate from CPU time, which is the collective calculation time of each processing core.

**Algorithmic Confidence:** The calculations performed should reflect knowledge of the physical phenomena of the heat transfer process. Several methods and tools attempt to simplify the calculations without justification. There are currently few highly-detailed tools available to provide an accurate benchmark for such simplifications. Common algorithmic simplifications for ground-coupled heat transfer include the following:

- One- or two-dimensional approximations of three-dimensional heat transfer.
- Convective and radiative boundary conditions approximated with constant coefficients (combining convection and radiation) or constant temperatures.
- Coarse representations of the foundation components that cannot characterize influential thermal bridges.
- Regression models that do not expose important variables.

Kiva's framework is a collection of interchangeable calculation routines specific to foundation heat transfer. The calculation of foundation heat transfer is comprised of several components including:

- the spatial and temporal discretization of the governing partial differential equation,
- the numerical scheme used to progress the simulation from one time-step to the next,
- the initialization of temperatures in the ground surrounding the building, and
- the coordinate system and number of dimensions describing the problem.

Each component listed can be addressed using a variety of different approaches, with each approach having different impacts on the computational performance and accuracy of the solution. The Kiva framework allows for testing of different combinations of approaches while maintaining consistency and reusing common computational methods and data structures.

The purpose of Kiva is to provide a framework with a highly capable and detailed reference solution against which the approximations and simplifications of subsequently developed solutions can be verified. At the time of this work, Kiva is a standalone computer program which simulates heat transfer through building foundations into the surrounding ground. Though it is not currently integrated into any whole-building simulation engines, the framework has been generalized to minimize such an effort.

## 3.2 Development Philosophy

For the most part, tools used for building energy simulation have been developed in a closed environment. This approach has led to several overlapping efforts to provide many of the same capabilities (e.g., DOE-2, EnergyPlus, and TRNSYS). There are occasions where this redundancy is beneficial, such as comparative testing. However, it also means that researchers must often reinvent the wheel. This is especially true for foundation heat transfer tools.

Several tools have been developed for graduate thesis research, including but not limited to Bahnfleth [9], Davies [33], Deru [39], Janssen [56], Krarti [62], Shen [101]. The code from several of these theses has since been incorporated in some fashion into currently used simulation engines: EnergyPlus (Bahnfleth [9]), DOE-2 (Shen [101]), SUNREL (Deru [39]), and APACHE (Davies [33]).

Without available source code, each of these authors spent a significant amount of time developing a software tool to perform their analyses. If the code were to be made available in an open-source environment, future researchers could use more of their time improving and enhancing the code that already exists in collaboration with other researchers rather than investing time creating yet another foundation heat transfer tool.

Many of the existing foundation heat transfer tools are written in Fortran, which is well established for its computational performance as a compiled language. However, the popularity, usage, and support of the Fortran language has declined considerably over the years as more modern languages, such as C++, have introduced improvements such as object-oriented design with a relatively small difference in computational performance. Using a more supported and modern language makes tool development accessible to a broader audience.

## 3.3 Modeling and Simulation Capabilities

The following sections describe the modeling and simulation capabilities of Kiva. As an open-source framework, anyone is free to adapt Kiva to include additional features and capabilities.



### 3.3.1 Foundation Design

The description of the foundation design is provided within the two-dimensional context illustrated in Figure 3.1. This profile is applied along the entire perimeter of the foundation.

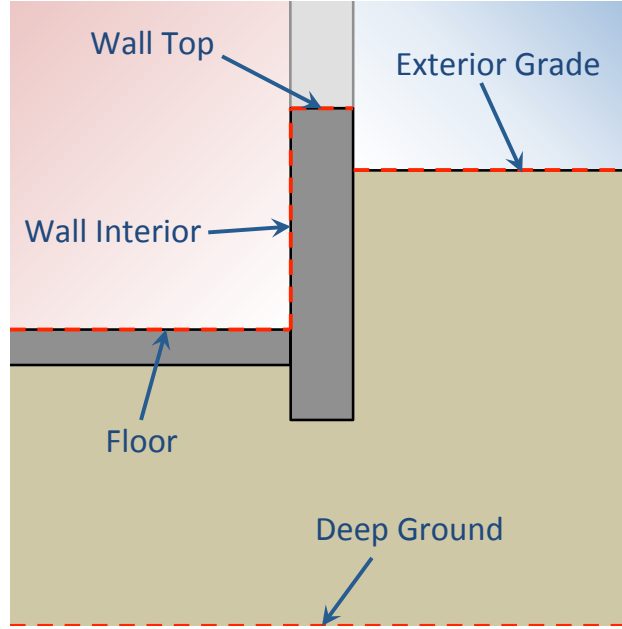


Figure 3.1: Two-dimensional context for defining foundation design in Kiva

Vertical dimensions are defined relative to the exterior grade at a  $z_{grade} = 0$ :

$$z_{wall-top} = z_{grade} + \Delta z_{wall-above-grade} \quad (3.1)$$

$$z_{floor} = z_{wall-top} - \Delta z_{foundation} \quad (3.2)$$

$$z_{deep-ground} = z_{grade} - \Delta z_{deep-ground} \quad (3.3)$$

where  $\Delta z_{wall-above-grade}$  and  $\Delta z_{foundation}$  are foundation design user-inputs and  $\Delta z_{deep-ground}$  is a simulation input with a default value of 40 meters.

The foundation type is defined by the combination of  $\Delta z_{wall-above-grade}$  and  $\Delta z_{foundation}$  illustrated in Table 3.1.

The foundation insulation and structural design are described by six elements illustrated in Figure 3.2. The components of the insulation and structural design elements each reference a

set of thermal properties: thermal conductivity, specific heat, and density. The locations of the rectangular insulation components are specified relative to the foundation wall.

**Foundation Wall:** The composition of the foundation wall is defined by a series of layers extending away from the interior wall surface. Although the footer is not explicitly described, the wall height user-input,  $\Delta z_{wall}$ , can be extended to represent the footer depth.

**Slab:** The slab is comprised of a series of layers extending below  $z_{floor}$ . Whole-slab insulation is modeled by assigning one of these layers to an insulating material. If no slab is specified by the user, the foundation floor will be directly exposed soil.

**Interior Vertical Insulation:** Interior vertical insulation begins at  $z_{wall-top}$  and extends downward and inward to a user-specified depth and thickness. The depth can be specified to model partial interior wall insulation.

**Interior Horizontal Insulation:** Interior horizontal insulation begins at the wall's interior surface and extends inward and downward to a user-specified width and thickness at a user-specified depth at or below  $z_{floor}$ .

**Exterior Vertical Insulation:** Exterior vertical insulation begins at  $z_{wall-top}$  and extends downward and outward to a depth (below grade) and thickness specified by the user.

**Exterior Horizontal Insulation:** Exterior horizontal insulation begins at the wall's exterior surface and extends outward and downward to a user-specified width and thickness at a user-specified depth at or below  $z_{grade}$ .

The slab and wall elements also describe the long-wave emissivity and short-wave absorptivity of the surface.

The level of specification available for each of the insulation and structural elements allows the user to describe the foundation system in great enough detail to simulate some of the important effects of thermal bridging.

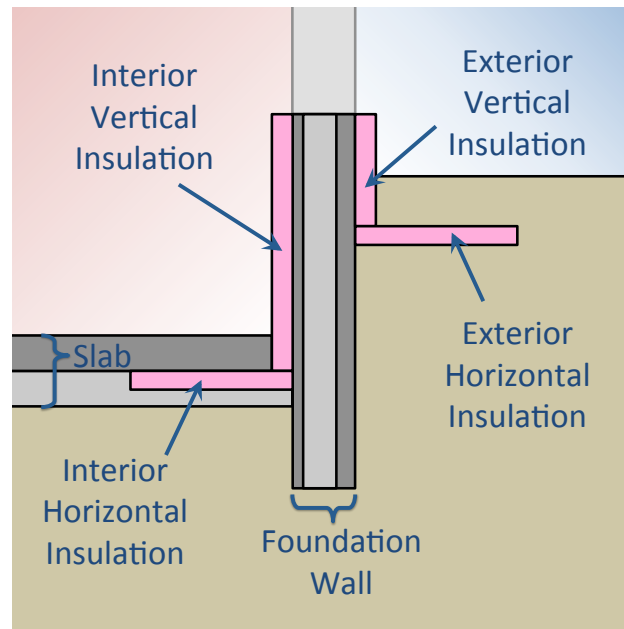


Figure 3.2: Insulation and structural design elements in Kiva

The foundation shape for three-dimensional simulations is defined by a rectilinear polygon, meaning that it must be comprised of right angles. However, circles can also be simulated in two-dimensions using axisymmetry in a cylindrical coordinate system. The polygon is specified by a list of  $x$ - $y$  Cartesian vertices tracing the foundation perimeter in a clockwise fashion (see Figure 3.3).

The perimeter of this polygon defines the location of the interior surface of the foundation wall in the profile shown in Figure 3.1. The positioning of the foundation insulation and structural components are translated into three-dimensional space internally.

The two-dimensional context for the foundation system description reduces the complexity for the user to create a fully three-dimensional spatial domain. However, this convenience imposes some limitations on the capability of the tool. For instance,

- Foundation types defined by variations in elevations cannot be modeled. Examples include walk-out basements, split-levels, and underground structures.

- It is not possible to simulate heat transfer between multiple thermal zones through the ground since only one interior environment is defined.

The far-field boundaries define the extent of the domain in all four of the lateral directions. These boundaries are created at a distance extending outward from a rectangle bounding the polygon specified by the user (Figure 3.3). The far-field distance is a simulation input that defaults to 40 meters.

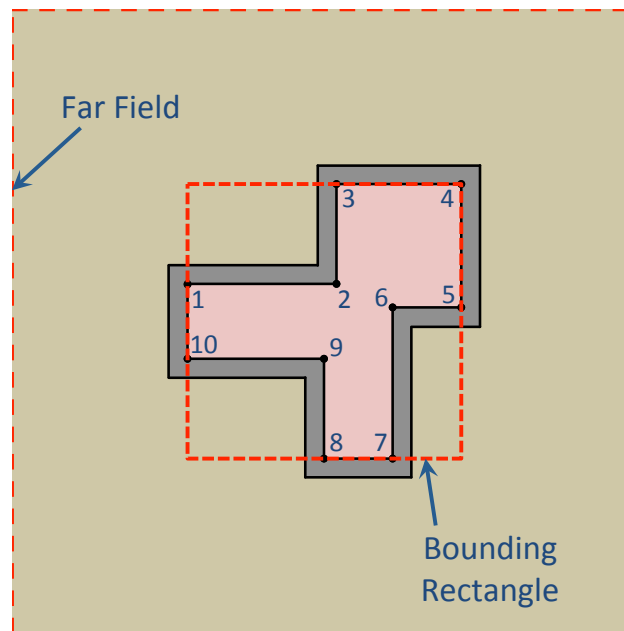


Figure 3.3: Plan view illustration of far-field boundary definition in three-dimensions and foundation shape vertex definition

### 3.3.2 Ground Domain

A reference to material definition sets the thermal properties (i.e., thermal conductivity, specific heat, and density) of the soil. Currently, the domain soil has spatially homogeneous properties and does not account for effects such as moisture content or freezing.

### **3.3.3 Boundary Conditions**

The following sections describe the algorithms used to determine boundary conditions in Kiva.

#### **3.3.3.1 Interior Convection**

The user assigns a temporally constant temperature for the interior thermal zone. This temperature is used to calculate interior convection according to Equation 2.1. The user can also override the interior convection coefficient to a constant value to replicate the idealistic constraints required for analytical verification.

#### **3.3.3.2 Interior Long-Wave Radiation**

Interior long-wave radiation calculation does not utilize an algebraic method to predict radiative exchange among interior surfaces. Instead, surface radiation is approximated as an exchange with a black-body enclosure at room temperature using Equation 2.3.

#### **3.3.3.3 Interior Short-Wave Radiation**

Kiva is programmed to account for incident short-wave solar radiation on the interior foundation surfaces. As a stand-alone tool, Kiva does not calculate transmitted solar through windows and assumes that interior solar incidence is zero.

#### **3.3.3.4 Foundation Wall**

The boundary at the top of the foundation wall is adiabatic. In the context of a whole building simulation, conduction through above-grade walls can still be simulated as a one-dimensional problem, implying that multi-dimensional impacts at the wall interface are neglected. The wall boundary can also be set as a constant linear temperature profile to replicate the idealistic constraints required for analytical verification.

### **3.3.3.5 Exterior Convection**

Weather data in the EnergyPlus Weather (EPW) file format drives the exterior boundary conditions in Kiva. Exterior convection is simulated using the relationships described in Section 2.2.3.4. Kiva assumes that the weather station is located in flat, open country at a height of 10 meters and adjusts the wind speed using a user-specified boundary layer thickness and terrain exponent from Table 2.2. A user-specified vegetation height defines the height for the wind speed adjustment and the roughness factors used for forced convection.

### **3.3.3.6 Exterior Long-Wave Radiation**

Exterior long-wave radiation is calculated according to Equation 2.16 to account for radiation exchange between the surface and the ground, air, and sky.

### **3.3.3.7 Exterior Short-Wave Radiation**

The EPW file provides the direct normal and diffuse horizontal components of solar radiation. The location latitude and longitude in the EPW file are used to calculate the solar incidence angle according to the solar position equations provided by Duffie and Beckman [43]. Kiva contains an experimental capability for simulating the effect of shading on exterior surfaces. This technique uses the graphics processing unit of the computer to count the pixels of a surface rendered from the perspective of the sun. The application of pixel counting for use in solar shading calculations was originally presented by Jones and Greenberg [58]. While Jones and Greenberg [58] demonstrated that this technique greatly improves the speed of shading calculations, their tests were applied to cases where the number of shading surfaces was high relative to the number of receiving surfaces. Preliminary tests of this technique applied to Kiva, where there are potentially thousands of receiving surfaces (one for each exterior surface cell), yielded prohibitively long computation times. The effect of shading is not explored further in this thesis, but remains an area for improvement within the Kiva framework. For the results presented here, Kiva applies unimpeded solar incidence to each surface based on orientation relative to the sun's position.

### 3.3.3.8 Other Boundaries

Kiva does not calculate the effects of evapotranspiration or snow cover.

The far-field boundary is applied as a zero-flux boundary. By default, the deep-ground boundary is a zero-flux boundary, but the user may choose to apply a constant temperature boundary using the annual average dry-bulb temperature or a user-specified temperature.

### 3.3.4 The Whole-Building Context

As an open-source framework, relatively little overhead effort is required to reuse the code in the context of an established whole-building energy simulation tool. Portions of the code have been written explicitly to accommodate a more dynamic interaction between a building and the ground domain, including variable interior temperatures, incident short-wave heat fluxes, and internal heat sources (such as radiant slab heating or ground-loop heat exchangers).

## 3.4 Computational Algorithms

This section describes the solution methods used in Kiva to calculate heat transfer from building foundation and through the surrounding soil.

### 3.4.1 Heat Diffusion

Heat transfer in the ground domain is solved using the diffusion equation

$$C_{H,T} \frac{\partial T}{\partial t} = \nabla \cdot [k \nabla T] \quad (3.4)$$

which assumes there is no moisture flow. The thermal properties,  $k$  and  $C_{H,T} = c_p \rho$ , are assigned by the materials referenced for the soil and the foundation design elements.

### 3.4.2 Discretization

#### 3.4.2.1 Spatial Domain

Equation 3.4 is solved for the solid portion of the domain bounded vertically by  $z_{wall-top}$  and  $z_{deep-ground}$ , and laterally by the far-field boundaries illustrated in Figure 3.3. For three-dimensional simulations the user can request that the domain use planes of symmetry if they exist for the foundation shape defined by the user. Kiva automatically detects symmetry in both the  $x$  and  $y$  directions and applies zero-flux boundaries to reduce the domain size. Orientation-specific boundary conditions, such as solar incidence and wind driven convection, are applied to the reduced domain using the average values of mirrored surfaces.

Kiva is capable of approximating the three-dimensional domain using a two-dimensional coordinate system. The effectiveness of several two-dimensional approximation methods is the focus of Chapter 5.

The spatial discretization is defined for four distinct regions of the domain. The region bounding the foundation wall and insulation elements defines the near-field region. All other regions are defined either laterally (interior and exterior regions) or vertically (deep region) relative to the near-field region. The near-field, interior, exterior, and deep regions are illustrated in Figure 3.4.

Cells grow geometrically towards the far-field, deep-ground, and symmetry boundaries. Cells grow towards the center of each element within regions that do not border one of the domain boundaries. Figure 3.5 illustrates cell growth and distribution for two examples, one in profile view and the other in plan view.

Cell size and growth are determined by five parameters: four which determine the cell growth coefficient in each of the regions and another parameter defining the minimum cell size for the entire domain. The minimum cell size defines the allowable number of cells between element or region boundaries. The cells' sizes are allowed to increase to fit within the element or region boundaries according to the growth and distribution of the cells. For example, the length of  $N$  consecutively



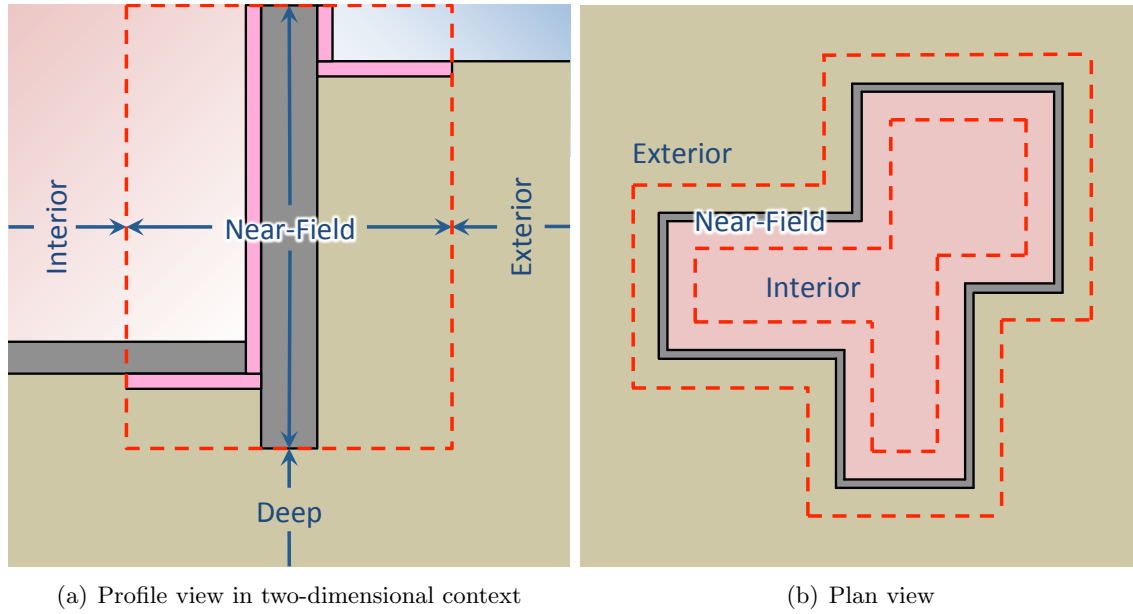


Figure 3.4: Discretization regions

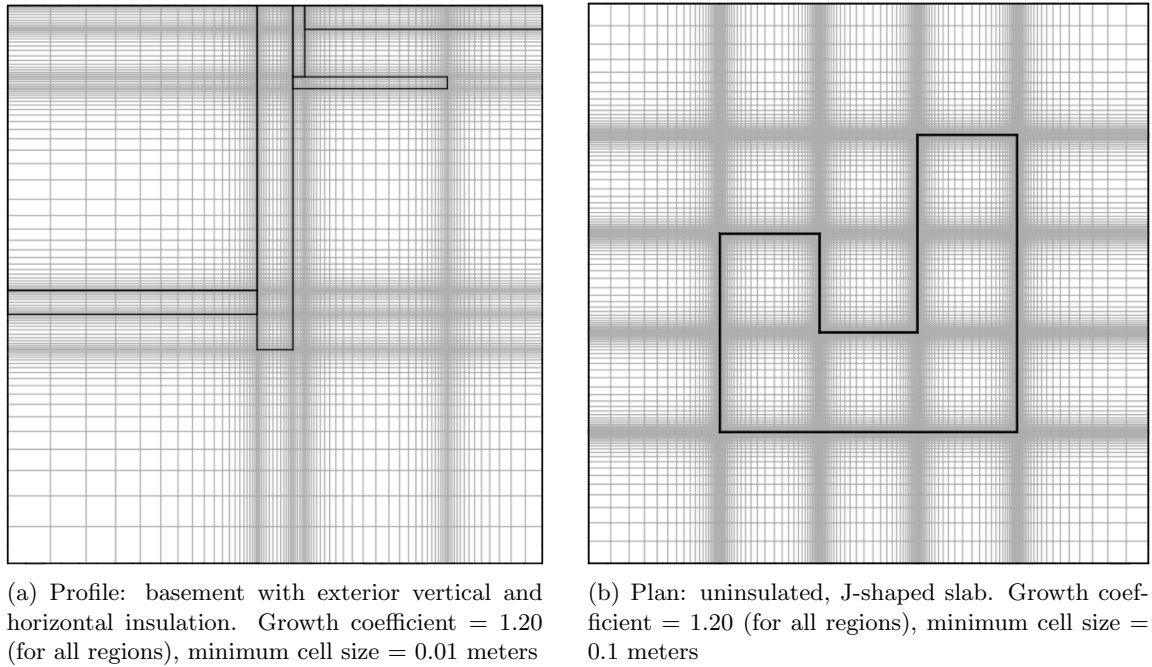


Figure 3.5: Example Kiva discretizations

growing cells is given by

$$l = \Delta x_{min} + \Delta x_{min} f_g + \Delta x_{min} f_g^2 + \dots + \Delta x_{min} f_g^N = \Delta x_{min} \sum_{i=0}^N f_g^i, \quad (3.5)$$

where  $\Delta x_{min}$  is the minimum cell size [m] and  $f_g$  is the growth coefficient. If  $l$  is greater than the distance between two element or region boundaries at  $N$  but not at  $N - 1$ , then the actual cell size is set using

$$\Delta x_{actual} = \frac{l}{\sum_{i=0}^{N-1} f_g^i}. \quad (3.6)$$

Kiva creates extra cells along the boundaries to represent surface temperatures and heat fluxes. These cells have no thickness and are completely planar with the surface boundaries. The other cells within the same plane as these boundary cells also have no thickness and require modified material properties if the normal cells on either side of them are different materials. Figure 3.6 exemplifies zero-thickness cells resulting from the wall and floor boundaries. In this figure, a node represents the center of each cell. The interior air cells are set to the interior air temperature and have no impact on the calculation of the other cell temperatures.

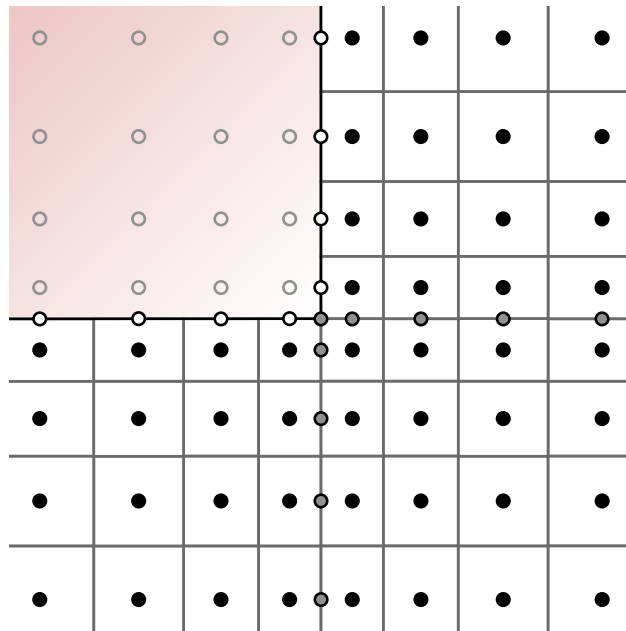


Figure 3.6: Boundary cells and resulting zero-thickness cells. Black nodes = normal solid cells, white nodes = boundary cells, gray nodes = zero-thickness cells, hollow nodes = air cells.

### 3.4.2.2 Temporal Domain

Kiva can simulate any number of years of building operation. The user can select any time-step duration. There are four initialization methods available: three traditional initialization methods (constant temperature, Kusuda, and steady-state) and an accelerated initialization method with several variants. The effectiveness of each of these initialization methods at predicting the steady-periodic conditions of the ground prior to a simulation is discussed in Chapter 4.

### 3.4.3 Finite Difference Methods

Of the various mathematical solutions employed by other tools and methods described in Table 2.3, the finite difference methods offer several benefits over the analytical and finite element methods. Finite difference methods allow for more flexibility in describing boundary conditions than analytical methods and are less mathematically abstract than finite element methods.

In general, the variants of finite difference methods are characterized by how the new time-step is solved relative to the previous time-step.

Consider a very simple one-dimensional problem, discretized into three cells (one internal cell,  $i$ , and two boundary cells,  $i - 1$  and  $i + 1$ ) as shown in Figure 3.7.

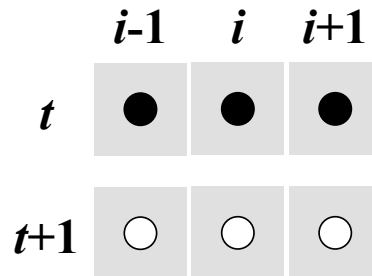


Figure 3.7: Example finite difference scheme (black nodes are known values, white nodes are unknown values)

The problem is always defined at the previous time-step,  $t$  (as defined by the initial conditions or subsequent time-step solutions). For some finite difference schemes, the solution for the new time-step,  $t+1$ , can depend solely on previous time-step's known values and can be solved independently (explicitly) to find the solution for the new time-step. Other solutions may depend on other unknown values and must be solved simultaneously (implicitly) using linear algebra techniques.

The manner in which each scheme solves the discretized solution will affect the computation time and the stability of the solution as well as how physically realistic the solution is. Though descriptions of each scheme can be found in the literature, they are rarely illustrated together using consistent notation. Understanding the differences between the schemes' mathematical implementations is essential to understanding the differences observed in the results.

### 3.4.3.1 Explicit Scheme

The simplest explicit scheme is one which only uses values from the previous time-step to solve for the new time-step. Each of the three unknowns shown in Figure 3.7 can be solved independently and sequentially based on the previous values of the node and its neighbors (indicated by the arrows) as shown in Figure 3.8.

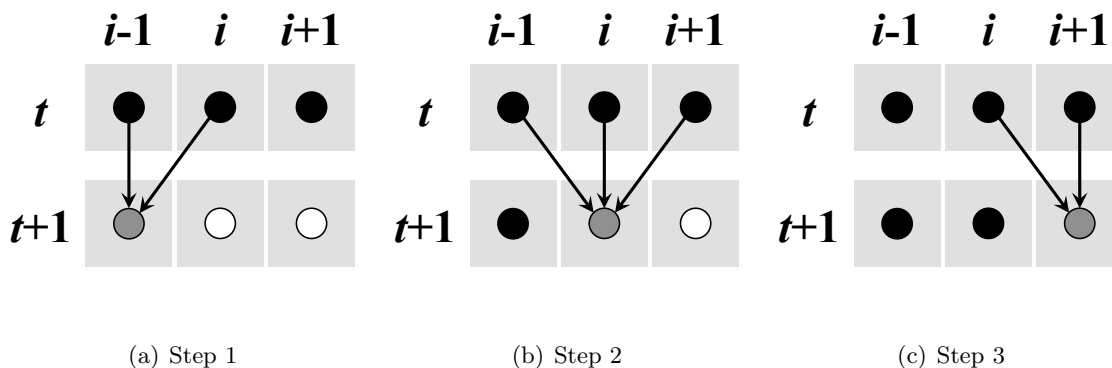


Figure 3.8: Illustration of simple explicit finite difference scheme

Mathematically, the dependencies are as follows:

$$\begin{aligned}
 T_{i-1}^{t+1} &= f(\mathbf{T}_{i-1}^t, \mathbf{T}_i^t) \\
 T_i^{t+1} &= f(\mathbf{T}_{i-1}^t, \mathbf{T}_i^t, \mathbf{T}_{i+1}^t) \\
 T_{i+1}^{t+1} &= f(\mathbf{T}_i^t, \mathbf{T}_{i+1}^t),
 \end{aligned}
 \tag{3.7}$$

where boldface terms values are known values.

The simple explicit scheme is conditionally stable and does not always provide physically realistic solutions. The solution becomes more stable with smaller time-steps and larger cell sizes.

### 3.4.3.2 Implicit Scheme

In an implicit scheme, all unknowns must be solved simultaneously since they cannot be explicitly calculated from known values. In the basic implicit scheme (often referred to as “fully” implicit), each unknown in the new time-step is calculated from its previous time-step value and the values of its neighbors in the new time-step. In Figure 3.9, there is only one step since all solutions must be simultaneous (as indicated by the bidirectional arrows).

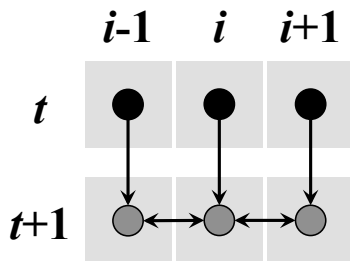


Figure 3.9: Illustration of fully implicit finite difference scheme

Mathematically, the dependencies are as follows:

$$\begin{aligned}
 T_{i-1}^{t+1} &= f(T_{i-1}^t, T_i^{t+1}) \\
 T_i^{t+1} &= f(T_i^t, T_{i-1}^{t+1}, T_{i+1}^{t+1}) \\
 T_{i+1}^{t+1} &= f(T_{i+1}^t, T_i^{t+1})
 \end{aligned}
 \tag{3.8}$$

Since each equation has multiple unknowns, implicit schemes require linear algebra techniques to solve the simultaneous set of equations. The linear system can be solved either directly (using Gaussian elimination) to arrive at an exact solution (within the floating point precision of the machine), or they can be solved iteratively within a specified convergence tolerance. In general, direct solvers are more robust but can require substantially more memory. While Kiva has the capability to use both types of solvers, it uses an iterative solver by default.

The fully implicit scheme is both unconditionally stable and always provides physically realistic solutions.

### 3.4.3.3 Crank-Nicolson Scheme

The Crank-Nicolson scheme is another implicit scheme, but it relies on the average neighboring values from both the previous time-step and the new time-step as a better approximation of the time derivative (Figure 3.10).

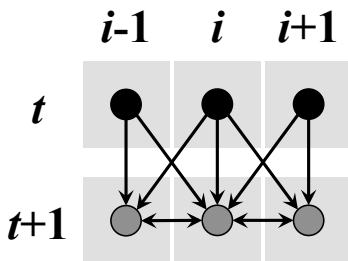


Figure 3.10: Illustration of Crank-Nicolson finite difference scheme

Mathematically, the dependencies are as follows:

$$\begin{aligned}
 T_{i-1}^{t+1} &= f(T_{i-1}^t, T_i^t, T_i^{t+1}) \\
 T_i^{t+1} &= f(T_{i-1}^t, T_i^t, T_{i+1}^t, T_{i-1}^{t+1}, T_{i+1}^{t+1}) \\
 T_{i+1}^{t+1} &= f(T_i^t, T_{i+1}^t, T_i^{t+1})
 \end{aligned} \tag{3.9}$$

#### 3.4.3.4 Alternating Direction Explicit (ADE) Scheme

A promising explicit scheme is the alternating direction explicit (ADE) scheme developed by Saul'yev [100]. This scheme is similar to the simple explicit scheme except that it uses the known values of the subsequently calculated neighbor nodes to calculate the value for the new time-step. The unknown values are solved independently using sweeps starting from each boundary (see Figures 3.11 and 3.12).

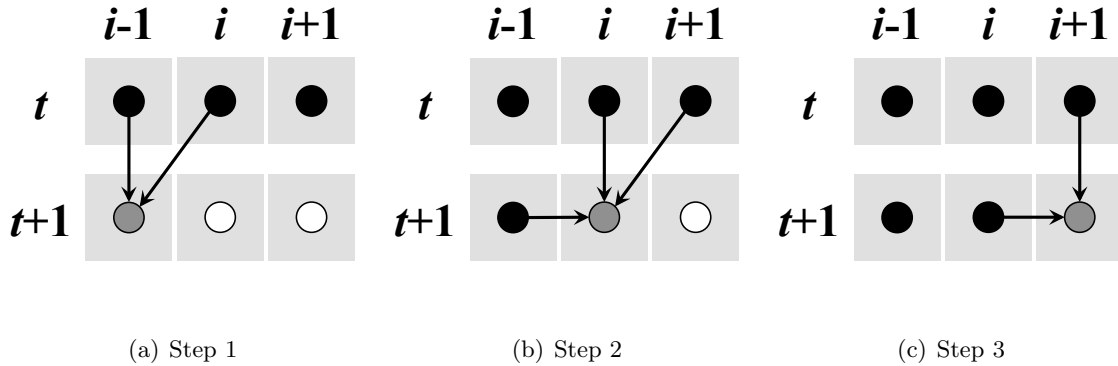


Figure 3.11: Illustration of ADE finite difference scheme: upward sweep

Mathematically, the dependencies for the upward sweep temperatures,  $U$ , and the downward sweep temperatures,  $V$ , are as follows:

$$\begin{aligned}
 U_{i-1}^{t+1} &= f(U_{i-1}^t, U_i^t) \\
 U_i^{t+1} &= f(U_{i-1}^{t+1}, U_i^t, U_{i+1}^t) \\
 U_{i+1}^{t+1} &= f(U_i^{t+1}, U_{i+1}^t)
 \end{aligned} \tag{3.10}$$

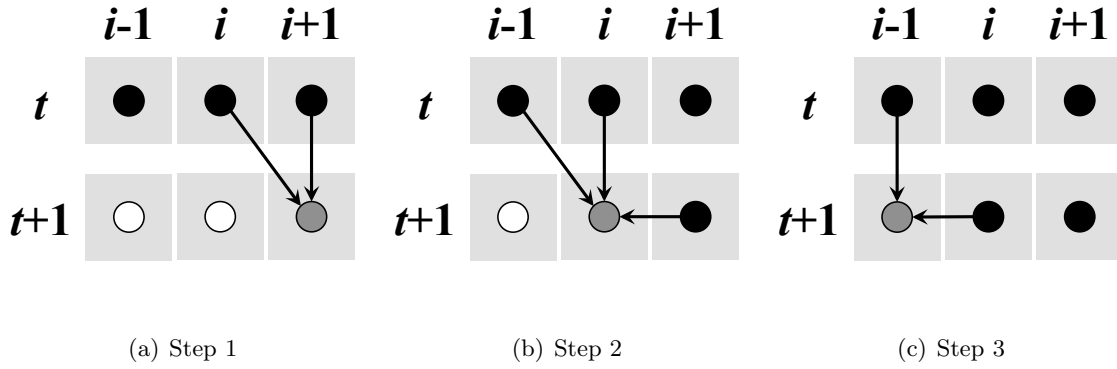


Figure 3.12: Illustration of ADE finite difference scheme: downward sweep

$$\begin{aligned}
 V_{i+1}^{t+1} &= f(V_i^t, V_{i+1}^t) \\
 V_i^{t+1} &= f(V_{i-1}^t, V_i^t, V_{i+1}^{t+1}) \\
 V_{i-1}^{t+1} &= f(V_{i-1}^t, V_i^{t+1})
 \end{aligned} \tag{3.11}$$

The final temperature,  $T$ , is then the average of the two independent solutions:

$$T = \frac{U + V}{2} \tag{3.12}$$

Because each solution is independent, they can be solved in parallel to further reduce computation time.

The ADE scheme has been shown to be unconditionally stable and give physically realistic results when used with a uniform grid. However, Fukuyo [46] has shown that the ADE method is in fact conditionally stable for nonuniform grids with some fairly loose stability requirements related to cell size and the relative growth of cells. For applications of foundation heat transfer, the ADE solution is significantly more stable than the standard explicit solution.

#### 3.4.3.5 Alternating Direction Implicit (ADI) Scheme

Each of the schemes described so far can be explained with a simple one-dimensional example. The alternating direction implicit (ADI) scheme applies only to problems with two or more



dimensions. In the typical implicit schemes described (i.e., fully implicit and Crank-Nicolson), each nonboundary cell requires an equation with three unknowns (i.e., the cell itself, the cell before, and the cell after). In a three-dimensional solution, each cell requires an equation with seven unknowns (i.e., itself, top, bottom, east, west, north, and south).

A common way to represent these problems is to show a matrix sparsity pattern. This plot shows a row for every equation and a column for every unknown in the discretized system. A block is filled in for each unknown that appears in the given equation. The sparsity pattern for a typical implicit scheme is shown in Figure 3.13.

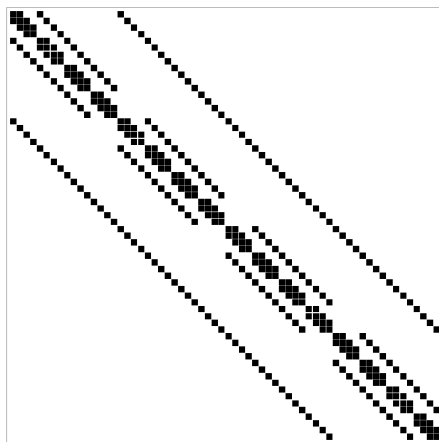


Figure 3.13: Typical implicit matrix sparsity pattern for three dimensions (up to seven unknowns per equation)

Unlike the ADE method, where “alternating direction” refers to the order in which the equations are solved (using alternating sweeps), the alternating direction in ADI refers to something entirely different. Here, each time-step is divided into smaller sub-time-steps: one for each dimension in the problem. Each sub-time-step is solved with only the unknowns along the corresponding dimension (e.g.,  $x$ ,  $y$ , or  $z$ ) being solved implicitly (at the new sub-time-step), with the values of the other directions using the values from the previous time-step similar to the simple explicit scheme.

The equations for each sub-time-step can be arranged so that all the unknowns fall along the three inner-most diagonals in the sparsity pattern (as shown in Figure 3.14).

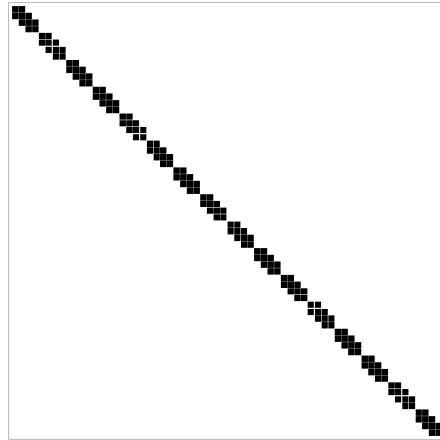


Figure 3.14: ADI matrix sparsity pattern for three dimensions (up to three unknowns per equation)

This linear algebra problem can be solved quickly and directly using a standard tri-diagonal matrix algorithm. This algorithm is significantly faster than an iterative solver and other more generalized direct solvers. It is, however, less efficient than the explicit schemes because it performs two serial passes over the data elements (i.e., it cannot be parallelized like the ADE approach), and it must calculate additional sub-time-steps within each time-step corresponding to each dimension in the problem.

The specific ADI scheme used in this work is described by Chang et al. [21]. This scheme introduces some nuances that can improve solution stability and accuracy, even at larger time-steps. Although one cannot guarantee stability for applications of foundation heat transfer, the stability of the ADI solution has not been found to be an issue.

#### 3.4.3.6 Discretized Equations

The formulations of the discretized approximations of Equation 3.4 for each of the finite difference methods described above are provided in Appendix A for a two-dimensional axisymmetric cylindrical coordinate system. Formulations for Cartesian two- and three-dimensional coordinate systems can be easily extended by omission or addition of certain terms as described in the appendix.

### 3.4.3.7 Solving Linear Systems of Equations

All implicit finite difference schemes require linear algebra techniques to solve a set of simultaneous equations resulting from discretized equations. The implicit schemes available in Kiva include fully implicit, Crank-Nicolson, and Alternating Direction Implicit (ADI) schemes. As previously mentioned, the tri-diagonal nature of the ADI scheme lends itself to a straightforward, computationally efficient solution for linear system of equations. The other schemes utilize iterative linear solvers available in the Library of Iterative Solvers (Lis) [106]. Lis is an open-source library with several types of iterative solvers including

- Conjugate gradient (CG),
- Biconjugate gradient (BiCG),
- Conjugate gradient squared (CGS),
- Biconjugate gradient stabilized (BiCGSTAB),
- Generalized product biconjugate gradient (GPBiCG),
- Transpose-free quazi-minimal residual (TFQMR),
- Orthomin,
- Generalized minimum residual method (GMRES),
- Jacobi,
- Gauss-Seidel, and
- Successive over-relaxation (SOR).

Lis also provides several preconditioners for accelerating the solution process including

- Jacobi,
- Incomplete LU factorization (ILU),

- Symmetric successive over-relaxation (SSOR), and
- Smoothed aggregation - algebraic multigrid (SA-AMG).

Each combination of a solver and, if selected, a preconditioner impacts the efficiency of the iterative process differently. A limited test of several combinations revealed that the biconjugate gradient stabilized (BiCGSTAB) solver, coupled with an incomplete LU factorization (ILU) preconditioner, provided the fastest convergence and most consistent results relative to other combinations tested. This is the default combination used in Kiva.

### 3.5 Outputs

Kiva has the capability of providing both time-series and graphical output. The time-series outputs are as follows:

- surface average heat flux [W/m<sup>2</sup>],
- surface average temperature [K],
- surface average effective temperature [C],
- surface total heat transfer rate [W],
- foundation average heat flux [W/m<sup>2</sup>],
- foundation average temperature [K], and
- foundation total heat transfer rate [W];

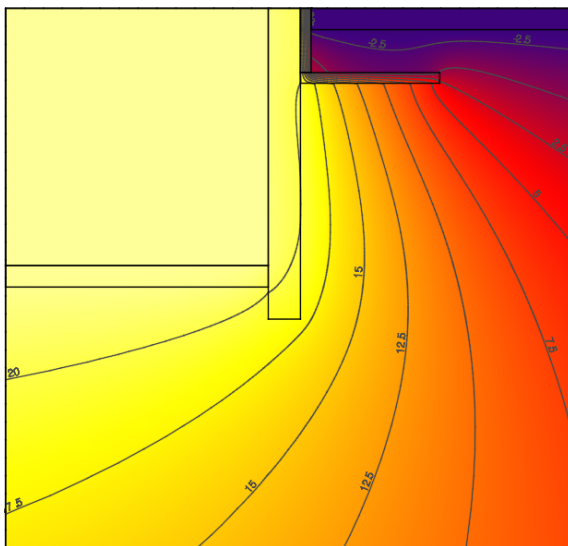
where effective temperature is the temperature that can be applied as a preprocessed boundary condition for foundation surfaces in a whole-building simulation tool. The optional surfaces available for output are the

- slab core,
- slab perimeter, and

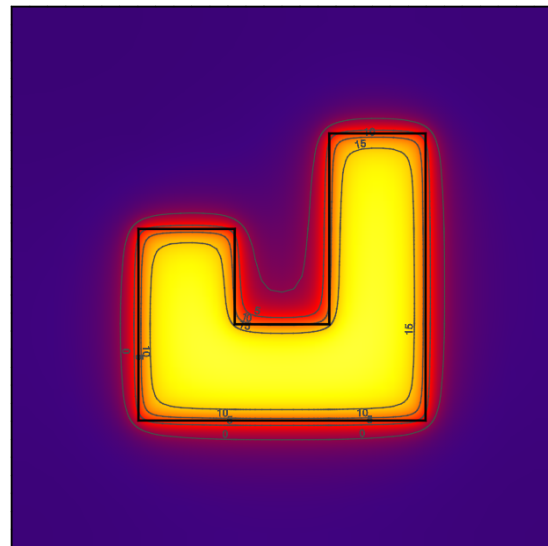
- foundation wall;

where the core and perimeter surfaces of the slab are defined by a user-specified distance inward from the foundation perimeter.

Kiva can output images representing any two-dimensional slice of the spatial domain and any point within the temporal domain. A series of images can be created at a user-specified frequency for compilation into an animation. Figure 3.15 demonstrates this capability with a profile slice and a plan slice for the same domains illustrated in Figure 3.5. Kiva can create plots of temperature, heat flux magnitude, and heat flux in the direction of any of the coordinate system axes.



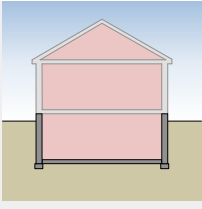
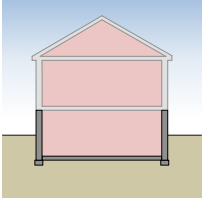
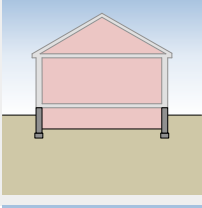
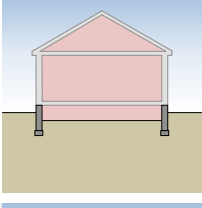
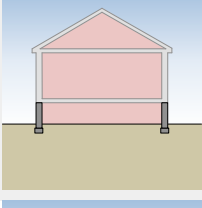
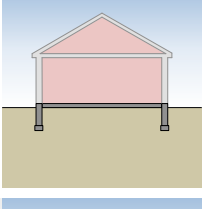
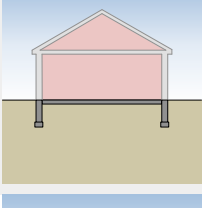
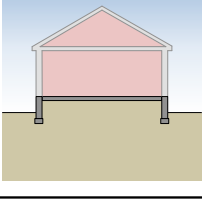
(a) Profile: basement with exterior vertical and horizontal insulation (isotherms equally spaced at  $2.5^{\circ}\text{C}$ )



(b) Plan: uninsulated, J-shaped slab at 3 meters depth (isotherms equally spaced at  $5.0^{\circ}\text{C}$ )

Figure 3.15: Example Kiva graphical output

Table 3.1: Example foundation types available in Kiva

Foundation Type	$\Delta z_{foundation}$ [m]	$\Delta z_{wall-above-grade}$ [m]	Illustration
Deep basement	2.4	0.3	
Shallow basement	2.4	1.2	
Below-grade crawlspace	1.0	0.3	
Shallow below-grade crawlspace	0.6	0.3	
Above-grade crawlspace	1.0	1.0	
Slab-on-grade	0.0	0.2	
Slab-in-grade	0.0	0.0	
Elevated slab	0.0	0.6	

## Chapter 4

### Solution Verification

It is important to distinguish between simulation validation and solution method verification. Simulation validation describes the effort of determining the accuracy of simulation outputs when compared to carefully measured results from a controlled experiment. Solution method verification describes the process of testing the correctness of the algorithms as programmed in a tool.

While, ultimately, an empirical validation may provide the best truth standard for determining a solution's accuracy, it is difficult to design an experiment where the properties of the foundation and ground domain are known within a reasonable degree of uncertainty. When creating a model of the foundation and ground system, this uncertainty propagates through the solution resulting in large error bounds on the output results of the simulation. Most attempts to validate a simulation of a foundation heat transfer result in a calibration of uncertain model inputs rather than a validation of the simulation outputs.

For this reason, validation is not an objective of this thesis. This is not intended to undermine the importance of validation, but given the challenges it presents and the evident need to improve on the computational performance and algorithmic confidence of current solution methods, validation is considered beyond the scope of this work.

Kiva provides a framework with several variants of the finite difference method allowing direct comparisons of the accuracy, computation time, and stability of each method as they are applied to solving the foundation heat transfer problem. Such comparisons have not been documented before in the literature.

Before the Kiva framework can be used to develop faster simplified solutions, each of the finite difference solution methods implemented in Kiva must be independently verified against an existing mathematical truth standard. This will establish Kiva as an accuracy benchmark for justifying future simplifications.

This chapter focuses on the verification of the finite difference solution methods implemented in Kiva and discussed in Section 3.4.3. This chapter also investigates solution sensitivity to selected numeric parameters as well as the efficiency of several initialization techniques within the context of an established, well-defined test specification.

#### 4.1 ***IEA BESTEST*** for Ground Coupled Heat Transfer

As all numerical discretizations are approximations of the continuous nature of heat diffusion, the goal is to compare the accuracy of these approximations against a known analytical solution. For foundation heat transfer, the known analytical solutions tend to be highly constrained, mathematically idealized, physically unrealistic cases that can only provide a starting point for verification. Beyond these solutions, the only available comparisons are to other independently developed numerical solutions. While these numerical solutions cannot be considered truth standards like the analytical solutions, a general consensus among detailed numerical solutions can establish a general range of acceptance.

The International Energy Agency Building Energy Simulation Test and Diagnostic Method (*IEA BESTEST*) [90] describes a methodology to verify solutions for foundation heat transfer against analytical solutions and verified numerical solutions. A single analytical solution developed by Delsante et al. [38] was used as a steady-state mathematical truth standard for a single test case. For the same test case, three detailed numerical solutions were developed and shown to give very close agreement with the analytical solution. These three solutions, TRNSYS [109], FLUENT [89], and MATLAB [31], were then used as secondary mathematical truth standards for the other steady-state and harmonic (unsteady) test cases. These are all idealized test cases with several inherent limitations:



- The test cases are for slab-*in*-grade foundations only. They do not test slabs-*on*-grade, basement, or crawlspace foundations.
- The test cases do not test the sensitivity to any level of insulation. The slabs are all uninsulated.
- The entire domain has homogeneous soil properties, meaning that the concrete of the slab and foundation wall has the same thermal properties as the soil.
- The boundary conditions are approximated with constant film coefficients. There is no distinction among natural convection, forced convection, and long-wave radiation.
- There is no incident solar radiation on the exterior soil surface.

Results from the analytical truth standard and the three verified numerical solutions are compared to the solution methods used in Kiva for each of the *BESTEST* test cases. Each case uses symmetry to reduce the size of the domain and, consequently, the number of computations (to 1/4). The *BESTEST* procedures do not specify any sort of pass/fail criteria for the solutions outside of subjective comparison. For the purposes of this paper, verification implies there are no statistical outliers among the different solutions.

Before this work, the accuracy and computation time of different finite difference schemes have not been compared side-by-side in a common framework for foundation heat transfer calculations. Traditionally, researchers have selected schemes based on (1) ease of implementation (typically explicit schemes), (2) stability (fully implicit methods), (3) or availability of commercial software (usually finite element). Each of the three secondary mathematical truth standards uses some form of implicit scheme requiring use of a linear solver:

- TRNSYS: Fully implicit finite difference with iterative solver
- FLUENT: Finite element method with iterative solver
- MATLAB: Fully implicit finite difference with direct solver

The original source of secondary mathematical truth standards is not available to measure their computation performance under a consistent computational environment, nor were the simulation times provided in the *BESTEST* literature. However, due to their implicit nature, each of the solutions is expected to require computation times on the same order of magnitude as Kiva's fully implicit solution.

#### 4.1.1 Steady-State Test Cases

Table 4.1 shows the specification of each of the steady-state test cases. The only distinction between cases not listed in Table 4.1 is that the boundary at the wall/ground interface is a constant temperature profile for the analytical test case (GC10a) and adiabatic for all other cases.

Table 4.1: *BESTEST* steady-state test case specifications

Case	Slab dimensions [m x m]	$h_{int}$ [W/m <sup>2</sup> ·K]	$h_{ext}$ [W/m <sup>2</sup> ·K]	Ground depth [m]	Far-field width [m]	Soil conductivity [W/m·K]
GC10a	12 x 12	$\infty$	$\infty$	$\infty$	$\infty$	1.9
GC30a	12 x 12	$\infty$	$\infty$	30	20	1.9
GC30b	12 x 12	100	100	15	15	1.9
GC30c	12 x 12	7.95	$\infty$	15	8	1.9
GC60b	12 x 12	7.95	100	15	15	1.9
GC65b	12 x 12	7.95	11.95	15	15	1.9

Other characteristics similar to all steady-state test cases include the following:

- Interior air temperature = 30 °C,
- Foundation wall thickness = 0.24 m,
- Outside air temperature = 10 °C, and
- Deep ground temperature = 10 °C.

The *IEA BESTEST* User's Manual specification (Part I of Neymark and Judkoff [90]) for the analytical steady-state comparison case, GC10a, states the following:

Demonstrate that the current level of modeling detail yields negligible ( $\leq 0.1\%$ ) change in results versus a lesser level of detail; examine the effects of shallower deep

ground boundary, shorter far-field boundary distance, and less detailed mesh (if applicable). For ground depth and far-field length variations, increase the number of mesh nodes proportionally to the increase in soil volume being modeled.

The following sections describe the sensitivity of the GC10a results to changes in mesh detail, boundary distances, and solver convergence tolerance. These analyses were performed using the steady-state finite difference solution. Other solutions are expected to have similar results, when scaled accordingly. The results from the sensitivity analysis are used to inform the numerical parameters used elsewhere in this study.

#### 4.1.1.1 Sensitivity to Mesh Detail

Each of the three secondary mathematical truth standards uses a nonuniform mesh where the mesh size increases geometrically with the distance from the foundation wall boundary. This is also the case with Kiva where the mesh is uniform along the wall boundary (in the  $x$  and  $y$  directions) and increases geometrically downward (towards the deep-ground boundary), inward (towards the center-of-slab planes of symmetry), and outward (towards the far-field boundaries). Figure 4.1 shows a profile of the mesh generated by Kiva near the wall boundary for the GC10a test case.

Sensitivity to mesh detail was tested by varying the minimum allowable cell dimension,  $\Delta x_{min}$ , and the geometric growth factor,  $f_g$ . The size of each cell,  $i$  cells away from the boundary cell is defined by Equation 4.1:

$$\Delta x_i = \Delta x_{min} \cdot f_g^{i-1} \quad (4.1)$$

The minimum allowable cell size is used to set the size and number of cells in the uniform mesh region. The actual cell size is allowed to increase in order to fit uniformly into the dimensions allotted (in this case, the width of the wall boundary). Similarly, the growth factor is allowed to decrease in order to fit an exact number of cells within the domain's boundaries.

To demonstrate that the tested mesh detail yields negligible change in results versus a less detailed mesh, Kiva was tested under a combination of different minimum cell dimensions and growth factors over a range of values. The results are shown in Figure 4.2. The approximated slab

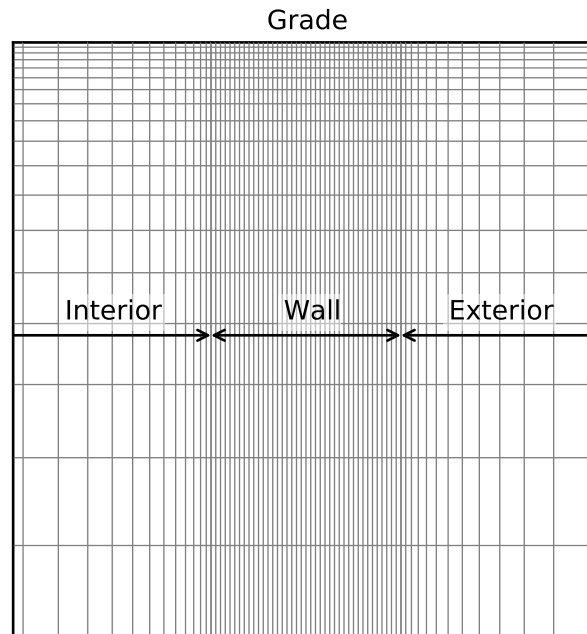


Figure 4.1: *BESTEST* GC10a mesh growth near the wall boundary

heat loss increases as the geometric growth factor decreases before settling near the value of the analytical solution at geometric growth factors less than 1.3. The slight peak at growth factors of 1.3 may be related to the actual sizing of the cells relative to the input minimum cell size and maximum growth factor. Simulations at higher levels of detail (i.e.,  $f_g < 1.10$ ) were beyond the memory limitations of the computing hardware, so it is difficult to say definitively whether the trends towards convergence continues.

No report from the three secondary mathematical truth standards indicated a complete parametric sweep across ranges of these two parameters. Instead, mesh independence was tested either with a single variable sweep (i.e., either  $\Delta x_{min}$  or  $f_g$ , but not both) or with a small subset of combinations. Therefore, it is difficult to know whether the other tools demonstrated similar trends towards convergence.

Figure 4.3 shows how the simulation wall time increases significantly as the geometric growth factor,  $f_g$ , and the minimum cell dimension,  $\Delta x_{min}$ , decrease.

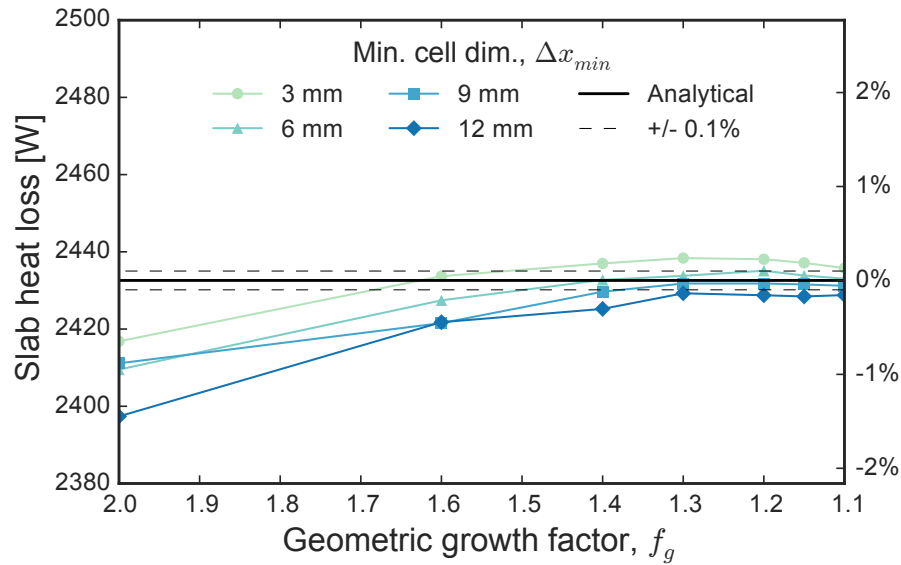


Figure 4.2: *BESTEST* GC10a slab heat loss sensitivity to mesh detail parameters

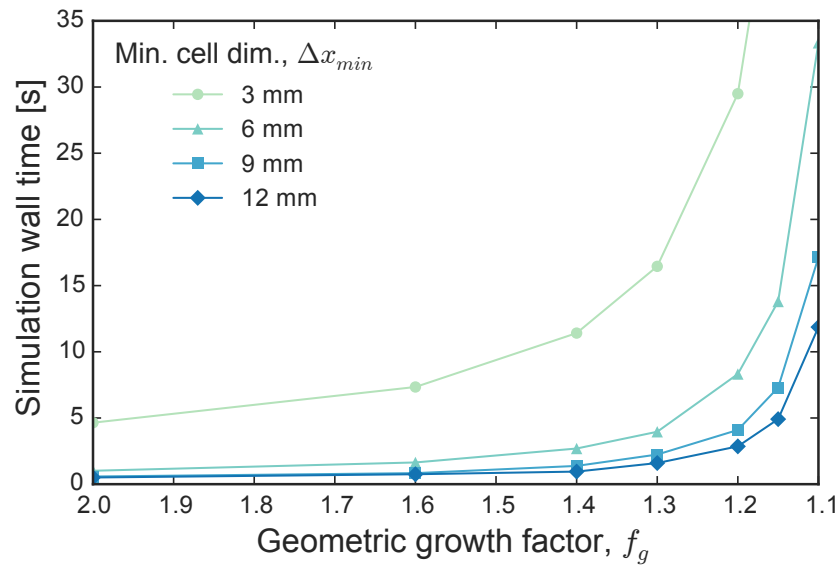


Figure 4.3: *BESTEST* GC10a simulation wall time sensitivity to mesh detail parameters

The combination of  $f_g$  and  $\Delta x_{min}$  selected for the Kiva *BESTEST* solutions is based on simulation wall time as well as the values selected by the other secondary mathematical truth

standards. These parameters are shown in Table 4.2 along with the selected values by the other tools.

Table 4.2: Mesh detail parameters selected by each tool for *IEA BESTEST* analyses

	<b>TRNSYS</b>	<b>FLUENT</b>	<b>MATLAB</b>	<b>Kiva</b>
$\Delta x_{min}$ [mm]	25.4	6.0	9.0-20.0	6.0
$f_g$	1.20-1.30	1.10	1.15-1.50	1.20

#### 4.1.1.2 Sensitivity to Boundary Distances

The analytical solution for GC10a represents the heat transfer through the slab into ground that extends infinitely outward and downward, so the numerical representation must demonstrate that variation in the boundary distances (i.e., the deep-ground depth and far-field width) yields negligible differences in the results.

The sensitivity to the boundary distances (far-field width and deep-ground depth) are shown in Figure 4.4. Generally, there is little sensitivity when the boundary distances are both 20 m or greater.

Figure 4.5 shows that simulation wall time has relatively little sensitivity to the boundary distances because the geometrically increasing mesh size requires very few additional cells near the boundary edges for increased boundary distances. Since there is little computation cost for improved accuracy, both boundary distances were set to 40 m for the GC10a test case.

#### 4.1.1.3 Sensitivity to Convergence Tolerance

*IEA BESTEST* specifies a similar test for the convergence of iterative solvers [90]:

If the software being tested allows user specification of convergence tolerance, demonstrate that the current level of heat-flow or temperature convergence tolerance yields negligible ( $\leq 0.1\%$ ) change in results versus the next finer convergence tolerance.

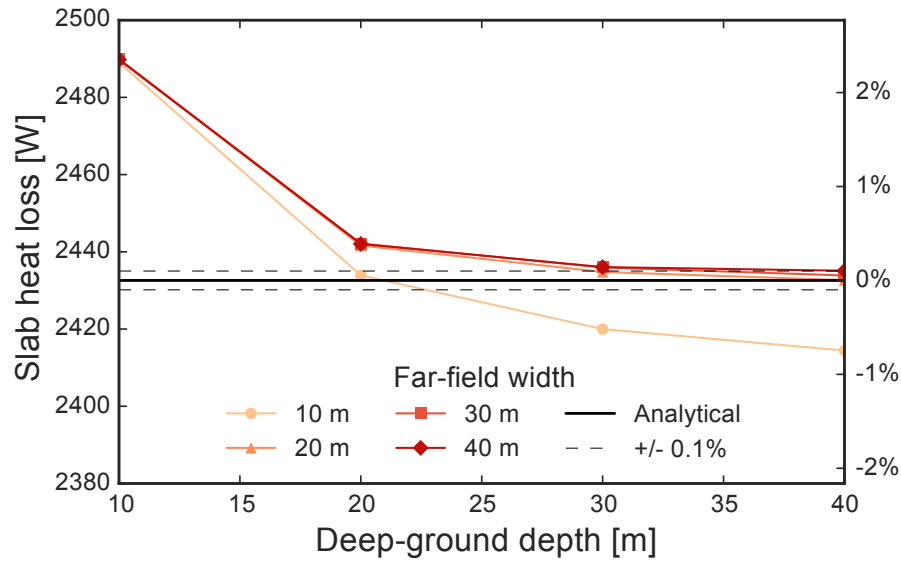


Figure 4.4: *BESTEST* GC10a slab heat loss sensitivity to boundary distances

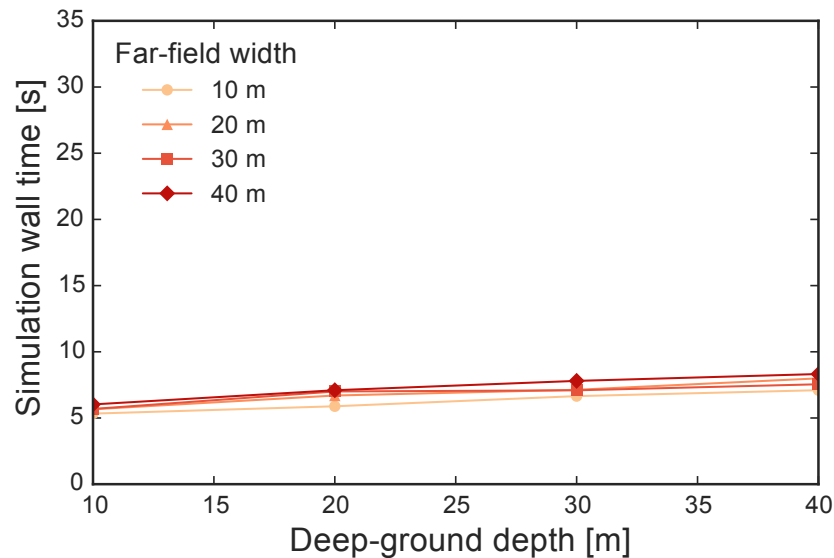


Figure 4.5: *BESTEST* GC10a simulation wall time sensitivity to boundary distances

Kiva uses the Library of Iterative Solvers (Lis) [106] to solve the system of equations at each time-step for the fully implicit, Crank-Nicolson, and steady-state solutions. As with any

iterative solver, it is necessary to specify a convergence tolerance. For the linear system,  $\mathbf{Ax} = \mathbf{b}$ , convergence in Lis is defined as such:

$$\|\mathbf{b} - \mathbf{Ax}\|_2 \leq tol \cdot \|\mathbf{b}\|_2, \quad (4.2)$$

where  $\|\mathbf{b} - \mathbf{Ax}\|_2$  is the  $\ell^2$ -norm of the residual.

Figure 4.6 shows the sensitivity of the slab heat loss and simulation wall time to tighter tolerances. By a tolerance of  $10^{-6}$  there is less than a 0.1% change in results. Tighter convergence tolerance has relatively small impact on simulation wall time.

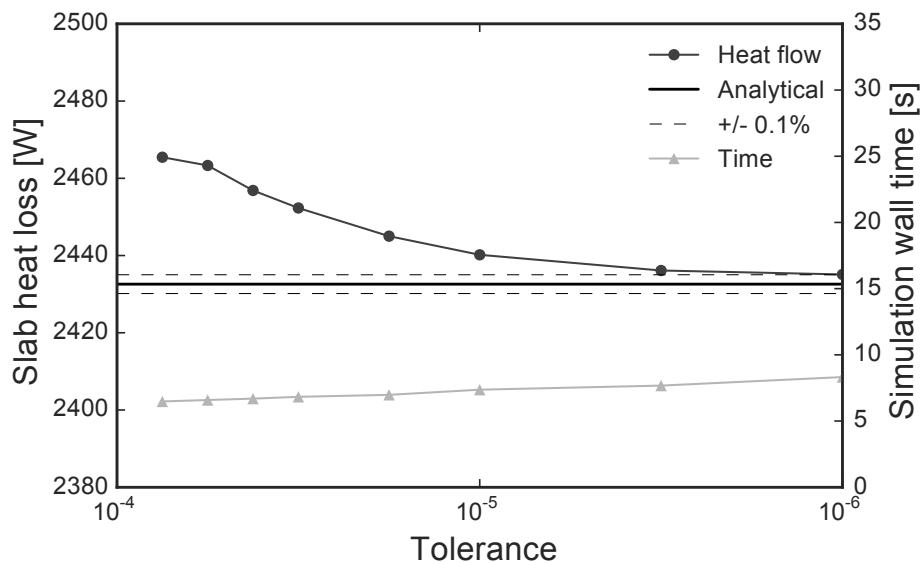


Figure 4.6: *BESTEST* GC10a slab heat loss and simulation wall time sensitivity to linear solver tolerance

#### 4.1.1.4 Sensitivity Analysis Summary

The previous sections demonstrate that the level of modeling detail for the GC10a test case yields a negligible change in results when compared to a lesser level of detail.

The numerical sensitivity results were derived from steady-state solutions of case GC10a. Extrapolating the results beyond this case implies the following assumptions:



- The accuracy for other cases, and other solution schemes, will show similar sensitivity.
- The computation wall time for other numerical schemes will demonstrate similar sensitivity and scale proportionally to that of the steady-state solution.

The selected parameters affecting the numerical approximation are shown in Table 4.3 and are used for all the remaining test cases and analyses unless otherwise specified.

Table 4.3: Selected numerical parameters for Kiva analyses

Parameter	Value
Time-step, $\Delta t$ [min]	60
Minimum cell dimension, $\Delta x_{min}$ [mm]	6.0
Maximum cell growth factor, $f_g$	1.20
Far-field width [m]	40
Deep-ground depth [m]	40
Tolerance	$10^{-6}$

#### 4.1.2 Steady-State Test Case Results

The slab heat loss for the steady-state *BESTEST* cases are shown in Figure 4.7 and in Table 4.4. It is evident that each of Kiva’s solution methods produce results within the statistical variation of the secondary truth standards.

All of Kiva’s solution methods provided accurate results, but, in some cases, the discretization parameters had to be relaxed in order to ensure stable solutions. If instabilities arose for a particular solution, the time-step was reduced first to ensure that there were no changes to the spatial discretization between solution methods. If a minute-long time-step was not enough to satiate the stability requirement, subsequent changes were made to the minimum cell dimension ( $\Delta x_{min}$ ).

For all the steady-state cases, the explicit solution method required a minute-long time-step and a minimum cell dimension of 20 mm. The ADE solution method required 30 minute time-steps for the cases with infinite convective coefficients (i.e., the *a* and *c* cases). These additional

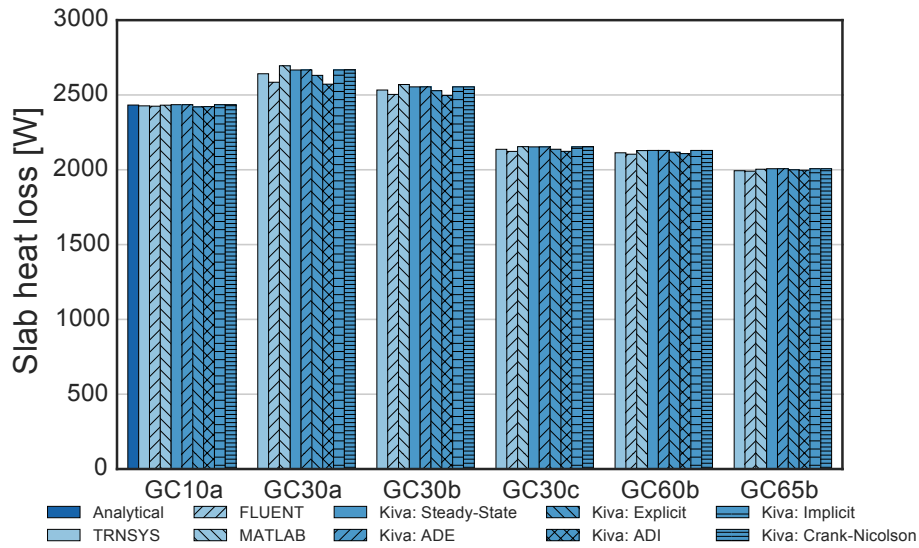


Figure 4.7: *BESTEST* steady-state test case slab heat loss

time-steps resulted in a proportional increase in simulation wall time. Figure 4.8 (note logarithmic  $y$ -axis) and Table 4.5 show the total simulation time required for each solution method and for each case. Each Kiva simulation was performed on a 24 core machine with 96 GB of available memory. The CPUs are Intel Xeon X5660 2.8 Ghz with 12 MB cache.

The *IEA BESTEST* User's Manual (Part I of Neymark and Judkoff [90]) specification for steady-state cases states the following:

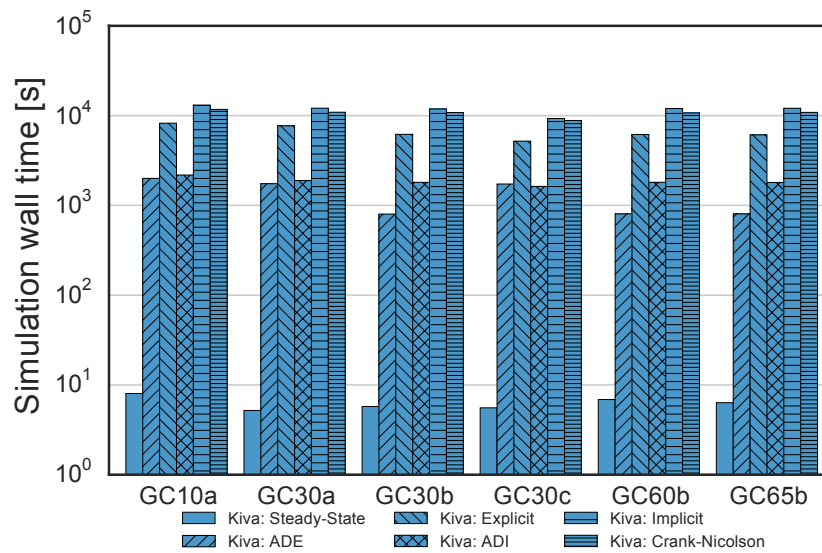
Initially (time < 0) the ground and slab are at 10 °C (50 °F) throughout; at the beginning of the simulation (time = 0) the zone air temperature steps to 30 °C (86 °F) and slab and soil temperatures begin to change accordingly.

and

If possible for the software being tested, the simulation should be run long enough that there is  $\leq 0.1\%$  variation between the floor slab conduction for the last hour of the last year of the simulation and the last hour of the preceding year of the simulation; i.e.,  $\leq 0.1\%$  variation over an interval of 8760 hours.

Table 4.4: *BESTEST* steady-state test case results: Slab heat loss [W]

	GC10a	GC30a	GC30b	GC30c	GC60b	GC65b
Analytical	2,433	–	–	–	–	–
TRNSYS	2,427	2,642	2,533	2,137	2,113	1,994
FLUENT	2,425	2,585	2,504	2,123	2,104	1,991
MATLAB	2,432	2,695	2,570	2,154	2,128	2,004
Kiva: Steady-State	2,435	2,667	2,554	2,153	2,129	2,007
Kiva: ADE	2,435	2,667	2,554	2,153	2,129	2,007
Kiva: Explicit	2,420	2,631	2,528	2,137	2,118	2,000
Kiva: ADI	2,422	2,572	2,497	2,123	2,108	1,997
Kiva: Implicit	2,435	2,667	2,554	2,153	2,129	2,007
Kiva: Crank-Nicolson	2,435	2,667	2,554	2,153	2,129	2,007

Figure 4.8: *BESTEST* steady-state test case simulation wall times (note logarithmic  $y$ -axis)Table 4.5: *BESTEST* steady-state test case simulation wall times [s]

	GC10a	GC30a	GC30b	GC30c	GC60b	GC65b
Kiva: Steady-State	8	5	6	6	7	6
Kiva: ADE	1,999	1,743	801	1,730	804	804
Kiva: Explicit	8,231	7,699	6,189	5,196	6,169	6,101
Kiva: ADI	2,180	1,891	1,807	1,628	1,809	1,802
Kiva: Implicit	13,108	12,103	11,852	9,273	11,995	12,080
Kiva: Crank-Nicolson	11,726	10,907	10,833	8,822	10,714	10,862

meaning that, as specified, the steady-state test cases must use a constant initialization method, simulated over as many years as required to reach the  $\leq 0.1\%$  criteria. However, the user's manual provides an exception (in section 1.2.1.6) if the software has other initialization methods:

If the program being tested allows for preconditioning (iterative simulation of an initial time period until temperatures or fluxes, or both, stabilize at initial values), use that capability.

Each of the unsteady solution methods were initialized with the steady-state solution. The slab heat loss reported is the final value after responding to the defined boundary conditions after a year's time of simulation, requiring significantly more time than the purely steady-state solution.

Important observations of the resulting simulation wall times follow:

- There is relatively little difference in wall time among *BESTEST* cases for the same solution. The ADE solution is the one exception as 30 minute time-steps were required in some cases (roughly doubling the wall time).
- Steady-state simulations are orders of magnitude faster since there is only a single calculation of the domain.
- ADE simulations are the fastest, though when the time-step is reduced to 30 minutes, they have nearly the same simulation time as the ADI simulations.
- Explicit simulations, due to their increased number of time-steps, have simulation times near those of the solutions that require an iterative solver (i.e., Implicit and Crank-Nicolson).
- Given the relatively small change in accuracy among each of the solution methods, the ADE and ADI methods show the most promise for typical annual energy analysis practices.

### 4.1.3 Harmonic (Unsteady) Test Cases

Table 4.6 shows the specification of each of the harmonic test cases. For each harmonic test case, the outdoor air dry-bulb temperature,  $T_{db,a}$  is given by:

$$T_{db,a} = (10 \text{ }^\circ\text{C}) - (6 \text{ }^\circ\text{C}) \cdot \cos\left(\frac{N_{day} - 15}{365} \cdot 2 \cdot \pi\right) - (2 \text{ }^\circ\text{C}) \cdot \cos\left(\frac{N_{hour} - 4}{24} \cdot 2 \cdot \pi\right) \quad (4.3)$$

where  $N_{day}$  is the  $N$ th day of the calendar year, and  $N_{hour}$  is the  $N$ th hour of the day (0 = midnight).

Table 4.6: *BESTEST* harmonic test cases specifications

Case	Slab dimensions [m x m]	$h_{int}$ [W/m <sup>2</sup> ·K]	$h_{ext}$ [W/m <sup>2</sup> ·K]	Ground depth [m]	Far-field width [m]	Soil conductivity [W/m·K]
GC40a	12 x 12	$\infty$	$\infty$	30	20	1.9
GC40b	12 x 12	100	100	15	15	1.9
GC40c	12 x 12	7.95	$\infty$	15	8	1.9
GC45b	36 x 4	100	100	15	15	1.9
GC45c	36 x 4	7.95	$\infty$	15	8	1.9
GC50b	80 x 80	100	100	15	15	1.9
GC55b	12 x 12	100	100	2	15	1.9
GC55c	12 x 12	7.95	$\infty$	5	8	1.9
GC70b	12 x 12	7.95	11.95	15	15	1.9
GC80b	12 x 12	100	100	15	15	0.5
GC80c	12 x 12	7.95	$\infty$	15	8	0.85

Other characteristics similar to all harmonic test cases include the following:

- Interior air temperature = 30 °C,
- Foundation wall thickness = 0.24 m,
- Deep ground temperature = 10 °C,
- Soil density = 1490 kg/m<sup>3</sup>, and
- Soil specific heat = 1800 J/kg·K.

#### 4.1.3.1 Initialization Method Analysis

As specified by the *IEA BESTEST* User's Manual (Part I of Neymark and Judkoff [90]) for harmonic test cases,

If possible for the software being tested, the simulation should be run long enough that there is  $\leq 0.1\%$  variation between the annual floor slab conduction for the last year of the simulation and the preceding year of the simulation.

Reducing the number of years required to initialize steady periodic conditions can significantly decrease computation time. *BESTEST* specifies that all temperatures in the ground domain be initialized to a spatially-constant temperature by default, but it allows room for other initialization methods as well:

If the program being tested allows for preconditioning (iterative simulation of an initial time period until temperatures or fluxes, or both, stabilize at initial values), use that capability.

This section explores the advantages and disadvantages of different preconditioning (referred to here as initialization) methods. There are three traditional initialization methods implemented in Kiva:

- (1) **Constant temperature:** Spatially-constant initial temperature.
- (2) **Kusuda:** A one-dimensional analytical solution developed by [75] that provides temperature variation as a function of depth driven by an annual harmonic temperature fluctuation. There is no temperature variation in either of the horizontal dimensions.
- (3) **Steady-state:** A steady-state solution scheme initializes the temperatures with the first time-step's boundary conditions. This provides an initial condition temperature variation in all dimensions.

Kiva's other initialization method, called the accelerated method, simulates the ground domain prior to the first time-step,  $t = 0$ . This presimulation period is itself initialized using a steady-state solution. The presimulation then commences with the following:

- (1) A period of long time-step (on the order of days to months), implicit calculations. Since the fully implicit method is unconditionally stable and physically realistic, these long time-

steps can be used to coarsely capture some of the thermal history driven by the annual weather cycle.

- (2) A subsequent period of normal time-step calculations prior to capture some of the shorter term dynamic effects.

The accelerated initialization method begins with a coarse timestep discretization and transitions to a finer discretization near the beginning of the simulation, similar to the way the spatial discretization becomes finer as it approaches the wall boundary.

Figure 4.9 shows the GC40a slab heat loss for the first year of simulation. Four traditional initialization methods (Kusuda, steady-state, and two different constant temperatures) are compared with an accelerated method and the “ideal” result, which is the steady periodic solution after several years of simulation (i.e., the net result is within 0.1% of the previous year’s heat loss). Figure 4.10 shows how the annual heat loss for each initialization method approaches the “ideal” steady periodic value over seven years (the percent difference is shown in Table 4.7).

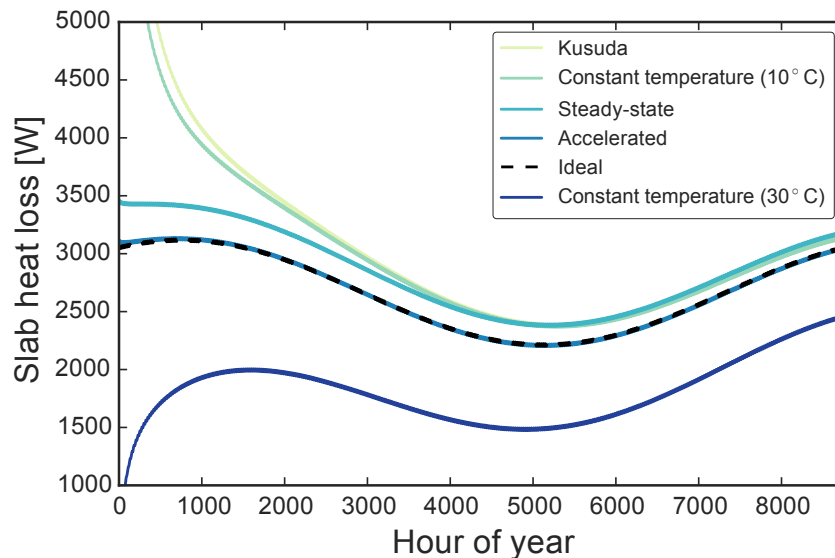


Figure 4.9: *BESTEST* GC40a comparison of initialization methods: First year slab heat loss

Important observations from these results are summarized below:

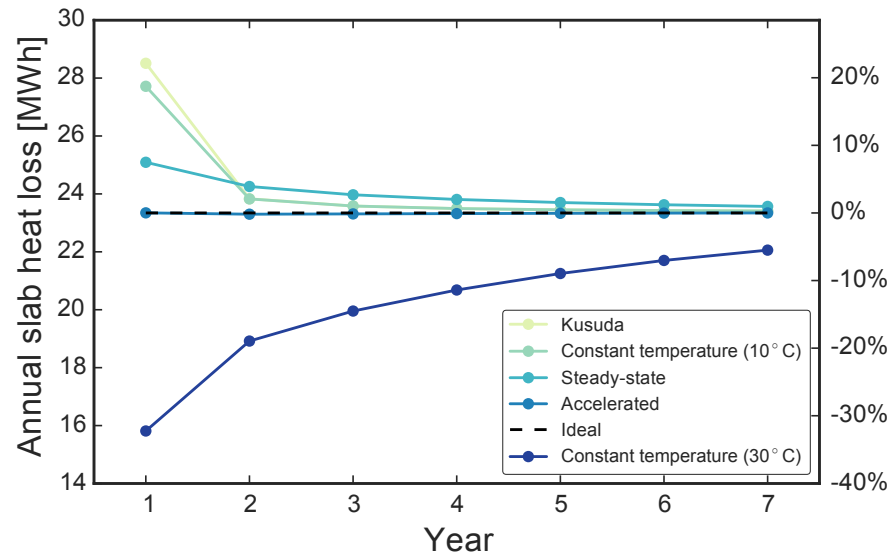


Figure 4.10: *BESTEST* GC40a comparison of initialization methods: Annual slab heat loss for seven years after initialization

- The accelerated method is nearly identical to the “ideal” result, with only a slight deviation near the beginning of the year.
- Of the four traditional methods, the steady-state initialization provides the best approximation of the “ideal” case for the first year, but the constant (10°C) and Kusuda initializations respond faster to the dynamics and provide a better approximation in subsequent years.
- By the second year, the constant (10°C) method is the best approximation among the traditional methods. However, the performance of this method depends on an appropriately selected initial temperature. Initializing to 30°C instead produces the worst approximation.
- Although the Kusuda method allows for spatially varying initial temperatures and may provide a reasonable approximation of the depth varying temperature in the far-field, it does a poor job of approximating the initial conditions near the building.

The acceleration method exemplified above is one of many possible variants. Other variants of the presimulation period can be defined using three parameters:



Table 4.7: *BESTEST* GC40a initialization method percent difference from “ideal” for seven years of simulation

Year	Kusuda	Constant temperature (10°C)	Steady-state	Accelerated	Constant temperature (30°C)
1	22.1%	18.7%	7.49%	0.01%	-32.3%
2	2.09%	2.07%	3.91%	-0.19%	-19.0%
3	1.02%	1.02%	2.69%	-0.14%	-14.5%
4	0.65%	0.65%	2.00%	-0.10%	-11.4%
5	0.46%	0.46%	1.54%	-0.06%	-8.96%
6	0.35%	0.36%	1.21%	-0.02%	-7.03%
7	0.28%	0.29%	0.96%	0.00%	-5.50%

- $\Delta t_{accel}$ : The time-step duration of the acceleration period (1 day, 1 week, 1 month, etc.)
- $t_{pre}$ : The total duration of the presimulation period
- $t_{warm-up}$ : The total duration of the warm-up period (directly before primary simulation on same time-step as primary simulation)

A wide range of potential accelerations were simulated to compare accuracy and relative simulation time. This range represents all combinations of the following parameter values (for the sake of consistency the duration of a month is defined as 4 weeks):

- Acceleration time-step,  $\Delta t_{accel}$ : 1 day, 1 week, 1 month
- Presimulation duration,  $t_{pre}$ : 3 months, 6 months, 12 months, 24 months
- Warm-up period,  $t_{warm-up}$ : none, 1 week, 1 month

In Kiva, the presimulation duration is not input by the user but is, instead, calculated internally as follows:

$$t_{pre} = \Delta t_{accel} \cdot N_{accel} + t_{warm-up}, \quad (4.4)$$

where  $N_{accel}$  is the number of acceleration time-steps used during the presimulation period and is an input into Kiva.

Figure 4.11 shows a comparison of the relative accuracy and wall time of all the initialization methods tested. In this figure, the relative difference in annual heat loss is the percent difference between the first year of simulation and the “ideal” steady periodic results. The additional simulation wall time represents the difference in time relative to the fastest simulation. The initial results revealed that the warm-up period,  $t_{warm-up}$ , has negligible impact on the accuracy of the results and added considerable time to the simulation. Variations of the warm-up period are not illustrated in Figure 4.11 to maximize legibility.

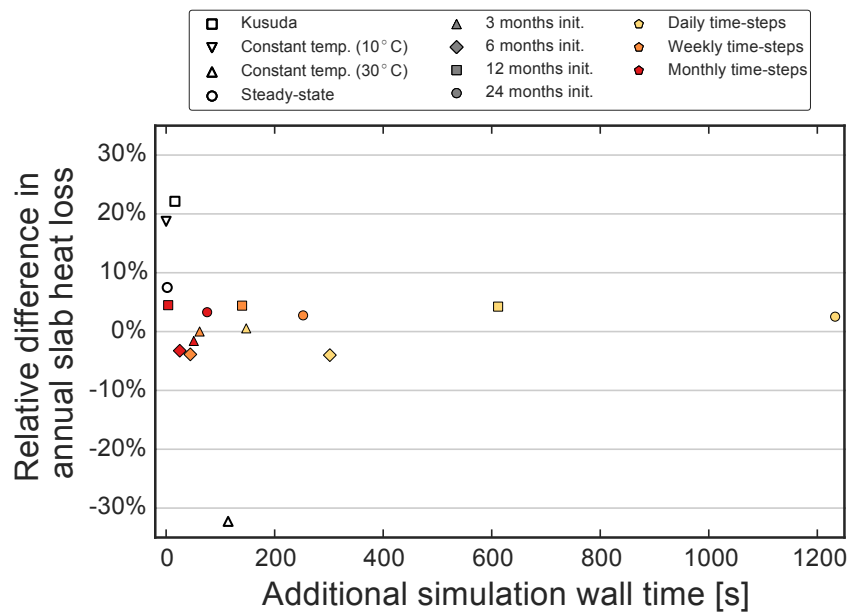


Figure 4.11: *BESTEST* GC40a comparison of first year slab heat loss for traditional and accelerated initialization methods

From Figure 4.11 we can infer the following conclusions:

- The acceleration method is consistently more accurate than the traditional initialization methods.
- Warm-up periods do not improve first year accuracy.

- There is not an acceleration time-step that is clearly more accurate than the others, though daily acceleration time-steps showed significant additional wall time without a consistent improvement in accuracy.
- There is no clear trend between the duration of the presimulation period and accuracy. By three months a majority of the thermal history has been captured by the presimulation.
- The most accurate presimulation initialization was found at weekly acceleration time-steps for a three month period. This may not be the best set of presimulation parameters for all cases as it could change depending on the thermal characteristics of the domain.

#### 4.1.4 Harmonic (Unsteady) Test Case Results

Each of the Kiva solution methods was used to simulate the *BESTEST* harmonic test cases. Each simulation leveraged an accelerated initialization followed by a full year of warm-up to satisfy the output requirements for allowable variation in slab heat loss between consecutive years. While the accelerated initialization method allows Kiva to simulate only two years, the secondary mathematical truth standard solutions required an average of seven years to initialize.

The results for the harmonic *BESTEST* cases are shown in Figure 4.12 and in Table 4.8. It is evident that each of the solution methods in Kiva produce results within the statistical variation of the secondary truth standards.

Table 4.8: *BESTEST* harmonic (unsteady) test case results: Annual slab heat loss [MWh]

	GC40a	GC40b	GC40c	GC45b	GC45c	GC50b	GC55b	GC55c	GC70b	GC80b	GC80c
TRNSYS	23.0	22.1	18.6	32.8	27.0	277.9	35.1	20.8	17.4	6.0	9.2
FLUENT	22.8	21.9	18.6	32.5	26.9	278.0	34.9	20.7	17.4	5.9	9.1
MATLAB	23.6	22.5	18.9	33.5	27.4	281.4	35.5	21.0	17.6	6.2	9.3
Kiva: ADE	23.3	22.4	18.9	33.4	27.5	279.5	35.2	20.9	17.6	6.1	9.3
Kiva: Explicit	23.0	22.2	18.8	33.0	27.3	278.4	35.0	20.8	17.6	6.0	9.2
Kiva: ADI	22.5	21.9	18.6	32.5	27.1	276.2	34.7	20.6	17.5	6.0	9.2
Kiva: Implicit	23.3	22.4	18.9	33.4	27.5	279.5	35.2	20.9	17.6	6.1	9.3
Kiva: Crank-Nicolson	23.3	22.4	18.9	33.4	27.5	279.5	35.2	20.9	17.6	6.1	9.3

*IEA BESTEST* procedures specify that annual time-series results must be provided for each of the GC40 cases (a, b, and c). In a plot of annual results (Figure 4.13), it can be difficult to

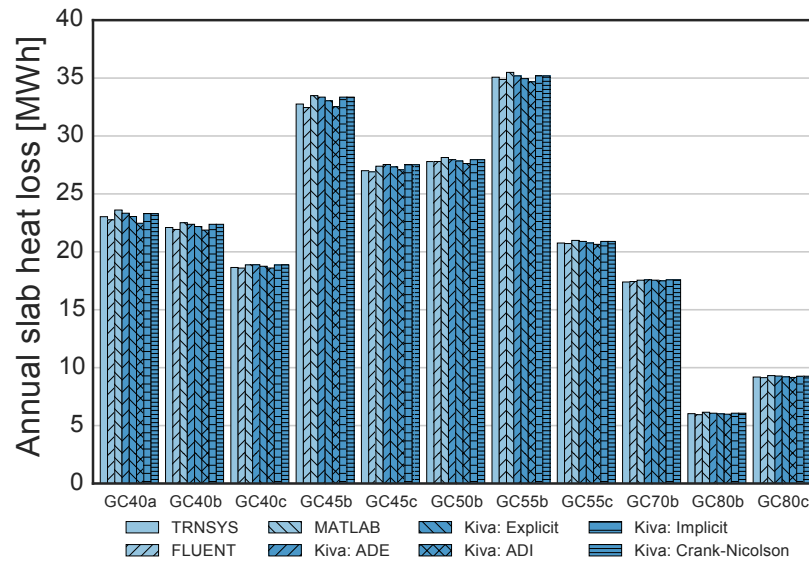


Figure 4.12: *BESTEST* harmonic (unsteady) test case annual slab heat loss (results for GC50b are divided by 10 to maintain a consistent scale)

notice some of the more subtle differences among the solution results at the time-step level. It is more informative to compare the annual and daily time-scale characteristics of the solutions. As the time-series solutions are driven by the sinusoidal variation in exterior temperature (Equation 4.3), the solution for slab heat loss takes a similar form:

$$\dot{Q} = \bar{Q} + \dot{Q}_{year} \cdot \cos\left(\frac{N_{day} - \Phi_{year} - 15}{365} \cdot 2 \cdot \pi\right) + \dot{Q}_{day} \cdot \cos\left(\frac{N_{hour} - \Phi_{day} - 4}{24} \cdot 2 \cdot \pi\right) \quad (4.5)$$

where each solution is represented by the following five harmonic parameters:

- $\bar{Q}$ : The average slab heat loss
- $\dot{Q}_{year}$ : The annual amplitude of the slab heat loss
- $\Phi_{year}$ : The annual phase shift of the slab heat loss (relative to the phase of the annual temperature variation)
- $\dot{Q}_{day}$ : The daily amplitude of the slab heat loss

- $\Phi_{day}$ : The daily phase shift of the slab heat loss (relative to the phase of the daily temperature variation)

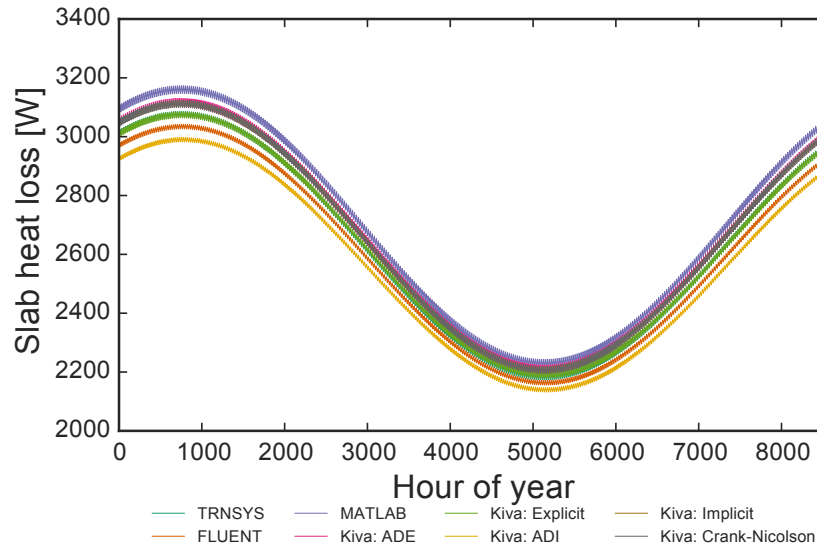


Figure 4.13: *BESTEST* GC40a harmonic (unsteady) test case hourly results

The values of each of the five harmonic parameters for the three GC40 cases are shown in Table 4.9. The annual slab heat loss never exceeds a 5% difference between solutions for a given case. For each case any deviation from the median parameter values is indicated by the degree of background shading (darker indicates more deviation). The only outliers occur for the daily parameters,  $\dot{Q}_{day}$  and  $\Phi_{day}$ , in the ADE solutions, which appears to be less accurate at shorter time scales.

Similar to the stability issues mentioned for the steady-state tests, the explicit solution method required the same restrictions on time-step and cell size (1 minute time-steps and 20 mm minimum cell size) to ensure stability. The ADE solution method required shorter time-steps for several cases involving infinite convective coefficients (the *a* and *c* cases). The stable time-steps used in verification for the ADE solutions are listed in Table 4.10.

Table 4.9: *BESTEST* GC40 harmonic parameters for each solution (shading indicates deviation from the median value for each case)

Case/Solution	$\bar{Q}$ [W]	$\dot{Q}_{year}$ [W]	$\Phi_{year}$ [days]	$\dot{Q}_{day}$ [W]	$\Phi_{day}$ [hours]
<b>GC40a:</b>					
TRNSYS	2,629	447	16.6	10.2	8.3
FLUENT	2,598	435	17.2	8.2	8.1
MATLAB	2,695	465	16.4	13.4	8.2
Kiva: ADE	2,664	453	16.4	13.7	2.3
Kiva: Explicit	2,631	443	16.9	10.6	9.4
Kiva: ADI	2,565	425	17.5	7.6	9.7
Kiva: Implicit	2,660	452	16.4	11.6	8.3
Kiva: Crank-Nicolson	2,660	453	16.4	12.6	8.9
<b>GC40b:</b>					
TRNSYS	2,523	412	17.9	6.4	9.3
FLUENT	2,504	405	18.3	5.6	8.9
MATLAB	2,570	424	18.0	8.1	9.3
Kiva: ADE	2,554	416	18.1	14.2	7.7
Kiva: Explicit	2,532	409	18.4	6.8	10.4
Kiva: ADI	2,497	399	18.7	5.2	10.4
Kiva: Implicit	2,554	415	17.9	6.9	9.3
Kiva: Crank-Nicolson	2,554	415	17.9	7.6	10.0
<b>GC40c:</b>					
TRNSYS	2,129	323	21.9	2.4	10.1
FLUENT	2,123	319	22.2	2.2	9.8
MATLAB	2,154	329	22.0	3.0	10.1
Kiva: ADE	2,156	325	22.5	1.1	8.8
Kiva: Explicit	2,141	321	22.4	2.4	11.4
Kiva: ADI	2,124	316	22.7	1.9	11.3
Kiva: Implicit	2,153	325	22.0	2.6	10.4
Kiva: Crank-Nicolson	2,154	325	22.0	3.0	11.1

Table 4.10: ADE time-step size for harmonic *BESTEST* cases

Case	Time-step [minutes]
GC40a	30
GC40b	60
GC40c	20
GC45b	60
GC45c	20
GC50b	60
GC55b	60
GC55c	20
GC70b	60
GC80b	60
GC80c	30

Figure 4.14 and Table 4.11 show the total simulation time required for each solution method and for each case. The following observations can be taken from these results:

- Variation among cases is caused mostly by changes in the domain size.
- ADE simulations are again the fastest, though when the time-step is reduced, there is a proportional increase in wall time.
- Explicit simulations, due to their increased number of time-steps, have simulation times near those of the solutions, which require a linear algebra solver (i.e., Implicit and Crank-Nicolson).
- Given the relatively small change in accuracy between each of the solution methods, the ADE and ADI methods remain the most promising for typical annual energy analysis practices.

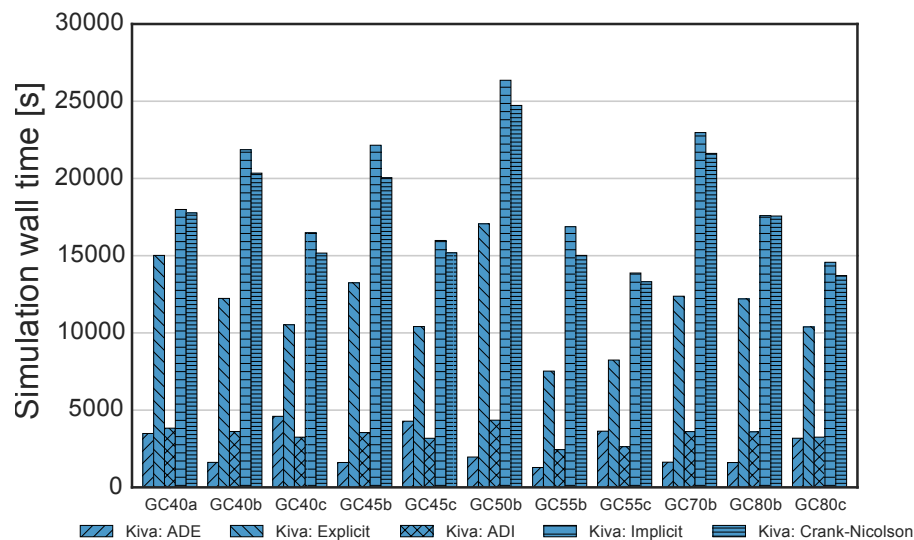


Figure 4.14: *BESTEST* harmonic (unsteady) test case simulation wall times

## 4.2 Summary and Conclusions

The results of the *BESTEST* comparison cases indicate that there are no statistical outliers with regard to total slab heat loss. Kiva's capability to utilize several different finite difference

Table 4.11: *BESTEST* harmonic (unsteady) test case results: Simulation wall time [s]

	GC40a	GC40b	GC40c	GC45b	GC45c	GC50b	GC55b	GC55c	GC70b	GC80b	GC80c
Kiva: ADE	3,488	1,618	4,599	1,610	4,283	1,963	1,286	3,637	1,630	1,607	3,180
Kiva: Explicit	15,017	12,233	10,528	13,243	10,411	17,063	7,527	8,242	12,376	12,201	10,387
Kiva: ADI	3,832	3,617	3,249	3,547	3,178	4,350	2,442	2,632	3,609	3,595	3,251
Kiva: Implicit	17,991	21,863	16,488	22,152	15,984	26,358	16,875	13,878	22,969	17,593	14,572
Kiva: Crank-Nicolson	17,771	20,344	15,169	20,051	15,184	24,728	15,018	13,314	21,623	17,567	13,712

solution methods makes it the first tool to directly compare multiple methods under the same computational framework, thus ensuring that differences among the solutions are isolated from other programming differences. Each method was evaluated regarding numerical accuracy, computation time, and stability.

In general, a fully implicit solution provides the most accurate results as it is not subject to some of the stability issues associated with the explicit schemes or the sub-time-step approximations of the ADI scheme. The Crank-Nicolson scheme provides a better approximation of time differencing than the fully implicit scheme though it is still subject to unrealistic oscillations.

Although the ADI solution tended to underapproximate the slab heat loss relative to the other solutions, it required less than one quarter of the computation time of the other implicit schemes. It is also superior to the ADE scheme in that it has less stringent stability criteria.

Finally, the investigation into initialization methods revealed that each of the traditional methods (Kusuda, constant temperature, and steady-state) required seven or more years to arrive at a steady harmonic response to the driving exterior temperature variation. Several variations of accelerated initializations were tested and were all found to provide a more accurate approximation of the first year heat loss than the traditional methods. Of these accelerated initializations, those with a short (three month) initialization period and relatively long acceleration time-steps (one week) provided a favorable trade-off between accuracy and the additional required simulation time.

On the whole, the simulation time required to perform foundation heat transfer calculations can be significantly reduced, relative to traditional approaches, without a significant loss in accuracy.



For the GC40a test case, a two-year simulation using the ADI solution method with accelerated initialization required 56.5 minutes in contrast to the projected 18.25 hours required for a seven-year simulation using the fully implicit method with a traditional initialization method (a nearly 95% reduction in simulation wall time).

## Chapter 5

### Two-Dimensional Approximation Methods

Chapter 4 demonstrated how computation time is reduced through the selection of the Alternating Direction Implicit (ADI) solution scheme and the accelerated initialization method, without significantly affecting the veracity of Kiva's calculations. Chapter 4 also established discretization independence for the solutions within the context of the *IEA BESTEST* procedures.

Further reductions in computation time are possible, but they require a more delicate balance with computational accuracy. Reducing the problem to two-dimensions is a common approach and can reduce the number of calculations by several orders of magnitude.

Many efforts have been taken to approximate three-dimensional effects using an equivalent two-dimensional geometry. Walton [114] noted that improper application of two-dimensional calculations can result in up to 50% error, relative to three-dimensional calculations. Only a few authors have compared their two-dimensional approximations to a three-dimensional reference solution.

It is generally accepted that the heat transfer from building foundations is strongly two-dimensional near the perimeter of the foundation. However, there is no consensus on how the two-dimensional simulation results should be scaled to represent the heat transfer within the actual, three-dimensional context. This chapter aims to resolve the disparity between two- and three-dimensional simulation results by exploring the implications of different two dimensional approximation methods using the Kiva numerical framework.

## 5.1 Current Approximation Methods

The sections below describe several established methods of scaling two-dimensional simulation results. Each approximation method uses the same vertical dimensions as the three-dimensional definition, but differs in how it defines the lateral dimension of the foundation floor,  $\Delta x_f$ , in Figure 5.1.

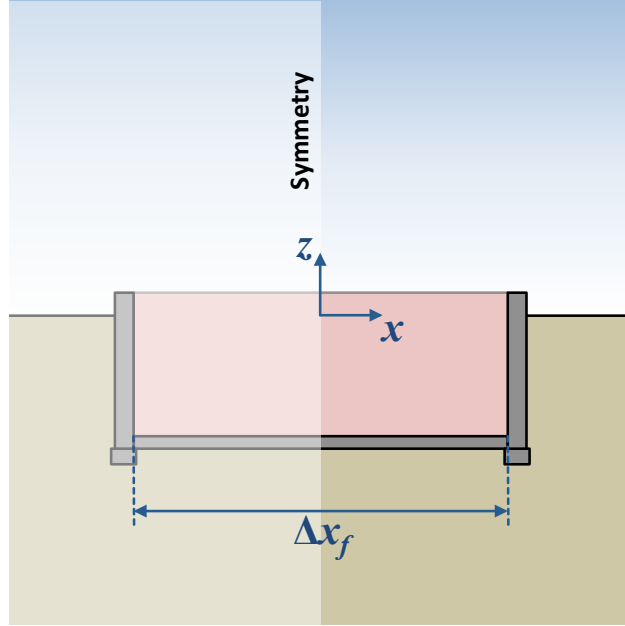


Figure 5.1: Typical context for two-dimensional approximations

Many authors refer to  $\Delta x_f/2$  as the “half-width,” which is the dimension used for the foundation in a symmetric domain [39, 24].

### 5.1.1 Perimeter

Many authors provide results normalized by foundation perimeter. Scaling by the perimeter is a logical first choice since the magnitude of the foundation heat transfer is stronger near the perimeter. The total representative three-dimensional heat transfer is calculated as follows:

$$\dot{Q}_{3D} = \Delta x_f P_{3D} \dot{q}_{cart,f} + \Delta z_w P \dot{q}_{cart,w}, \quad (5.1)$$

where

- $\dot{Q}_{3D}$  is the three-dimensional heat transfer rate [W],
- $P_{3D}$  is the perimeter [m] of the foundation shape in three-dimensions,
- $\dot{q}_{cart,f}$  is the two-dimensional heat flux [W/m<sup>2</sup>] through the foundation floor calculated in a Cartesian coordinate system,
- $\Delta z_w$  is the height [m] of the foundation wall, and
- $\dot{q}_{cart,w}$  is the two-dimensional heat flux [W/m<sup>2</sup>] through the foundation wall calculated in a Cartesian coordinate system.

Beausoleil-Morrison et al. [16] developed a modified perimeter-scaled approximation called the ‘‘Corner Correction Method.’’ This method introduces corner correction factors that relate the heat transfer at the corners of the foundation to the heat transfer of the center portions of the foundation perimeter, where heat transfer is more two-dimensional:

$$F_c = \left[ \frac{\dot{q}_{corner}}{P_{corner}} \right] \left[ \frac{\dot{q}_{center}}{P_{center}} \right]^{-1} \quad (5.2)$$

Corner correction factors were calculated from a regression based on 3,024 numerical simulations of rectangular basements. The result is a table of 19 regression coefficients that correlate the correction factors to six independent variables related to insulation configuration, soil thermal properties, and foundation geometry.

Scaling by the perimeter does not strictly define the value of foundation floor width,  $\Delta x_f$ , needed to create the two-dimensional domain. Both Bazjanac et al. [13] and Deru [39] defined the foundation width as the narrow dimension of a rectangular foundation. However, instead of using the relationship defined by Equation 5.1, Bazjanac et al. [13] weighted the floor results by the area of discrete rectangular annuli corresponding to different locations along the floor width.

### 5.1.2 Area-to-Perimeter Ratio

Bahnfleth [9] and Bahnfleth and Pedersen [11] simulated a series of three-dimensional square, rectangular, and L-shaped slabs with a range of foundation areas and perimeter lengths. They

demonstrated that heat transfer does not vary linearly with the perimeter of the foundation, and indicated that the area of the foundation also plays an important role. They concluded that the average heat flux through rectangular and L-shaped slabs could be calculated as a function of the area-to-perimeter ratio  $A/P$ :

$$\dot{q} = c[A/P]^{-d}, \quad (5.3)$$

where

- $\dot{q}$  is the average slab heat flux [ $\text{W}/\text{m}^2$ ],
- $c$  is a correlation constant [ $\text{W}/\text{m}^{2+d}$ ],
- $A$  is the slab area [ $\text{m}^2$ ],
- $P$  is the slab perimeter [ $\text{m}$ ], and
- $d$  is a dimensionless correlation constant.

The area-to-perimeter ratio also appears in the study of fluid flow—another diffusion driven phenomenon. Fluid flowing through channels is often characterized by a single characteristic length, the hydraulic diameter, defined by the following:

$$D_h = 4 \left[ \frac{A}{P} \right], \quad (5.4)$$

where  $A$  is the cross-sectional area of the channel and  $P$  is the wetted perimeter.

The hydraulic diameter defines the effective diameter of a circular channel, allowing any channel to use similar flow calculations. It is logical that that the same relationship applies to heat diffusion through building foundations.

Extrapolating Equation 5.3 beyond rectangular and L-shaped slabs implies that foundation heat transfer can be calculated by scaling heat fluxes by foundation area. Therefore, heat transfer from geometrically complicated shapes can be calculated from simpler shapes with the same characteristic length.

Although Bahnfleth and Pedersen [11] never developed a two-dimensional approximation method themselves, a number of authors have utilized the  $A/P$  characteristic length for scaling two-dimensional results [95, 24, 25]. The  $A/P$  characteristic length leads to two possible shapes that can be simulated in two dimensions: one for an axisymmetric cylindrical coordinate system and another for a Cartesian coordinate system.

In axisymmetric cylindrical coordinates, any foundation shape can be represented by a circle of radius

$$r = 2 \left[ \frac{A}{P} \right] \quad (5.5)$$

as shown in Figure 5.2.

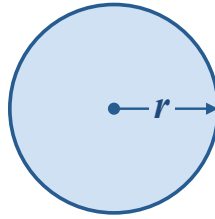


Figure 5.2: Characteristic length of a circle in a cylindrical coordinate system

With  $\Delta x_f = 2r$ , the total representative three-dimensional heat transfer for the circular method is as follows:

$$\dot{Q}_{3D} = A_{3D} \dot{q}_{cyl,f} + P_{3D} \Delta z_w \dot{q}_{cyl,w}, \quad (5.6)$$

where

- $A_{3D}$  is the area [ $\text{m}^2$ ] of the three-dimensional foundation shape,
- $\dot{q}_{cyl,f}$  is the two-dimensional heat flux [ $\text{W}/\text{m}^2$ ] through the foundation floor calculated in a cylindrical coordinate system, and

- $\dot{q}_{cyl,w}$  is the two-dimensional heat flux [W/m<sup>2</sup>] through the foundation wall calculated in a cylindrical coordinate system.

In Cartesian coordinates, any foundation shape can be represented by an infinite rectangle of length,  $l$ , and width,  $w$ . The area-to-perimeter ratio can be expressed as follows:

$$\left[ \frac{A}{P} \right] = \frac{lw}{2l + 2w} = \frac{w}{2 + \frac{2w}{l}}, \quad (5.7)$$

and as  $l \rightarrow \infty$ ,

$$\left[ \frac{A}{P} \right] \rightarrow \frac{w}{2}, \quad (5.8)$$

which means any foundation shape can be represented by an infinite rectangle of width

$$w = 2 \left[ \frac{A}{P} \right]. \quad (5.9)$$

as shown in Figure 5.3.

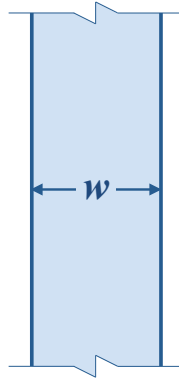


Figure 5.3: Characteristic length of a infinite rectangle in a Cartesian coordinate system

With  $\Delta x_f = w$ , the total representative three-dimensional heat transfer for the infinite rectangle method is as follows:

$$\dot{Q}_{3D} = A_{3D}\dot{q}_{cart,f} + P_{3D}\Delta z_w\dot{q}_{cart,w}, \quad (5.10)$$

where

- $\dot{q}_{cart,f}$  is the two-dimensional heat flux [W/m<sup>2</sup>] through the foundation floor calculated in a Cartesian coordinate system, and
- $\dot{q}_{cart,w}$  is the two-dimensional heat flux [W/m<sup>2</sup>] through the foundation wall calculated in a Cartesian coordinate system.

Chuangchid [24] and Chuangchid and Krarti [25] verified that both circular and infinite rectangular shapes in two-dimensional coordinates provide reasonable approximations for insulated circular, rectangular, and square slabs in three dimensions.

### 5.1.3 Rounded Rectangle

Walton [114] developed an approximation method that produced two-dimensional results within 2% of a three-dimensional reference. This method, called the “rounded rectangle,” or RR method, transforms any three-dimensional foundation geometry into a rounded rectangle foundation of the same perimeter and area. The rounded rectangle allows entire problems to be solved using the superposition of heat transfer calculated using a Cartesian coordinate system (for the straight sides) and a cylindrical coordinate system (for the rounded ends). From the area,  $A$ , and perimeter,  $P$ , the dimensions of the rounded rectangle can be calculated as follows:

$$a = \left( P - \sqrt{P^2 - 4\pi A} \right) / \pi, \quad (5.11)$$

and

$$b = (P - \pi a) / 2. \quad (5.12)$$

as shown in Figure 5.4.

With  $\Delta x_f = a$  for both coordinate systems, the total representative three-dimensional heat transfer is as follows:

$$\dot{Q}_{3D} = ab\dot{q}_{cart,f} + 2b\Delta z_w\dot{q}_{cart,w} + \pi a^2\dot{q}_{cyl,f} + 2\pi a\Delta z_w\dot{q}_{cyl,w}. \quad (5.13)$$



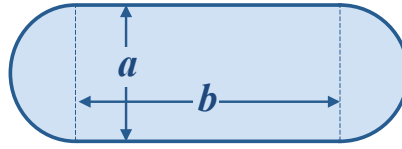


Figure 5.4: Dimensions of a rounded rectangle with equivalent area and perimeter

Walton verified his rounded rectangle approximations for uninsulated rectangular basements and slabs under a steady-state solution, while results for X-shaped and H-shaped basements showed up to a 6.3% difference in some cases.

The rounded rectangle approximation method uses two characteristic lengths,  $a$  and  $b$ , which allow for an additional degree of freedom in determining the representative heat transfer. In this case, the additional degree of freedom requires two independent two-dimensional simulations, one for each coordinate system. However, because the simulations are independent, they can be calculated on parallel processors without significantly more computation time than a single simulation.

## 5.2 Heat Transfer from Concave Foundation Shapes

Bahnfleth and Pedersen [11] and Walton [114] explain that two-dimensional results can better approximate three-dimensional results when scaled by both area and perimeter of the shape, not just perimeter. Bahnfleth and Pedersen [11] also introduced the characteristic length,  $A/P$ , which can be used to generate representative heat fluxes in two-dimensional geometry. However, no established approximation method developed thus far accounts for concave foundation shapes. Even the corner-correction method developed by Beausoleil-Morrison et al. [16] only provides adjustments for convex rectangular corners.

Shape cavities are defined relative to the shape's convex hull. The convex hull is the smallest convex polygon that envelops the original polygon. The spatial difference between the original shape (Figure 5.5(a)) and the convex hull (Figure 5.5(b)) defines the set of cavities (Figure 5.5(c)).

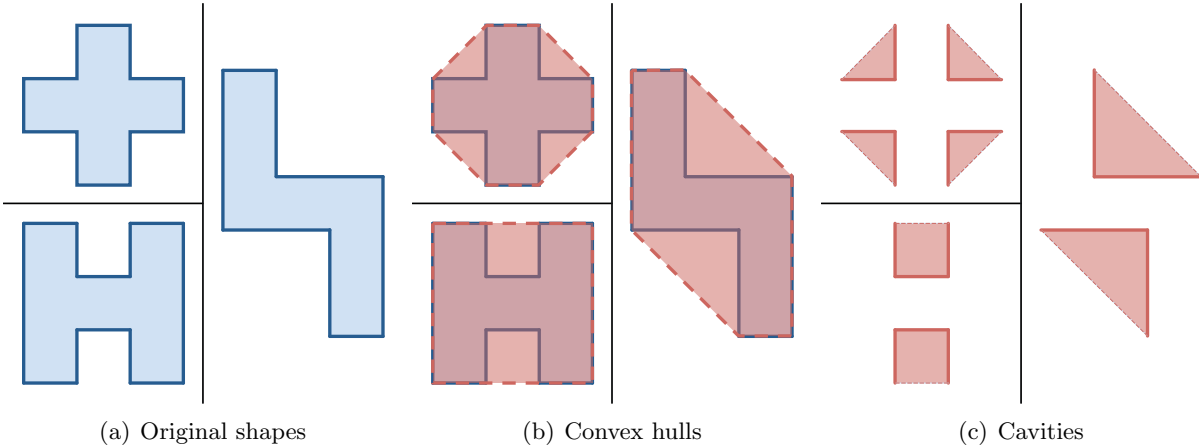


Figure 5.5: Determination of cavities for various shapes

While heat transferred from convex edges is largely unaffected by other edges, the ground within cavities is warmer because of the additive heat flow from neighboring concave edges. This results in reduced heat transfer from the foundation. The influence of neighboring concave edges on heat transfer can be observed in Figure 5.6 for three-dimensional simulation results. Heat flux is higher through the ground near the concave slab corner, relative to heat fluxes further from the corner. Consequently, heat flux is lower through the slab in proximity to the warmer ground.

The degree of heat transfer reduction within cavities depends on several factors beyond the shape itself. These influential factors are illustrated by isolating the concave effects. The following sections describe two separate types of interactive effects that occur between concave foundation edges.

### 5.2.1 Opposing Parallel Edges

The first example of interaction between concave edges occurs when two parallel edges come within close proximity of each other. This effect can be isolated by simulating heat transfer from

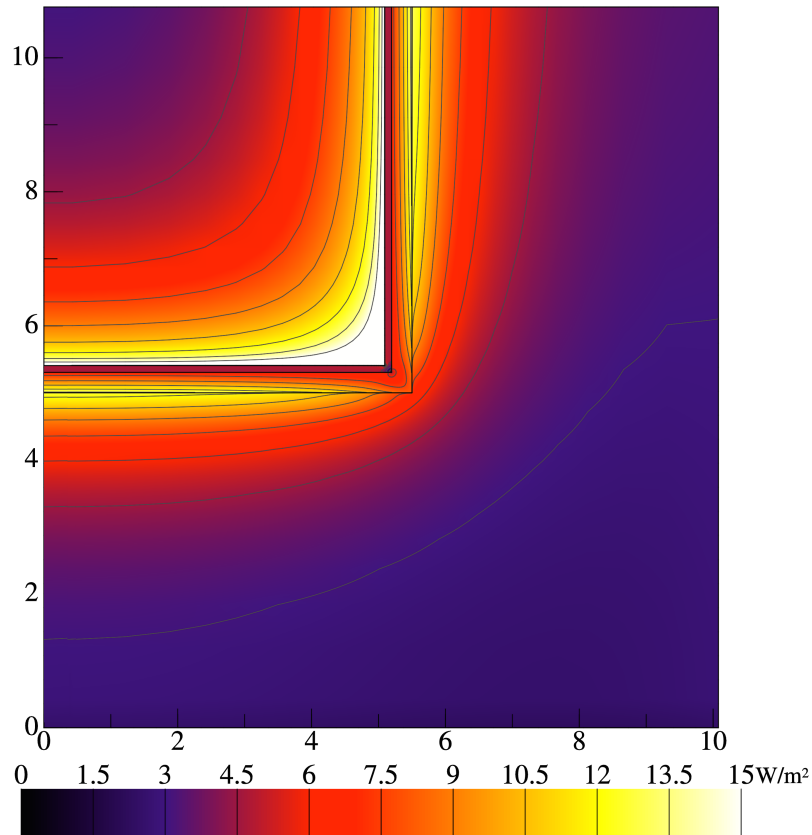


Figure 5.6: Plan view cross-section at grade height of heat flux near a concave slab corner (exterior grade in the upper left)

two infinitely long rectangles separated by a distance,  $p$  (Figure 5.7). This arrangement can be simulated in two-dimensions with two planes of symmetry. This exercise demonstrates how the heat flux is reduced as the distance  $p$  decreases.

The extent of the impact of opposing parallel edges will depend on the actual perimeter of opposing edges. In the example of infinite rectangles, heat transfer reduces to zero as the distance between the edges closes. Actual foundation shapes are enclosed, which means that the effect applies to less than half of the perimeter, at most (in the case of long U-shaped foundations).

Parallel concave edges are simulated for a combination of area-to-perimeter ratios, soil conductivity, and insulation levels. All simulations are steady-state with an indoor-outdoor temperature difference of 20°C. Unless stated otherwise, the foundations are slabs-on-grade with exterior horizontal insulation extending roughly one meter from the perimeter. The results presented in

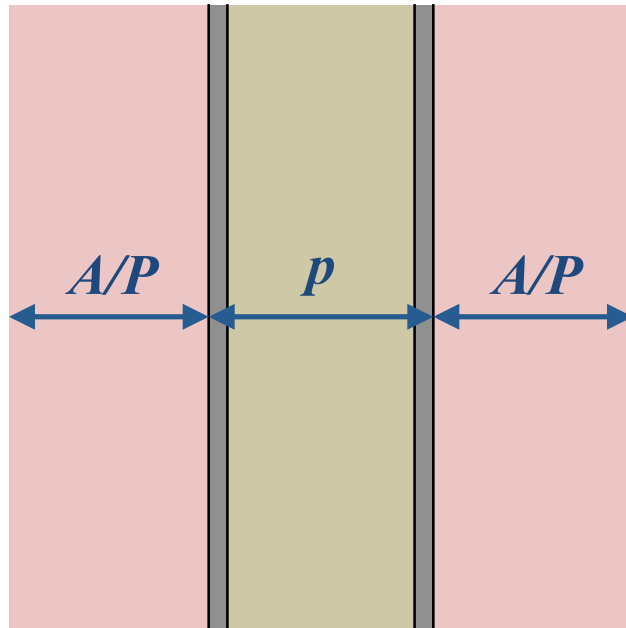


Figure 5.7: Plan view of parallel concave edges

Figures 5.8–5.10 demonstrate the sensitivity of opposing parallel edges for a single example foundation.

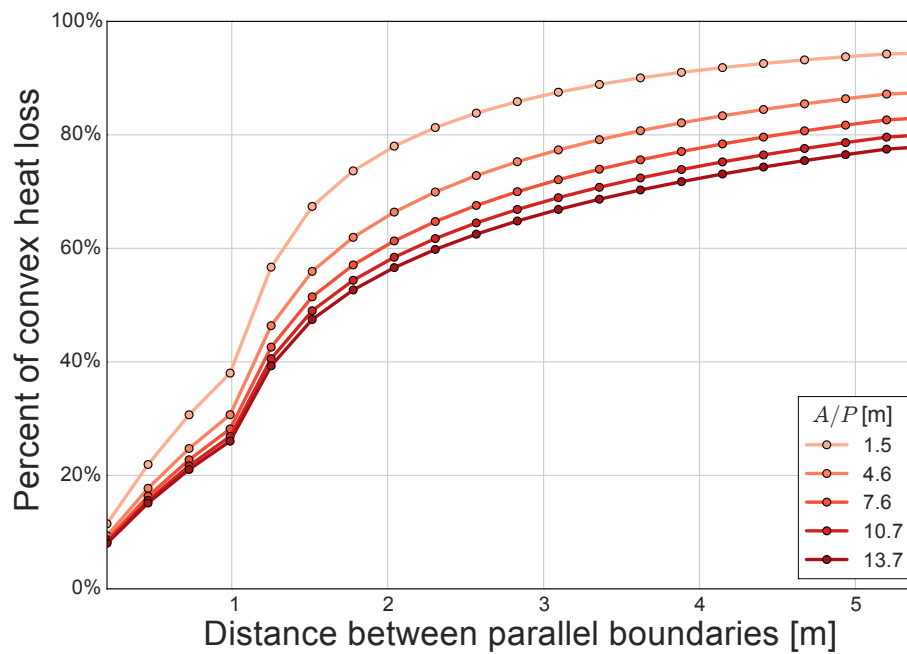


Figure 5.8: Reduction in heat loss between two parallel concave edges over a range of area-to-perimeter ratios ( $k_{soil} = 1.0 \text{ W/m}\cdot\text{K}$ , R-10 insulation)

As the area-to-perimeter ratio increases, the heat loss reduction relative to a convex (i.e., with no opposing edge) infinite rectangle decreases. Therefore the interaction effect has a higher impact for larger foundations. Smaller foundations see a less gradual reduction and are relatively unaffected until the two edges are very close, at which point heat transfer drops steeply.

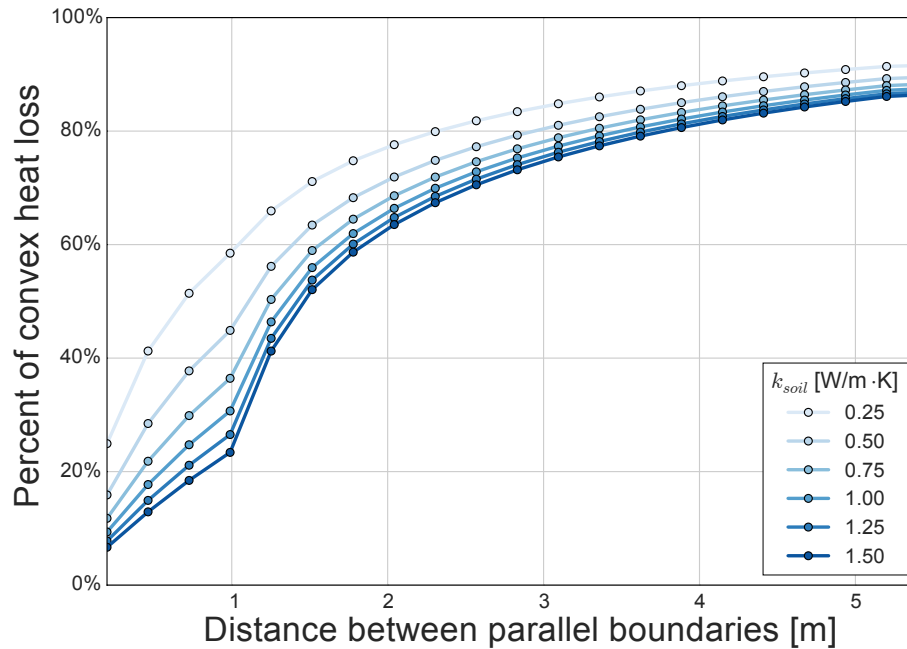


Figure 5.9: Reduction in heat loss between two parallel concave edges over a range of soil conductivity ( $A/P = 4.6$  m, R-10 insulation)

As the soil conductivity increases, the interaction between the two edges becomes stronger. Higher soil conductivity allows heat to flow further from the foundation, causing a greater impact on the opposing edge.

With increased levels of insulation, the path of heat flow is driven further from foundation perimeter, where there is a higher potential for interaction with the opposing edge. As a result, the heat transfer is reduced more at higher levels of insulation.

The shape of the curves in Figures 5.8–5.10 represents reduced heat loss as the two edges grow closer together. The curves show a noticeable change where the distance between the two edges is less than the width of the insulation. At long distances there is little effect, but within

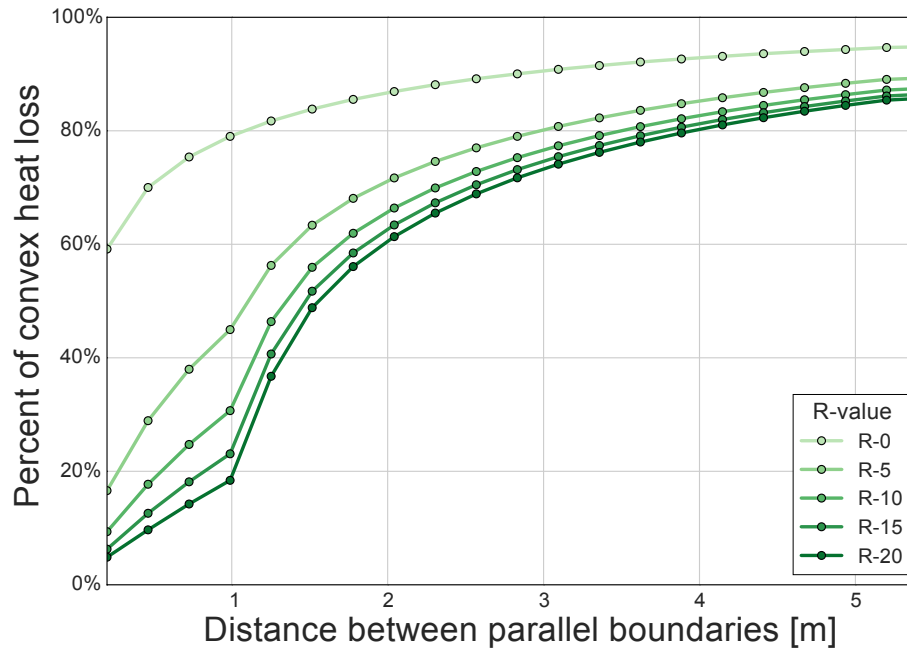


Figure 5.10: Reduction in heat loss between two parallel concave edges over a range of insulation R-values [ $\text{hr}\cdot\text{ft}^2\cdot\text{R}/\text{Btu}$ ] ( $k_{soil} = 1.0 \text{ W/m}\cdot\text{K}$ ,  $A/P = 4.6 \text{ m}$ )

the last several meters the heat transfer reduction drops drastically toward zero. The heat transfer reduction is related to the magnitude of heat flux from the foundation, which is strong near the perimeter and drops quickly to zero beyond a few meters. Though the distance where the magnitude drops to zero is difficult to quantify precisely, it is similar to the concept of a boundary layer in fluid mechanics. The boundary of heat flow near the perimeter of the foundation progressively transitions to a constant value sufficiently far away from the foundation.

The profile of this boundary layer can be calculated for any vertical cross-section extending from the perimeter of the foundation. The boundary layer is defined by the vertical heat flux along the grade plane. Figure 5.11 illustrates the boundary layer profile for a slab with exterior horizontal insulation.

The integral of the boundary layer profile from the foundation perimeter yields the function,  $\delta(x)$ . This function is normalized to represent the fraction of total heat transfer within any distance,

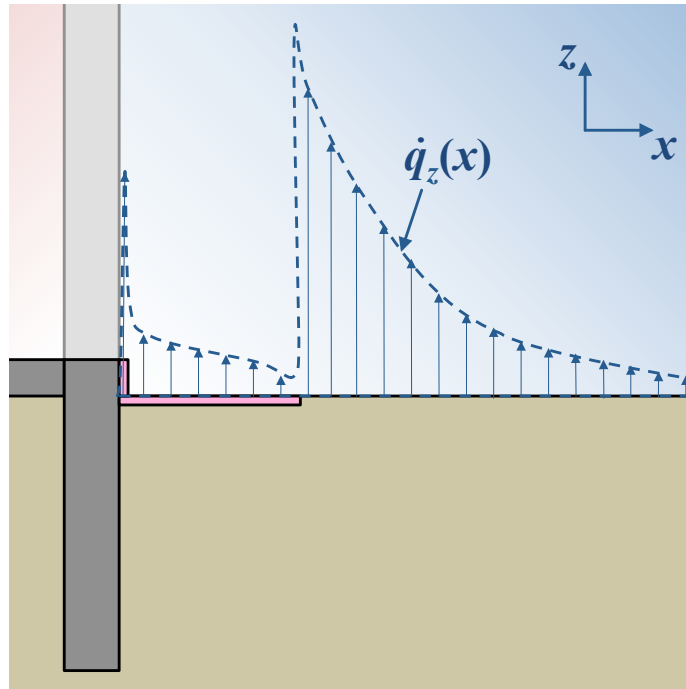


Figure 5.11: Illustration of a heat flux boundary layer profile for a slab with exterior horizontal insulation

$x$ , of the perimeter. In the limit as  $x$  approaches infinity, the value of  $\delta(x)$  approaches unity:

$$\lim_{x \rightarrow \infty} \delta(x) = 1. \quad (5.14)$$

Figure 5.12 shows examples of the normalized boundary layer profile,  $\dot{q}_z(x)$ , and the integrated boundary layer profile,  $\delta(x)$ .

The boundary layer interaction of the two opposing edges causes reduced heat transfer proportional to the value of the integrated boundary layer function at a given distance. For any shape cavity, the degree of interaction is related to the integrated boundary layer profile. The next section demonstrates this relationship for concave corners.

### 5.2.2 Concave Corners

Depending on the angle of a corner, the boundary layer will be more or less constrained. Sharper angles will cause a higher level of interaction within a cavity. As Kiva is only capable of

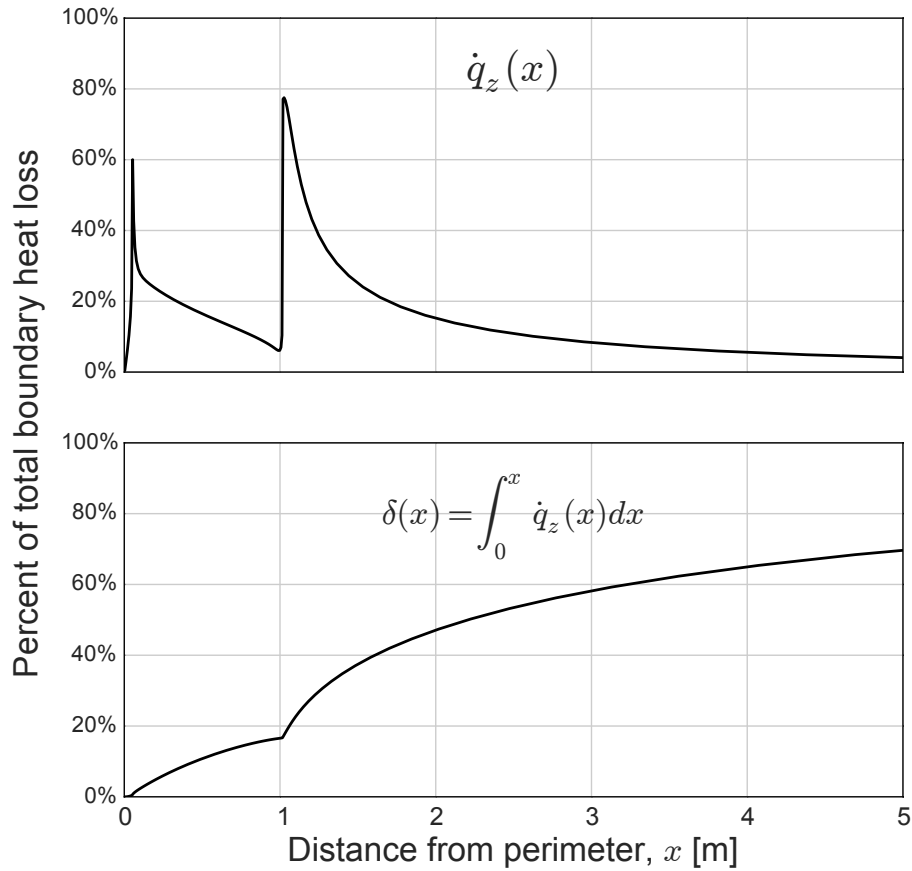


Figure 5.12: Example boundary layer profile for a slab with exterior horizontal insulation ( $k_{soil} = 1.0 \text{ W/m}\cdot\text{K}$ ,  $A/P = 4.6 \text{ m}$ , R-10 insulation)

simulating rectilinear foundation shapes, the effects in concave corners can only be demonstrated for right angles.

The effect of corners can be isolated by defining shapes with the same area and perimeter, but with a different number of corners. The range of shapes with corners is somewhat limited as complex shapes with many corners create several instances of near-field mesh refinements that can drastically increase the computational requirements. For this reason, only four shapes are selected to demonstrate the effect of concave corners on foundation heat transfer. These shapes are illustrated in Figures 5.13.

Heat transfer from slabs of each of these shapes was simulated under the same range of area-to-perimeter ratios, soil conductivities, and insulation levels that were simulated for the parallel



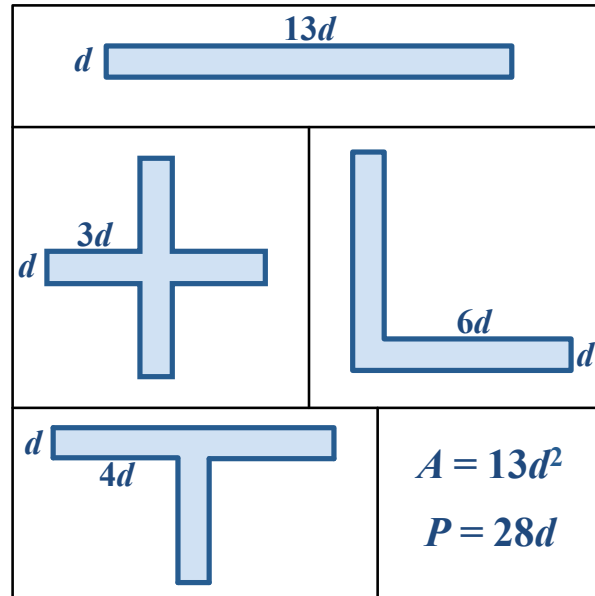


Figure 5.13: Shapes with equal area and perimeter but different number of concave corners

concave edge example. The proportion of the shapes remains constant even with different area-to-perimeter ratios. For a given area-to-perimeter ratio,  $A/P$ , the shape thickness,  $d$ , is defined as

$$d = \frac{28}{13} [A/P]. \quad (5.15)$$

Figures 5.14–5.16 show the sensitivity of heat loss reduction to changes in area-to-perimeter ratio, soil conductivity, and insulation R-value. Results are presented for each concave shape relative to the convex rectangle.

The jump from zero corners (the rectangle shape at 100%) to a single corner (the L shape) is much larger than the difference between one corner and two corners (the T shape). By four corners (the + shape) the impact of additional corners continues to drop. Although the fraction of the perimeter affected by the corners increases proportionally to the number of corners, the heat flux does not also decrease proportionally.

Unlike the opposing parallel edges, the reduction effect for corners increases as the area-to-perimeter ratio decreases. For lower area-to-perimeter ratios, the interaction effect for corners

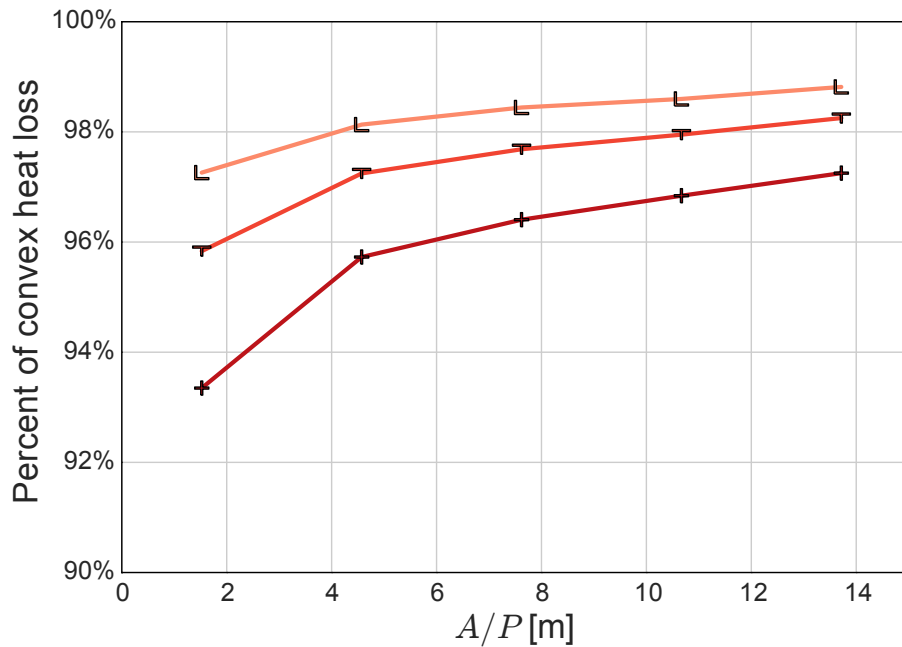


Figure 5.14: Reduction in heat loss due to corners over a range of area-to-perimeter ratios ( $k_{soil} = 1.0 \text{ W/m}\cdot\text{K}$ , R-10 insulation)

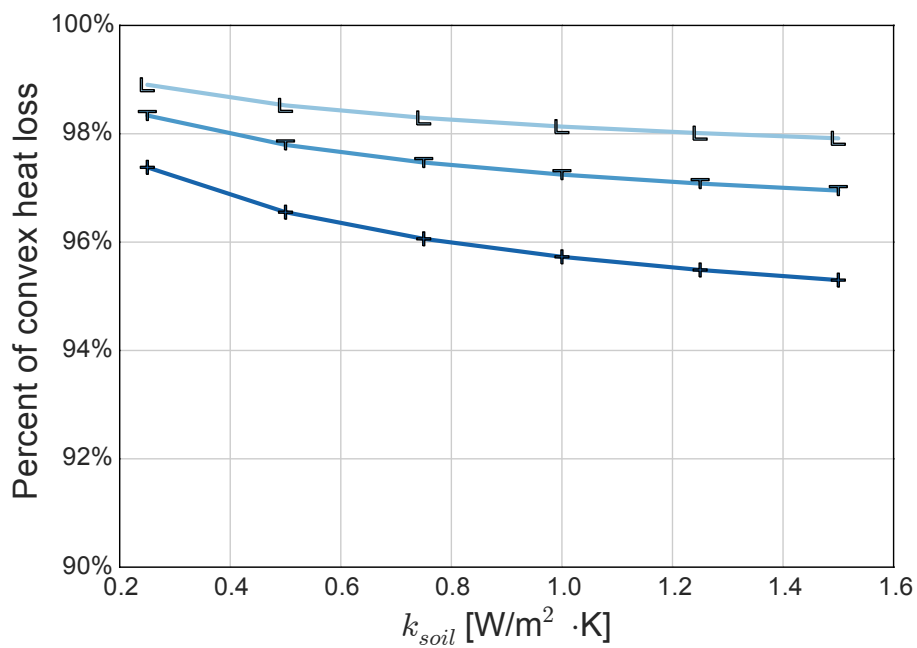


Figure 5.15: Reduction in heat loss due to corners over a range of soil conductivity ( $A/P = 4.6 \text{ m}$ , R-10 insulation)

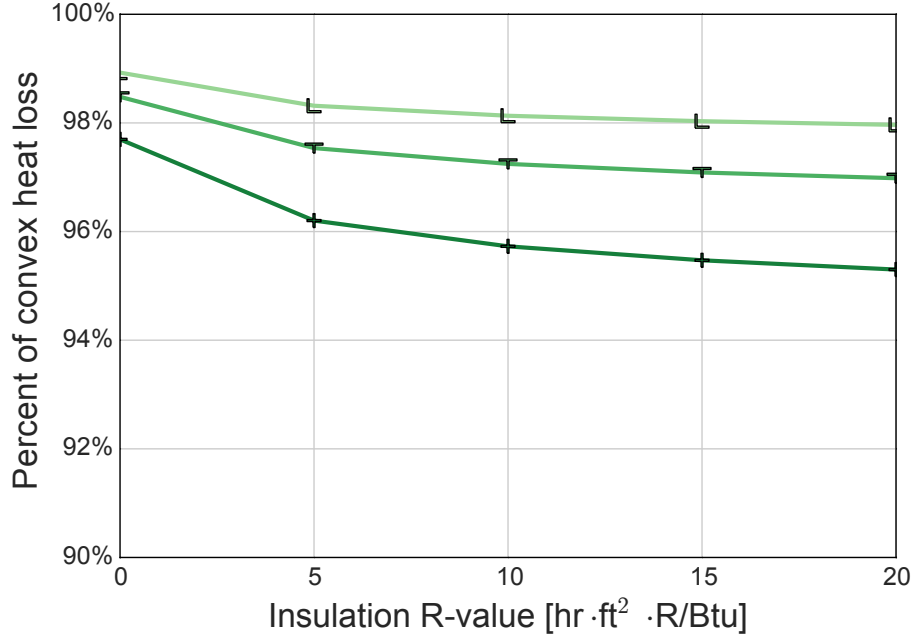


Figure 5.16: Reduction in heat loss due to corners over a range of insulation R-values ( $k_{soil} = 1.0$  W/m·K,  $A/P = 4.6$  m)

between shorter edges impacts a larger portion of the perimeter causing a larger heat transfer reduction. For larger area-to-perimeter ratios, the corners represent a smaller portion of the total perimeter, and therefore the heat transfer reduction is less impactful. In the limit as the area-to-perimeter ratio approaches infinity, the impacts of corners become negligible.

The impact of increasing soil conductivity and insulation R-value for corners is similar to the impact for parallel edges as shown in Figures 5.15 and 5.16, respectively.

The boundary layer profile is amplified near the corner due to interactions between the two intersecting concave edges. Figure 5.17 illustrates example cross-sections for both corner bisector and unaffected edge profiles.

The boundary layer heat flux profile along a corner bisector,  $\dot{q}_{z,b}(x)$ , can be estimated from an unaffected edge profile,  $\dot{q}_z(x)$  as

$$\dot{q}_{z,b}(x) = \dot{q}_z(x \sin(\theta/2)) [1 + \cos(\theta/2)] \quad (5.16)$$

where

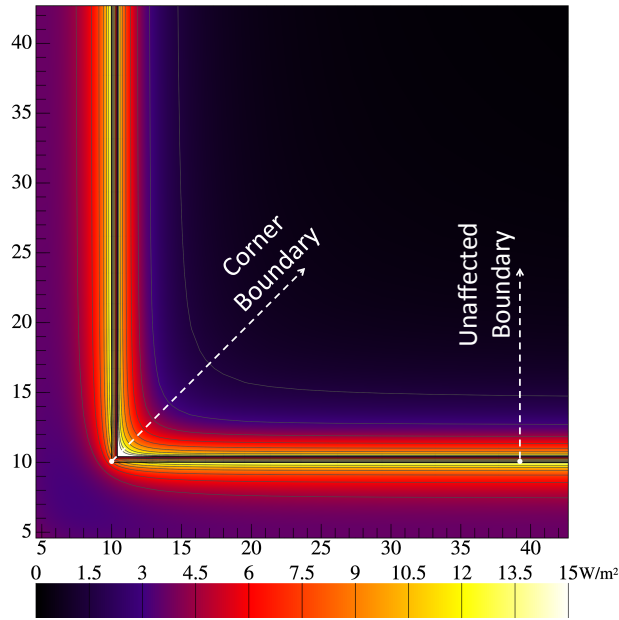


Figure 5.17: Illustration of corner bisector and unaffected edge boundary profile cross-sections

- $x$  is the distance from the perimeter [m],
- $\theta$  is the angle of the corner,
- the  $\sin(\theta/2)$  accounts for the change in dimensions of the foundation elements along the bisector,
- the  $1 + \cos(\theta/2)$  accounts for increased heat flux in the corner due to interacting boundary layer profiles.

Kiva can only simulate right angles, and cannot confirm this relationship for other angles. Figure 5.18 validates the estimated bisector boundary layer profile and the calculated two-dimensional, unaffected boundary layer profile against three-dimensional simulation results. The discrete points in Figure 5.18 represent the three-dimensional heat flux calculated along each cross-section. The curves represent the generated unaffected boundary layer profile, and the calculated boundary layer profile using the relationship in Equation 5.16. There is near-perfect agreement between the three dimensional profiles and those estimated based on two dimensional simulations.

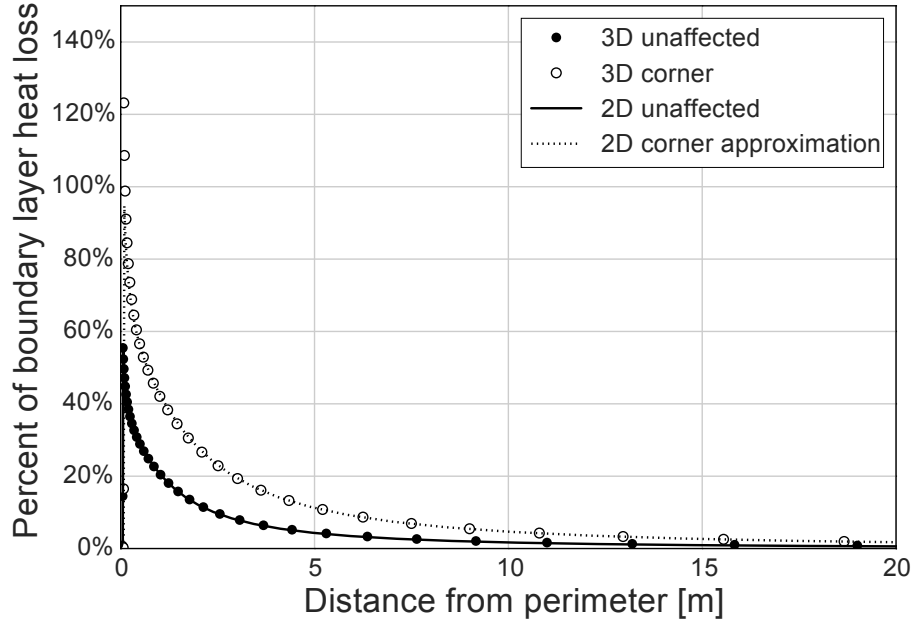


Figure 5.18: Comparison of straight boundary profile and corner bisector

Integrating the bisector boundary layer profile yields

$$\delta_b(x) = \int_0^x \dot{q}_{z,b}(x) dx = \delta(x \sin(\theta/2)) \frac{1 + \cos(\theta/2)}{\sin(\theta/2)}. \quad (5.17)$$

The heat transfer reduction near concave corners is related to differences between the bisector integrated boundary layer profile and the integrated boundary layer profile of an unaffected edge.

### 5.2.3 Compounding Cavity Effects

Many shapes exhibit both opposing parallel edges and corners. The interactive effects combine as illustrated in Figure 5.19 for an H-shaped slab. The cavities of the H-shape are adjusted by varying the dimensions of the web (the connector) and flanges (the parallel sides), while maintaining constant area and perimeter. Figure 5.19 demonstrates the progression of heat transfer reduction at discrete intervals between convex extremes where the shape has no flanges or no web.

The flange and web thickness,  $d$ , is set to 10 meters, and the area-to-perimeter ratio is

$$A/P = \frac{13d^2}{28d} = 4.64 \text{ m}. \quad (5.18)$$

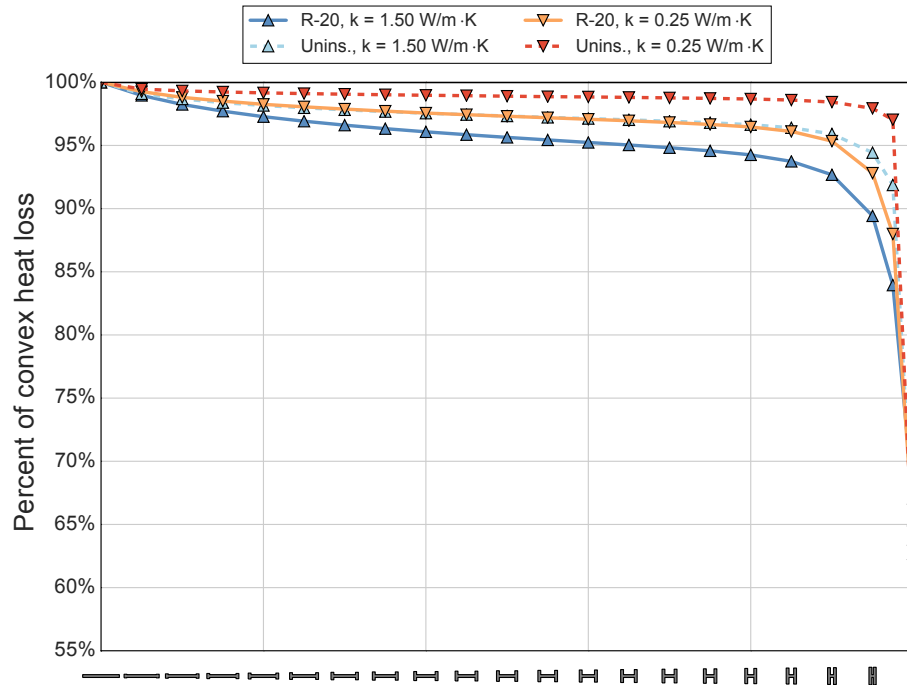


Figure 5.19: Heat loss reduction from H-shaped slabs

The four curves in Figure 5.19 represent bounding values of soil conductivity and insulation level for exterior vertical insulation.

On the left-hand side of Figure 5.19, there is relatively little heat transfer reduction where the flanges are not long enough to form an unaffected boundary layer. For the cases with narrow boundary layers (e.g., uninsulated with low soil conductivity), the relative heat transfer settles at a constant value for shorter flanges, while shapes with wide boundary layers require longer flanges before an unaffected boundary layer is formed. In the case of a high insulation value and high soil conductivity, the unaffected boundary layer is not established before the interaction between the opposing parallel edges begins to further reduce heat transfer.

The established approximation methods described in Section 5.1 fail to account for heat transfer reduction in cavities and thus predict the same heat loss for each shape on a given curve in Figure 5.19. In the extreme case with no web, there is a potential 40% error in the approximations

relative to the three-dimensional solution. It is not coincidence that the opposing parallel edges in this extreme comprise 40% of the total foundation perimeter.

### 5.3 Boundary Layer Adjustment Method

The integrated boundary layer profile can be used to estimate heat transfer reduction for a foundation shape with cavities. The profile can be calculated easily within the existing computational framework, and it contains all of the information about the domain which influences heat transfer within shape cavities. There is no need to develop regressions for all of the variables which impact the heat transfer reduction within cavities because the profile is specific to the combination of foundation design characteristics and soil thermal properties defined for a given model.

Bahnfleth and Pedersen [11] demonstrated that as the area-to-perimeter ratio of a foundation increases, the average heat flux from the foundation decreases. The concept behind the boundary layer adjustment method is to adjust the dimensions of parallel edges and concave corners, based on the integrated boundary layer profile, to produce a new adjusted area-to-perimeter ratio. The adjusted area-to-perimeter ratio defines the dimensions for a representative two-dimensional domain and is calculated as follows:

$$\left[ \frac{A}{P} \right]_{adj} = \frac{A}{P - \sum_i^{N_v} P_{v,i}}, \quad (5.19)$$

where

- $A$  is the original area [m<sup>2</sup>] of the foundation shape,
- $P$  is the original perimeter [m] of the foundation shape,
- $N_v$  is the number of concave features (either parallel edges or corners),
- $P_{v,i}$  is the perimeter adjustment [m] for concave feature  $i$ .

The value of  $P_v$  for each concave feature of the foundation shape depends on the integrated boundary layer profile function. If thermal properties are linear, then the boundary layer profile

is independent of temperature and can be calculated using a single steady-state, two-dimensional simulation with an arbitrary non-zero temperature difference. The values of vertical heat flux are integrated along the grade plane to generate a mapping of the percent total heat flux to the distance from the perimeter at each discrete cell. The map is as coarse as the spatial discretization in the lateral direction. The value of the integrated boundary layer profile,  $F$ , at any distance,  $x$ , is evaluated using a linear interpolation between mapped values. The inverse of the integrated boundary layer profile function,  $\delta^{-1}(F)$ , also uses the same map to provide the distance,  $x$ , corresponding to a given fraction of total heat loss,  $F$ .

### 5.3.1 Opposing Parallel Edges

For opposing parallel edges, the edge perimeters are adjusted as follows:

$$P_v = 2a[1 - \delta(p)]. \quad (5.20)$$

where  $p$  is the distance between the edges, and  $a$  is the common length of the parallel edges as illustrated in Figure 5.20.

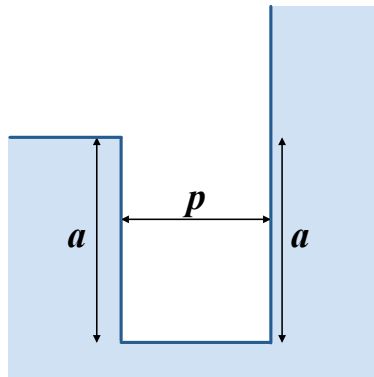


Figure 5.20: Variables used to adjust perimeter of opposing parallel edges



### 5.3.2 Concave Corners

For concave corners, the perimeter is adjusted based on the integrated boundary layer profile of the bisector described in Equation 5.17, the angle of the corner,  $\theta$ , and the lengths,  $A$  and  $B$ , of the edges intersecting at the corner.

A chamfer at a distance,  $x_c$ , from the corner along the bisector, as shown in Figure 5.21, defines the adjustment to the perimeter.

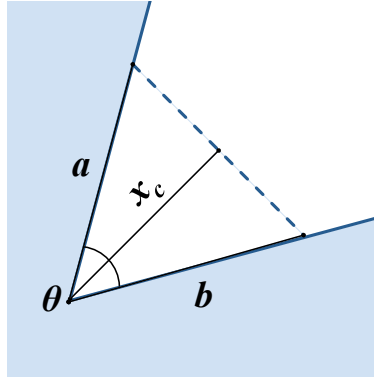


Figure 5.21: Variables used to adjust perimeter of concave corners

The value  $x_c$  is selected such that the total heat flux beyond the chamfer is the same as the total heat flux from an unaffected edge. The total relative heat flux along the bisector is

$$\lim_{x \rightarrow \infty} \delta_b(x) = \frac{1 + \cos(\theta/2)}{\sin(\theta/2)}. \quad (5.21)$$

Therefore, the bisector's integrated boundary profile at  $x_c$  is

$$\delta_b(x_c) = \frac{1 + \cos(\theta/2)}{\sin(\theta/2)} - 1. \quad (5.22)$$

which, when substituting in Equation 5.17, gives

$$\delta(x_c \sin(\theta/2)) \frac{1 + \cos(\theta/2)}{\sin(\theta/2)} = \frac{1 + \cos(\theta/2)}{\sin(\theta/2)} - 1. \quad (5.23)$$

Solving Equation 5.23 for  $x_c$  gives:

$$x_c = \frac{\delta^{-1}(1 - \tan(\theta/4))}{\sin(\theta/2)}. \quad (5.24)$$

where  $\delta^{-1}(x)$  is the inverse of the integrated boundary profile function.

The distance,  $d$ , from the angle to the points where the chamfer intersects the edges is calculated as

$$d = \frac{x_c}{\cos(\theta/2)}. \quad (5.25)$$

The final dimensions of the edges used depend on the lengths of the edges relative to  $d$ :

$$a = \min(A, d), \quad (5.26)$$

and

$$b = \min(B, d). \quad (5.27)$$

The perimeter adjustment,  $P_v$ , for each corner is calculated as follows:

$$P_v = a + b - \sqrt{a^2 + b^2 - 2ab \cos(\theta)}. \quad (5.28)$$

## 5.4 Description of Approximation Method Tests

The verification testing in Chapter 4 was based solely on the *IEA BESTEST* test case specifications for slab-on-grade foundations. These test cases are constrained to idealized conditions and do not cover the breadth of modeling capability in Kiva. The two-dimensional approximation methods discussed in this chapter are tested in a more realistic context under a wider range of parameters.

All simulations performed to test approximation methods use the set of conditions described in Table 5.1. All three-dimensional simulations are modeled using planes of symmetry where they exist to reduce domain size.

Several other parameters are varied between tests to highlight potential sensitivities in results. The ranges of these parameters are described in the following sections.

### 5.4.1 Climates

Approximation methods are tested using realistic weather data representing a range of climates. The selection of weather locations is based on the range of outdoor dry-bulb temperatures

Table 5.1: Approximation method testing conditions

<b>Description</b>	<b>Value</b>
Foundation wall thickness	0.3 m
Slab thickness	0.2 m
Interior temperature	22.2 °C
Soil conductivity	0.864 W/m·K
Soil density	1,510 kg/m <sup>3</sup>
Soil specific heat	1,260 J/kg·K
Surface absorptivity	0.8
Deep-ground boundary depth	40 m
Deep-ground boundary condition	Zero-flux
Far-field boundary width	40 m
Minimum cell dimension	0.006 m
Cell growth coefficient	1.20
Time-step duration	60 minutes
Numerical method	ADI
Initialization acceleration time-step duration	1 week
Initialization acceleration period duration	12 weeks
Initialization warm-up duration	1 year

in Typical Meteorological Year (TMY3) data [117]. Figure 5.22 illustrates the ranges of dry-bulb temperatures selected for the representative hot (Phoenix, Arizona), mixed (Albuquerque, NM), and cold (Anchorage, Alaska) climates.

#### 5.4.2 Foundation Designs

The approximation method test covers a total of 25 different foundation designs. These designs represent the three most common foundation types. Insulation configurations are shown in Figures 5.23, 5.24, and 5.25 for slabs, crawlspaces, and basements, respectively. For each of the insulated configurations, there are two designs at different insulation levels: R-5 (0.88 m<sup>2</sup>·K/W) and R-20 (3.52 m<sup>2</sup>·K/W).

All basements are modeled with an 8-foot (2.4 m) foundation depth, crawlspaces are modeled with a 4-foot (1.2 m) foundation depth, and slabs are modeled 8 inches (0.2 m) above grade. The foundation wall footer is 5-feet-8-inches (1.7 m) deep for slabs and crawlspaces, and 9-feet-8-inches (2.9 m) deep for basements.

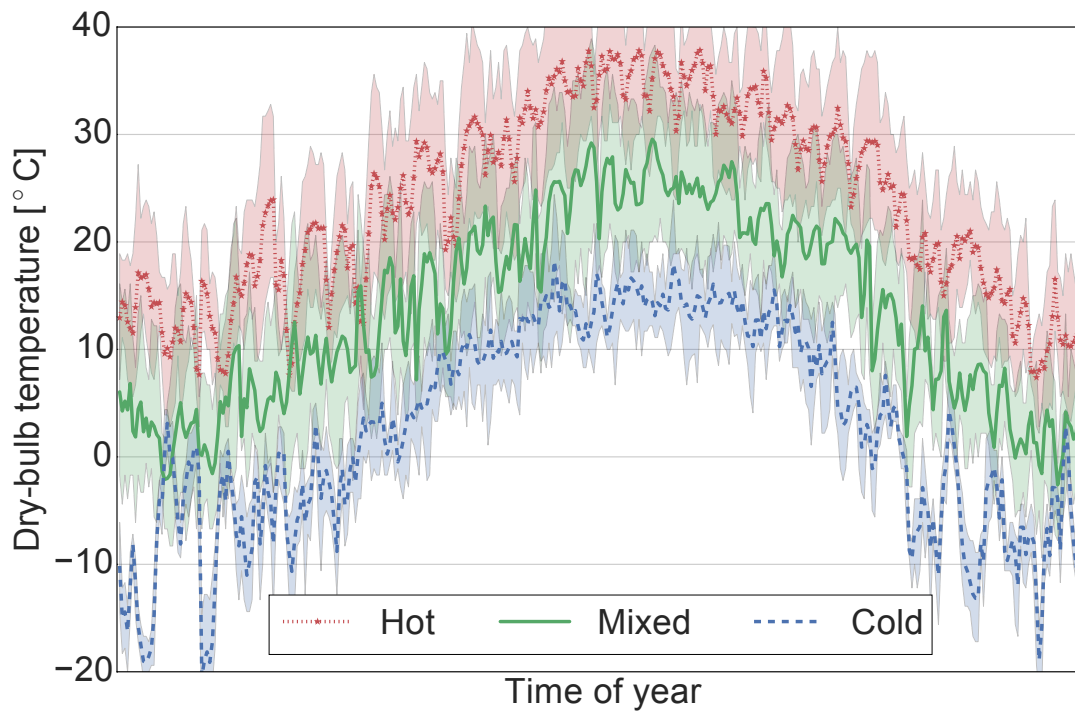


Figure 5.22: Annual outdoor dry-bulb temperatures from weather data files for selected climates. Hot = Phoenix, Arizona; Mixed = Albuquerque, New Mexico; Cold = Anchorage, Alaska

### 5.4.3 Foundation Shapes

The foundation shapes selected for testing two-dimensional approximation methods represent a range of characteristic length, compactness, and concavity.

The characteristic length, defined by the area-to-perimeter ratio,  $A/P$ , describes the relative size of the foundation. The range of characteristic lengths used in the tests are as follows:

- $A/P = 1.5$  m (5 feet)
- $A/P = 4.6$  m (15 feet)
- $A/P = 13.7$  m (45 feet)

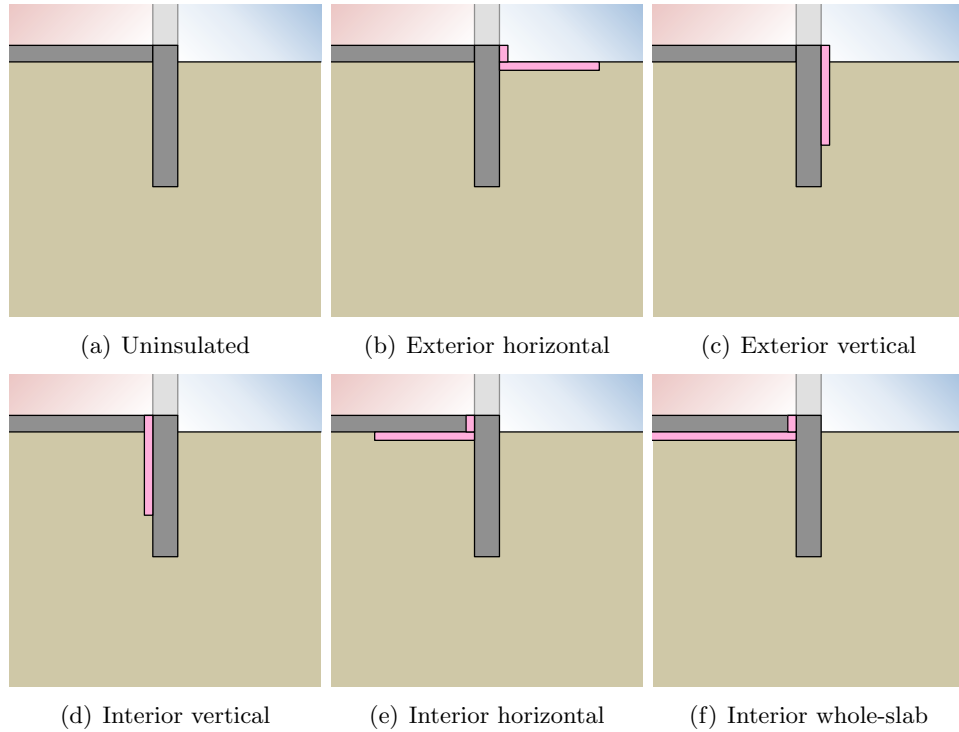


Figure 5.23: Slab insulation configurations for approximation method tests

Compactness is a nondimensional characteristic that ranges between zero and one, defined by the following equation:

$$C = 4\pi \left[ \frac{A}{P^2} \right]. \quad (5.29)$$

Table 5.2 demonstrates the compactness of several shapes. Each of the shapes shown in Table 5.2 can be simulated in Kiva with the exception of the equilateral triangle, because it is neither rectilinear nor described by a two-dimensional coordinate system. The equilateral cross and square shapes are included in the approximation tests. Two variations of the H-shape are also included to represent different distances between the opposing parallel edges: a narrow-H with 3 meters (10 feet) between flanges, and a wide-H with 122 meters (400 feet) between flanges.

The final set of shapes used in the approximation method tests includes four shapes simulated in three-dimensional Cartesian coordinates (square, cross, narrow-H, and wide-H), a circle in two-dimensional axisymmetric cylindrical coordinates, and an infinite rectangle in two-dimensional Cartesian coordinates.

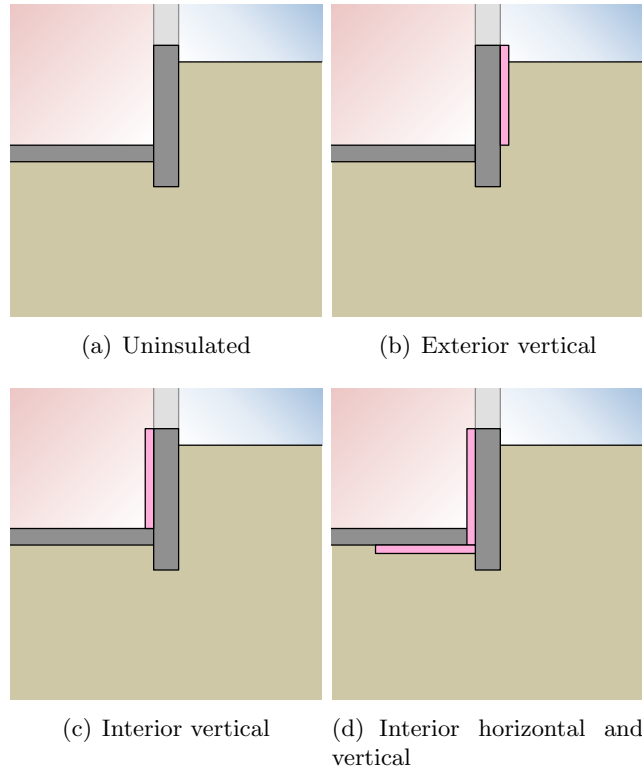


Figure 5.24: Crawlspace insulation configurations for approximation method tests

## 5.5 Initial Shape Analysis

The shapes simulated in three-dimensional Cartesian coordinates are shown in Figure 5.26 for each value of the characteristic length,  $A/P$ .

Initial simulation results for the mixed climate revealed notable differences in foundation heat flux among shapes with the same characteristic length. Figure 5.27 shows deviation from the mean heat flux for uninsulated foundation walls and floors, across all shapes.

Figure 5.27 illustrates a number of important shape-related effects on heat transfer:

- The absolute difference in heat transfer is calculated as:

$$\dot{Q} = A\dot{q}_f + P\Delta z_w\dot{q}_w \quad (5.30)$$

where  $\dot{q}_f$  and  $\dot{q}_w$  are the heat fluxes through the floor and wall, respectively. Although the crawlspace and foundation heat flux deviates more through floors than through walls, it

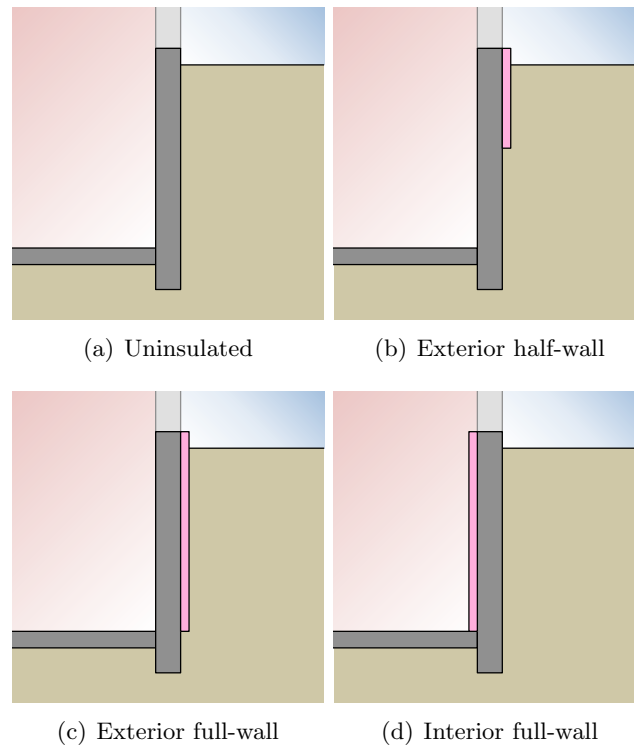
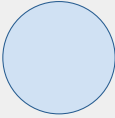
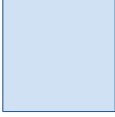
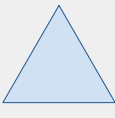

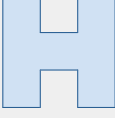



Figure 5.25: Basement insulation configurations for approximation method tests

is also a lower magnitude. Depending on the dimensions of the foundation, this deviation may have a small impact on the overall heat transfer.

- Heat flux is less sensitive to foundation shape for shallower foundations. The area-to-perimeter ratio, which Bahnfleth and Pedersen [11] demonstrated characterizes heat transfer through slab foundations, does not extend as effectively to crawlspace and basement foundations.
- For crawlspaces and basements, there are two independent trends worth noting:
  - Shapes with higher compactness have proportionally higher heat flux than the infinite rectangle (where compactness is zero).
  - As explained for Figure 5.19, shapes with concavities have lower heat fluxes than the convex shapes due to higher levels of interaction within the concavities.

Table 5.2: Compactness of various shapes

Description	Shape	Compactness
Circle		1
Square		$\frac{\pi}{4} \approx 0.785$
Equilateral triangle		$\frac{\pi}{3\sqrt{3}} \approx 0.605$
Equilateral cross		$\frac{5\pi}{36} \approx 0.436$
Equal-spaced H		$\frac{7\pi}{64} \approx 0.344$
Infinite rectangle		0

- The magnitude of deviation decreases proportionally as the characteristic length increases.

When comparing different insulation designs, engineers are often more concerned with relative differences among designs rather than absolute heat transfer from foundations. Figure 5.28 illustrates the reduction in heat flux for different insulation designs relative to the uninsulated foundations portrayed in Figure 5.27. Floor heat flux reductions are not shown for crawlspaces and basements because their magnitudes are substantially lower than heat flux through walls. Similar heat flux reductions are demonstrated among all shapes, with a slight disparity for shapes with higher compactness.



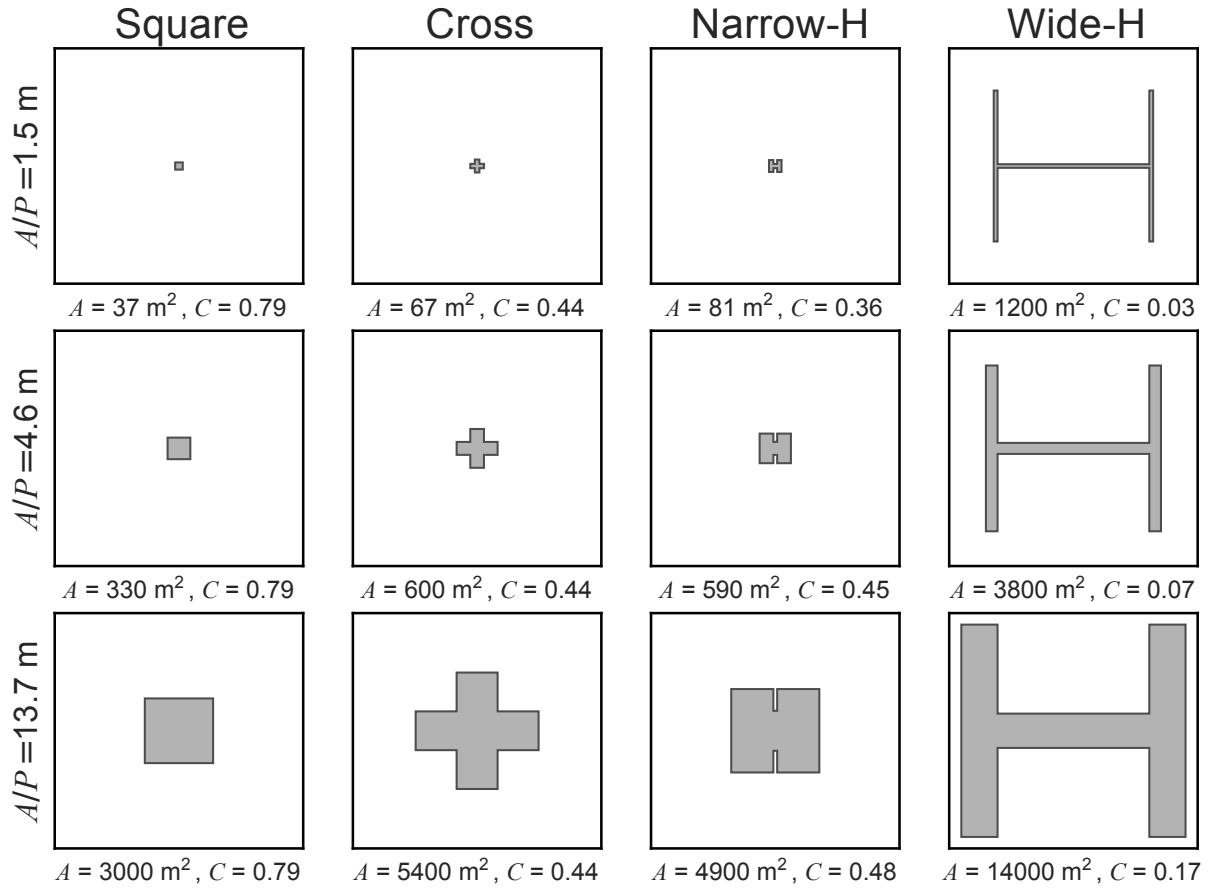


Figure 5.26: Shapes simulated in three dimensions for approximation method testing. Each plot is  $200 \text{ m} \times 200 \text{ m}$ .  $A$  = Area,  $C$  = Compactness.

## 5.6 Approximation Method Accuracy

The four two-dimensional approximation methods tested are listed in Table 5.3.

Table 5.3: List of two-dimensional approximation methods tested

Method	Characteristic Length(s)	Coordinate System(s)
Circle	$A/P$	Cylindrical
Infinite rectangle	$A/P$	Cartesian
Rounded rectangle	$a, b$	Cartesian and Cylindrical
Boundary layer adjustment	$[A/P]_{adj}$	Cartesian

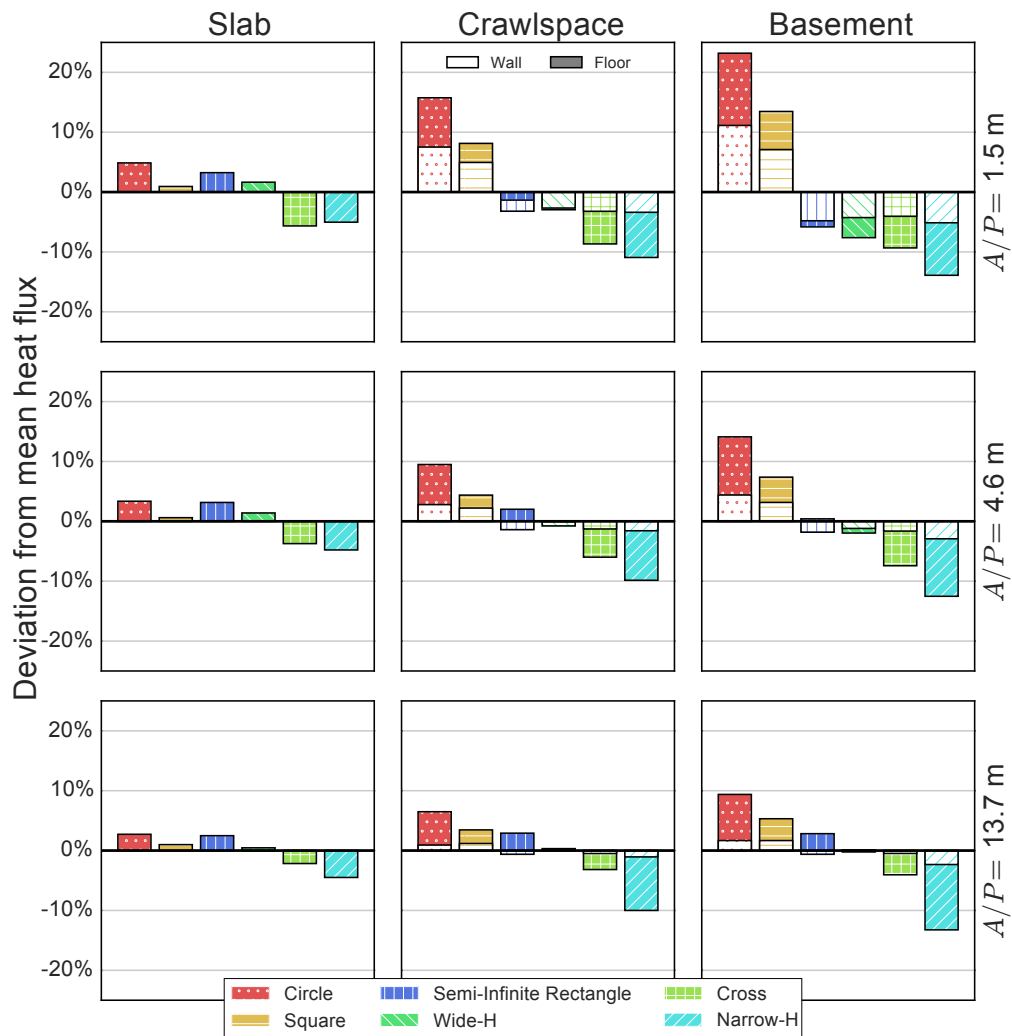


Figure 5.27: Comparison of heat flux from a range of uninsulated foundation shapes

The approximation methods are compared to three-dimensional simulation results for a combination of:

- 3 climates,
- 25 foundation designs,
- 3 characteristic lengths, and
- 4 foundation shapes.

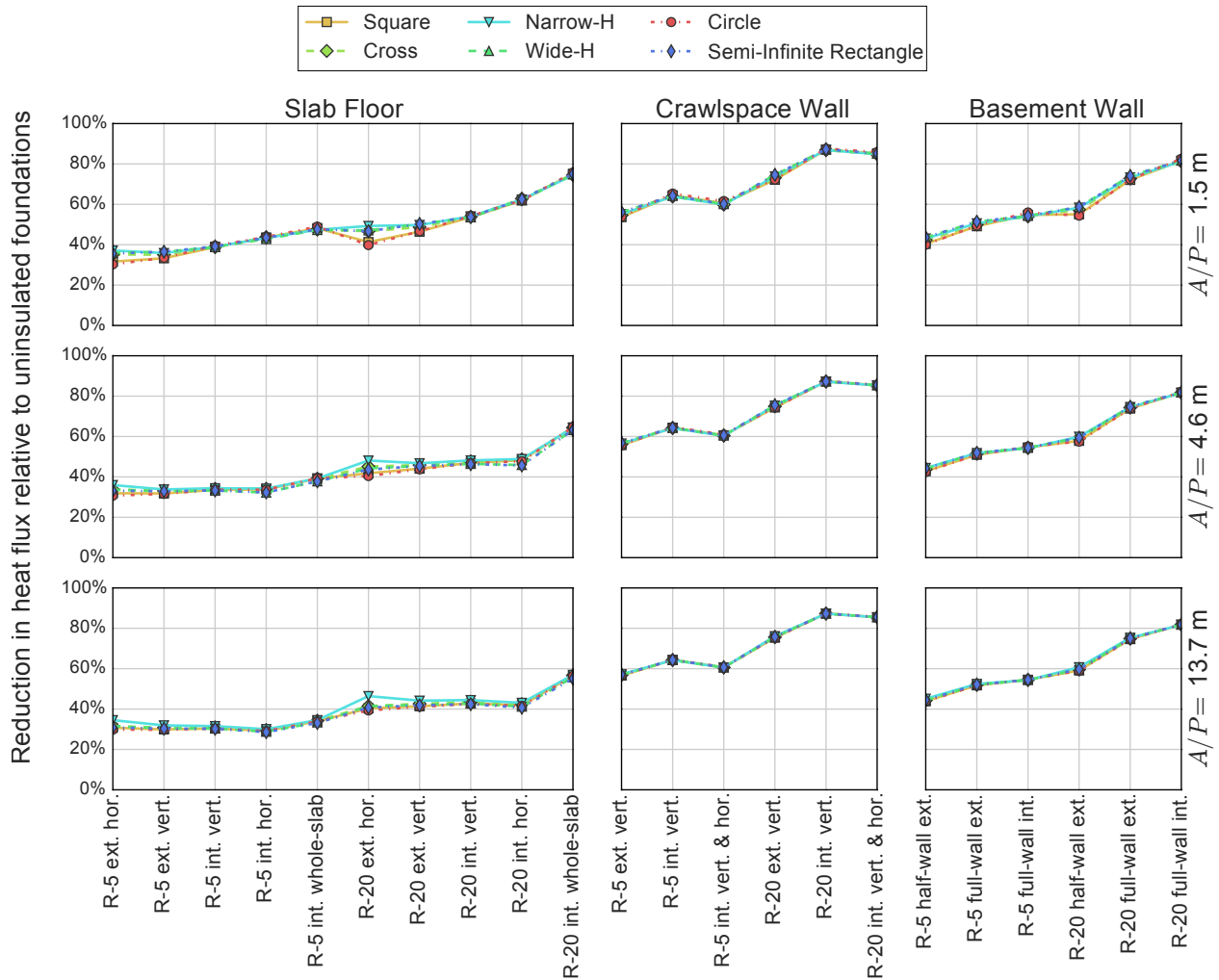


Figure 5.28: Heat flux reduction relative to uninsulated foundations in mixed climate for a range of foundation shapes

The results presented in Figures 5.29–5.31 represent a total of 4,500 simulations. Each plot compares approximated two-dimensional annual total heat transfer to three-dimensional annual total heat transfer. The results demonstrate generally good agreement among each of the approximation methods with the exception of the circle approximation, which tended to over-predict three dimensional heat transfer. Mean absolute deviation (MAD), and mean bias deviation (MBD) are shown for each approximation method. Although the differences between the infinite rectangle, rounded rectangle, and boundary layer adjustment methods are not clearly visible in the plots,

these metrics show that the former two methods have MAD values of 4–5%, while the boundary layer adjustment method has MAD values of 2.5–3%.

The boundary layer adjustment method provides a more accurate representation of three-dimensional heat transfer than previously established approximation methods. This is achieved with no observable increase in simulation time.

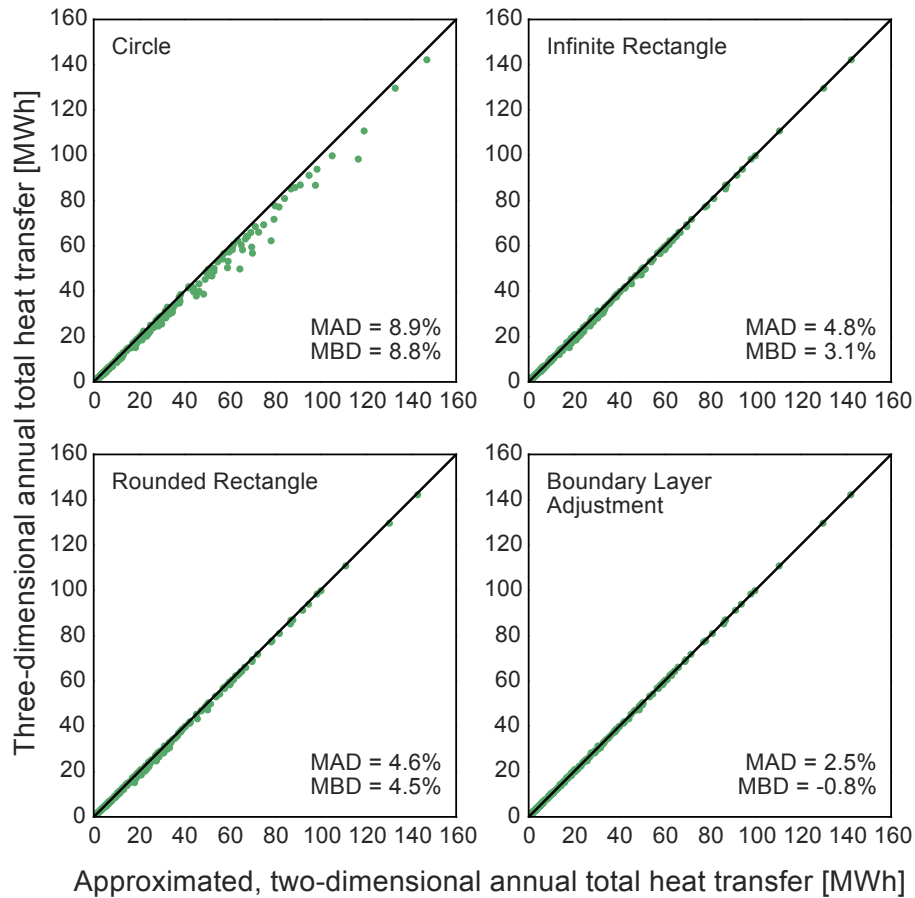


Figure 5.29: Comparison of annual total heat transfer between three-dimensions and two-dimensional approximations for mixed climate simulations

More detailed results are presented for mixed, cold, and hot climates in Appendices B, C, and D, respectively. In these figures, the deviations of each approximation method are compared for each three-dimensional simulation. Observations from these figures that are not apparent in Figures 5.29–5.31 include:

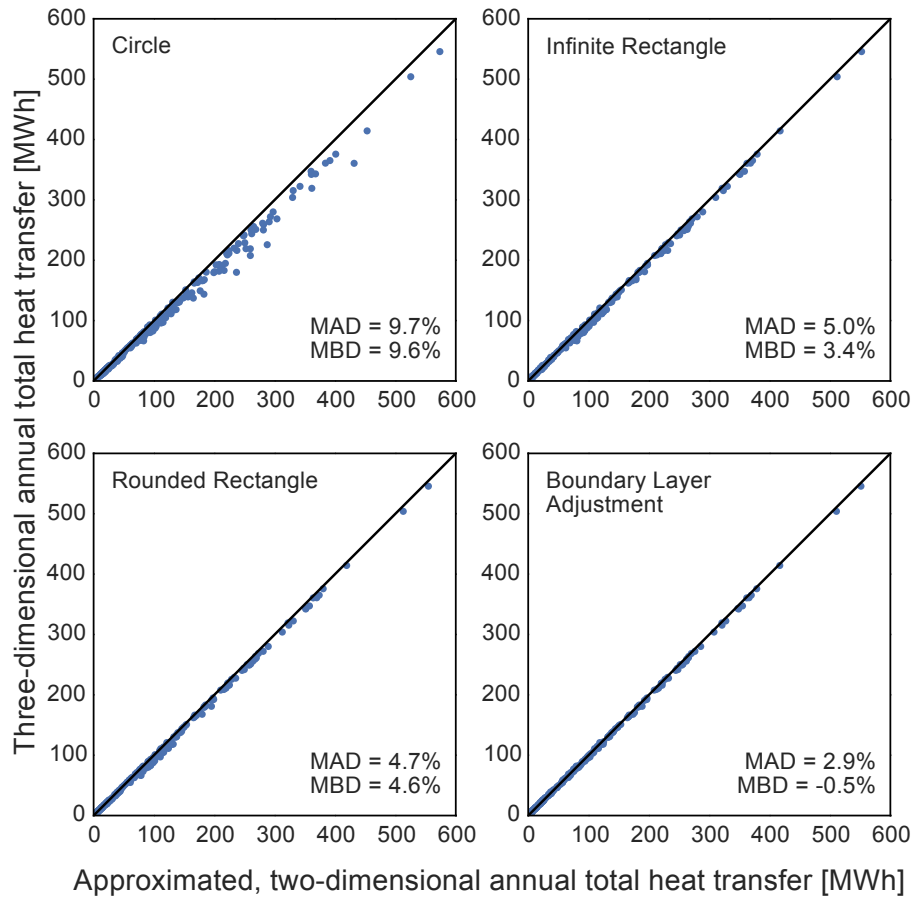


Figure 5.30: Comparison of annual total heat transfer between three-dimensions and two-dimensional approximations for cold climate simulations

- Methods other than the boundary layer adjustment method tend to over-predict concave shape heat transfer.
- The approximation methods perform better for shapes with larger area-to-perimeter ratios, especially for deeper foundations.

While annual total heat transfer is often the most important metric for energy design of building foundations, variations in heat transfer throughout the year also impact peak heating and cooling loads in a building used to calculate the appropriate capacity of HVAC equipment. Figure 5.32 demonstrates the time varying accuracy of the boundary layer adjustment method for a cross-

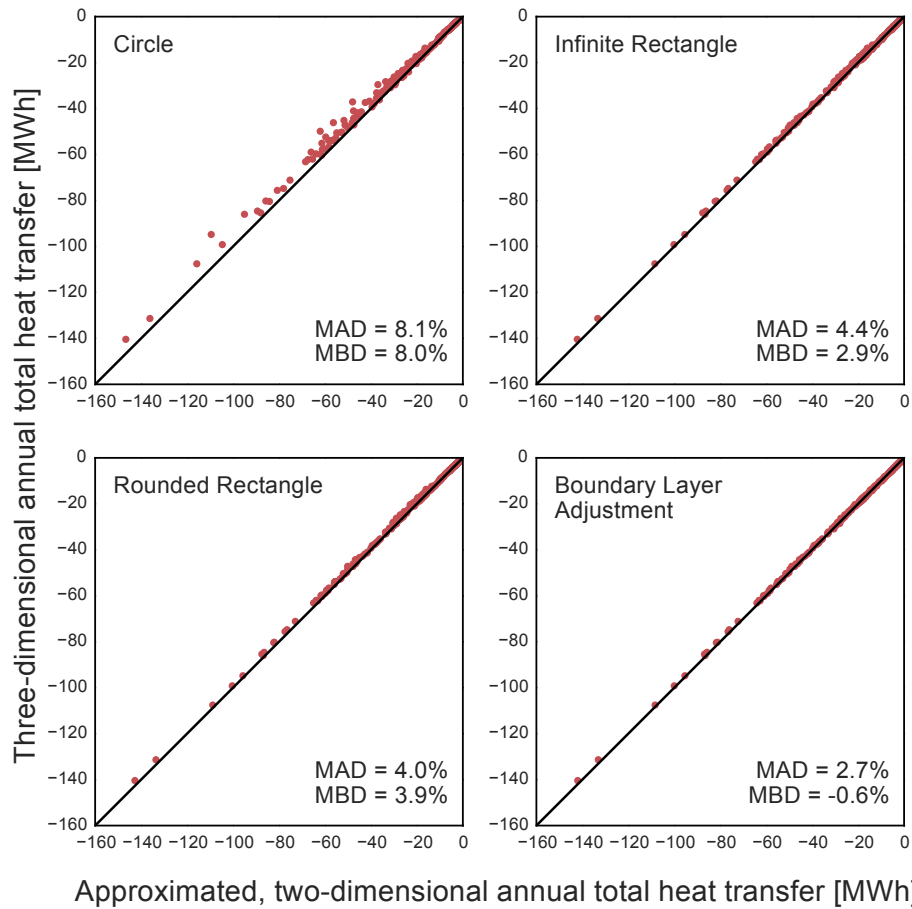


Figure 5.31: Comparison of annual total heat transfer between three-dimensions and two-dimensional approximations for hot climate simulations

shaped basement with exterior, half-wall R-20 insulation. The three-dimensional results and the two-dimensional approximation are virtually indistinguishable from each other.

Appendix E contains figures comparing annual minimum and maximum heat transfer rates for all the tested combinations. The trends of agreement are similar to the comparisons of annual total heat transfer. The boundary layer adjustment method provides the best approximation of minimum and maximum heat transfer rates.

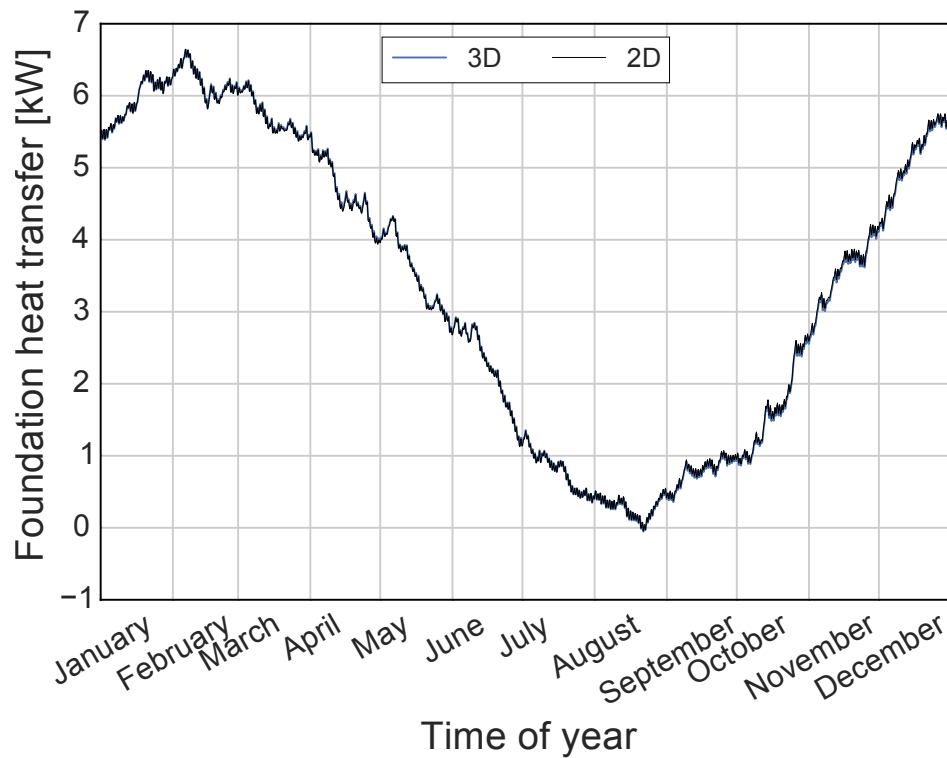


Figure 5.32: Example comparison of hourly three-dimensional heat transfer and approximated two-dimensional heat transfer

## 5.7 Approximation Method Simulation Time

Table 5.4 presents the average simulation wall time for each of the two-dimensional approximation methods. The methods that use only a Cartesian coordinate system require less time because their domains are typically smaller.

Table 5.4: Average simulation wall time for two-dimensional approximation methods

Method	Average Simulation Time [s]
Circle	40.9
Infinite rectangle	37.4
Rounded rectangle	40.2
Boundary layer adjustment	34.8

Within a two-dimensional context, the largest driver of simulation time is the foundation design. Figure 5.33 demonstrates the variability of simulation time across foundation designs for

the boundary layer adjustment method. Simulations with more foundation elements require more cells to define the near-field discretization region and therefore take longer to simulate.

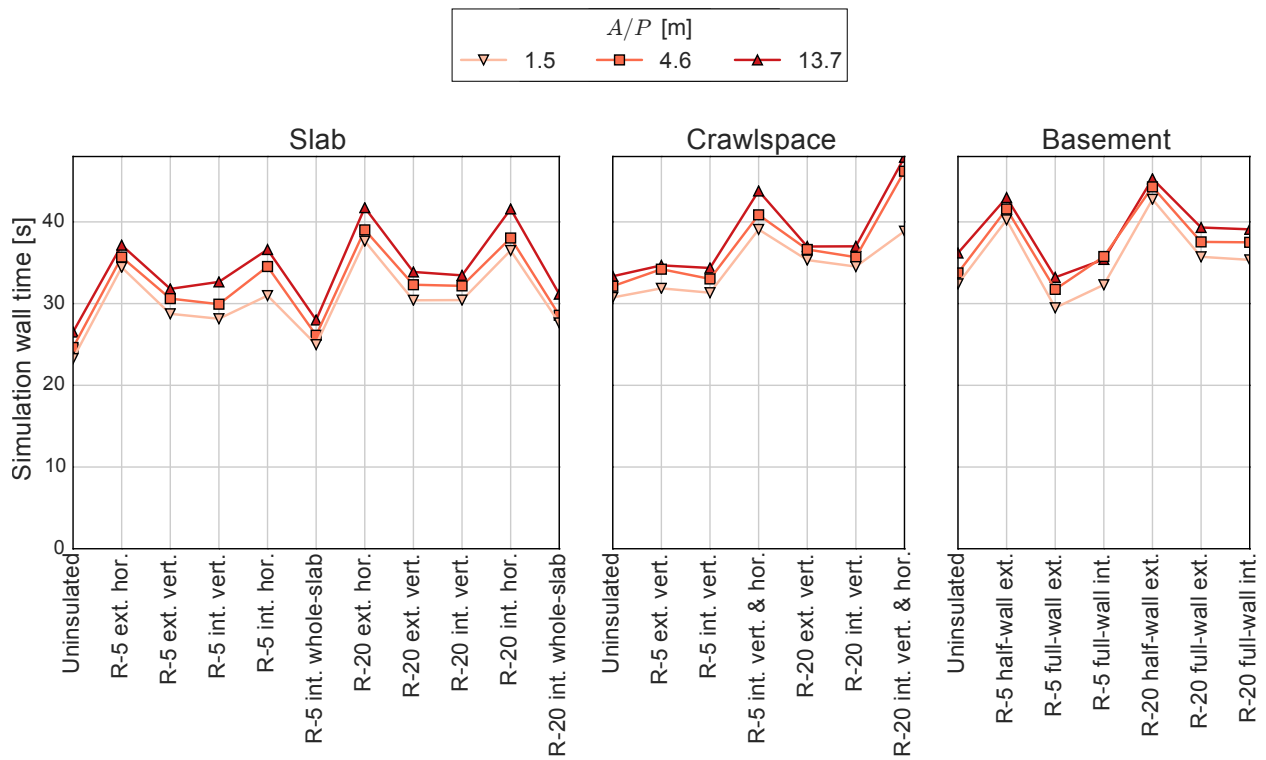


Figure 5.33: Two-dimensional approximation simulation wall times

The average simulation wall time of the boundary layer adjustment method is approximately 35 seconds. This is considerably faster than three-dimensional alternatives, but it still represents a considerably large portion of the total simulation time for a whole-building energy simulation. Further reductions in simulation time can be achieved by relaxing the refinement of the spatial discretization. All simulations performed in approximation method tests used a minimum cell dimension,  $\Delta x_{min}$ , of 6 millimeters, and a cell growth factor,  $f_g$ , of 1.2. Figure 5.34 illustrates the reduction in simulation wall time and corresponding impact on approximation accuracy for



the foundation design with the longest simulation time, a cross-shaped basement with exterior, half-wall, R-20 insulation and an area-to-perimeter ratio of 13.7 meters.

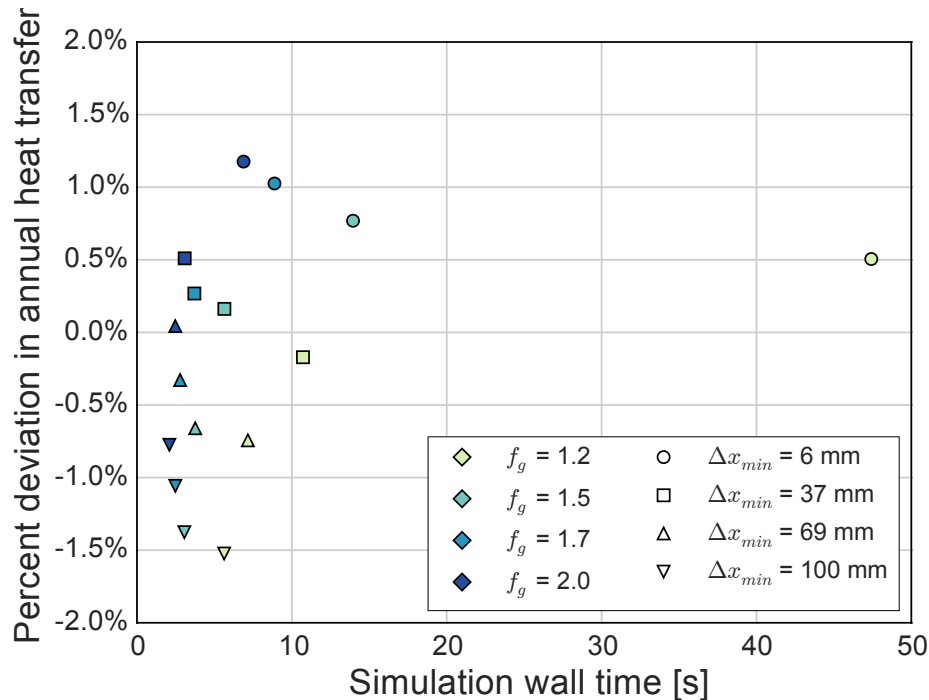


Figure 5.34: Deviation from three-dimensional annual heat transfer vs. simulation wall time for different combinations of discretization parameters

Increasing the cell growth factor results in larger positive deviations in approximation accuracy. Increasing the minimum cell dimension results in larger negative deviations in approximation accuracy. These counteracting results cannot be relied upon to generate faster, more accurate simulations. However, it is possible to relax either or both of the discretization parameters to reduce simulation wall time within 10 seconds without introducing deviations greater than 2%.

## 5.8 Summary and Conclusions

The accuracy and computational performance of the boundary layer adjustment method demonstrate how the Kiva framework is applied to improve foundation heat transfer calculations. Testing approximations against a verified, three-dimensional solution bolsters the algorithmic confidence behind the calculations. Each simplification, whether to the spatial discretization, the

numerical scheme, the initialization method, or the number of dimensions, is justified through comparative analysis.

Foundation heat transfer, which would take several days to simulate in three-dimensions on a supercomputer, is approximated within five seconds on a laptop with less than 5% deviation in results. The boundary layer adjustment method, with a suitably coarse spatial discretization, would account for a suitably small fraction of total simulation time in a whole-building energy simulation context.

## Chapter 6

### Conclusions and Future Work

#### 6.1 Conclusions

Kiva provides a balance of capability, complexity, computational performance and algorithmic confidence that is not available in other simulation tools or calculation methods.

Generalized descriptions of the foundation construction elements allow for assessment of a fully continuous range of insulation design options. The boundary layer adjustment method allows for accurate simulations of almost any foundation shape. Automated discretization of domain dramatically decreases the complexity of the problem, requiring the user to only input information about the foundation system, and not details of numerical methods used to solve the problem.

Three different components of the foundation heat transfer calculation were tested within the Kiva framework to assess their impact on both computational performance and accuracy. These components include the numerical scheme, the initialization method, and the two-dimensional approximation of three-dimensional heat transfer. Of the numerical schemes tested, the Alternating Direction Implicit (ADI) scheme demonstrates the best balance between accuracy, performance, and numerical stability. The new accelerated initialization approach significantly reduces the required years of presimulation. The boundary layer adjustment method improves accuracy over other established two-dimensional approximation methods with a negligible increase in computation time. This method accounts for reduced heat transfer from concave foundation shapes, which has not been adequately addressed to date. Within the Kiva framework, three-dimensional heat transfer

that can require several days to simulate is approximated in two-dimensions in a matter of seconds while maintaining accuracy within 5%.

Two-dimensional approximations are able to capture the strongest directional dependence of foundation heat transfer providing algorithmic confidence without the computational burden required of three-dimensional analyses.

The combined recommendations presented in Table 6.1 result in reliably efficient and accurate foundation heat transfer calculations that can be performed in the context of whole-building energy analysis.

Table 6.1: Recommended methods and numerical parameters for foundation heat transfer

<b>Description</b>	<b>Value</b>
Minimum cell dimension	0.02 m
Cell growth coefficient	1.50
Time-step duration	60 minutes
Numerical method	ADI
Initialization method	Accelerated
Initialization acceleration time-step duration	1 week
Initialization acceleration period duration	12 weeks
Initialization warm-up duration	1 year
Two-dimensional approximation	Boundary layer adjustment method

## 6.2 Future Work

The flexible framework and open source development positions Kiva for extension into future studies and further improvements to calculating heat transfer from building foundations.

### 6.2.1 Whole-Building Energy Simulation Tools

Kiva must be integrated into a whole-building energy simulation engine before its advantages are fully utilized by energy modeling professionals. The Kiva framework was designed with integration in mind, by exposing access to important run-time variables that determine the heat balance between the foundation system and the rest of the building. Once integrated, Kiva will provide

convective heat flux from foundation surfaces to thermal zones in a whole-building energy model, which, in turn, provides the thermal zone temperatures that determine heat transfer through the foundation in the following time-step.

In addition to interior zone temperatures, the whole-building simulation engine will provide information from HVAC systems that interact with the foundation and the surrounding ground. Kiva will use heat source values to simulate radiant slabs, ground source heat pumps, and snow-melt systems.

### 6.2.2 Foundation Design Guidelines

Once Kiva is integrated into a whole-building simulation engine, it can be used to help inform changes to foundation design guidelines. Current guidelines for foundation insulation design include the *Builder's Foundation Handbook* [20], which includes insulation recommendations based on analysis performed in 1988 [77] and *ASHRAE Standard 90.1* [8], which defines levels of insulation based on analysis performed in 1991 [12]. The underlying methodology behind both sets of guidelines are woefully out of date. Both the recommendations in the *Builder's Foundation Handbook* and the standard insulation levels in *ASHRAE Standard 90.1* can be updated based on new, more accurate analyses using Kiva.

### 6.2.3 Additional Capabilities

There are several capabilities mentioned in the literature review chapter (Chapter 2) that were not incorporated into Kiva by the time of this thesis. Some suggested capabilities are listed below in order of priority:

- Multiple foundation types within a single building
- Multiple interior thermal zones
- Spatially varying soil properties
- Spatially varying surface properties

- Coupled heat and moisture transfer calculations with dynamic thermal properties

#### **6.2.4 Sensitivity to Model Parameters**

Two types of sensitivity analyses can be performed using the Kiva framework. The first type of analysis tests computational performance and accuracy impacts of certain computational routines. There are several routines that are not included in Kiva because of their perceived impact on computational performance. The goal of these analyses is to quantify the trade-off between computational performance and accuracy of their respective routines. Potential routines include:

- shading of incident solar on the ground,
- coupled heat and moisture transfer,
- soil freezing and thawing,
- snow cover, and
- evapotranspiration

The other type of analysis involves exploration of propagation of uncertainty in model inputs. Because there are many relevant inputs to a foundation heat transfer model that are difficult to measure within reasonable certainty, it is important to understand the implications of this uncertainty as it propagates into results and, ultimately, recommended foundation insulation levels. Two important inputs to investigate are the thermal properties of the soil, and the deep ground boundary condition, which is strongly influenced by the presence of a high water table.

#### **6.2.5 Performance Optimization**

The source code of Kiva has not been optimized for memory utilization or CPU performance. There are likely several areas in the source code that can be improved to increase Kiva's speed and accessibility. There are several tools available to profile the execution of Kiva's source code to identify potential bottlenecks in the simulation process.

Iterative solvers have also improved drastically over the past several decades. Many authors cite Algebraic Multigrid (AMG) methods with computational efficiencies comparable to the Alternating Direction Implicit (ADI) method. AMG methods do not require a structured grid, and can be solved using parallel processes [19]. With the increasing trend of parallel architecture in computing, AMG methods should be evaluated as a potential replacement for the ADI method.

## Bibliography

- [1] M.H. Adjali, M. Davies, and J. Littler. Three-Dimensional Earth-Contact Heat Flows: A Comparison of Simulated and Measured Data for a Buried Structure. Renewable Energy, 15: 356–359, April 1998.
- [2] M.H. Adjali, M. Davies, and J. Littler. Earth-Contact Heat Flows: Review and Application of Design Guidance Predictions. Building Services Engineering Research and Technology, 19 (3):111–121, 1998.
- [3] M.H. Adjali, M. Davies, and J. Littler. A Numerical Simulation of Measured Transient Temperatures in the Walls, Floor and Surrounding Soil of a Buried Structure. International Journal of Heat and Mass Transfer, 9(4):405–422, 1999.
- [4] M.H. Adjali, M. Davies, S.W. Rees, and J. Littler. Temperatures in and under a Slab-on-Ground Floor: Two- and Three-Dimensional Numerical Simulations and Comparison with Experimental Data. Building and Environment, 35:655–662, October 2000.
- [5] M.H. Adjali, M. Davies, and S.W. Rees. A Comparative Study of Design Guide Calculations and Measured Heat Loss through the Ground. Building and Environment, 39(11):1301–1311, November 2004.
- [6] A. Al-Anzi and M. Krarti. Local/global analysis of transient heat transfer from building foundations. Building and Environment, 39(5):495–504, May 2004.
- [7] ASHRAE. ASHRAE Handbook—Fundamentals. ASHRAE, Atlanta, Georgia, 2009.
- [8] ASHRAE. ANSI/ASHRAE/IES Standard 90.1-2013: Energy Standard for Buildings Except Low-Rise Residential Buildings, 2013.
- [9] W. Bahnfleth. Three-Dimensional Modeling of Heat Transfer from Slab Floors. Ph.d. thesis, University of Illinois at Urbana Champaign, 1989.
- [10] W. Bahnfleth and J. Amber. Algorithms for Slab-on-Grade Heat Transfer Calculations. Technical report, US Army Corps of Engineers Construction Engineering Research Laboratory, Champaign, IL, 1990.
- [11] W. Bahnfleth and C. Pedersen. A Three-Dimensional Numerical Study of Slab-on-Grade Heat Transfer. ASHRAE Transactions, 96(2):61–72, 1990.



- [12] D. Baylon and M. Kennedy. Calculating the Impact of Ground Contact on Residential Heat Loss. In Proceedings of Thermal Performance of the Exterior Envelopes of Buildings X, Clearwater, Florida, 2007. ASHRAE.
- [13] V. Bazjanac, Y. Huang, and F. Winkelmann. DOE-2 Modeling of Two-Dimensional Heat Flow in Underground Surfaces. Technical report, California Energy Commission, 2000.
- [14] I. Beausoleil-Morrison and M. Krarti. Predicting Foundation Heat Losses: Neural Networks Versus the BASESIMP Correlations. In Proceedings of Building Simulation 1997, Prague, Czech Republic, 1997. IBPSA.
- [15] I. Beausoleil-Morrison and G. Mitalas. BASESIMP: A residential-foundation heat-loss algorithm for incorporating into whole-building energy-analysis programs. In Proceedings of Building Simulation 1997, Prague, Czech Republic, 1997. IBPSA.
- [16] I. Beausoleil-Morrison, G. Mitalas, and H. Chin. Estimating Three-Dimensional Below-Grade Heat Losses from Houses Using Two-Dimensional Calculations. In Proceedings of Thermal Performance of the Exterior Envelopes of Buildings VI, pages 95–99, Clearwater, Florida, 1995. ASHRAE.
- [17] I. Beausoleil-Morrison, G. Mitalas, and C. McLarnon. BASECALC(TM): New Software for Modelling Basement and Slab-on-Grade Heat Losses. In Proceedings of Building Simulation 1995, Madison, Wisconsin, 1995. IBPSA.
- [18] C. Booten, N. Kruis, and C. Christensen. Identifying and Resolving Issues in EnergyPlus and DOE-2 Window Heat Transfer Calculations. Technical Report August, NREL, Golden, Colorado, 2012.
- [19] W. Briggs, V. Hensen, and S. McCormick. A Multigrid Tutorial. Society of Industrial and Applied Mathematics, Philadelphia, Pennsylvania, 2 edition, 2000.
- [20] J. Carmody, J. Christian, and K. Labs. Builder's Foundation Handbook. Oak Ridge National Laboratory, Oak Ridge, Tennessee, 1991.
- [21] M. Chang, L. Chow, and W. Chang. Improved Alternating-Direction Implicit Method for Solving Transient Three-Dimensional Heat Diffusion Problems. Numerical Heat Transfer: Part B: Fundamentals, 19:69–84, 1991.
- [22] S. Choi and M. Krarti. Heat transfer for slab-on-grade floor with stepped ground. Energy Conversion and Management, 39(7):691–701, 1998.
- [23] S. Choi and M. Krarti. Thermally optimal insulation distribution for underground structures. Energy and Buildings, 32(3):251–265, September 2000.
- [24] P. Chuangchid. Heat Gain from Slab-on-Grade Floor of Refrigerated Structures. Ph.d. thesis, University of Colorado at Boulder, 2000.
- [25] P. Chuangchid and M. Krarti. Steady-State Component of Three-Dimensional Slab-on-Grade Foundation Heat Transfer. Journal of Solar Energy Engineering, 123(1):18, 2001.
- [26] J. Claesson and C.E. Hagentoft. Heat loss to the ground from a building—I. General theory. Building and Environment, 26(2):195–208, 1991.

- [27] D. Claridge. Design Methods for Earth-Contact Heat Transfer. In Karl Böer, editor, Advances in Solar Energy: An Annual Review of Research and Development, chapter 7, pages 305–351. American Solar Energy Society, Inc., Boulder, CO, 4 edition, 1988.
- [28] J. Clark and M. Korybalski. Algebraic Methods for the Calculation of Radiation Exchange in an Enclosure. Wärme - und Stoffübertragung, 7(1):31–44, 1974.
- [29] E. Clements. Three Dimensional Foundation Heat Transfer Modules for Whole-Building Energy Analysis. Master’s thesis, Pennsylvania State University, 2004.
- [30] C. Cogil. Modeling of Basement Heat Transfer and Parametric Study of Basement Insulation for Low Energy Housing. Master’s thesis, Pennsylvania State University, 1998.
- [31] M. Crowley. Modeler Report for BESTEST Cases GC10a-GC80c, MATLAB 7.0.4.365 (R14) Service Pack 2. Technical report, Dublin Institute of Technology, Dublin, Ireland, 2007.
- [32] J. Cullin, L. Xing, E. Lee, J. Spitler, and D. Fisher. Feasibility of Foundation Heat Exchangers for Residential Ground Source Heat Pump Systems in the United States. ASHRAE Transactions, 118(1):1039–1048, 2012.
- [33] M. Davies. Computational and Experimental Three-Dimensional Conductive Heat Flows in and around Buildings. Ph.d. thesis, University of Westminster, 1994.
- [34] M. Davies, S. Zoras, and M.H. Adjali. A Potentially Fast, Flexible and Accurate Earth-Contact Heat Transfer Simulation Method. In Proceedings of Building Simulation 1999, number 1987, Kyoto, Japan, 1999. IBPSA.
- [35] D. De Vries. Simultaneous Transfer of Heat and Moisture in Porous Media. American Geophysical Union Transactions, 39(5):909–916, 1958.
- [36] D. De Vries. Thermal Properties of Soils. In W Van Wijk, editor, Physics of Plant Environment, chapter 7, pages 210–235. North-Holland Publishing Co., Amsterdam, 1966.
- [37] A. Delsante. The effect of water table depth on steady-state heat transfer through a slab-on-ground floor. Building and Environment, 28(3):369–372, 1993.
- [38] A. Delsante, A. Stokes, and P. Walsh. Application of Fourier Transforms to Periodic Heat Flow into the Ground Under a Building. International Journal of Heat and Mass Transfer, 26(1):121–132, 1983.
- [39] M. Deru. A Model for Ground-Coupled Heat and Moisture Transfer from Buildings A Model for Ground-Coupled Heat and Moisture Transfer from Buildings. Technical Report June, National Renewable Energy Laboratory, Golden, Colorado, 2003.
- [40] M. Deru, R. Judkoff, and J. Neymark. Whole Building Energy Simulation with a Three-Dimensional Ground-Coupled Heat Transfer Model. ASHRAE Transactions, 109(1):557–565, 2003.
- [41] G.H. dos Santos and N. Mendes. Multidimensional Effects of Ground Heat Transfer on the Dynamics of Building Thermal Performance. ASHRAE Transactions, 110(2):345–354, 2004.
- [42] G.H. dos Santos and N. Mendes. Simultaneous heat and moisture transfer in soils combined with building simulation. Energy and Buildings, 38(4):303–314, April 2006.

- [43] J. Duffie and W. Beckman. Solar Engineering of Thermal Processes. John Wiley & Sons Ltd, Hoboken, New Jersey, third edit edition, 2006.
- [44] D. Fisher and S. Rees. Modeling Ground Source Heat Pump Systems in a Building Energy Simulation Program (EnergyPlus). In Proceedings of Building Simulation 2005, pages 311–318, Montreal, Canada, 2005. IBPSA.
- [45] P. Fritzson. Principles of Object-Oriented Modeling and Simulation with Modelica 2.1. Wiley-IEEE Press, 2003. ISBN 0471471631.
- [46] K. Fukuyo. Conditional Stability of Larkin Methods with Non-Uniform Grids. Theoretical and Applied Mechanics, 37(2):139–159, 2010. ISSN 1450-5584. doi: 10.2298/TAM1002139F.
- [47] R. Gilpin and B. Wong. "Heat-Valve" Effects in the Ground Thermal Regime. Journal of Heat Transfer, 98(4):537–542, 1976.
- [48] C.E. Hagentoft. Heat Loss to the Ground from a Building: Slab on the Ground and Cellar. Ph.d. thesis, Lund Institute of Technology, Sweden, 1988.
- [49] C.E. Hagentoft. Heat Losses and Temperature in the Ground under a Building with and without Ground Water Flow—I. Infinite Ground Water Flow Rate. Building and Environment, 31(1):3–11, January 1996.
- [50] C.E. Hagentoft. Steady-State Heat Loss for an Edge-Insulated Slab : Part I. Building and Environment, 37(1):19–25, January 2002.
- [51] C.E. Hagentoft and J. Claesson. Heat Loss to the Ground from a BuildingII. Slab on the Ground. Building and Environment, 26(4):395–403, 1991.
- [52] C.E. Hagentoft and J. Claesson. Influence of Rain Water Percolation on Ground Heat Losses and Temperature for Basement Foundation. In Proceedings of the 3rd International Conference on Research in Building Physics and Building Engineering, Montreal, Canada, 2006.
- [53] H. Hottel and A. Sarofim. Radiative Transfer. McGraw Hill Book Co., 1967.
- [54] Y. Huang, L. Shen, J. Bull, and L. Goldberg. Whole-house simulation of foundation heat flows using the DOE-2.1 C program. ASHRAE Transactions, 94(2):936–958, 1988.
- [55] James J. Hirsch & Associates. DOE-2, 2010. URL <http://www.doe2.com/>.
- [56] H. Janssen. The Influence of Soil Moisture Transfer On Building Heat Loss Via the Ground. Ph.d. thesis, Katholieke Universiteit Leuven, July 2002.
- [57] H. Janssen, J. Carmeliet, and H. Hens. The Influence of Soil Moisture Transfer on Building Heat Loss via the Ground. Building and Environment, 39(7):825–836, July 2004.
- [58] N. Jones and D. Greenberg. Fast Computation of Incident Solar Radiation from Preliminary to Final Building Design. In Proceedings of Building Simulation 2011, pages 14–16, Sydney, Australia, 2011. IBPSA.

- [59] R. Judkoff and J. Neymark. Home Energy Rating System Building Energy Simulation Test (HERS BESTEST) Volume 1 Tier 1 and Tier 2 Tests User's Manual. Technical Report November, National Renewable Energy Laboratory, Golden, Colorado, 1995.
- [60] R. Judkoff and J. Neymark. Model Validation and Testing : The Methodological Foundation of ASHRAE Standard 140. ASHRAE Transactions, 112(2):367–376, 2006.
- [61] B.D. Kay and E. Perfect. State of the art: Heat and mass transfer in freezing soils. In Proceedings of 5th International Symposium on Ground Freezing, Rotterdam, Netherlands, 1988. Balkema, Rotterdam.
- [62] M. Krarti. Developments in Ground-Coupled Heat Transfer. Ph.d. thesis, University of Colorado, 1987.
- [63] M. Krarti. Time-Varying Heat Transfer From Slab-on-Grade Floors with Vertical Insulation. Building and Environment, 29(1):55–61, January 1994.
- [64] M. Krarti. Comparison of a Neural Network Model with a Regression Model for Foundation Heat Loss Calculation. In Proceedings of Thermal Performance of the Exterior Envelopes of Buildings VI, pages 79–85, Clearwater, Florida, 1995. ASHRAE.
- [65] M. Krarti. Effect of Spatial Variation of Soil Thermal Properties on Slab-on-Ground Heat Transfer. Building and Environment, 31(1):51–57, January 1996.
- [66] M. Krarti. Building Foundation Heat Transfer. In Yogi Goswami and Karl Böer, editors, Advances in Solar Energy: An Annual Review of Research and Development, chapter 6, pages 241–315. American Solar Energy Society, Inc., Boulder, CO, 13 edition, 1999.
- [67] M. Krarti. Impact of Above-Grade Walls on Three-Dimensional Building Foundation Heat Transfer From Slab-On Grade Floors. Journal of Solar Energy Engineering, 136(1), 2013.
- [68] M. Krarti and S. Choi. Simplified Method for Foundation Heat Loss Calculation. ASHRAE Transactions, 102(1):140–152, 1996.
- [69] M. Krarti and S. Choi. A Simulation Method for Fluctuating Temperatures in Crawlspace Foundations. Energy and Buildings, 26(2):183–188, 1997.
- [70] M. Krarti, D. Claridge, and J. Kreider. ITPE Technique Applications to Time-Varying Two-Dimensional Ground-Coupling Problems. International Journal of Heat and Mass Transfer, 31(9):1899–1911, 1988.
- [71] M. Krarti, D. Claridge, and J. Kreider. The ITPE Technique Applied to Steady-State Ground-Coupling Problems. International Journal of Heat and Mass Transfer, 31(9):1885–1898, 1988.
- [72] M. Krarti, J. Kreider, and D. Claridge. ITPE Technique Applications to Time-Varying Three-Dimensional Ground-Coupling Problems. Journal of Heat Transfer, 112:849–856, 1990.
- [73] M. Krarti, P. Chuangchid, and P. Ihm. Foundation Heat Transfer Module for EnergyPlus Program. In Proceedings of Building Simulation 2001, pages 931–938, Rio de Janeiro, Brazil, 2001. IBPSA.
- [74] N. Kruis. Kiva, 2014. URL <https://github.com/nealkruis/kiva>.

- [75] T. Kusuda and P.R. Achenbach. Earth temperature and thermal diffusivity at selected stations in the United States. ASHRAE Transactions, 73:61–75, 1965.
- [76] T. Kusuda and J.W. Bean. Simplified Methods for Determining Seasonal Heat Loss from Uninsulated Slab-on-Grade Floors. ASHRAE Transactions, 90(1):611–632, 1984.
- [77] K. Labs, J. Carmody, R. Sterling, L. Shen, Y. Huang, and D. Parker. Building Foundation Design Handbook. Oak Ridge National Laboratory, Oak Ridge, Tennessee, 1988.
- [78] A. Lachenbruch. Three-Dimensional Heat Conduction in Permafrost Beneath Heated Buildings. In U. S. Geological Survey: Experimental and Theoretical Geophysics: Bulletin 1052, chapter B, pages 51–69. United States Government Printing Office, Washington D.C., 1959.
- [79] J. Latta and G. Boileau. Heat Losses from House Basements. Canadian Building, XIX(10): 39–42, 1969.
- [80] Lawrence Berkeley National Laboratory and James J. Hirsch & Associates. DOE-2.2: Building Energy Use and Cost Analysis Program. Volume 2: Dictionary. James J. Hirsch & Associates, Camarillo, California, 2009. URL <http://www.doe2.com/>.
- [81] N. Li, F. Chen, B. Xu, and G. Swoboda. Theoretical Modeling Framework for an Unsaturated Freezing Soil. Cold Regions Science and Technology, 54:19–35, 2008.
- [82] X. Liu, S. Rees, and J. Spitler. Modeling Snow Melting on Heated Pavement Surfaces. Part I: Model Development. Applied Thermal Engineering, 27(5-6):1115–1124, April 2007.
- [83] C. Ludeman. Passive Project Foundation and Slab Insulation, 2009. URL <http://www.100khouse.com/2009/06/11/passive-project-foundation-slab-insulation/>.
- [84] X. Ma, B. Cheng, J. Mao, W. Liu, and D. Zi. Finite Element Modelling of Coupled Heat and Moisture Transfer in Typical Earth-Sheltered Building Envelope. In Proceedings of Building Simulation 2009, pages 1850–1856, Glasgow, Scotland, 2009. IBPSA.
- [85] J. MacArthur, G. Meixel, and L. Shen. Application of Numerical Methods for Predicting Energy Transport in Earth Contact Systems. Applied Energy, 13:121–156, 1983.
- [86] T. McDowell, J. Thornton, and M. Duffy. Comparison of a Ground-coupling Reference Standard Model to Simplified Approaches. In Proceedings of Building Simulation 2009, pages 591–598, Glasgow, Scotland, 2009. IBPSA.
- [87] G. Mitalas. Calculation of Below-Grade Residential Heat Loss: Low-Rise Residential Building. ASHRAE Transactions, 93(1):743–783, 1987.
- [88] F. Moukalled and Y. Saleh. Heat and Mass Transfer in Moist Soil, Part I. Formulation and Testing. Numerical Heat Transfer: Part B: Fundamentals, 49(5):467–486, October 2006.
- [89] A. Nakhi. Modeler Report for BESTEST Cases GC10a-GC80c, FLUENT Version 6.0.20. Technical report, Public Authority for Applied Education and Training, Kuwait, 2007.

- [90] J. Neymark and R. Judkoff. International Energy Agency Building Energy Simulation Test and Diagnostic Method ( IEA BESTEST ): In-Depth Diagnostic Cases for Ground Coupled Heat Transfer Related to Slab-on-Grade Construction. Technical Report September, National Renewable Energy Laboratory, Golden, Colorado, 2008.
- [91] J. Rantala and V. Leivo. Heat Loss into Ground from a Slab-on-Ground Structure in a Floor Heating System. International Journal of Energy Research, 30(12):929–938, October 2006.
- [92] S. Rees, J. Spitler, and X. Xiao. Transient Analysis of Snow-Melting System Performance. ASHRAE Transactions, 108(2):406–423, 2002.
- [93] S.W. Rees and H. Thomas. Two-Dimensional Heat Transfer beneath a Modern Commercial Building: Comparison of Numerical Prediction with Field Measurement. Building Services Engineering Research and Technology, 18(3):169–174, 1997.
- [94] S.W. Rees, R. Lloyd, and H. Thomas. A Numerical Simulation of Measured Transient Heat Transfer through a Concrete Ground Floor Slab and Underlying Substrata. International Journal of Numerical Methods for Heat & Fluid Flow, 5(8):669–683, 1995.
- [95] S.W. Rees, H. Thomas, and Z. Zhou. Ground Heat Transfer: Some Further Insights into the Influence of Three-Dimensional Effects. Building Services Engineering Research and Technology, 21(4):233–239, 2000.
- [96] S.W. Rees, Z. Zhou, and H. Thomas. The Influence of Soil Moisture Content Variations on Heat Losses from Earth-Contact Structures : An Initial Assessment. Building and Environment, 36:157–165, 2001.
- [97] S.W. Rees, H. Thomas, and Z. Zhou. A Numerical and Experimental Investigation of Three-Dimensional Ground Heat Transfer. Building Services Engineering Research and Technology, 27(3):195–208, 2006.
- [98] S.W. Rees, Z. Zhou, and H. Thomas. Ground Heat Transfer: A Numerical Simulation of a Full-Scale Experiment. Building and Environment, 42(3):1478–1488, March 2007.
- [99] B. Rock. Sensitivity Study of Slab-on-Grade Transient Heat Transfer Model Parameters. ASHRAE Transactions, 110(1):177–184, 2004.
- [100] V. Saul'yev. Integration of Equations of Parabolic Type by the Method of Nets. Pergamon Press, New York, 1964.
- [101] L. Shen. An Investigation of Transient, Two-Dimensional Coupled Heat and Moisture Flow in Soils. Ph.d. thesis, University of Minnesota, 1986.
- [102] L. Shen and J. Ramsey. An Investigation of Transient, Two-Dimensional Coupled Heat and Moisture Flow in the Soil Surrounding a Basement Wall. International Journal of Heat and Mass Transfer, 31(7):1517–1527, 1988.
- [103] B. Sibbitt, D. Mcclenahan, R. Djebbar, J. Thornton, and B. Wong. The Performance of a High Solar Fraction Seasonal Storage District Heating System Five Years of Operation. Energy Procedia, 30(SHC 2012):856–865, 2012.

- [104] Solar Energy Laboratory. TRNSYS 17: a TRaNsient SYstem Simulation program. Solar Energy Laboratory, University of Wisconsin-Madison, Madison, Wisconsin, 2010.
- [105] R. Sterling, S. Gupta, L. Shen, and L. Goldberg. Assessment of Soil Thermal Conductivity for Use in Building Design and Analysis. Technical report, ASHRAE, Atlanta, GA, 1993.
- [106] The Scalable Software Infrastructure Project. Lis User Guide. The Scalable Software Infrastructure Project, Fukuoka, Japan, 2014.
- [107] H. Thomas and S.W. Rees. The Thermal Performance of Ground Floor Slabs—a Full Scale in-situ experiment. Building and Environment, 34:139–164, March 1999.
- [108] H. Thomas and S.W. Rees. Measured and Simulated Heat Transfer to Foundation Soils. Géotechnique, 59(4):365–375, 2009.
- [109] J. Thornton. Modeler Report for BESTEST Cases GC10a-GC80c, TRNSYS Version 16.1. Technical report, Thermal Energy Systems Specialists, Madison, Wisconsin, 2007.
- [110] H. Trethowen and A. Delsante. A Four-Year Site Measurement of Heat Flow in Slab-on-Ground Floors with Wet Soils. In Proceedings of Thermal Performance of the Exterior Envelopes of Buildings VII, Clearwater, Florida, 1998. ASHRAE.
- [111] United States Department Of Energy (DOE). EnergyPlus: Input Output Reference. The Board of Trustees of the University of Illinois and the Regents of the University of California through the Ernest Orlando Lawrence Berkeley National Laboratory, Berkeley, California, version 8. edition, 2014.
- [112] B. Usowicz, J. Lipiec, and A. Ferrero. Prediction of soil thermal conductivity based on penetration resistance and water content or air-filled porosity. International Journal of Heat and Mass Transfer, 49(25-26):5010–5017, December 2006.
- [113] G. Walton. Thermal Analysis Research Program Reference Manual. U.S. Dept. of Commerce, National Bureau of Standards, Washington D.C., 1983.
- [114] G. Walton. Estimating 3-D heat loss from rectangular basements and slabs using 2-D calculations. ASHRAE Transactions, 93(1):791–797, 1987.
- [115] F. Wang. Mathematical Modeling and Computer Simulation of Insulation Systems in Below Grade Applications. In Proceedings of Thermal Performance of the Exterior Envelopes of Buildings I, pages 456–471, Clearwater, Florida, 1979. ASHRAE.
- [116] E. Wentzel. Thermal Modeling of Walls, Foundations and Whole Buildings Using Dynamic Thermal Networks. Ph.d. thesis, Chalmers University of Technology, 2005.
- [117] S. Wilcox and W. Marion. Users Manual for TMY3 Data Sets. Technical report, National Renewable Energy Laboratory, Golden, Colorado, 2008.
- [118] F. Winkelmann. Underground Surfaces: How To Get A Better Underground Surface Heat Transfer Calculation In DOE-2.1E. DOE-2 Articles from the Building Energy Simulation User News, 23(5):5–14, 2002.

- [119] X. Xie, Y. Jiang, and J. Xia. A New Approach to Compute Heat Transfer of Ground-Coupled Envelope in Building Thermal Simulation Software. Energy and Buildings, 40(4):476–485, 2008.
- [120] M. Yazdanian and J. Klems. Measurement of the exterior convective film coefficient for windows in low-rise buildings. ASHRAE Transactions, 100(1), 1994. URL <http://btech.lbl.gov/papers/34717.pdf>.
- [121] C. Zhang and G. Ding. A novel thermal response factor method for the dynamic load calculation of buildings. Journal of Asian Architecture and Building Engineering, 1(1):75–79, 2002.



## Appendix A

### Finite Difference Discretizations

The discretization equations for each of the finite difference methods implemented in Kiva are provided for a two-dimensional axisymmetric cylindrical coordinate system.

#### A.1 Continuous Equation

Heat transfer in the ground domain is solved using the diffusion equation

$$C_{H,T} \frac{\partial T}{\partial t} = \nabla [k \nabla T] + \dot{q} \quad (\text{A.1})$$

where:

- $C_{H,T}$  is the thermal heat capacitance [J/m<sup>3</sup>-K]
- $T$  is the temperature at a given spatial position and point in time [K]
- $t$  is time [s]
- $\nabla$  is the differential spatial gradient operator
- $k$  is the thermal conductivity [W/m-K]
- $\dot{q}$  is the heat source or sink in [W/m<sup>3</sup>]

The spatial gradient operator creates different equations depending on the coordinate system.

For Cartesian coordinates in three-dimensions, Equation A.74 becomes

$$C_{H,T} \frac{\partial T}{\partial t} = + \frac{\partial}{\partial x} \left[ k \frac{\partial T}{\partial x} \right] + \frac{\partial}{\partial y} \left[ k \frac{\partial T}{\partial y} \right] + \frac{\partial}{\partial z} \left[ k \frac{\partial T}{\partial z} \right] + \dot{q}. \quad (\text{A.2})$$

For Cartesian coordinates in two-dimensions, Equation A.74 becomes

$$C_{H,T} \frac{\partial T}{\partial t} = + \frac{\partial}{\partial x} \left[ k \frac{\partial T}{\partial x} \right] + \frac{\partial}{\partial z} \left[ k \frac{\partial T}{\partial z} \right] + \dot{q}. \quad (\text{A.3})$$

For Axisymmetric cylindrical coordinates in two-dimensions, Equation A.74 becomes

$$C_{H,T} \frac{\partial T}{\partial t} = \frac{1}{r} \frac{\partial}{\partial r} \left[ rk \frac{\partial T}{\partial r} \right] + \frac{\partial}{\partial z} \left[ k \frac{\partial T}{\partial z} \right] + \dot{q}. \quad (\text{A.4})$$

## A.2 Boundary Conditions

There are four types of boundary conditions encountered in Kiva. The formulation of the boundary conditions are framed generically for a direction  $w$ , which is perpendicular to the surface.

Interior flux boundaries in Kiva fall along the foundation floor, the foundation wall, and the under-side of any partial wall insulation.

$$-k \frac{\partial T}{\partial w} = [h_c + h_r] [T_\infty - T(w)] + \dot{q}_{sw}, \quad (\text{A.5})$$

where

- $h_c$  is the convection coefficient [ $\text{W}/\text{m}^2 \cdot \text{K}$ ],
- $h_r$  is the long-wave radiation coefficient [ $\text{W}/\text{m}^2 \cdot \text{K}$ ],
- $T_\infty$  is the ambient air temperature [ $\text{K}$ ],
- $T(w)$  is the boundary temperature [ $\text{K}$ ], and
- $\dot{q}_{sw}$  is the incident short-wave radiation flux [ $\text{W}/\text{m}^2$ ].

Exterior flux boundaries are very similar to the interior boundaries except that they include a separate long-wave radiation term which accounts for the difference between the radiative temperature,  $T_\infty F^{*1/4}$ , and the outdoor ambient temperature,  $T_\infty$ . This boundary is applied to the grade surface and the exterior wall surface if it is exposed.

$$-k \frac{\partial T}{\partial w} = h_c [T_\infty - T(w)] + h_r [T_\infty F^{*1/4} - T(w)] + \dot{q}_{sw} \quad (\text{A.6})$$

where  $F^*$  is a correction factor to account for the difference between the sky temperature and the ambient air temperature.

Zero-flux boundaries occur at far-field, deep-ground and symmetry planes as well as the top of the foundation wall.

$$\frac{\partial T}{\partial w} = 0 \quad (\text{A.7})$$

Constant temperature boundaries are found either at deep-ground or at the wall-top (to mimic the constraints of some analytical solutions).

$$T(w) = T_c \quad (\text{A.8})$$

where  $T_c$  is a constant temperature [K] applied to the boundary.

### A.3 Discretized Equations

The following sections describe the discretized equations for each of the finite difference methods implemented in Kiva. The equations presented here correspond to the continuous partial differential equation for a two-dimensional cylindrical coordinate system (Equation A.75). Formulations for Cartesian two- and three-dimensional coordinate systems can be easily extended by omission or addition of certain terms.

The only difference between the different finite difference schemes is the time-step associated with the temperature terms. A generic finite difference scheme with temperatures  $T^*$  will provide a basis for the more specific formulations:

$$\begin{aligned} \frac{T_{i,j}^{n+1} - T_{i,j}^n}{\Delta t} C_{H,T} = & \frac{1}{r_i} \left[ \frac{\Delta r_m}{\Delta r_m + \Delta r_p} k_{r,p} \frac{T_{i+1,j}^* - T_{i,j}^*}{\Delta r_p} + \frac{\Delta r_p}{\Delta r_m + \Delta r_p} k_{r,m} \frac{T_{i,j}^* - T_{i-1,j}^*}{\Delta r_m} \right] \\ & + \frac{2}{\Delta r_m + \Delta r_p} \left[ k_{r,p} \frac{T_{i+1,j}^* - T_{i,j}^*}{\Delta r_p} - k_{r,m} \frac{T_{i,j}^* - T_{i-1,j}^*}{\Delta r_m} \right] \\ & + \frac{2}{\Delta z_m + \Delta z_p} \left[ k_{z,p} \frac{T_{i,j+1}^* - T_{i,j}^*}{\Delta z_p} - k_{z,m} \frac{T_{i,j}^* - T_{i,j-1}^*}{\Delta z_m} \right] + \dot{q}. \end{aligned} \quad (\text{A.9})$$

where

- $i$  and  $j$  are spatial indices,

- $n$  is the temporal index,
- $\Delta t$  is the time-step [s], and

$$\Delta r_p = \frac{\Delta r_i + \Delta r_{i+1}}{2}, \quad (\text{A.10})$$

$$\Delta r_m = \frac{\Delta r_i + \Delta r_{i-1}}{2}, \quad (\text{A.11})$$

$$\Delta z_p = \frac{\Delta z_i + \Delta z_{i+1}}{2}, \quad (\text{A.12})$$

$$\Delta z_m = \frac{\Delta z_i + \Delta z_{i-1}}{2}, \quad (\text{A.13})$$

$$k_{r,p} = \left[ \frac{\Delta r_i}{2\Delta r_p k_{i,j}} + \frac{\Delta r_{i+1}}{2\Delta r_p k_{i+1,j}} \right]^{-1}, \quad (\text{A.14})$$

$$k_{r,m} = \left[ \frac{\Delta r_i}{2\Delta r_m k_{i,j}} + \frac{\Delta r_{i-1}}{2\Delta r_m k_{i-1,j}} \right]^{-1}, \quad (\text{A.15})$$

$$k_{z,p} = \left[ \frac{\Delta z_j}{2\Delta z_p k_{i,j}} + \frac{\Delta z_{j+1}}{2\Delta z_p k_{i,j+1}} \right]^{-1}, \quad (\text{A.16})$$

$$k_{z,m} = \left[ \frac{\Delta z_j}{2\Delta z_m k_{i,j}} + \frac{\Delta z_{j-1}}{2\Delta z_m k_{i,j-1}} \right]^{-1}, \quad (\text{A.17})$$

where

- $\Delta r$  is the cell width [m], and
- $\Delta z$  is the cell height [m].

The nontemperature terms can then be collected into constant coefficients to simplify the formulation of the discretized equations:

$$\theta = \frac{\Delta t}{C_{H,T}}, \quad (\text{A.18})$$

$$c'_{r,p} = \theta \frac{\Delta r_m k_{r,p}}{r_i [\Delta r_m + \Delta r_p] \Delta r_p}, \quad (\text{A.19})$$

$$c'_{r,m} = \theta \frac{\Delta r_p k_{r,m}}{r_i [\Delta r_m + \Delta r_p] \Delta r_m}, \quad (\text{A.20})$$

$$c_{r,p} = \theta \frac{2k_{r,p}}{[\Delta r_m + \Delta r_p] \Delta r_p}, \quad (\text{A.21})$$

$$c_{r,m} = -\theta \frac{2k_{r,m}}{[\Delta r_m + \Delta r_p] \Delta r_m}, \quad (\text{A.22})$$

$$c_{z,p} = \theta \frac{2k_{z,p}}{[\Delta z_m + \Delta z_p] \Delta z_p}, \quad (\text{A.23})$$

$$c_{z,m} = -\theta \frac{2k_{z,m}}{[\Delta z_m + \Delta z_p] \Delta z_m}. \quad (\text{A.24})$$

For Cartesian coordinates, the radial terms ( $c'_{r,p}$ ,  $c'_{r,m}$ ,  $c_{r,p}$ , and  $c_{r,m}$ ) will be omitted (set to zero), and the  $x$  and  $y$  terms ( $c_{x,p}$ ,  $c_{x,m}$ ,  $c_{y,p}$ , and  $c_{y,m}$ ) can be defined in a similar fashion as the  $z$  terms.

With the definitions of the constant coefficients, Equation A.9 can be re-written as:

$$\begin{aligned} T_{i,j}^{n+1} - T_{i,j}^n &= c'_{r,p} [T_{i+1,j}^* - T_{i,j}^*] + c'_{r,m} [T_{i,j}^* - T_{i-1,j}^*] + c_{r,p} [T_{i+1,j}^* - T_{i,j}^*] \\ &+ c_{r,m} [T_{i,j}^* - T_{i-1,j}^*] + c_{z,p} [T_{i,j+1}^* - T_{i,j}^*] + c_{z,m} [T_{i,j}^* - T_{i,j-1}^*] + \theta \dot{q}. \end{aligned} \quad (\text{A.25})$$

The spatial derivative in the boundary condition relationships can be discretized as follows:

$$\frac{\partial T}{\partial w} \approx \frac{T_{l-1}^* - T_l^*}{\Delta w_m} \quad (\text{A.26})$$

where  $l$  is the spatial index in the direction normal to the boundary, and

$$\Delta w_m = \Delta w_{l-1}/2. \quad (\text{A.27})$$

This results in the following discretized boundary conditions:

$$-k_{w,m} \frac{T_{l-1}^* - T_l^*}{\Delta w_m} = [h_c + h_r] [T_\infty - T_l^*] + \dot{q}_{sw}, \quad (\text{A.28})$$

$$-k_{w,m} \frac{T_{l-1}^* - T_l^*}{\Delta w_m} = h_c [T_\infty - T_l^*] + h_r [T_\infty F^{*1/4} - T_l^*] + \dot{q}_{sw}, \quad (\text{A.29})$$

$$\frac{T_{l-1}^* - T_l^*}{\Delta w_m} = 0, \quad (\text{A.30})$$

$$T_l^* = T_c. \quad (\text{A.31})$$

### A.3.1 Explicit Scheme

In the explicit scheme, all the temperatures on the right-hand side of Equation A.9 represent the previous time-step,  $n$ :

$$T_{i,j}^{n+1} - T_{i,j}^n = c'_{r,p} [T_{i+1,j}^n - T_{i,j}^n] + c'_{r,m} [T_{i,j}^n - T_{i-1,j}^n] + c_{r,p} [T_{i+1,j}^n - T_{i,j}^n] + c_{r,m} [T_{i,j}^n - T_{i-1,j}^n] + c_{z,p} [T_{i,j+1}^n - T_{i,j}^n] + c_{z,m} [T_{i,j}^n - T_{i,j-1}^n] + \theta \dot{q}. \quad (\text{A.32})$$

This equation can be solved explicitly for the temperature at the new time-step,  $n + 1$ :

$$T_{i,j}^{n+1} = T_{i,j}^n [1 + c'_{r,m} + c_{r,m} + c_{z,m} - c'_{r,p} - c_{r,p} - c_{z,p}] + T_{i-1,j}^n [-c'_{r,m} - c_{r,m}] + T_{i+1,j}^n [c'_{r,p} + c_{r,p}] + T_{i,j-1}^n [-c_{z,m}] + T_{i,j+1}^n [c_{z,p}] + \theta \dot{q}. \quad (\text{A.33})$$

#### A.3.1.1 Boundary Conditions

For interior flux boundaries, the discretized equation becomes

$$-k_{w,m} \frac{T_{l-1}^n - T_l^{n+1}}{\Delta w_m} = [h_c + h_r] [T_\infty - T_l^{n+1}] + \dot{q}_{sw}, \quad (\text{A.34})$$

which solves for  $T_l^{n+1}$  as

$$T_l^{n+1} = \frac{\frac{k_{w,m}}{\Delta w_m} T_{l-1}^n + [h_c + h_r] T_\infty - \dot{q}_{sw}}{\frac{k_{w,m}}{\Delta w_m} + [h_c + h_r]}. \quad (\text{A.35})$$

For exterior flux boundaries, the discretized equation becomes

$$-k_{w,m} \frac{T_{l-1}^n - T_l^{n+1}}{\Delta w_m} = h_c [T_\infty - T_l^{n+1}] + h_r [T_\infty F^{*1/4} - T_l^{n+1}] + \dot{q}_{sw}, \quad (\text{A.36})$$

which solves for  $T_l^{n+1}$  as

$$T_l^{n+1} = \frac{\frac{k_{w,m}}{\Delta w_m} T_{l-1}^n + [h_c + h_r F^{*1/4}] T_\infty - \dot{q}_{sw}}{\frac{k_{w,m}}{\Delta w_m} + [h_c + h_r]}. \quad (\text{A.37})$$

For zero-flux boundaries, the discretized equation becomes

$$\frac{T_{l-1}^n - T_l^{n+1}}{\Delta w_m} = 0, \quad (\text{A.38})$$

which solves for  $T_l^{n+1}$  as

$$T_l^{n+1} = T_{l-1}^n. \quad (\text{A.39})$$

For constant temperature boundaries, the discretized equation becomes

$$T_l^{n+1} = T_c. \quad (\text{A.40})$$

### A.3.2 Fully Implicit Scheme

In the fully implicit scheme, all the temperatures on the right-hand side of Equation A.9 represent the new time-step,  $n + 1$ :

$$\begin{aligned} T_{i,j}^{n+1} - T_{i,j}^n = & c'_{r,p} [T_{i+1,j}^{n+1} - T_{i,j}^{n+1}] + c'_{r,m} [T_{i,j}^{n+1} - T_{i-1,j}^{n+1}] + c_{r,p} [T_{i+1,j}^{n+1} - T_{i,j}^{n+1}] \\ & + c_{r,m} [T_{i,j}^{n+1} - T_{i-1,j}^{n+1}] + c_{z,p} [T_{i,j+1}^{n+1} - T_{i,j}^{n+1}] + c_{z,m} [T_{i,j}^{n+1} - T_{i,j-1}^{n+1}] + \theta \dot{q}. \end{aligned} \quad (\text{A.41})$$

This equation can be rearranged with all the unknown temperatures at the new time-step,  $n + 1$ , on the left-hand side of the equation with constant coefficients and all the constant terms on the right-hand side:

$$\begin{aligned} T_{i,j}^{n+1} [1 + c'_{r,p} + c_{r,p} + c_{z,p} - c'_{r,m} - c_{r,m} - c_{z,m}] + T_{i-1,j}^{n+1} [c'_{r,m} + c_{r,m}] \\ + T_{i+1,j}^{n+1} [-c'_{r,p} - c_{r,p}] + T_{i,j-1}^{n+1} [c_{z,m}] + T_{i,j+1}^{n+1} [-c_{z,p}] = T_{i,j}^n + \theta \dot{q} \end{aligned} \quad (\text{A.42})$$

#### A.3.2.1 Boundary Conditions

For interior flux boundaries, the discretized equation becomes

$$-k_{w,m} \frac{T_{l-1}^{n+1} - T_l^{n+1}}{\Delta w_m} = [h_c + h_r] [T_\infty - T_l^{n+1}] + \dot{q}_{sw}, \quad (\text{A.43})$$

which can be arranged with the unknown temperatures on the left-hand side as

$$T_l^{n+1} \left[ \frac{k_{w,m}}{\Delta w_m} + [h_c + h_r] \right] - T_{l-1}^{n+1} \left[ \frac{k_{w,m}}{\Delta w_m} \right] = [h_c + h_r] T_\infty - \dot{q}_{sw}. \quad (\text{A.44})$$

For exterior flux boundaries, the discretized equation becomes

$$-k_{w,m} \frac{T_{l-1}^{n+1} - T_l^{n+1}}{\Delta w_m} = h_c [T_\infty - T_l^{n+1}] + h_r [T_\infty F^{*1/4} - T_l^{n+1}] + \dot{q}_{sw}, \quad (\text{A.45})$$

which can be arranged with the unknown temperatures on the left-hand side as

$$T_l^{n+1} \left[ \frac{k_{w,m}}{\Delta w_m} + [h_c + h_r] \right] - T_{l-1}^{n+1} \left[ \frac{k_{w,m}}{\Delta w_m} \right] = [h_c + h_r F^{*1/4}] T_\infty - \dot{q}_{sw}. \quad (\text{A.46})$$

For zero-flux boundaries, the discretized equation becomes

$$\frac{T_{l-1}^{n+1} - T_l^{n+1}}{\Delta w_m} = 0, \quad (\text{A.47})$$

which can be arranged with the unknown temperatures on the left-hand side as

$$T_l^{n+1} - T_{l-1}^{n+1} = 0. \quad (\text{A.48})$$

For constant temperature boundaries, the discretized equation becomes

$$T_l^{n+1} = T_c. \quad (\text{A.49})$$

### A.3.3 Crank-Nicolson Scheme

In the Crank-Nicolson scheme, the right-hand side of the equation is the average of the explicit and fully implicit schemes: In the fully implicit scheme, all the temperatures on the right-hand side of Equation A.9 represent the new time-step,  $n + 1$ :

$$\begin{aligned} T_{i,j}^{n+1} - T_{i,j}^n = & \frac{1}{2} \left[ \left[ c'_{r,p} [T_{i+1,j}^{n+1} - T_{i,j}^{n+1}] + c'_{r,m} [T_{i,j}^{n+1} - T_{i-1,j}^{n+1}] + c_{r,p} [T_{i+1,j}^{n+1} - T_{i,j}^{n+1}] \right. \right. \\ & \left. \left. + c_{r,m} [T_{i,j}^{n+1} - T_{i-1,j}^{n+1}] + c_{z,p} [T_{i,j+1}^{n+1} - T_{i,j}^{n+1}] + c_{z,m} [T_{i,j}^{n+1} - T_{i,j-1}^{n+1}] \right] \right. \\ & \left. + [c'_{r,p} [T_{i+1,j}^n - T_{i,j}^n] + c'_{r,m} [T_{i,j}^n - T_{i-1,j}^n] + c_{r,p} [T_{i+1,j}^n - T_{i,j}^n] + c_{r,m} [T_{i,j}^n - T_{i-1,j}^n] \right. \\ & \left. + c_{z,p} [T_{i,j+1}^n - T_{i,j}^n] + c_{z,m} [T_{i,j}^n - T_{i,j-1}^n] \right] + \theta \dot{q}. \end{aligned} \quad (\text{A.50})$$

This equation can be rearranged with all the unknown temperatures at the new time-step,  $n + 1$ , on the left-hand side of the equation with constant coefficients and all the constant terms on the right-hand side:

$$\begin{aligned} & T_{i,j}^{n+1} \left[ 1 + \frac{1}{2} [c'_{r,p} + c_{r,p} + c_{z,p} - c'_{r,m} - c_{r,m} - c_{z,m}] \right] + T_{i-1,j}^{n+1} \frac{1}{2} [c'_{r,m} + c_{r,m}] \\ & + T_{i+1,j}^{n+1} \frac{1}{2} [-c'_{r,p} - c_{r,p}] + T_{i,j-1}^{n+1} \frac{1}{2} [c_{z,m}] + T_{i,j+1}^{n+1} \frac{1}{2} [-c_{z,p}] \\ & = T_{i,j}^n \left[ 1 + \frac{1}{2} [c'_{r,m} + c_{r,m} + c_{z,m} - c'_{r,p} - c_{r,p} - c_{z,p}] \right] + T_{i-1,j}^n \frac{1}{2} [-c'_{r,m} - c_{r,m}] \\ & + T_{i+1,j}^n \frac{1}{2} [c'_{r,p} + c_{r,p}] + T_{i,j-1}^n \frac{1}{2} [-c_{z,m}] + T_{i,j+1}^n \frac{1}{2} [c_{z,p}] + \theta \dot{q}. \end{aligned} \quad (\text{A.51})$$

#### A.3.3.1 Boundary Conditions

The boundary conditions for the Crank-Nicolson scheme are identical to those of the fully implicit scheme.



### A.3.4 Alternating Direction Explicit (ADE) Scheme

In the ADE scheme, two discretized equations are solved independently. In the upward sweep, all the lower indexed temperature differences on the right-hand side of Equation A.9 represent the new time-step,  $n + 1$  and all the higher indexed temperature differences represent the previous time-step,  $n$ . The temperatures calculated in the upward sweep are designated by  $U$ :

$$U_{i,j}^{n+1} - U_{i,j}^n = c'_{r,p} [U_{i+1,j}^n - U_{i,j}^n] + c'_{r,m} [U_{i,j}^{n+1} - U_{i-1,j}^{n+1}] + c_{r,p} [U_{i+1,j}^n - U_{i,j}^n] + c_{r,m} [U_{i,j}^{n+1} - U_{i-1,j}^{n+1}] + c_{z,p} [U_{i,j+1}^n - U_{i,j}^n] + c_{z,m} [U_{i,j}^{n+1} - U_{i,j-1}^{n+1}] + \theta \dot{q}. \quad (\text{A.52})$$

This equation can be solved explicitly for the temperature at the new time-step,  $n + 1$ :

$$U_{i,j}^{n+1} = \left[ U_{i,j}^n [1 - c'_{r,p} - c_{r,p} - c_{z,p}] - U_{i-1,j}^{n+1} [c'_{r,m} + c_{r,m}] + U_{i+1,j}^n [c'_{r,p} + c_{r,p}] - U_{i,j-1}^{n+1} [c_{z,m}] + U_{i,j+1}^n [c_{z,p}] + \theta \dot{q} \right] [1 - c'_{r,m} - c_{r,m} - c_{z,m}]^{-1} \quad (\text{A.53})$$

In the downward sweep, all the higher indexed temperature differences on the right-hand side of Equation A.9 represent the new time-step,  $n + 1$  and all the lower indexed temperature differences represent the previous time-step,  $n$ . The temperatures calculated in the downward sweep are designated by  $V$ :

$$V_{i,j}^{n+1} - V_{i,j}^n = c'_{r,p} [V_{i+1,j}^{n+1} - V_{i,j}^{n+1}] + c'_{r,m} [V_{i,j}^n - V_{i-1,j}^n] + c_{r,p} [V_{i+1,j}^{n+1} - V_{i,j}^{n+1}] + c_{r,m} [V_{i,j}^n - V_{i-1,j}^n] + c_{z,p} [V_{i,j+1}^{n+1} - V_{i,j}^{n+1}] + c_{z,m} [V_{i,j}^n - V_{i,j-1}^n] + \theta \dot{q}. \quad (\text{A.54})$$

This equation can be solved explicitly for the temperature at the new time-step,  $n + 1$ :

$$V_{i,j}^{n+1} = \left[ V_{i,j}^n [1 + c'_{r,m} + c_{r,m} + F] - V_{i-1,j}^n [c'_{r,m} + c_{r,m}] + V_{i+1,j}^{n+1} [c'_{r,p} + c_{r,p}] - V_{i,j-1}^n [F] + V_{i,j+1}^{n+1} [c_{z,p}] + \theta \dot{q} \right] [1 + c'_{r,p} + c_{r,p} + c_{z,p}]^{-1} \quad (\text{A.55})$$

The final temperature is calculated as follows:

$$T_{i,j}^{n+1} = \frac{U_{i,j}^{n+1} + V_{i,j}^{n+1}}{2}. \quad (\text{A.56})$$

### A.3.4.1 Boundary Conditions

The ADE boundary conditions follow the same pattern of higher and lower indices. The equations below provide only the cases where indices are increasing in a direction normal to the boundary. Cases where indices are decreasing can be derived by inference.

For interior flux boundaries, the discretized equation for the upward sweep becomes

$$-k_{w,m} \frac{U_{l-1}^{n+1} - U_l^{n+1}}{\Delta w_m} = [h_c + h_r] [T_\infty - U_l^{n+1}] + \dot{q}_{sw}, \quad (\text{A.57})$$

which solves for  $T_l^{n+1}$  as

$$U_l^{n+1} = \frac{\frac{k_{w,m}}{\Delta w_m} U_{l-1}^{n+1} + [h_c + h_r] T_\infty - \dot{q}_{sw}}{\frac{k_{w,m}}{\Delta w_m} + [h_c + h_r]}. \quad (\text{A.58})$$

The discretized equation for the downward sweep becomes

$$-k_{w,m} \frac{V_{l-1}^n - V_l^{n+1}}{\Delta w_m} = [h_c + h_r] [T_\infty - V_l^{n+1}] + \dot{q}_{sw}, \quad (\text{A.59})$$

which solves for  $T_l^{n+1}$  as

$$V_l^{n+1} = \frac{\frac{k_{w,m}}{\Delta w_m} V_{l-1}^n + [h_c + h_r] T_\infty - \dot{q}_{sw}}{\frac{k_{w,m}}{\Delta w_m} + [h_c + h_r]}. \quad (\text{A.60})$$

For exterior flux boundaries, the discretized equation for the upward sweep becomes

$$-k_{w,m} \frac{U_{l-1}^{n+1} - U_l^{n+1}}{\Delta w_m} = h_c [T_\infty - U_l^{n+1}] + h_r [T_\infty F^{*1/4} - U_l^{n+1}] + \dot{q}_{sw}, \quad (\text{A.61})$$

which solves for  $T_l^{n+1}$  as

$$U_l^{n+1} = \frac{\frac{k_{w,m}}{\Delta w_m} U_{l-1}^{n+1} + [h_c + h_r F^{*1/4}] T_\infty - \dot{q}_{sw}}{\frac{k_{w,m}}{\Delta w_m} + [h_c + h_r]}. \quad (\text{A.62})$$

The discretized equation for the downward sweep becomes

$$-k_{w,m} \frac{V_{l-1}^n - V_l^{n+1}}{\Delta w_m} = h_c [T_\infty - V_l^{n+1}] + h_r [T_\infty F^{*1/4} - V_l^{n+1}] + \dot{q}_{sw}, \quad (\text{A.63})$$

which solves for  $T_l^{n+1}$  as

$$V_l^{n+1} = \frac{\frac{k_{w,m}}{\Delta w_m} V_{l-1}^n + [h_c + h_r F^{*1/4}] T_\infty - \dot{q}_{sw}}{\frac{k_{w,m}}{\Delta w_m} + [h_c + h_r]}. \quad (\text{A.64})$$

For zero-flux boundaries, the discretized equation for the upward sweep becomes

$$\frac{U_{l-1}^{n+1} - U_l^{n+1}}{\Delta w_m} = 0, \quad (\text{A.65})$$

which solves for  $T_l^{n+1}$  as

$$U_l^{n+1} = U_{l-1}^{n+1}. \quad (\text{A.66})$$

The discretized equation for the downward sweep becomes

$$\frac{V_{l-1}^n - V_l^{n+1}}{\Delta w_m} = 0, \quad (\text{A.67})$$

which solves for  $T_l^{n+1}$  as

$$V_l^{n+1} = V_{l-1}^n. \quad (\text{A.68})$$

For constant temperature boundaries, the discretized equation for both sweeps becomes

$$T_l^{n+1} = T_c. \quad (\text{A.69})$$

### A.3.5 Alternating Direction Implicit (ADI) Scheme

In the ADI scheme, each sub-time-step is represented by a different discretized equation. In two dimensions, there are two sub-time-steps within each time-step, and the value of  $\theta$  in Equation A.18 should be adjusted to reflect the sub-time-step size,  $\Delta t/2$ .

In the first sub-time-step, all the temperatures in the  $r$  terms represent the new sub-time-step,  $n + 1/2$ , and all the temperatures in the  $z$  represent the previous sub-time-step,  $n$ :

$$\begin{aligned} T_{i,j}^{n+1/2} - T_{i,j}^n &= [2 - f] \left[ c'_{r,p} \left[ T_{i+1,j}^{n+1/2} - T_{i,j}^{n+1/2} \right] + c'_{r,m} \left[ T_{i,j}^{n+1/2} - T_{i-1,j}^{n+1/2} \right] \right] \\ &+ c_{r,p} \left[ T_{i+1,j}^{n+1/2} - T_{i,j}^{n+1/2} \right] + c_{r,m} \left[ T_{i,j}^{n+1/2} - T_{i-1,j}^{n+1/2} \right] \\ &+ f \left[ c_{z,p} \left[ T_{i,j+1}^n - T_{i,j}^n \right] + c_{z,m} \left[ T_{i,j}^n - T_{i,j-1}^n \right] \right] + \theta \dot{q}. \end{aligned} \quad (\text{A.70})$$

where  $f$  is the implicit weighting factor.

This equation can be rearranged with all the unknown temperatures at the new sub-time-step,  $n + 1/2$ , on the left-hand side of the equation with constant coefficients and all the constant terms on the right-hand side:

$$\begin{aligned}
& T_{i,j}^{n+1/2} [1 + [2 - f] [c'_{r,p} + c_{r,p} - c'_{r,m} - c_{r,m}]] \\
& + T_{i-1,j}^{n+1/2} [2 - f] [c'_{r,m} + c_{r,m}] + T_{i+1,j}^{n+1/2} [2 - f] [-c'_{r,p} - c_{r,p}] \\
& = T_{i,j}^n [1 + f [c_{z,m} - c_{z,p}]] - T_{i,j-1}^n f [c_{z,m}] + T_{i,j-1}^n f [-c_{z,p}] + \theta \dot{q}
\end{aligned} \tag{A.71}$$

In the second sub-time-step, all the temperatures in the  $z$  terms represent the new sub-time-step,  $n + 1$ , and all the temperatures in the  $r$  represent the previous sub-time-step,  $n + 1/2$ :

$$\begin{aligned}
T_{i,j}^{n+1} - T_{i,j}^{n+1/2} &= f [c'_{r,p} [T_{i+1,j}^{n+1/2} - T_{i,j}^{n+1/2}] + c'_{r,m} [T_{i,j}^{n+1/2} - T_{i-1,j}^{n+1/2}]] \\
& + c_{r,p} [T_{i+1,j}^{n+1/2} - T_{i,j}^{n+1/2}] + c_{r,m} [T_{i,j}^{n+1/2} - T_{i-1,j}^{n+1/2}] \\
& + [2 - f] [c_{z,p} [T_{i,j+1}^{n+1} - T_{i,j}^{n+1}] + c_{z,m} [T_{i,j}^{n+1} - T_{i,j-1}^{n+1}]] + \theta \dot{q}.
\end{aligned} \tag{A.72}$$

This equation can be rearranged with all the unknown temperatures at the new sub-time-step,  $n + 1$ , on the left-hand side of the equation with constant coefficients and all the constant terms on the right-hand side:

$$\begin{aligned}
& T_{i,j}^{n+1} [1 + [2 - f] [c_{z,p} - c_{z,m}]] + T_{i,j-1}^{n+1} [2 - f] [c_{z,m}] + T_{i,j-1}^{n+1} [2 - f] [-c_{z,p}] \\
& = T_{i,j}^{n+1/2} [1 + f [c'_{r,m} + c_{r,m} - c'_{r,p} - c_{r,p}]] \\
& - T_{i-1,j}^{n+1/2} f [c'_{r,m} + c_{r,m}] + T_{i+1,j}^{n+1/2} f [c'_{r,p} + c_{r,p}] + \theta \dot{q}
\end{aligned} \tag{A.73}$$

### A.3.5.1 Boundary Conditions

The boundary conditions for the ADI scheme are identical to those of either the explicit scheme or the fully implicit scheme depending on the orientation of the boundary relative to the implicit direction,  $r$  or  $z$ , for the sub-time-step. When the implicit direction is perpendicular to the boundary the conditions are fully implicit, and when the implicit direction is parallel to the boundary the conditions are explicit.

### A.3.6 Steady-State Solution

The steady-state finite difference formulation, used for some of the initialization methods in Kiva, solves a different continuous equation:

$$\nabla [k\nabla T] + \dot{q} = 0, \quad (\text{A.74})$$

which in an axisymmetric cylindrical coordinate system resolves to

$$\frac{1}{r} \frac{\partial}{\partial r} \left[ rk \frac{\partial T}{\partial r} \right] + \frac{\partial}{\partial z} \left[ k \frac{\partial T}{\partial z} \right] + \dot{q} = 0. \quad (\text{A.75})$$

This equation is independent of time and is discretized as:

$$\begin{aligned} c'_{r,p} [T_{i+1,j} - T_{i,j}] + c'_{r,m} [T_{i,j} - T_{i-1,j}] + c_{r,p} [T_{i+1,j} - T_{i,j}] \\ + c_{r,m} [T_{i,j} - T_{i-1,j}] + c_{z,p} [T_{i,j+1} - T_{i,j}] + c_{z,m} [T_{i,j} - T_{i,j-1}] + \theta \dot{q} = 0. \end{aligned} \quad (\text{A.76})$$

Each of the constant coefficients contains  $\theta$ , which can be divided out of the equation, but it is kept in the equation for consistency with the other finite difference scheme descriptions.

This equation can be rearranged with all the unknown temperatures on the left-hand side of the equation with constant coefficients and all the constant terms on the right-hand side:

$$\begin{aligned} T_{i,j} [c'_{r,m} + c_{r,m} + c_{z,m} - c'_{r,p} - c_{r,p} - c_{z,p}] + T_{i-1,j} [-c'_{r,m} - c_{r,m}] \\ + T_{i+1,j} [c'_{r,p} + c_{r,p}] + T_{i,j-1} [-c_{z,m}] + T_{i,j+1} [c_{z,p}] = -\theta \dot{q} \end{aligned} \quad (\text{A.77})$$

#### A.3.6.1 Boundary Conditions

The boundary conditions for the steady-state solution are identical to those of the fully implicit scheme.

## A.4 Solving the Linear System of Equations

The system of equations generated for the set of discretized cells is generalized as

$$\begin{aligned}
 a_{1,1}T_1 + a_{1,2}T_2 + \dots + a_{1,m}T_m + \dots + a_{1,N}T_N &= b_1 \\
 a_{2,1}T_1 + a_{2,2}T_2 + \dots + a_{2,m}T_m + \dots + a_{2,N}T_N &= b_2 \\
 \vdots & \\
 a_{n,1}T_1 + a_{n,2}T_2 + \dots + a_{n,m}T_m + \dots + a_{n,N}T_N &= b_n \\
 \vdots & \\
 a_{N,1}T_1 + a_{N,2}T_2 + \dots + a_{N,m}T_m + \dots + a_{N,N}T_N &= b_N
 \end{aligned} \tag{A.78}$$

where

- $n$  is equation index,
- $m$  is the cell index,
- $a_{n,m}$  is the constant coefficients for the temperature of cell  $m$  in equation  $n$ ,
- $T_m$  is the temperature of cell  $m$  [K],
- $N$  is the total number of cells in the problem, and
- $b_n$  is the constant term on the right-hand side of equation  $n$

Equation A.78 is represented by a linear system in matrix notation ( $\mathbf{Ax} = \mathbf{b}$ ):

$$\begin{bmatrix} a_{1,1} & a_{1,2} & \cdots & a_{1,N} \\ a_{2,1} & a_{2,2} & \cdots & a_{2,N} \\ \vdots & \vdots & \ddots & \vdots \\ a_{N,1} & a_{N,2} & \cdots & a_{N,N} \end{bmatrix} \begin{bmatrix} T_1 \\ T_2 \\ \vdots \\ T_N \end{bmatrix} = \begin{bmatrix} b_1 \\ b_2 \\ \vdots \\ b_N \end{bmatrix}. \tag{A.79}$$

If there is a single unknown per equation, then the system is solved explicitly, and no linear algebra techniques need be applied. For implicit schemes, where there are potentially multiple unknowns in an equation, the linear system is solved either directly, using Gaussian elimination, or iteratively. The ADI method uses a simplified form of Gaussian elimination specific to tridiagonal matrices (each equation has up to three consecutive non-zero coefficients centered at  $n, n$ ).

## Appendix B

### Mixed Climate Two-Dimensional Approximation Method Test Results

The following results were simulated according to the two-dimensional approximation method test description provided in Section 5.4.

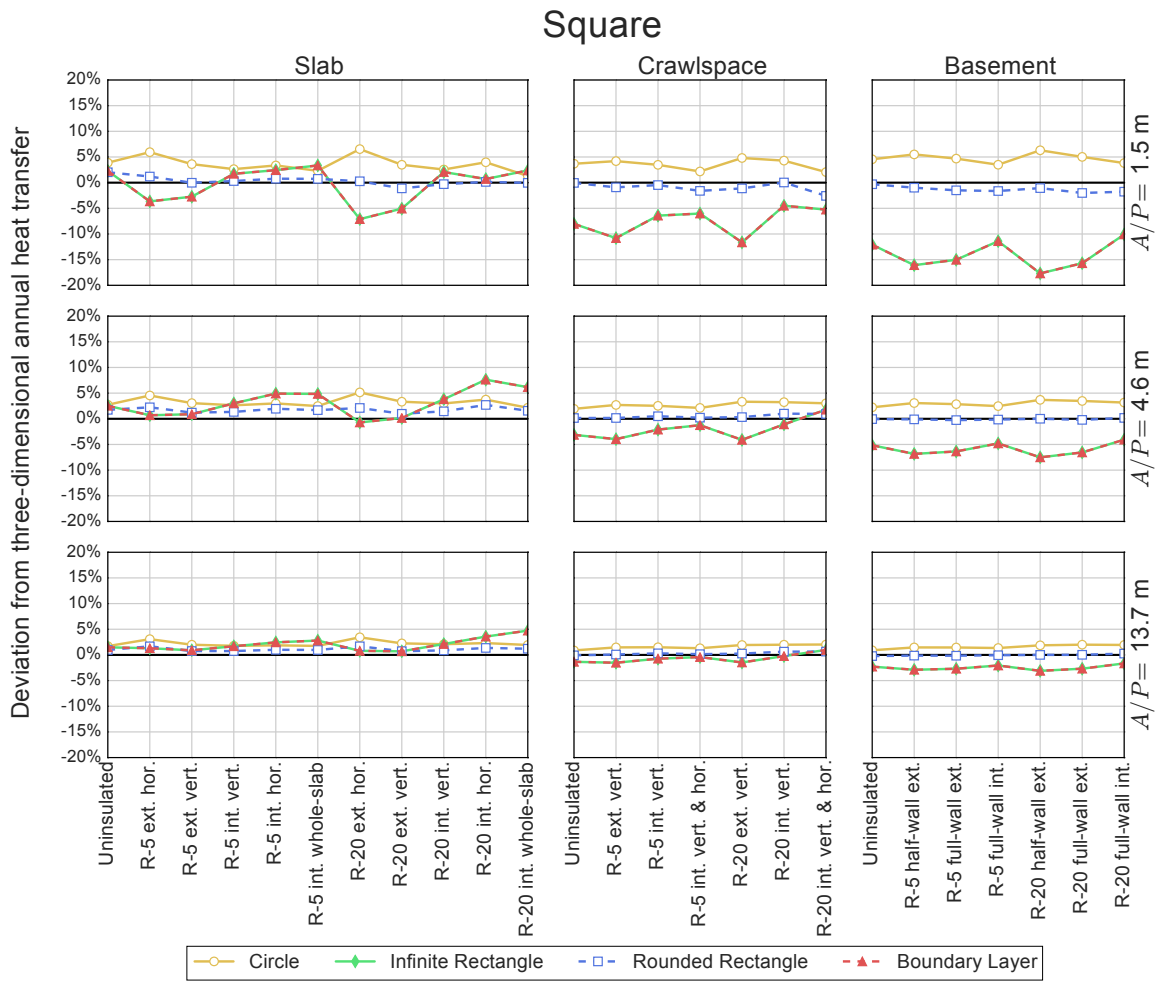


Figure B.1: Percent difference in annual heat transfer between three-dimensional square foundation shapes and two-dimensional approximations



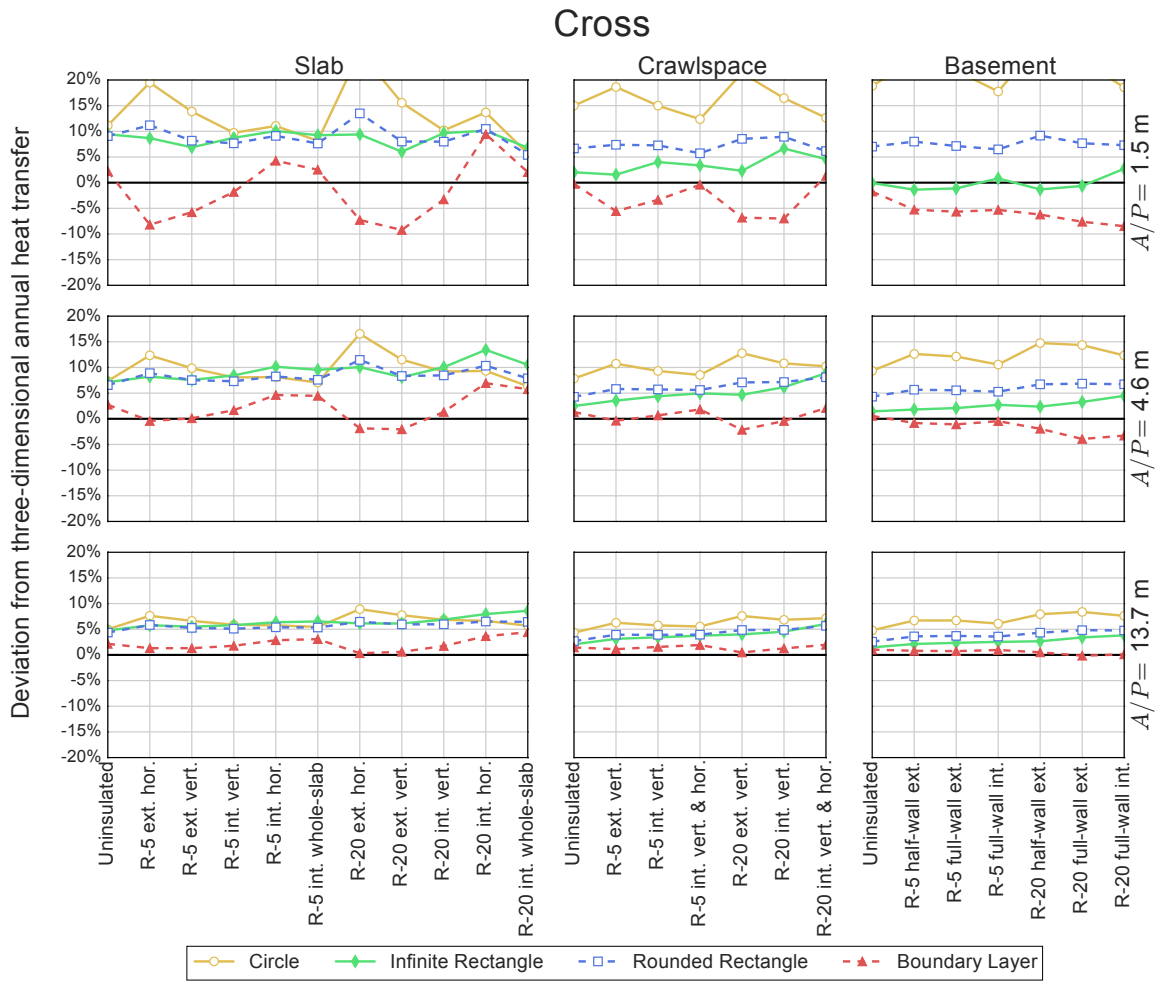


Figure B.2: Percent difference in annual heat transfer between three-dimensional cross-shaped foundations and two-dimensional approximations

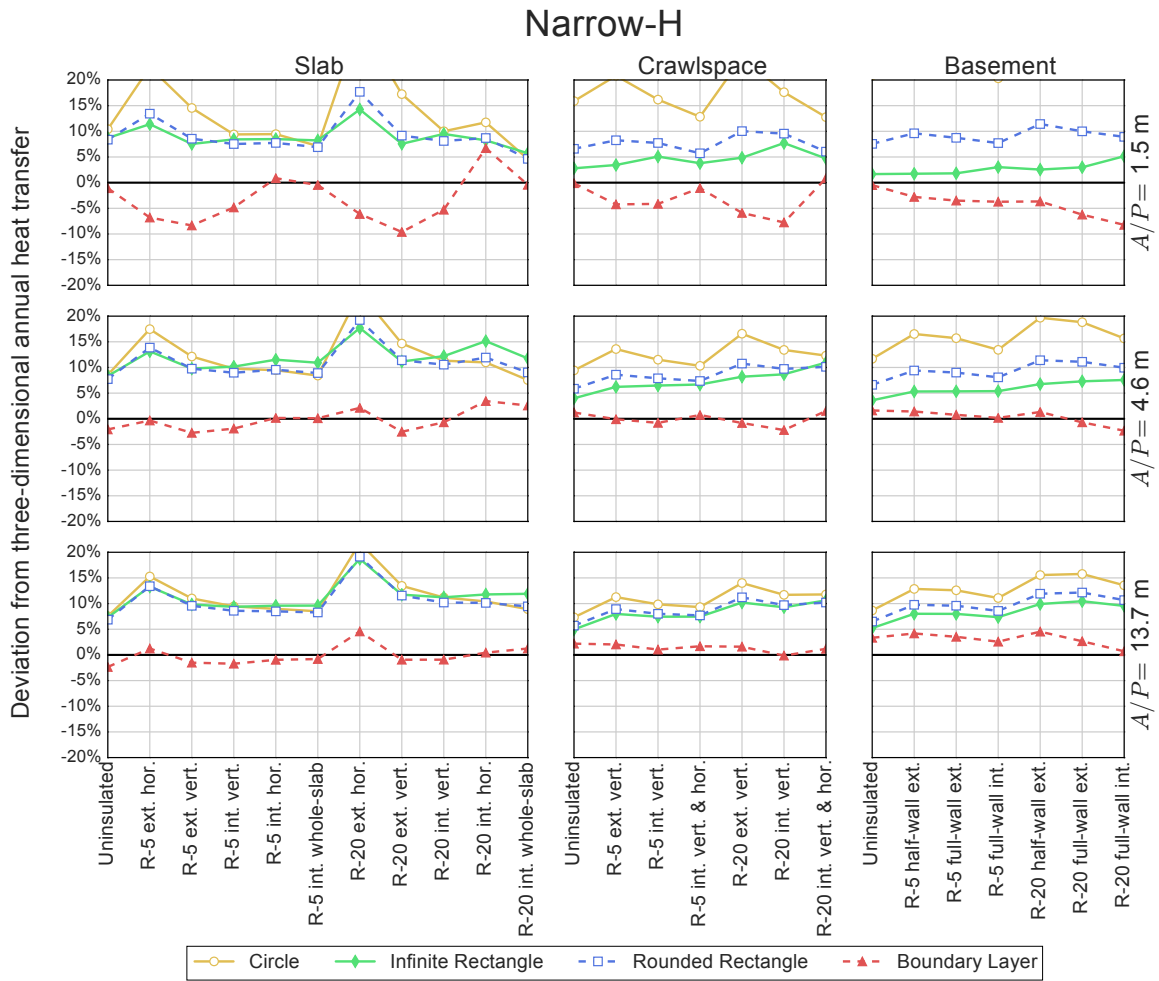


Figure B.3: Percent difference in annual heat transfer between three-dimensional narrow-H foundation shapes and two-dimensional approximations

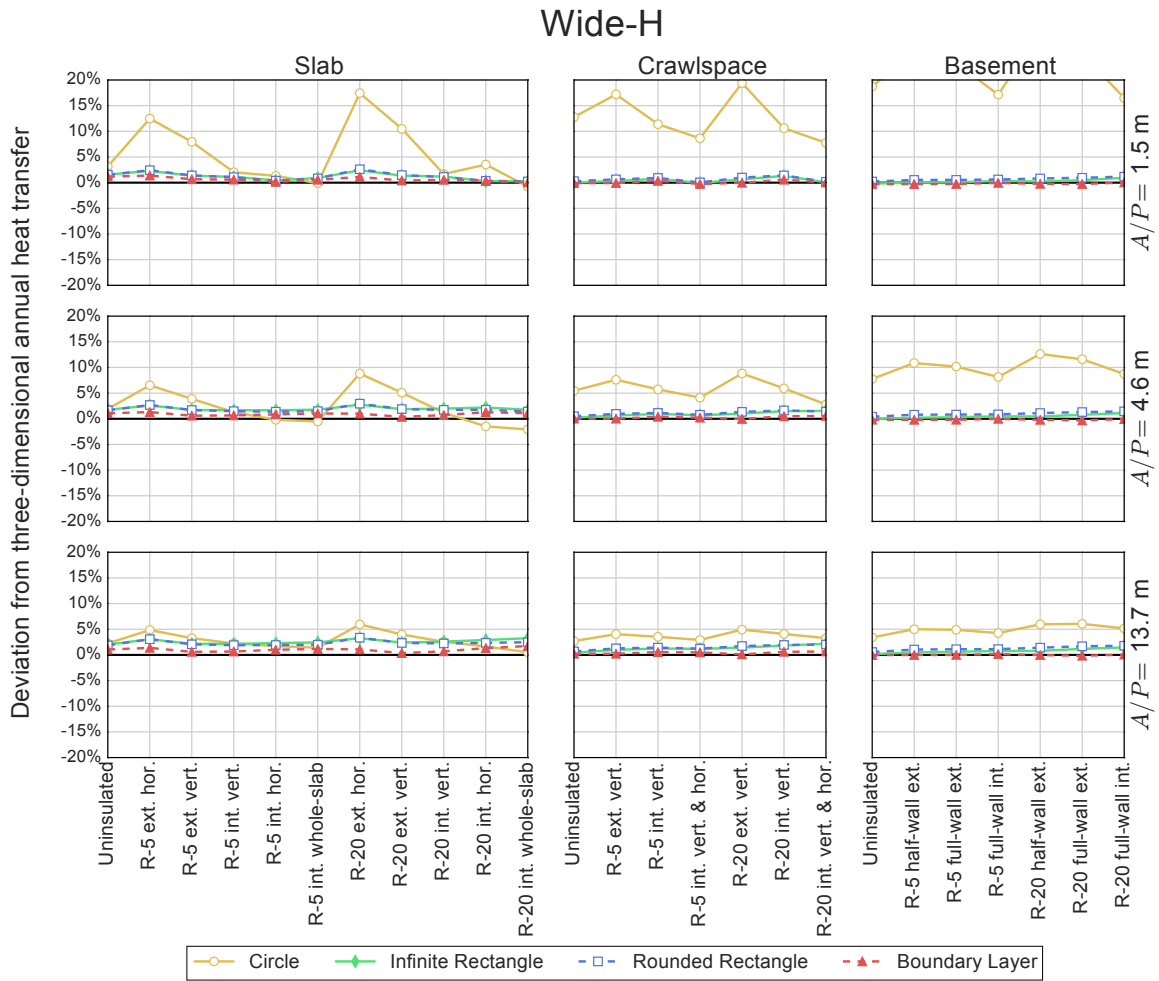


Figure B.4: Percent difference in annual heat transfer between three-dimensional wide-H foundation shapes and two-dimensional approximations

## Appendix C

### Cold Climate Two-Dimensional Approximation Method Test Results

The following results were simulated according to the two-dimensional approximation method test description provided in Section 5.4.

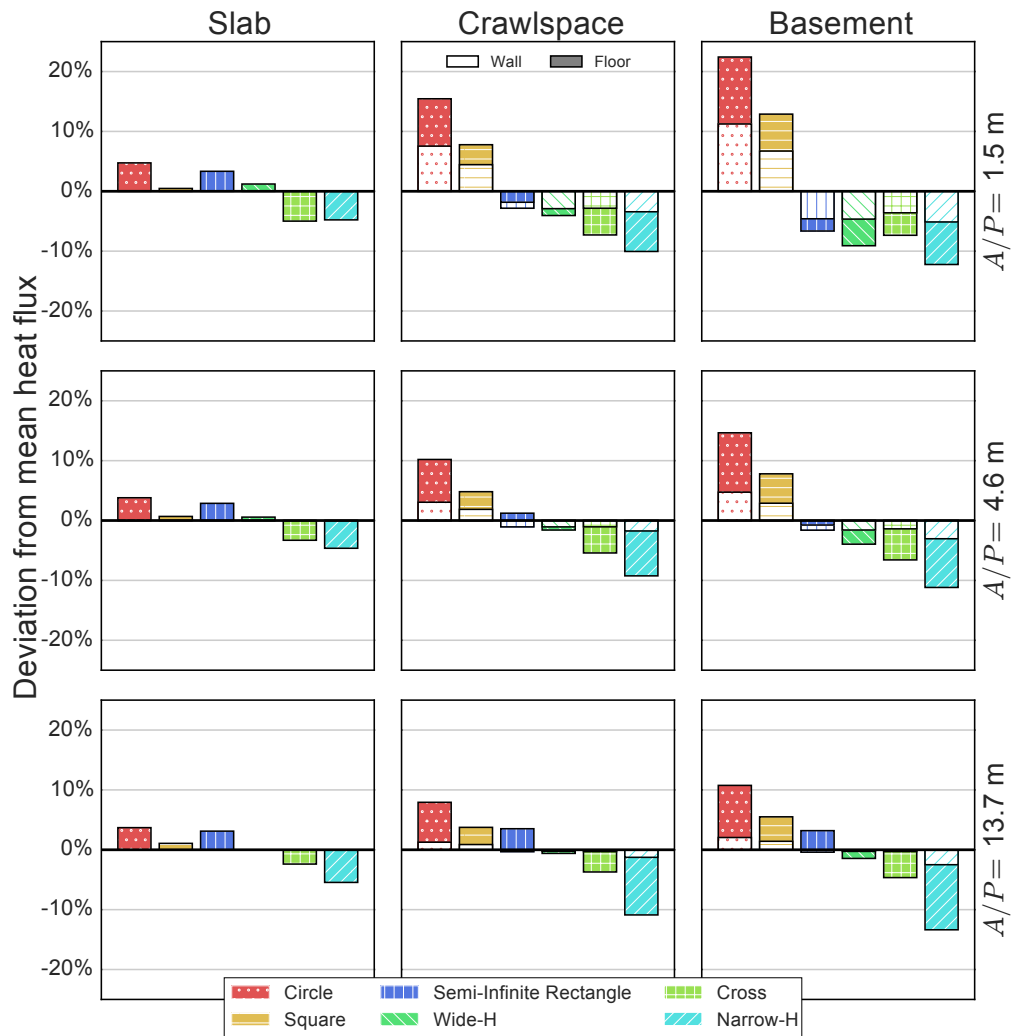


Figure C.1: Comparison of heat flux from a range of uninsulated foundation shapes in the cold climate

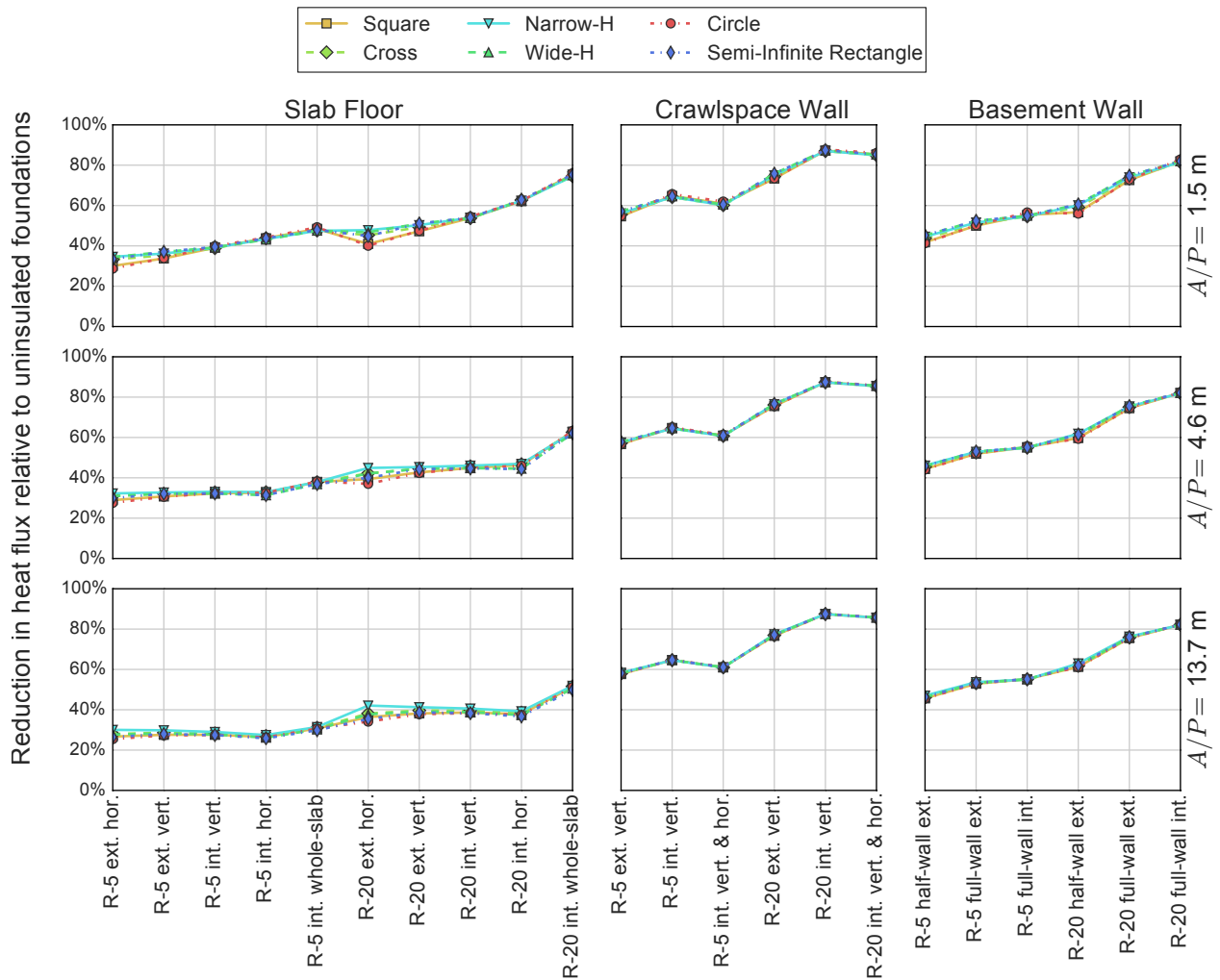


Figure C.2: Heat flux reduction relative to uninsulated foundations in mixed climate for a range of foundation shapes in the cold climate

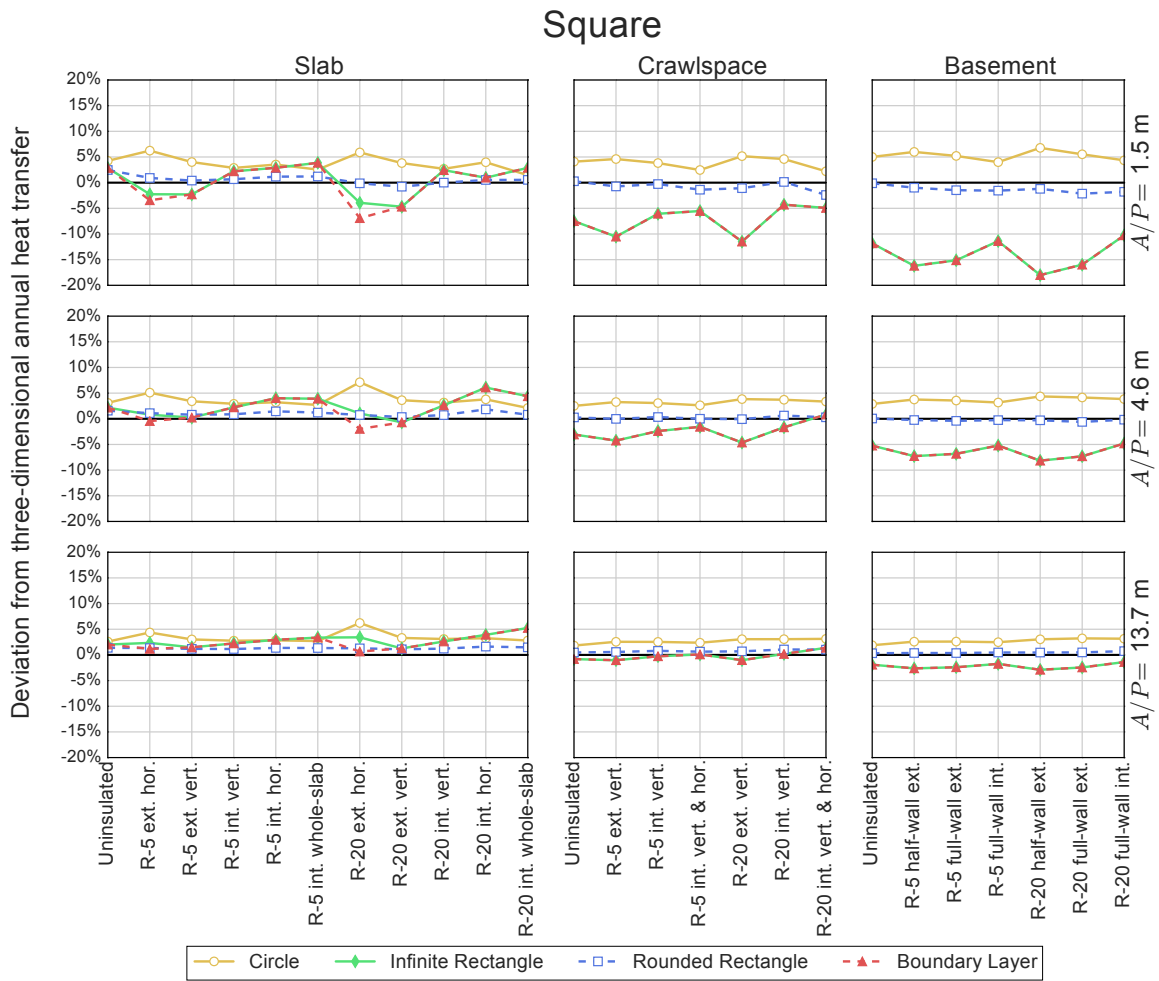


Figure C.3: Percent difference in annual heat transfer between three-dimensional square foundation shapes and two-dimensional approximations in the cold climate

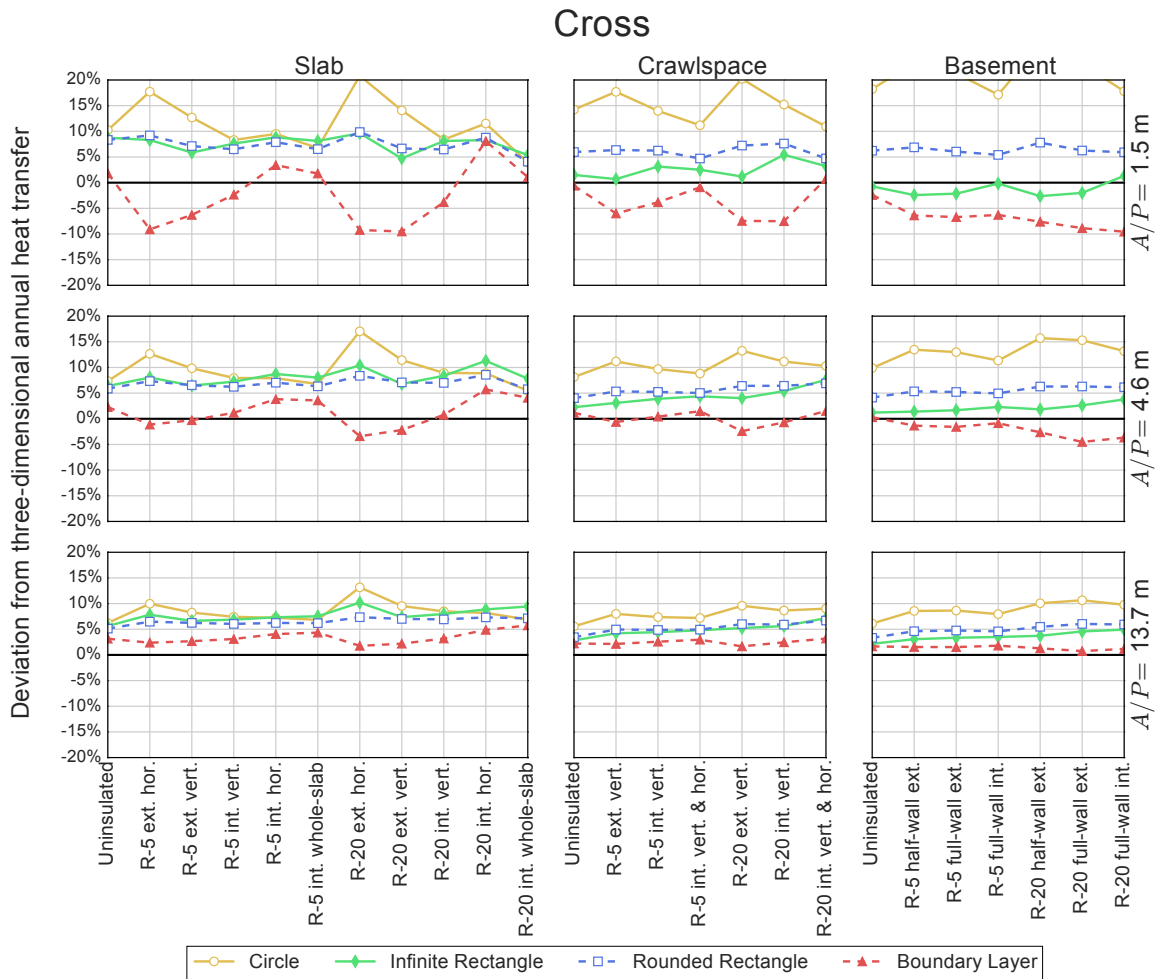


Figure C.4: Percent difference in annual heat transfer between three-dimensional cross-shaped foundations and two-dimensional approximations in the cold climate



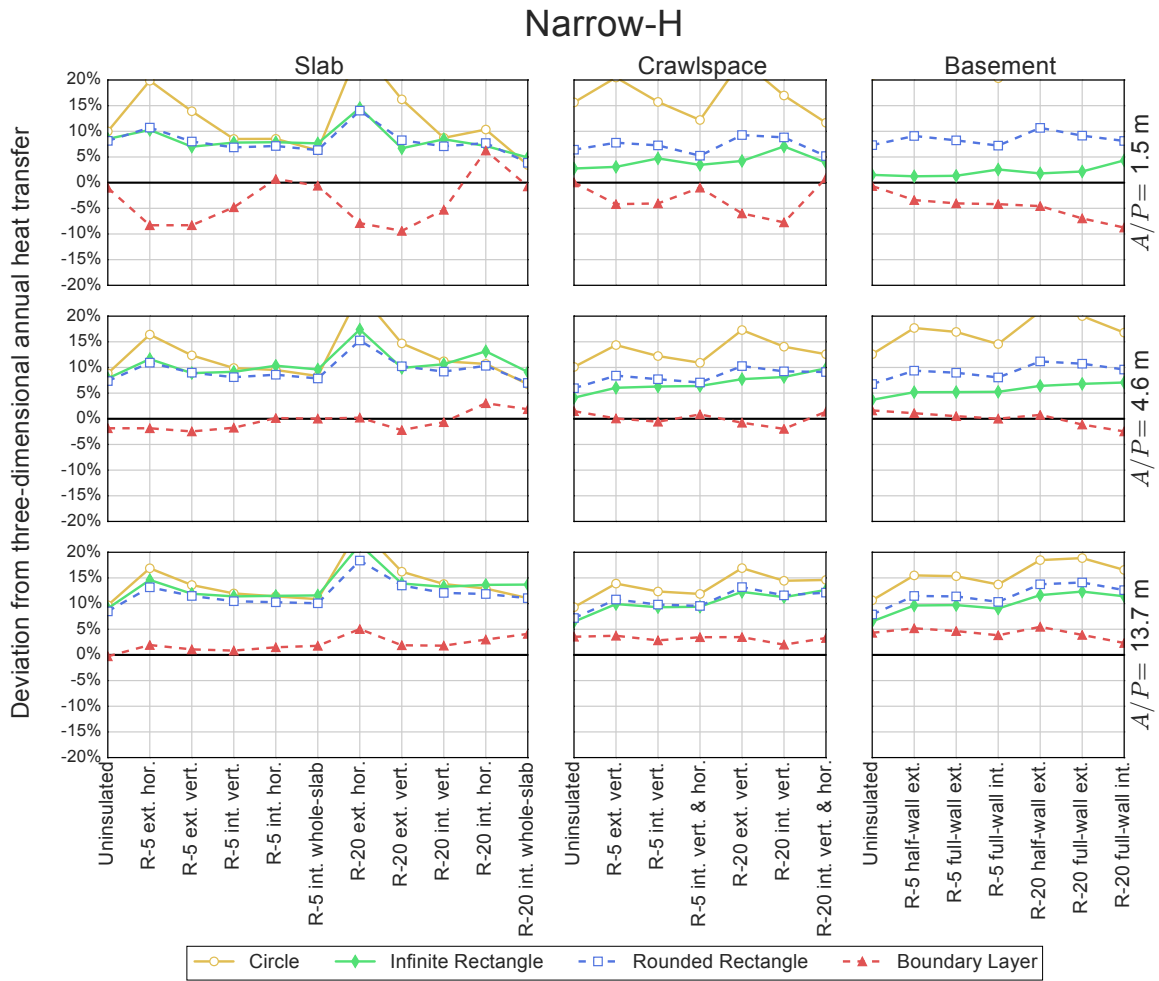


Figure C.5: Percent difference in annual heat transfer between three-dimensional narrow-H foundation shapes and two-dimensional approximations in the cold climate

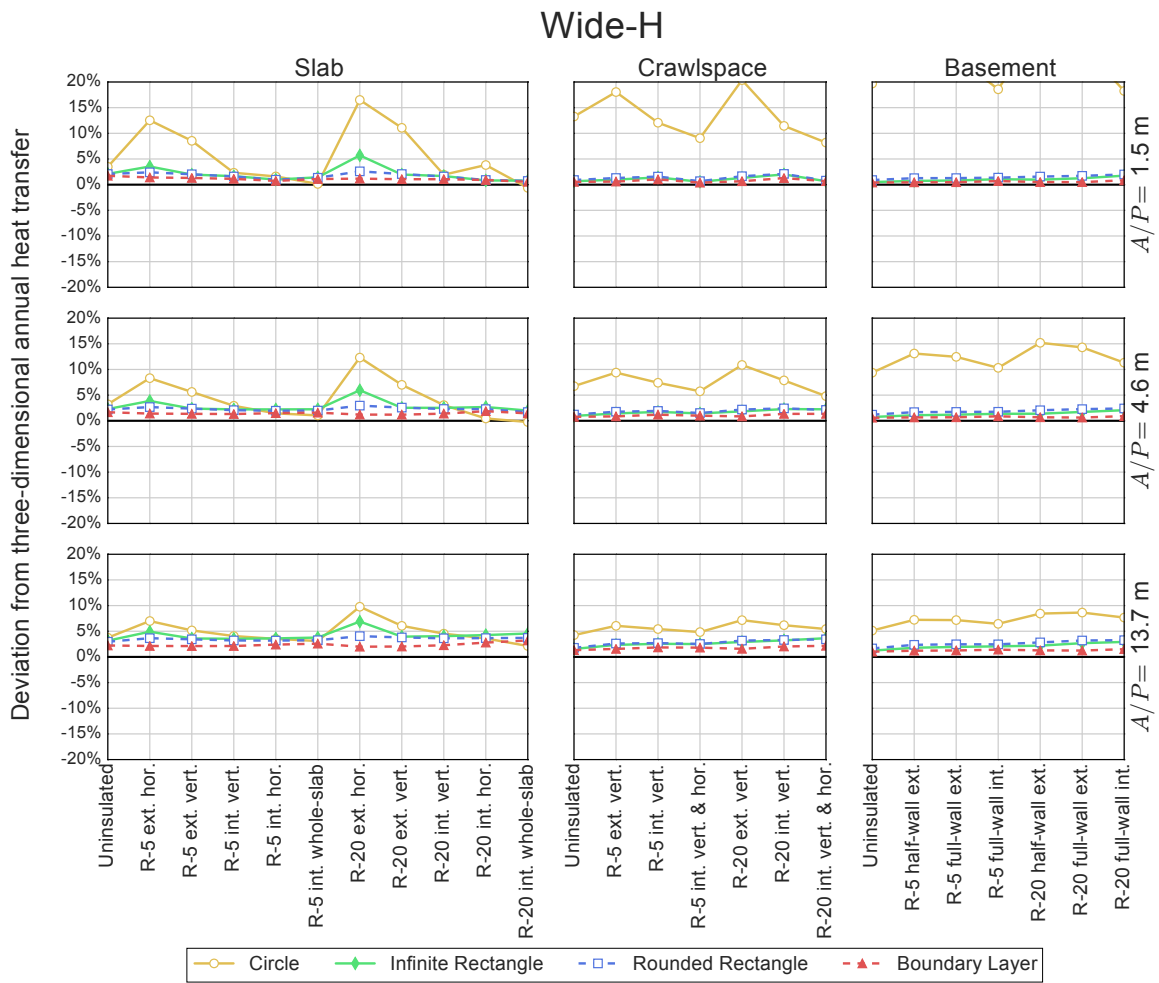


Figure C.6: Percent difference in annual heat transfer between three-dimensional wide-H foundation shapes and two-dimensional approximations in the cold climate

## Appendix D

### Hot Climate Two-Dimensional Approximation Method Test Results

The following results were simulated according to the two-dimensional approximation method test description provided in Section 5.4.

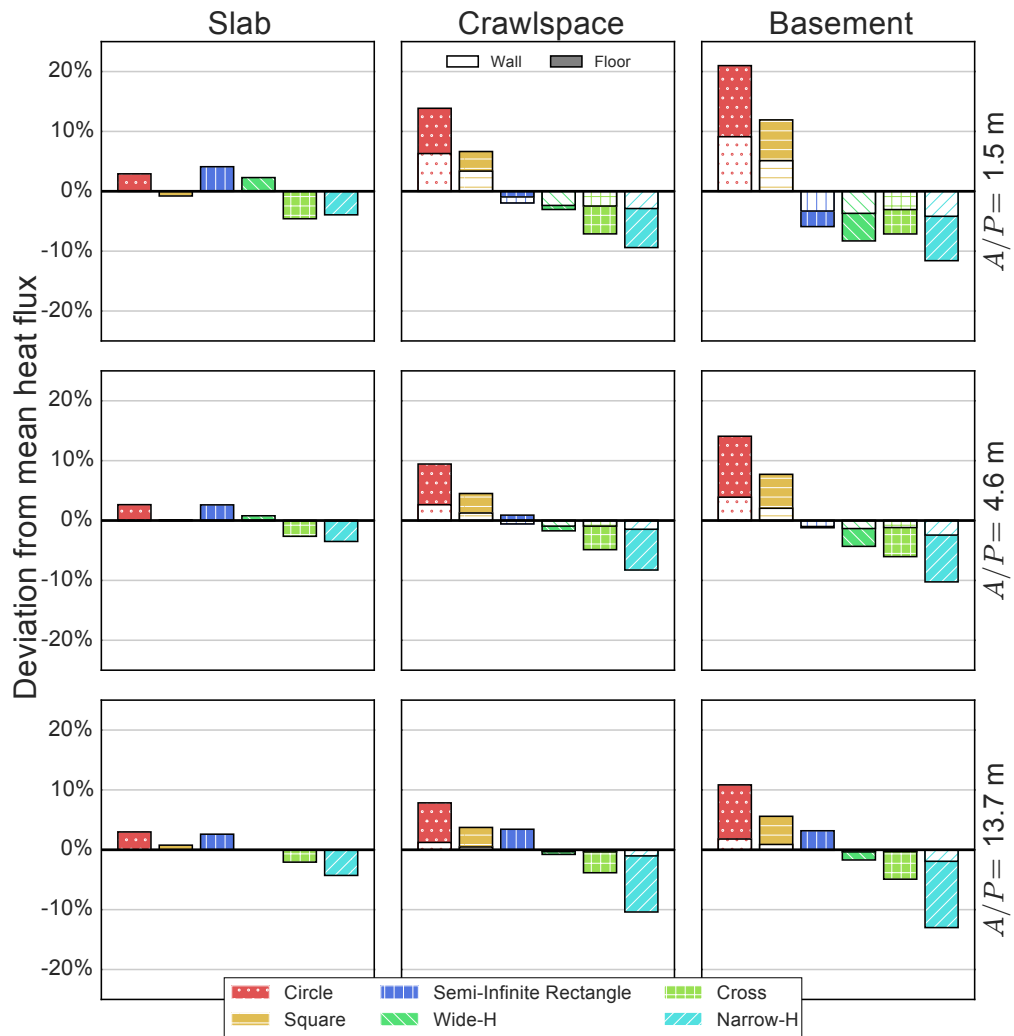


Figure D.1: Comparison of heat flux from a range of uninsulated foundation shapes in the hot climate

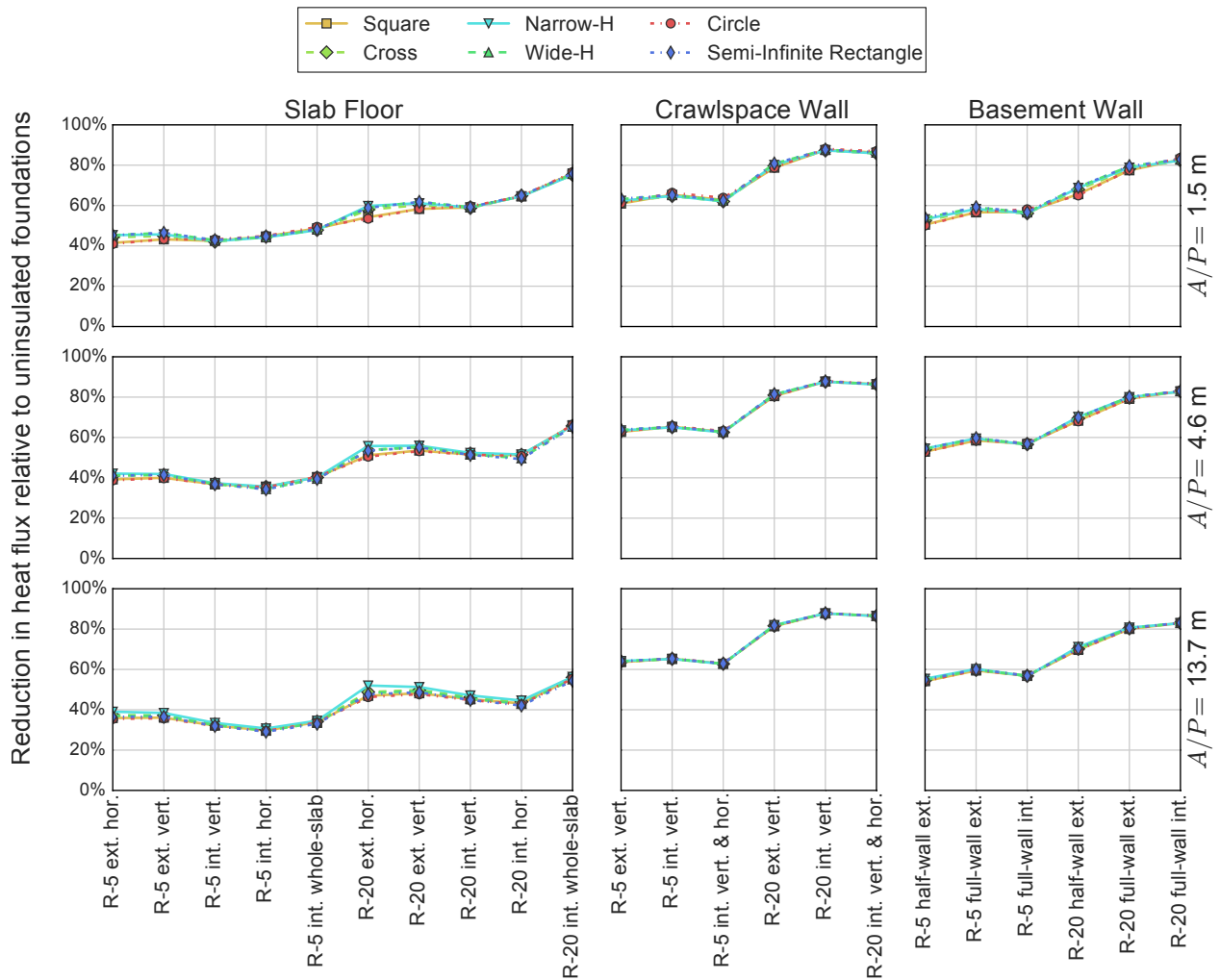


Figure D.2: Heat flux reduction relative to uninsulated foundations in mixed climate for a range of foundation shapes in the hot climate

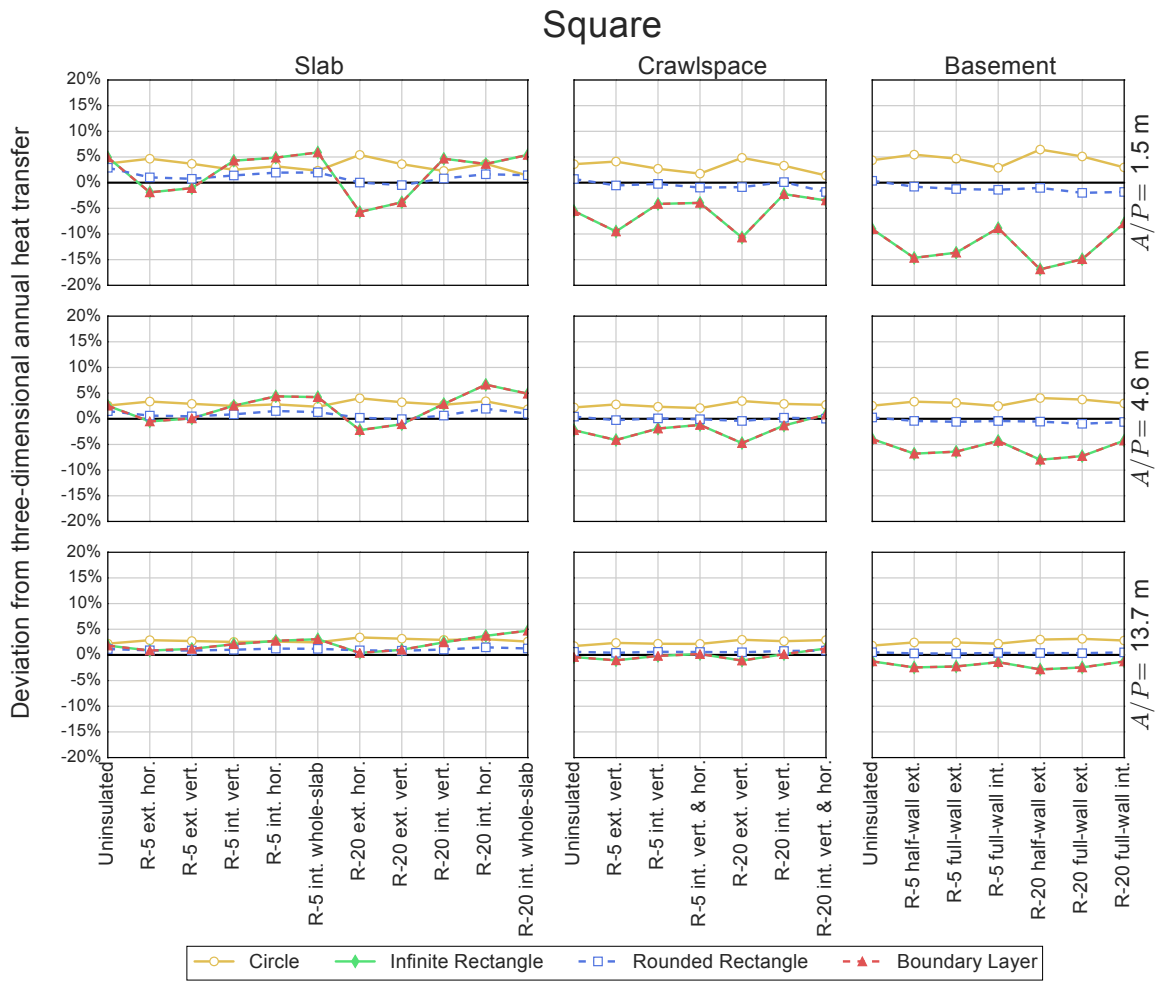


Figure D.3: Percent difference in annual heat transfer between three-dimensional square foundation shapes and two-dimensional approximations in the hot climate

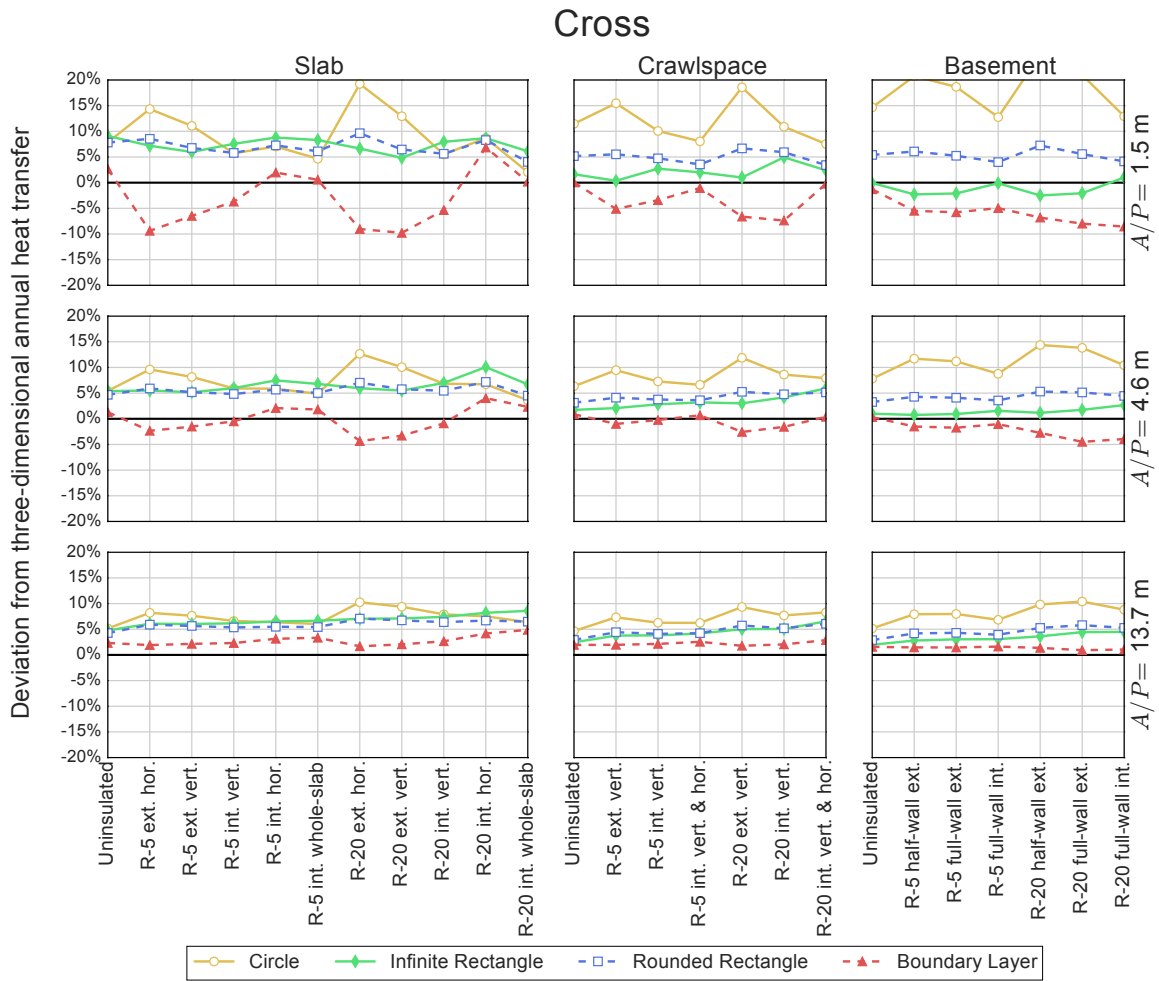


Figure D.4: Percent difference in annual heat transfer between three-dimensional cross-shaped foundations and two-dimensional approximations in the hot climate

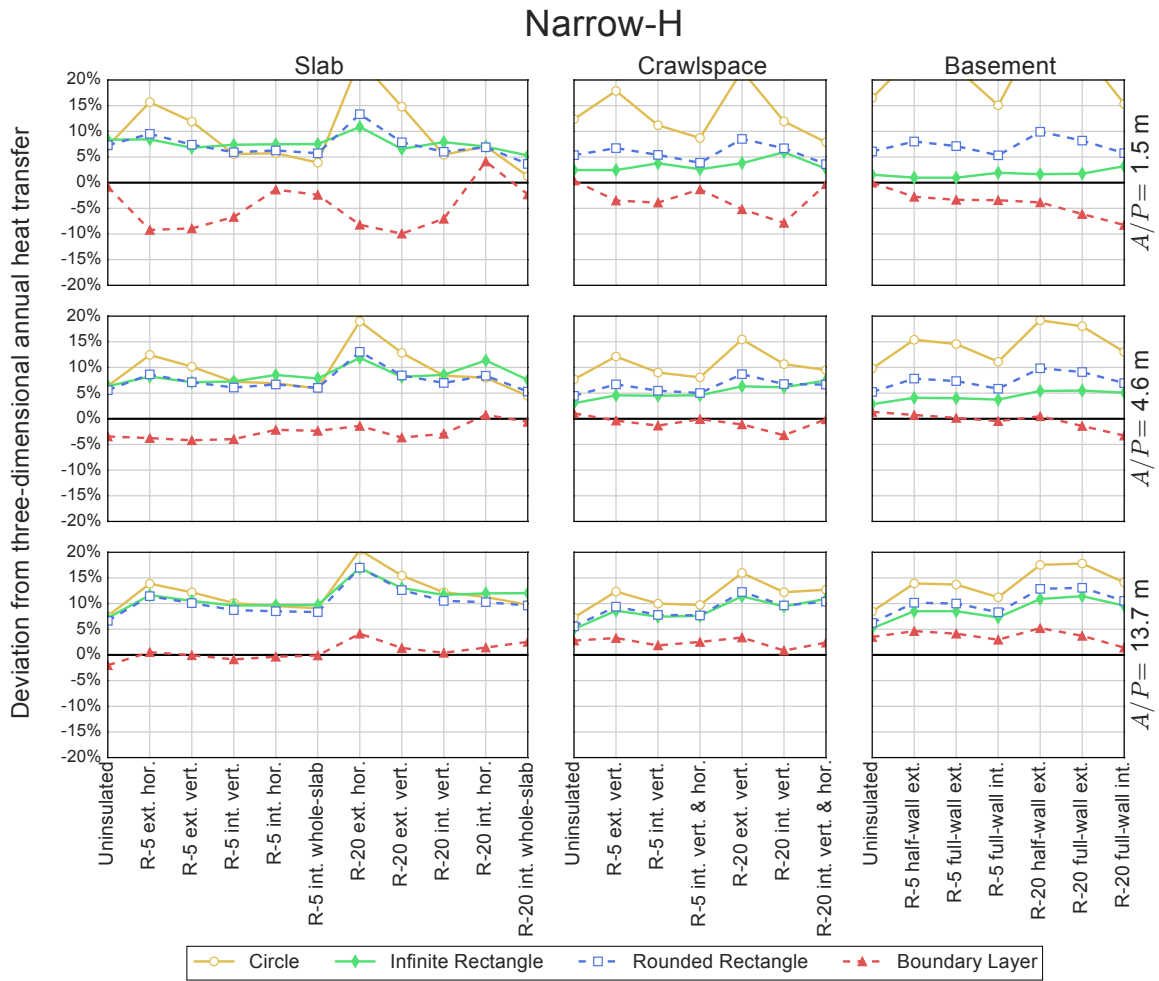


Figure D.5: Percent difference in annual heat transfer between three-dimensional narrow-H foundation shapes and two-dimensional approximations in the hot climate



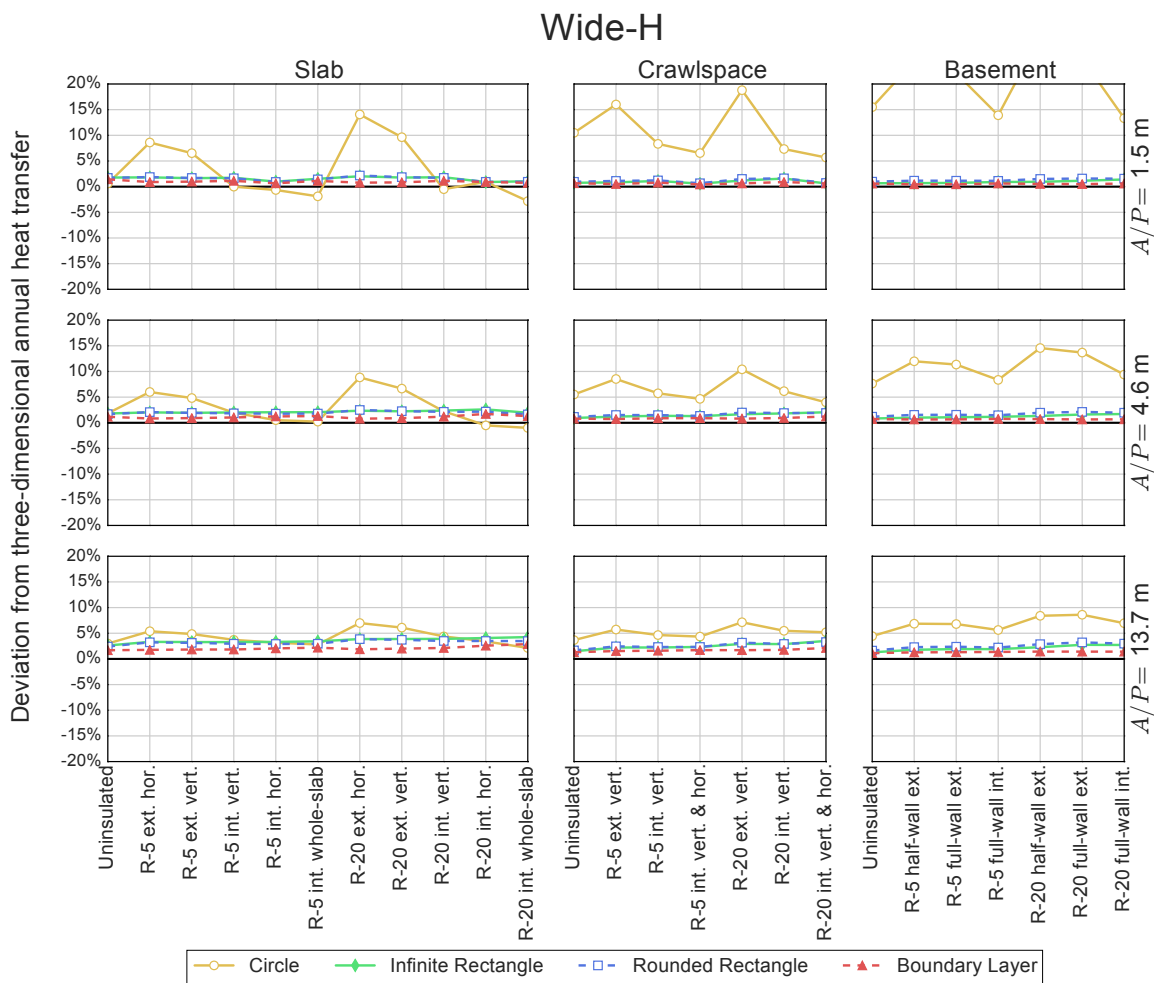


Figure D.6: Percent difference in annual heat transfer between three-dimensional wide-H foundation shapes and two-dimensional approximations in the hot climate

## Appendix E

### Comparisons of Minimum and Maximum Foundation Heat Transfer

The following figures compare simulated annual minimum and maximum heat transfer rates for each two-dimensional approximation method to corresponding three-dimensional simulation results. Results were simulated according to the two-dimensional approximation method test description provided in Section 5.4.

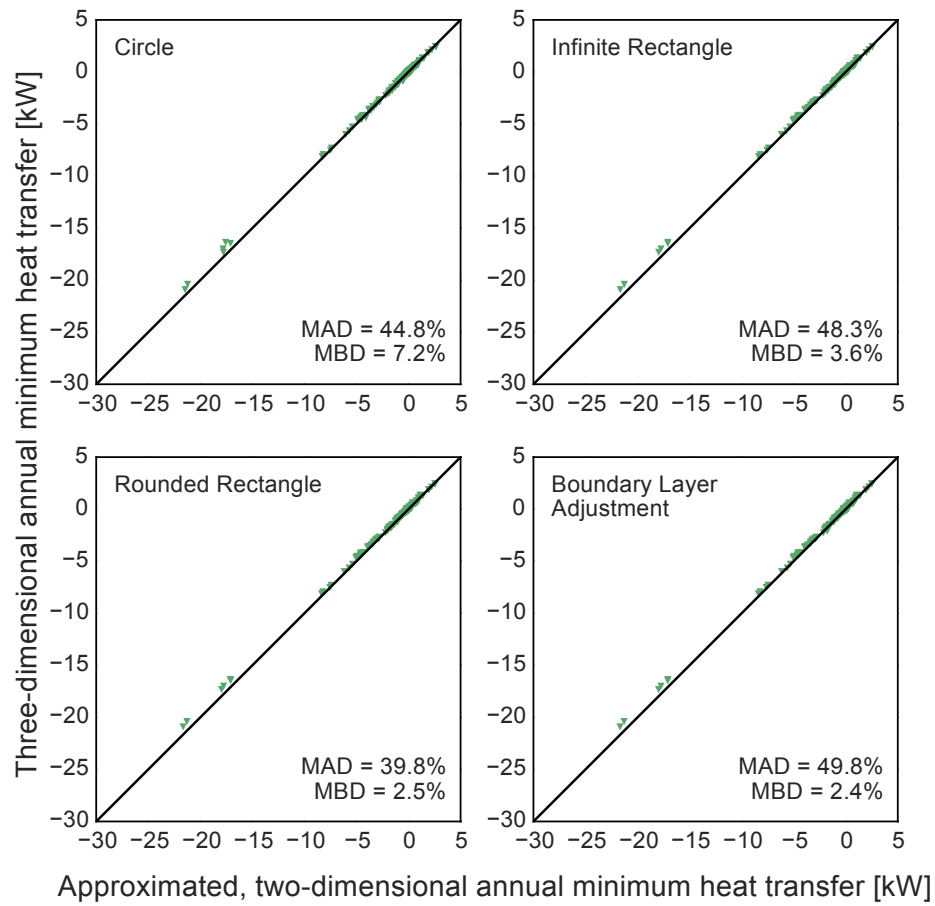


Figure E.1: Comparison of annual minimum heat transfer between three-dimensions and two-dimensional approximations for mixed climate simulations

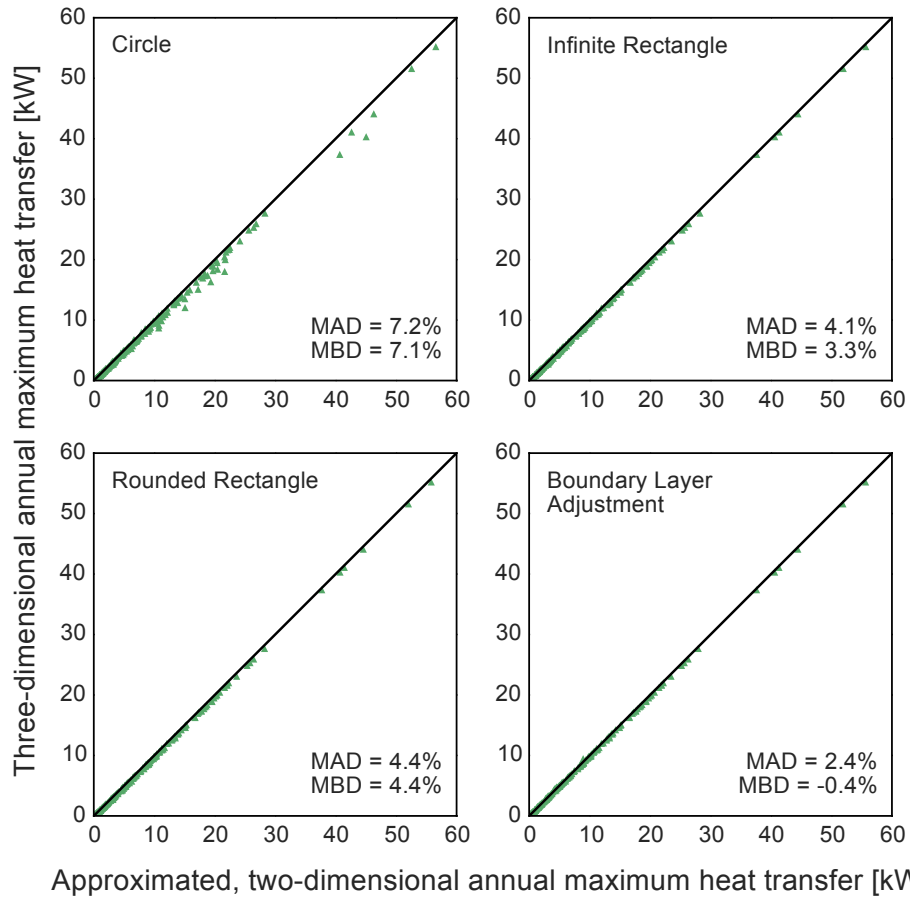


Figure E.2: Comparison of annual maximum heat transfer between three-dimensions and two-dimensional approximations for mixed climate simulations

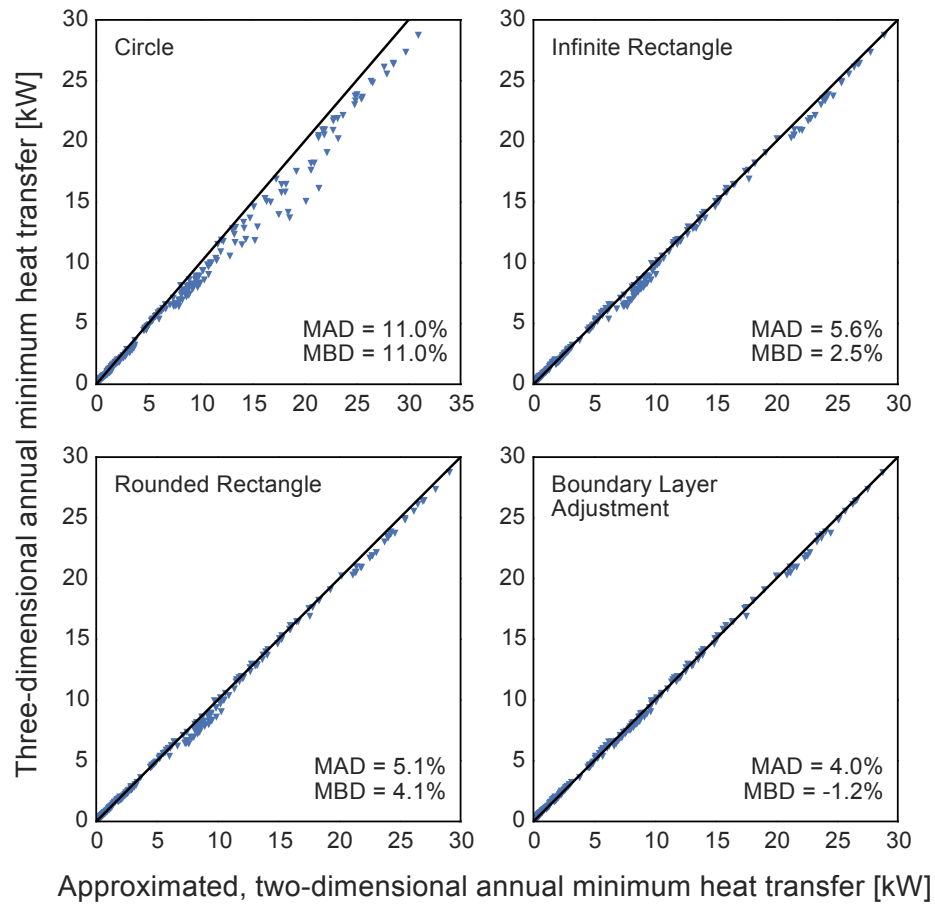


Figure E.3: Comparison of annual minimum heat transfer between three-dimensions and two-dimensional approximations for cold climate simulations

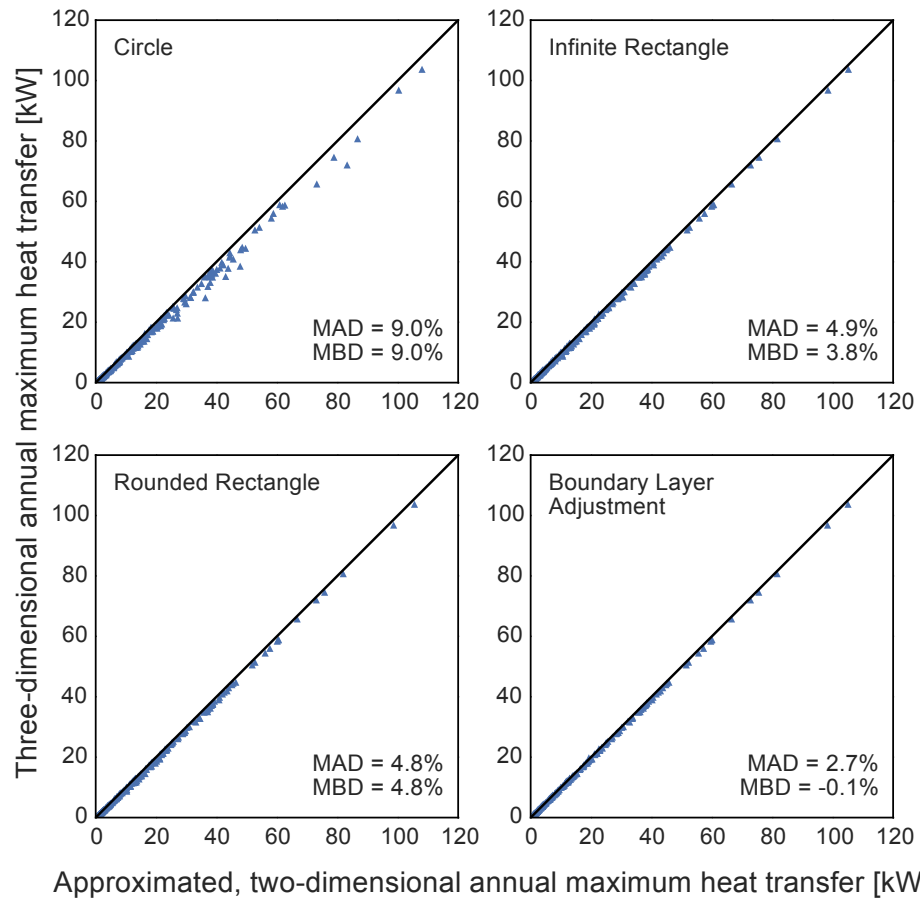


Figure E.4: Comparison of annual maximum heat transfer between three-dimensions and two-dimensional approximations for cold climate simulations

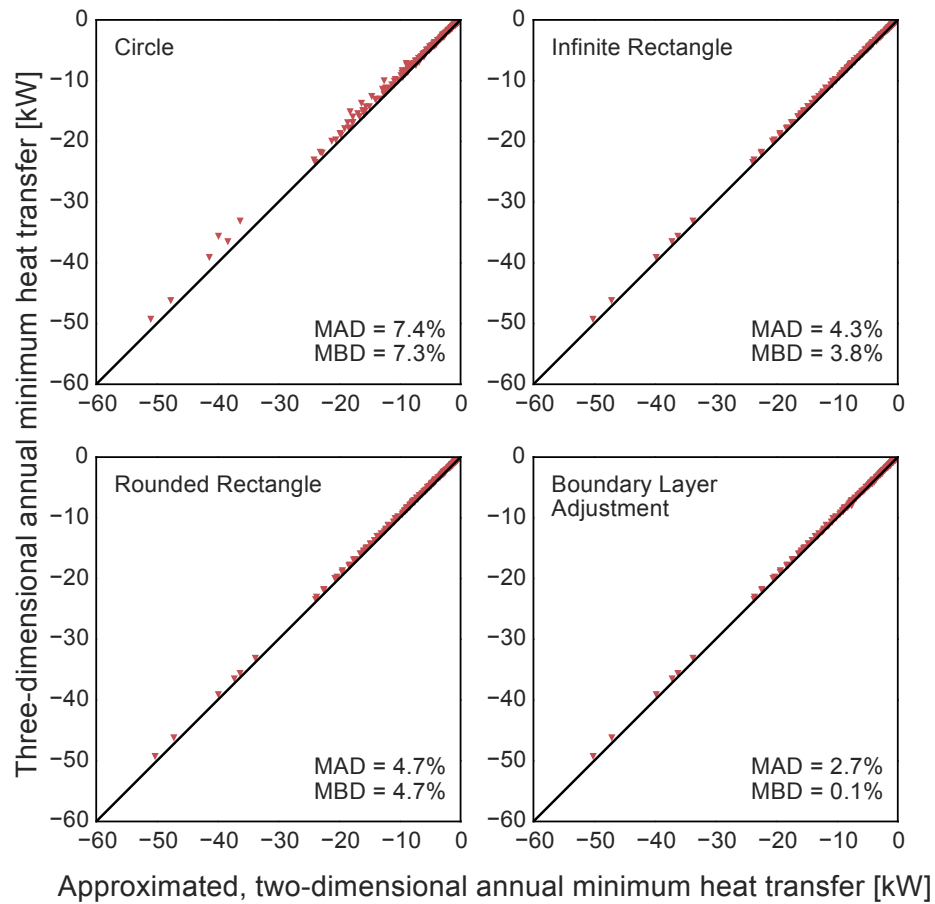


Figure E.5: Comparison of annual minimum heat transfer between three-dimensions and two-dimensional approximations for hot climate simulations

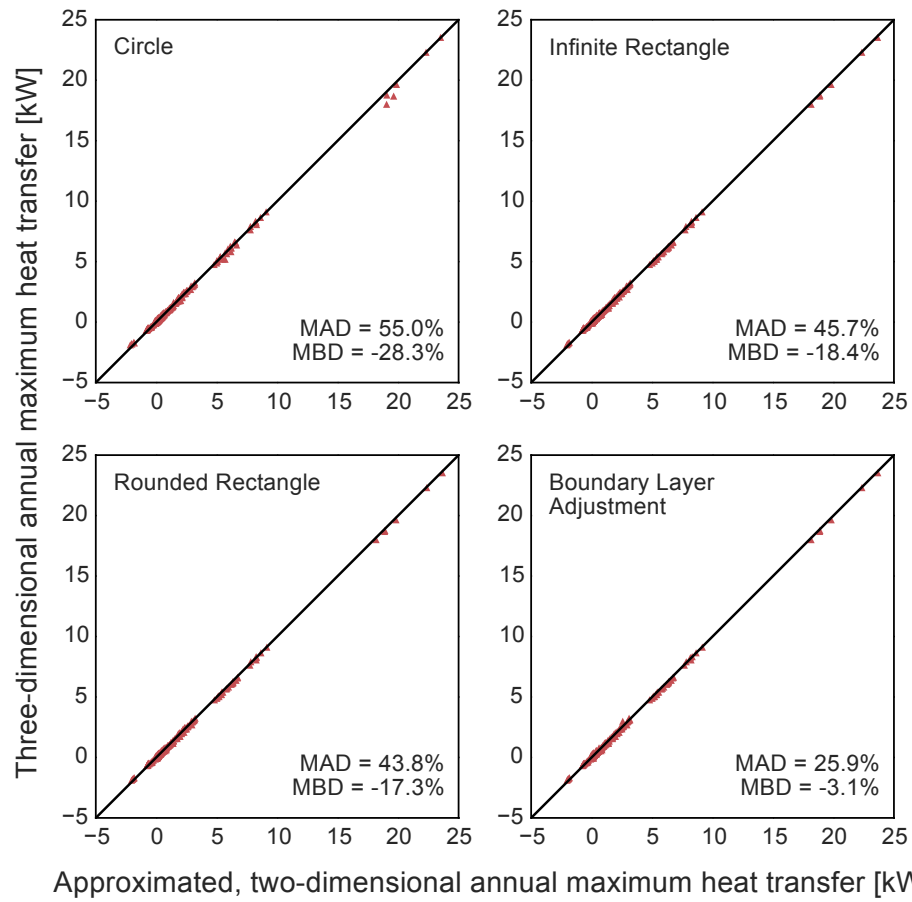


Figure E.6: Comparison of annual maximum heat transfer between three-dimensions and two-dimensional approximations for hot climate simulations